UNIVERSITY *of* TASMANIA

Experimental and Numerical Investigations into the Underwater Explosion Induced Whipping Response of Submerged Platforms

Steven De Candia

BMechEng(hons)

National Centre for Maritime Engineering & Hydrodynamics

Australian Maritime College

Submitted in fulfilment of the requirements for the degree of

Doctor of Philosophy (Maritime Engineering)

University of Tasmania

November, 2018

Abstract

This thesis reports the findings of an experimental and numerical investigation into the whipping response of a submerged platform, due to loading from near-field, non-contact underwater explosion (UNDEX) events.

The experimental investigation examined the whipping response of a generic submerged platform subjected to UNDEX. Eight scenarios were investigated, using different explosive charge sizes, longitudinal, and transverse stand-off locations, to explore the effects of these variables on the platform's whipping response, and to provide validation data for the numerical investigation. It was found that UNDEX stand-off locations near the anti-node of the first bending mode shape induced the most severe whipping responses, while stand-offs near the node of the first bending mode shape had greatly reduced whipping responses.

A numerical model was developed and validated against the experimental results, using incident pressure and strain measurements. Three numerical studies were conducted with the validated numerical model, investigating the effects of additional stand-off distances at the previously explored longitudinal stand-off locations, the whipping response from an intermediate charge size, and the effects of the UNDEX bubble loading on the whipping response by using a shock-only loading model.

From these studies, the following novel contributions were made:

The stand-off distance was found to only affect the whipping severity while the charge size and stand-off location determined the modal contributions of the whipping response.

A comparison of the peak whipping response to the bubble pressure impulse suggests that three distinct forms of whipping could be induced, and these can be determined by the proximity of the UNDEX stand-off location to the nodes and anti-nodes of the platform's first bending mode shape. These were classified as critical, resilient, and general whipping responses.

The critical whipping response occurred when the UNDEX stand-off location was near the anti-node of the first bending mode shape. This was characterised by a dominant response of the first bending mode and minimal contribution from other bending modes in the overall response. The severity of this response increased nonlinearly as the bubble impulse increased and when the bubble pulsation frequency was similar to the first bending mode frequency. This is the most severe form of UNDEX induced whipping.

The resilient whipping response occurred when the UNDEX stand-off location was near the node of the first bending mode shape. This was characterised by minimal contribution of the first bending mode compared to others in the overall response. From these scenarios, the bubble loading had minimal effect on the whipping response. This was confirmed from good correlation in comparisons of the strain responses from experimental measurements and the results from the numerical shock-only loading study. This is the least severe form of UNDEX induced whipping and the most desirable outcome from an unavoidable UNDEX threat.

The general whipping response occurred when the UNDEX stand-off location was between the nodes and anti-nodes of the first bending mode shape. This was characterised by similar contributions of multiple bending mode responses in the overall response. The severity from this response increased linearly for increases in the bubble impulse. It is suggested this is the most likely form of UNDEX induced whipping to occur, based on the large number of variables involved with UNDEX loading and platform response scenarios.

Current analysis methodologies are able to identify the resilient whipping response but some methods that focus on the shock response of a platform may not identify the critical and general whipping responses. This was demonstrated by comparison of the experimental measurements to a numerical shock-only loading models for the most severe UNDEX scenarios, where shock-only loading and response assumptions under-predicted the whipping response by 39 % and 54 % for the critical and general whipping responses respectively.

The relative increase in the severity of the whipping response from a reduction in the stand-off distance was consistent for all similar forms of whipping. This suggests that the whipping severity from many different stand-off distances can be approximated through analysis of only a few scenarios at different stand-off locations on a specific naval platform. It is suggested that this knowledge may allow a rapid assessment tool to be developed that could determine a platform's survivability from a wide variety of UNDEX scenarios.

The trends from each form of whipping severity compared to bubble pressure impulse were examined with limited extrapolation. This suggested that four whipping response analysis regimes exist: far-field elastic, near-field and non-contact elastic, non-contact plastic, and contact damage. Exact limits of these regimes were not identified, and all are promising areas for further investigation.

Acknowledgements

Declarations

Authority of access

The published content of this thesis may be made available for loan and limited copying and communication in accordance with the Copyright Act 1968.

Statement of originality

This thesis contains no material which has been accepted for a degree or diploma by the University of Tasmania or any other institution. To the best of my knowledge and belief, this thesis does not contain any material that infringes copyright or has been previously published or written by another person, except where due acknowledgement is made in the text of the thesis.

Signed: _____   Date: $\underline{30^{th} \text{ October } 2018}$

Steven De Candia

Statement of co-authorship

The following people and institutions contributed to the publication of work undertaken as a part of this thesis:

Candidate:	Mr Steven De Candia	Australian Maritime College, University of Tasmania
Author 1:	Dr Roberto Ojeda	Australian Maritime College, University of Tasmania
Author 2:	A/Prof Jonathan Binns	Australian Maritime College, University of Tasmania
Author 3:	Dr Stuart Cannon	Australian Maritime College, University of Tasmania; Defence Science and Technology Group, Department of Defence
Author 4:	Dr Max Ratcliffe	Babcock Australasia
Author 5:	Mr Warren Reid	Defence Science and Technology Group, Department of Defence
Author 6:	Dr Craig Flockhart	Defence Science and Technology Group, Department of Defence

As part of this PhD investigation the candidate and the aforementioned authors produced three peer-reviewed publications. The individual contributions to the work undertaken for each publication is detailed below:

1. De Candia, S., Ojeda, R., Reid, W. D., Ratcliffe, M. & Binns, J. *The Whipping Response of a Submerged Free-Free Cylinder Due to Underwater Explosions*. in *International Maritime Conference - Pacific 2017*. Sydney, NSW. (2017).

This first publication is a conference paper that consists of a partial literature review that is also presented within Chapter 2 of this thesis. It also provides a limited overview of the experimental investigation that is presented in Chapter 3 of this thesis.

The Candidate was lead author of this paper and contributed 80 % to the planning and execution of the research and resulting paper.

Authors 1, 2, 4, and 5 contributed 5 % each to the interpretation of the work and critical revision of the paper.

2. De Candia, S., Flockhart, C. & Cannon, S. M. *Whipping analysis of a submerged free-free cylinder*. in *9th Australasian Congress on Applied Mechanics (ACAM9)*. Sydney, NSW. (Institution of Engineers Australia, 2017).

The second publication is a conference paper and reviews literature that is presented in Chapter 2 of this thesis. An initial numerical validation study was also conducted, which formed the requirements for a more detailed validation process that is presented in Chapter 4 of this thesis. This publication was awarded first prize for best student paper and presentation at the conference.

The Candidate was lead author of this paper and contributed 90 % to the planning and execution of the research and resulting paper.

Authors 3 and 6 contributed 5 % each to the interpretation of the work and critical revision of the paper.

3. De Candia, S., Ojeda, R., Ratcliffe, M. & Reid, W. D. *The whipping response of a submerged platform subjected to near-field, non-contact underwater explosions*. Report No.: DST-Group-RR-0451, (Defence Science and Technology Group, Fishermans Bend, VIC, 2018).

The third publication is a DST Group Research Report. This report a comprehensive overview of the experimental investigation which is also presented in Chapter 3 of this thesis.

The Candidate was lead author of this paper and contributed 85 % to the planning and execution of the research and resulting paper.

Authors 1, 4, and 5 contributed 5 % each to the interpretation of the work and critical revision of the report.

We the undersigned agree with the above stated "proportion of work undertaken" for each of the above published peer-reviewed manuscripts contributing to the thesis:

Signed:

        Dr Roberto Ojeda   A/Prof Shuhong Chai
        Primary Supervisor   *Head of School*
        National Centre for Maritime   National Centre for Maritime
        Engineering & Hydrodynamics   Engineering & Hydrodynamics
        Australian Maritime College   Australian Maritime College
        University of Tasmania   University of Tasmania

Date: 30th October 2018

Acronyms and abbreviations

ALE	Arbitrary Lagrangian-Eulerian
AMC	Australian Maritime College
BEM	Boundary Element Method
BM	Bending Mode
CFD	Computational Fluid Dynamics
CM	Circumferential Mode
CPU	Central Processing Unit
DAA	Doubly Asymptotic Approximation
DDAM	Dynamic Design Analysis Method
DNA	Defence Nuclear Agency
DOF	Degree of Freedom
DST Group	Defence Science and Technology Group, formally DSTO
E	Experimental event
EFD	Energy Flux Density
EN	Numerical result of experimental event
FFT	Fast Fourier Transform
FR	Frequency Range damping
FSI	Fluid Structure Interaction
MKS	Meters-Kilograms-Seconds unit system
N	Numerical event
NAVSEA	Naval Sea Systems Command
NS	Numerical shock-only loading event
ONR	Office of Naval Research
PETN	Pentaerythritol tetranitrate
PHS-BUB	Price-Hicks shock bubble model
PVSS	Pseudo Velocity Shock Spectra
RD	Rayleigh damping
RDFR	Combined Rayleigh and Frequency Range damping
SOP	Stand-off point
SPH	Smoothed Particle Hydrodynamics
SRS	Shock Response Spectra

TNT	Trinitrotoluene
TOA	Time of arrival
UD	Undamped
UETF	Underwater Explosion Test Facility
UNDEX	Underwater Explosion
US	United States of America
USA	Underwater Shock Analysis code
WWI	World War I
WWII	World War II

Nomenclature

A_n	Maximum bubble radius for cycle n	[m]
c	Structure acoustic velocity	[m/s]
c_f	Fluid acoustic velocity	[m/s]
D	Depth	[m]
EFD	Energy Flux Density	[m.MPa]
F_1, F_2	Frequency damping range	[Hz]
g	Acceleration due to gravity	[m/s^2]
HSF	Hull Shock Factor	[kg$^{1/2}$/m]
I	Pressure impulse	[MPa.ms]
I_B	Bubble pressure impulse	[MPa.ms]
I_S	Shock wave pressure impulse	[MPa.ms]
I_T	Total pressure impulse	[MPa.ms]
J_n	Maximum bubble radius coefficient for cycle n	[m$^{4/3}$/kg$^{1/3}$]
K_n	Bubble period coefficient for cycle n	[s.m$^{5/6}$/kg$^{1/3}$]
KSF	Keel Shock Factor	[kg$^{1/2}$/m]
L	Stand-off location from amidships	[m]
L_e	Element length	[m]
L_n	Normalised length	
L_P	Platform length	[m]
n	Bubble cycle	
P	Pressure	[MPa]
P_{atm}	Atmospheric (Hydrostatic) pressure	[MPa]
P_M	Peak pressure	[MPa]
PV	Pseudo Velocity	[m/s]
R	Stand-off distance	[m]
R^2	Coefficient of determination	
S	Similitude parameter	[kg$^{1/3}$/m]
SF	Shock Factor	[kg$^{1/2}$/m]
t	Time	[ms]
T_n	Bubble period for cycle n	[ms]
W	Charge mass	[kg]

z_{max}	Maximum displacement	[m]
γ	Bubble proximity parameter	
Δ	Difference between experimental and numerical results	[%]
δ	Buoyancy parameter	
ΔP	Difference between ambient and saturated vapour pressure	[Pa]
ΔT	Explicit numerical timestep	[s]
ζ	Damping factor	
θ	Shock wave decay constant	[ms]
λ	Bubble relative size parameter	
ρ_f	Fluid density	[kg/m^3]
Φ	Angle of incidence	[°]
ω	Response frequency	[rad/s]

Table of Contents

List of Figures

List of Tables

Chapter 1. Background and objectives

1.1. Background and context

A submarine and its crew can have a significant impact in many peace and wartime operations. In its modern iteration, a submarine is one of the most dynamic vessels within any navy, with the capability to conduct intelligence gathering, troop deployment, and act as both an offensive deterrence and front-line combatant. Stealth is the most significant advantage of the submarine, and this is provided very effectively by the underwater environment. However, the natural hostility of the environment does not grant this willingly, and a submarine is in constant conflict with natural forces, in addition to potential man-made threats. This can easily turn the advantage over to adversaries if left unchecked.

Submarines for military applications have been tried and tested with different levels of success since the early 16th century. During the end of the 19th century, John Phillip Holland designed and demonstrated the first modern submarine *Holland I*, which was later adopted by the British and U.S. Navies [1]. Improvements to propulsion technology, energy storage and weaponry significantly increased the interest in submarines by many nations. However, at that time, the role of the submarine was mainly limited to coastal and harbour defence operations [2].

The onset of the World War I (WWI) saw a shift from the small and lightly armed defensive submarines to larger and more heavily armed sea-going vessels, purposely designed for offensive open ocean warfare. The use of submarines during WWI and World War II (WWII) proved to be extremely effective, with more than ten million gross tonnage of allied and neutral vessels sunk by submarines in each war. In the case of WWII, submarines accounted for over 68% of the total gross tonnage sunk [2].

To combat the submarine's success, Anti-Submarine Warfare (ASW) technologies were developed. ASW is focussed on two key areas: detection and destruction, with the former aided by the development of radar and sonar technologies. Destruction based ASW was achieved using an underwater explosion (UNDEX) from existing mine and torpedo weapons. Depth charges were developed as a dedicated ASW method to force a submarine either to the surface or the sea floor.

Threats to modern submarines are still largely defined by technology from the 19th century. Even the most modern submarines maintain the general stiffened pressure hull structure of *Holland I*, and the explosion physics of UNDEX weaponry remain the same. Modern advancements have focused more on detection, avoidance, and counter-measures. The sophistication and complexity of modern weapons and counter-measures, as well as the environment in which they operate, make it difficult to accurately predict the outcome between these technologies. It is therefore of great necessity for any navy to consider the UNDEX threat for the submarine structure, its crew, and mounted equipment. Naval platforms and their on-board equipment are required to undergo an exhaustive structural assessment process to ensure they can meet operational requirements, and it is critical that the assessment procedures accurately represent the UNDEX threat and are capable of identifying a platform's limitations.

In the following sub-sections, an overview of the UNDEX event and the UNDEX induced structural response of surface and submerged naval platform's is provided. An overview and the objectives of this research investigation are outlined for the following chapters.

1.1.1. Underwater explosions

Explosions are reactions that rapidly convert the state of matter, liberating energy in the form of pressure and heat. This process is typically associated with a large increase in volume of the explosive substance, which is visible from the bubble produced in the underwater environment in Figure 1-1. There are three types of explosions: mechanical, nuclear, and chemical [3], all of which have been used for the purposes of UNDEX weaponry and platform assessment [4-6]. For present ASW UNDEX weaponry, chemical explosives are favoured due to their cost and safety. Explosive materials that undergo detonation, known as high-explosives, are the most common for UNDEX and are the primary consideration of this work. Under detonation, the burn-rate of the explosive is faster than the acoustic velocity within the material and a shock wave is formed. The explosive reaction is continued as the shock wave propagates through the remaining material, shock loading the remaining explosive material into detonation.

Figure 1-1   Gas bubble produced by an underwater explosion [7]

The shock wave

Within the explosive, the shock wave travels at the detonation velocity of the explosive material, which is approximately 6900 m/s for the common explosive compound trinitrotoluene (TNT). Eventually the shock wave reaches the water contact surface. The large difference in impedance across the contact surface causes the propagation velocity of the transmitted shock wave to rapidly reduce towards the acoustic wave velocity of water (approximately 1500 m/s). The reduction in velocity leads to a substantial increase in the pressure of the shock wave just beyond the contact surface, as per Bernouli's principle [8]. The shock wave in water is best described by an incident pressure measurement, taken at some distance R away from the charge centre. A general pressure profile is shown in Figure 1-2, where key aspects of the shock wave are noted. One of the most important characteristics of the shock wave is the rapid rise time towards the peak pressure P_M. This has been idealised as an instantaneous rise in Figure 1-2, which is a very close approximation. This near instantaneous rise in pressure is the first damage mechanism from the shock wave. As the shock wave passes through the material it may even result in a temporary or permanent phase change over the brief loading duration. The P_M will also be substantial compared to the atmospheric pressure P_{atm}, where even a small explosive charge of 1 kg can result in P_M magnitudes of 1 to 100 MPa above P_{atm} [6].

The initial shock front P_M is followed by a rapid exponential decay as the fluid returns to equilibrium. This decay is characterised by the decay constant θ, which is the time it takes for the pressure to reduce from P_M to P_M/e^1. The shock wave follows the exponential decay rate for approximately one θ, after which it decays at a slower rate [6]. The duration of the shock wave for analysis and calculation of additional shock wave parameters is generally taken as five θ, which is typically no more than a few milliseconds [8].
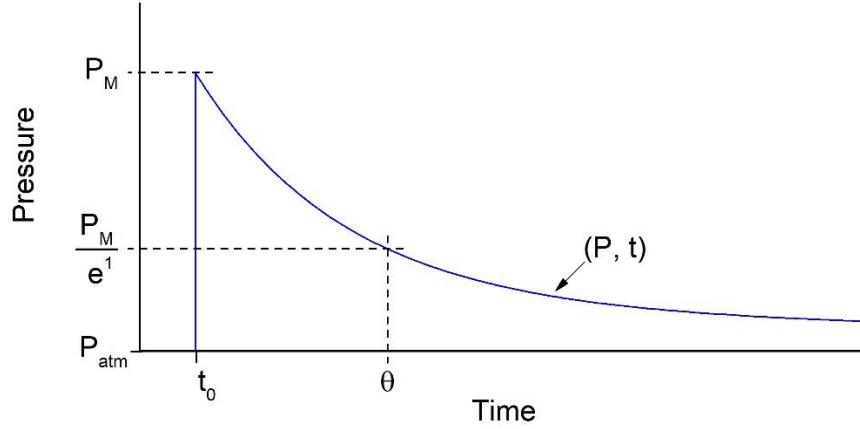
Figure 1-2   Shock wave pressure profile

At a short distance beyond the contact surface, the temperature within the shockwave reduces to that of the surrounding ambient fluid and the energy of the shock wave is characterised by a stable combination of kinetic energy and volumetric strain energy of the hydrostatically compressed fluid medium, the later energy component being dominant. Along with near acoustic velocity of the shock wave, these are considered as the far-field shock wave conditions. Under these conditions, the peak pressure and duration characteristics of the spherically spreading shock wave remain proportional with respect to charge mass W and stand-off distance R between the charge centre and stand-off point. Cole [8] observed this dispersed energy using the Energy Flux Density (EFD) or energy per unit area, which is the total energy of the wave over the area of a sphere, as shown in Figure 1-3. For the initial shock front, the EFD can be calculated using Equation 1.1, where ρ_f and c_f are the density and acoustic velocity of water respectively, and collectively form the acoustic impedance.

$$EFD = \frac{1}{\rho_f c_f} \int_{t_0}^{5\theta} P^2(t)\, dt \qquad [\text{m.MPa}] \qquad\qquad 1.1$$
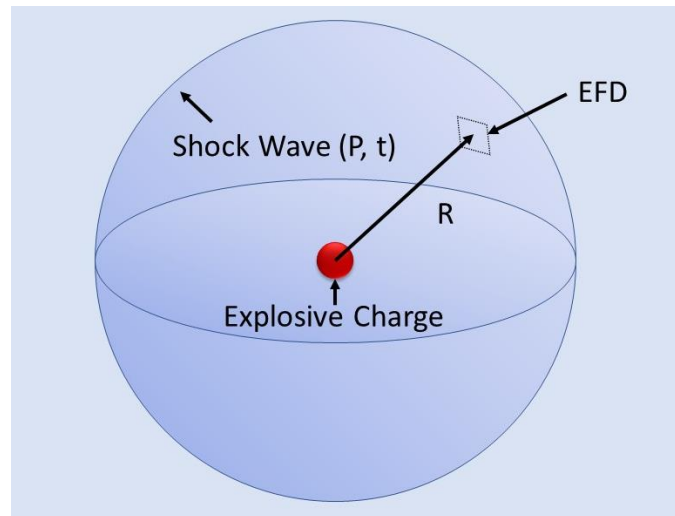
Figure 1-3   Shock wave energy flux density

Based on observations of the proportionality in EFD measurements for shock waves, Cole [8] applied the spherical wave propagation theory from Kirkwood and Bethe [9] and developed the shock wave similarity principle in Equation 1.2, where S is the similarity factor. Empirical similitude equations were developed from this principle and have been used to describe the primary characteristics of the shock wave.

$$S = \frac{(W)^{1/3}}{R} \qquad [\text{kg}^{1/3}/\text{m}] \qquad\qquad 1.2$$

The pulsating bubble

Once the explosive material has completely detonated underwater and the shock wave has been emitted, a gas by-product of the chemical reaction remains trapped by the hydrostatic pressure in the form of a bubble. The bubble undergoes a series of pulsation cycles as the internal and external pressures attempt to equalise. This is best observed from a free-field pressure gauge measurement taken at some distance R away from the bubble itself. A generalised illustration of the bubble pulsation cycles and pressure responses is shown in Figure 1-4. The pulsating bubble phase lasts considerably longer than the shock wave, in the order of 100 – 1000 ms, depending on the explosive type, mass and the charge detonation depth. The incident pressure from the bubble shown in Figure 1-4, consists of long durations of negative gauge pressure due to the increasing fluid velocity as the bubble expands, referred to as the bubble under-pressure. This under-pressure is at its lowest when the bubble reaches its maximum radius. As the bubble collapses the incident pressure increases and immediately after this point of collapse, a high-pressure pulse is emitted, referred to as the bubble pulse. Each pulsation of the bubble is considered as one bubble cycle (shock wave to first bubble pulse, first bubble pulse to second bubble pulse, etc.).
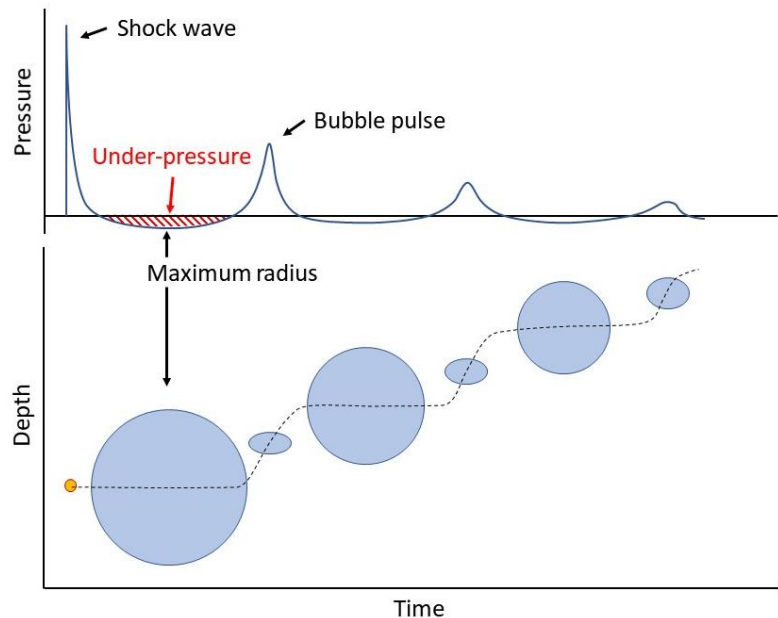
Figure 1-4   The pulsating bubble cycles and characteristic incident pressure

Analytical solutions can be used to calculate the transient bubble period from the pressure difference using the Rayleigh-Plesset equation. In practice, it is difficult to obtain an accurate measurement of the internal pressure in the extreme UNDEX environment. The internal pressure is dependent on the explosive charge material and mass W, while the hydrostatic pressure depends on the fluid density (which is assumed to be constant) and detonation depth D. The material, W, and D quantities are much easier to obtain in the experimental environment.

Swift and Decius [10] were able to use these quantities to study the response of UNDEX bubbles through pressure gauge measurements and produce empirical relations for the maximum radius A_n in Equation 1.3, and the period of the pulsation T_n in Equation 1.4, where n is the bubble cycle and J_n and K_n are the bubble radius and period coefficients respectively. These coefficients can be obtained from several sources [6, 10, 11] for different explosive charge materials.

$$A_n = J_n \frac{(W)^{1/3}}{(D + 10)^{1/3}} \qquad \text{[m]} \qquad \qquad 1.3$$

$$T_n = K_n \frac{(W)^{1/3}}{(D + 10)^{5/6}} \qquad \text{[s]} \qquad \qquad 1.4$$

Loading contributions of shock wave and bubble

The contribution of UNDEX loading from the shock wave and bubble depends on the explosive material, mass, and distance from detonation point. The previously discussed EFD can be used to determine the amount of explosive energy that goes into the shock wave and what remains in the bubble. Cole [8] showed from experimental and analytical calculations that at one charge radius from the detonation point of a spherical TNT charge, 53% of the total explosive energy was contained in the shock wave while the remaining 47% was in the bubble. Weaponised UNDEX devices may also use additives to control the energy proportions, where aluminium is commonly used to increase the proportion of bubble energy [6, 12, 13].

Cole [8] noted that direct measurement of energy is difficult to obtain in the severe UNDEX environment. When assessing the loading of explosions on structures, it is common to assess the impulse per unit area, or pressure impulse [14, 15] of an incident pressure measurement taken at some R distance. The pressure impulse can be calculated through the integration of a pressure-time history by Equation 1.5. The time bounds of the integration depend on the pressure impulse of interest. For the shock wave pressure impulse, it is common practice to take the integral from $t = 0 \ to \ 5\theta$ but may be extended to a time when $P = 0$, which indicates the pressure has reached the hydrostatic level. For the bubble, the pressure impulse is taken over the duration of the under-pressure and pulse components.

$$I = \int_{t0}^{t1} P \, dt \qquad \text{[MPa.ms]} \qquad \qquad 1.5$$

Figure 1-5 presents a pressure impulse example with the integral taken over the entire shock wave and first bubble cycle duration, where the components of the shock wave I_S, bubble under-pressure I_B, and bubble pulse are noted. This transient pressure impulse splits the contribution of the bubble pressure impulse into positive and negative components for both the under-pressure and pulse components, noted for the bubble under-pressure component as $+I_B$ and $-I_B$ in Figure 1-5. The I_B value should be considered as a summation of the absolute values of $+I_B$ and $-I_B$. From Figure 1-5 it is shown that I_B is almost double the value of I_S, and effectively unloads all the shock wave impulse and reloads in the opposite direction. The following pressure impulse from the bubble pulse then reverses this again, and this cyclic loading continues over the duration of the pulsating bubble, with decay between each cycle.
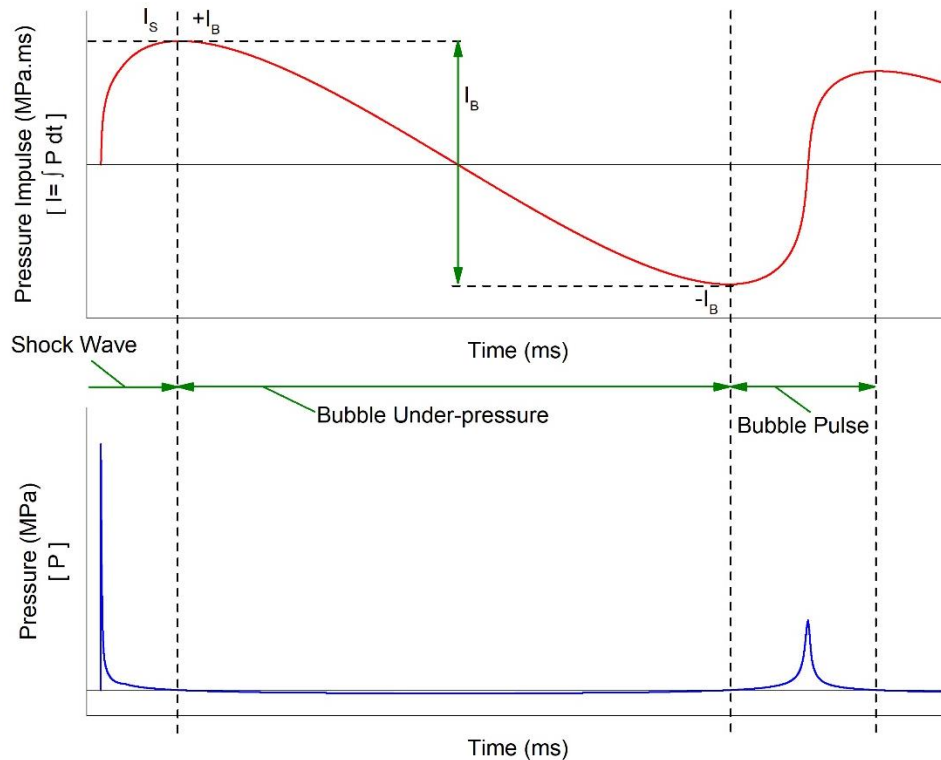
Figure 1-5   Pressure impulse and source pressure time histories

Cole [8] made the important note that the larger pressure impulse from the pulsating bubble does not indicate the bubble has greater potential to cause damage compared to the shock wave, as the bubble pulse EFD is in the order of $1 - 5$ % of the shock wave EFD, and the peak pressure of the bubble pulse is also substantially lower. However, the pressure impulse is a relevant measurement for analysis of the dynamic response of the fluid and objects within it. This demonstrates that the pulsating bubble has a more significant effect on the fluid response, as opposed to the near-instantaneous transfer of energy by the shock wave. The pressure impulse that arises from the controlled distribution of energy during the pulsating bubble is of interest for investigating the relationship between the bubble and structural responses, as the pulsating bubble has potential to continue forcing the structural response long after the shock wave loading has ceased.

Additional UNDEX loading contributions

Boundaries are present in most underwater environments that produce reflected waves which can also load a platform. Common underwater boundaries and the UNDEX loading paths that a submerged platform might experience from these are shown Figure 1-6. Three common loading paths are considered:

1. Direct wave

    This is the shortest path (line of sight) between the UNDEX and the platform. It is the initial compressive shock wave source of all loading paths, and it is typically the most severe shock loading the platform will experience.

2. Surface reflection waves

    The surface reflection occurs due to the direct wave reflecting off the free-surface. The flexibility of the free-surface boundary produces a tensile reflected wave, as opposed to the compressive direct wave. Due to the rapid decrease in pressure from this reflection wave,

it is often referred to as the surface cut-off wave [8, 16]. This surface cut-off interaction with the direct wave is illustrated in Figure 1-7.

3. Ground reflection waves

    The direct wave may also reflect off the sea floor, producing a ground reflection wave. The sea floor is typically a rigid boundary and produces a compressive reflected wave. The ground wave will arrive after the direct wave and cause additional loading, as shown in Figure 1-7.

In addition, UNDEX events close to the sea floor may also induce a seismic response that can also load the structure. This type of loading is not considered for this investigation.
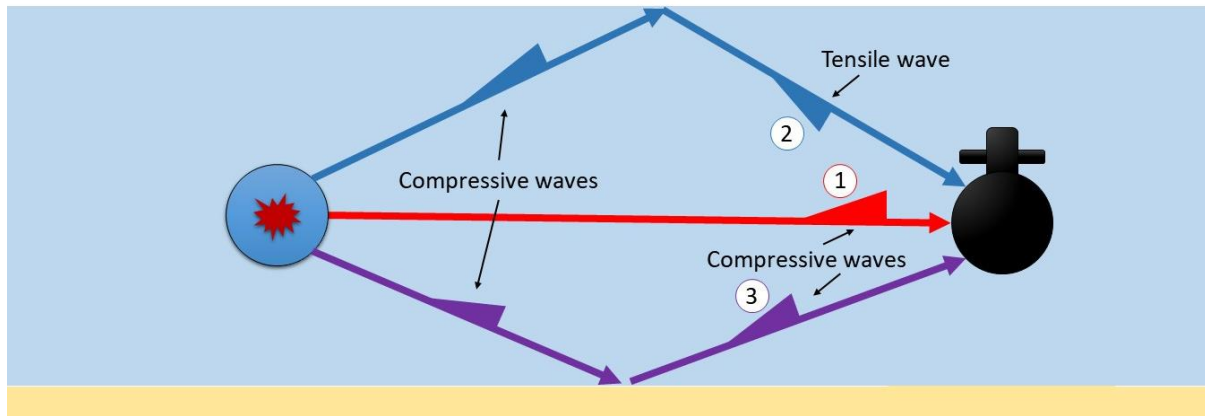
Figure 1-6   Common environment boundaries and UNDEX loading pathways

Upon reflection of the compressive UNDEX shock wave from the water free-surface, a tensile relief wave of equal magnitude will propagate from the affected free-surface area. The interaction of the tensile wave front with the direct shock wave can lead to a net pressure below the P_{atm} at a finite depth below the free-surface. If the net pressure falls below the local vapour pressure of the water cavitation will occur, effectively inducing a localised phase change in the water. The substantial under-pressure of the surface reflection wave can cause the net pressure to approach absolute zero pressure P_0 at which point the response is characterised by a cavitation cut-off of the pressure-time history, noted in Figure 1-7.

The interaction of the direct and surface reflection waves can take place over a large area and produce a zone of cavitated water near the free-surface, known as a bulk cavitation [11]. The eventual collapse of the bulk cavitation zone, due to the weight of the water above the cavitation zone, may result in significant additional loading of nearby structures. The flexible response of a platform's hull plate may also induce cavitation, referred to as hull cavitation. Hull cavitation will occur if the relief wave generated by movement of the flexible surface in response to the incident shock wave is of sufficient magnitude to drive the local pressure to below the cavitation pressure. As in the case of bulk cavitation, collapse of the hull cavitation zone may result in significant additional loading of the adjacent structure.
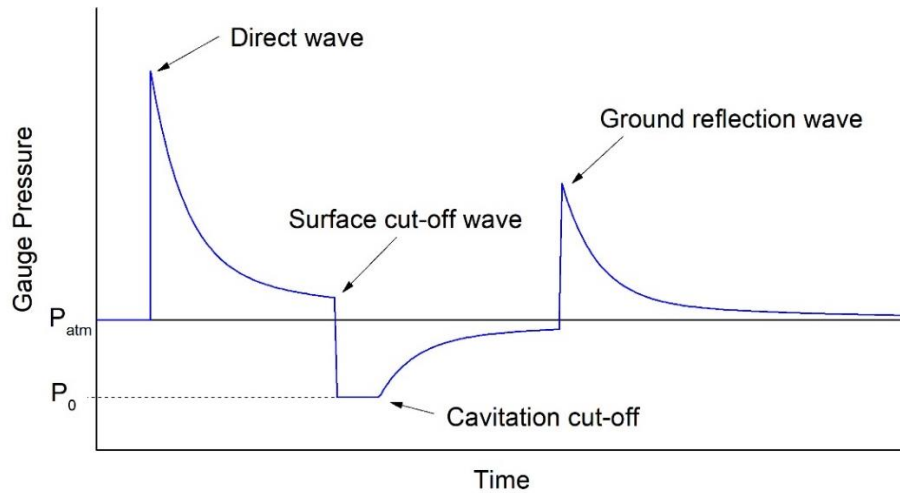
Figure 1-7   Shock wave incident pressure with ideal reflection waves

1.1.2. Platform response

All structures possess fundamental vibratory response dictated by their geometry, material, and boundary conditions. Most maritime platforms can be idealised as a long and slender beam (that may have a variable cross section). This beam is generally assumed to be unconstrained and partially or fully submerged in a dense fluid. In the fully submerged condition, the platform is free to move in any direction, while in the surfaced condition, motion is strongly affected by the water and air boundary. Bishop and Price [17] distinguished structural responses as motion and distortion responses in the maritime context. Motion responses consist of six rigid body motions: three translational and three rotational, which are detailed in Figure 1-8 using the maritime nomenclature. These motions are responsible for the rigid platform dynamics and do not include the deformation of the structure.
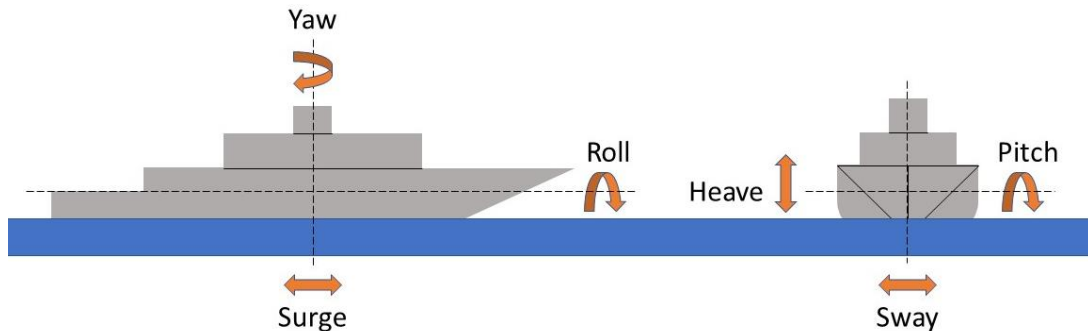
Figure 1-8   Motion responses of a maritime platform

Distortional responses are dynamic responses which induce deformation in the structure. These can take the form of different shapes based on the distortion modes. Distortional modes include bending, circumferential, torsional, and translational responses. The beam-like behaviour of maritime platforms means that global bending of the platform is generally the dominant distortional mode. Blevins [18] provided a comprehensive collection of modal response formulas, and the notation is adopted for this work.

Bending Modes (BM) are caused through alternating tensile and compressive axial strain about the beam neutral axis. These consist of nodes and anti-nodes along the axial direction that react to external loading. Anti-nodes are locations of maximum deflection in the mode shape and are the most sensitive locations to external loading. Nodes experience no relative deflection in the mode shape and have no distortional response from any external loading. A platform's response

8

may consist of multiple modes and therefore nodes from one mode may still be subjected to distortional response from another mode. Both nodes and anti-nodes may still undergo rigid body motion which can affect measurements of the platform's motion which can make it difficult to identify these through motion measurements (velocity and acceleration). Stress and strain can only be induced by distortional responses and provide better measurements of just the distortional responses. An example of the first three BM shapes for a free-free uniform beam are shown in Figure 1-9, denoted by Blevins notation, where j is the number of half waves in the BM response.

BM1 ($j=1$)

BM2 ($j=2$)

BM3 ($j=3$)
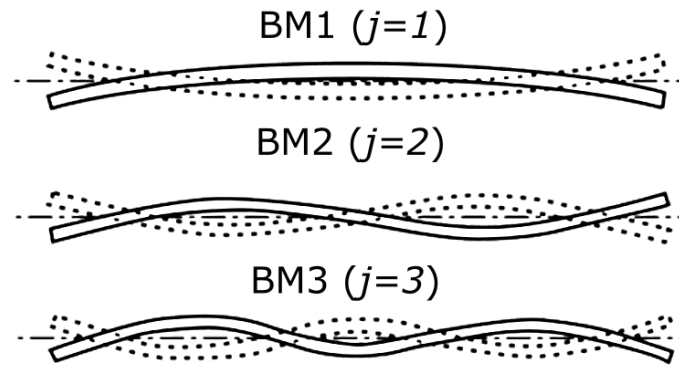
Figure 1-9   Bending mode shapes of a uniform free-free beam

In addition to global BM responses, localised responses may occur in hull plating. The simplest example of this may arise from an unstiffened cylindrical pressure hull that approximates a shell structure. These responses are referred to as Circumferential Modes (CM) [18] or lobar modes [19], which can be excited in both the circumferential and axial directions. The nomenclature for these modes is adopted from Blevins [18], where i denotes the number of circumferential waves and j denotes the number of axial half waves of each CM shape, as shown in Figure 1-10.

CIRCUMFERENTIAL NODAL PATTERN

i = 0   i = 1   i = 2   i = 3   i = 4

AXIAL NODAL PATTERN

j = 1   j = 2   j = 3

NODAL ARRANGEMENT
FOR i = 3, j = 4

CIRCUMFERENTIAL NODE

AXIAL NODE
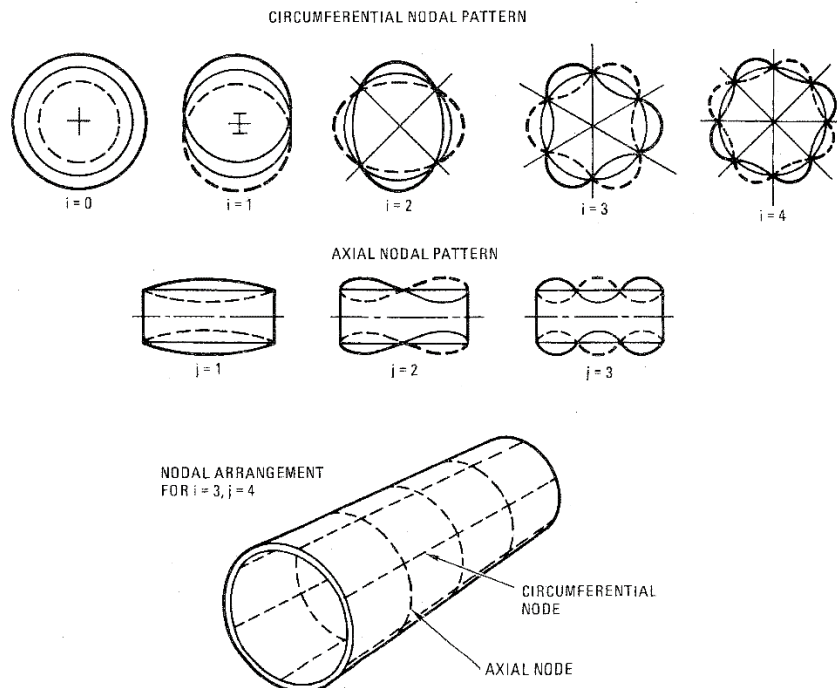
Figure 1-10 Circumferential mode shapes of a uniform free-free cylinder, from Blevins [18]

Torsional and translational distortional modes may also be present in the overall structural response. For the present investigations these are not considered as the structure and scenarios considered in these investigations are designed to primarily induce bending mode responses.

When considering a platform's response, the fluid must also be taken into consideration as its density results in a significant inertia on the systems motion, much like the pulsating bubble. This is commonly referred to as the added fluid mass. An approximate added mass can be calculated from the total displacement of simple forms (e.g. a cylinder). Blevins [18] provided a number of these solutions for simple cross-sections, summarised from Lewis [20], and also briefly considered the effects of environment boundary conditions for some cross sections. The added mass of more complex forms can be approximated with geometric transform equations, such as those from Lewis [20]. Numerical analysis methods also allow for this approximation to be achieved with boundary integral solutions, such as those from Deruntz and Geers [21]. Due to the added mass, a partially or fully submerged platform has both dry and wet modal response frequencies for each mode shape, with wet modal responses including the added fluid mass. For this research, the wet modal responses are assumed for discussion purposes unless otherwise stated.

The shock response

The shock wave is essentially pure pressure strain energy [8] and consists of a near infinite range of frequencies and may excite a broad range of structural responses. On contact with a structural element, part of the shock wave energy is transferred into the structure and the remaining energy is reflected. The amount of energy transferred/reflected depends on the structure material and interaction geometry. The transferred energy induces significant localised deformation at the point of impact, and the kinetic energy of this motion is enough to cause solid matter to temporarily behave more like a fluid as the shock wave passes through the area [22].

Keil [23] described in great detail the potential damage from an UNDEX shock wave on surface platforms. In the extreme case of a charge at proximity, the explosion products may make direct contact with the hull shell, causing rupture of the hull and potentially rupturing surrounding bulkheads due to the rapid pressure change within the affected compartments. High velocity fragmentation from the ruptured structure is also a significant concern, with potential to compromise the water-tight integrity of platform compartments. While contact damage is devastating, it is generally localised on large platforms and the hull's reserve buoyancy can accommodate this during recovery operations. The absence of reserve buoyancy on a submarine platform means that compromised water-tight integrity is of a far greater concern to the platform's survivability and recoverability. At further stand-off distances, plastic deformation damage may occur from the initial shock wave without rupturing the hull. Large deformation of stiffened panels and bulkheads may cause the stiffeners to buckle or "trip [1]" which significantly reduces their effectiveness and leaves these areas more susceptible to rupture from shock wave reflection or bubble loads.

Shock wave energy that is not reflected or does not cause permanent deformation will exist as kinetic energy in the platform. This energy causes significant motion and high acceleration loading throughout the platform. These responses can be especially severe for mounted equipment and last long after the initial shock wave impact. Keil [23] observed a number of different equipment failures that result from this loading, such as failure of equipment foundations and fasteners.

The immediate shock response is not the primary focus of this study, but the unavoidable presence of the shock wave will be considered where applicable in the present investigation.

The whipping response

The broad frequency content and high energy of the shock wave can induce an ongoing bending response in a structure. For naval platforms this is referred to as an UNDEX induced whipping response [24]. If the UNDEX is small and/or relatively far away, the shock loading is the most significant threat. For larger and/or closer UNDEX, the bubble also plays a crucial role in the platform's response. The frequency of the bubble pulse loading may be similar to the wet BM response frequency of a platform, and in this situation the whipping response may be amplified as a momentary resonant effect is induced. Depending on the proximity of the bubble, the platform can experience direct interaction with the bubble's pulsation cycle, bending upwards (hogging) as it expands and downwards (sagging) as it collapses, illustrated in Figure 1-11.
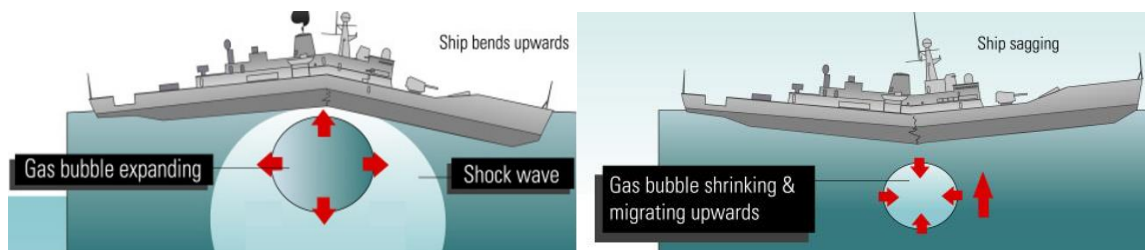
Figure 1-11 Stages of UNDEX induced whipping for a surface platform

The flow field produced by the bubble expansion may also draw the platform towards the bubble source, increasing the loading from the bubble. If the platform is close enough, the bubble may directly impact the hull, which causes a phenomenon known as bubble jetting. Bubble jetting causes a column of water to rapidly accelerate up through the bubble cavity towards the impact location. In weaponised applications, this water jet is capable of breaching through the hull and all decks of a platform, causing catastrophic damage [23]. This effect is famously visible on a sinking exercise conducted on the decommissioned HMAS Torrens (DE 53) in Figure 1-12 (also viewable on YouTube [25]). In this example, the use of a heavy weight torpedo on the relatively small destroyer platform (compared to modern destroyers) resulted in the ship breaking in half, a failure aided by the whipping response prior to the jet impact.

Figure 1-12 Bubble jet damage from a heavy weight torpedo detonation under the amidships section of the decommissioned HMAS Torrens [26]

Mines are far more common in modern incidents [27, 28], and are less likely to result in the catastrophic failure shown in Figure 1-12, but still pose a significant threat to a platform's overall structural integrity. A mine strike incident on the USS Princeton (CG-59) [27] demonstrated this, and the resulting buckling damage to the external hull plating is shown in Figure 1-13. A mine is also more likely to produce contact damage where much of the energy from the shock wave and bubble go into deforming and piercing the hull plate and supporting structure.

Figure 1-13 Buckling damage to the hull plate from UNDEX induced whipping due to a mine strike on USS Princeton (CG-59) [29]

For whipping assessment purposes, there is an ideal scenario where the bubble is too far away to collapse and jet, but close enough to drive the whipping response. In such a scenario, the responses of the bubble and structure can be coupled. Little is known about this range and the parameters of the UNDEX and platform that affect this bubble-structure coupling. The general term of whipping is also used liberally and can often cause confusion in discussion of the response. The whipping response induced by wave loading while similar physically, is at a completely different scale of time and global displacement compared to the UNDEX induced counterpart. Further clarification of the UNDEX induced whipping response and the characterisation and causation for different modal responses may help to differentiate UNDEX induced whipping from the generalised whipping response term.

The whipping response is of concern to both surface and submarine platforms, but in each environment the response can be quite different. For surface platforms, the whipping response will predominantly occur in the vertical direction, due to the air-water interface [24]. In this case, the greatest threat from a whipping response is damage to the keel and buckling of the hull, which put the platform's structural and water-tight integrity at risk. However, a surface platform has the benefit of reserve buoyancy, which can allow for some recovery, post event. As the response is most likely in the vertical direction, it is also relatively easy to predict the response and protect onboard equipment from this.

Burcher and Rydill [1] made note that submarine platforms have a far greater risk from a whipping response. The stiffened pressure hull design, while strong under dominant hoop stress conditions from hydrostatic pressure, has an inherent weakness to dominant longitudinal stress from a global bending response. The longitudinal stresses concentrate at the stiffener locations and will vary from being tensile or compressive. This loading on the stiffeners may induce tripping failure which can then lead to interframe buckling (sometimes referred to as concertina

mode) failure. Global buckling failure of the pressure hull may also be induced from a very large bending response. As the pressure hull is responsible for both the structural and watertight integrity of the submarine platform, any damage to this structure could result in catastrophic failure of the platform. The whipping response on a submarine platform can also occur in any direction, as it is generally submerged during operation. This is of particular concern to mounted equipment, which must therefore be resilient to loading from any direction. The greater risk of submerged platforms to a whipping response forms the primary consideration for this research.

At present, the variables of the UNDEX and platform that affect the whipping response are generally understood, but defined limitations of these variables have not been reported. There is also little information regarding the sensitivity of these variables on the UNDEX induced whipping response.

1.2. Research overview and objectives

The objective of this present investigation is to explore the UNDEX induced whipping response of a fully submerged platform. The aim of this is to clarify which variables of the UNDEX and platform are important to consider on this whipping response, and to determine the sensitivity of the whipping response to these variables. This investigation will also seek to better define UNDEX induced whipping and coupled bubble-structure responses, using a generalised and where possible, a dimensionless characterisation of the responses. Improved understanding of these effects could better inform design and operational decisions for current and future naval platforms.

For this objective, three research questions were considered:

1. **What variables of the UNDEX event and platform design contribute to the whipping response?**

   Before assessment of different analysis methods, better understanding of the variables that affect the UNDEX induced whipping response on a submerged platform was required. Previous experimental work is examined in Chapter 2 which found existing data was not suitable and could be largely improved through a new experiment. An experiment on a generic submerged platform is described in Chapter 3, which explores the effects of the charge size, stand-off distance, stand-off location along the platform length, and the relative size of the bubble to the platform on the UNDEX induced whipping response. A numerical model is developed and validated in Chapter 4, and further studies on the effects that different charge sizes and stand-off distances have on the whipping response are explored and reported in Chapter 5.

2. **Are existing assessment methods appropriate for analysing the UNDEX induced whipping response of a platform?**

   There is uncertainty as to whether analysis methods used are able to consider the effects of the whipping response for modern platforms, particularly if these are based on legacy empirical observations. Chapter 2 explores current available methods for UNDEX loading assessment of naval platforms and determined that further experimental analysis was required to understand the submerged whipping response, which is discussed in Chapter 3. Numerical analysis using a Boundary Element Method (BEM) was the most promising analysis tool for this problem and this is explored in Chapter 4.

3. **How can the UNDEX induced whipping response and bubble-structure coupling be better defined?**

   There is a need to better define the interaction between bubble and structure, and the UNDEX induced whipping response to maintain consistency across the application of legacy and new datasets to this problem. Categorisation of the bubble response and interaction near boundaries is examined in Chapter 2. In Chapter 3 the bubble loading is compared against the peak whipping responses of the experimental events. The relationship of the bubble loading and whipping response is further explored in the numerical environment in Chapter 5 and from these results detailed definitions of different UNDEX induced whipping responses are suggested.

Chapter 2. Literature review

2.1. Introduction

In this chapter, the complications of bubbles interacting with boundaries are reviewed and the relationship of bubble proximity and relative size to a platform are considered for their effects on the bubble-structure coupling. Analysis techniques for assessing a platform's response to UNDEX loading are investigated, with consideration of their validity to conduct a submerged whipping analysis.

The modern research of UNDEX and platform response research began during WWI, where the availability of explosive warheads from both purpose designed UNDEX weapons such as sea mines and torpedos, and inaccurate explosive shells detonating in water posed significant threat to ships of the period. A large escalation of research into the UNDEX phenomenon occurred after WWI and WWII, to improve the effectiveness of weapons and the survivability of ships [23]. Much of this work was compiled after the WWII by British and American research agencies into a three volume compendium [16], which explored the key aspects of the underwater explosion event: the shock wave, the gas globe (now more commonly known as the bubble), and the damage processes that arise from these. A comprehensive overview of the UNDEX event itself was produced by Cole [8], who considered the novel contributions of the compendium and presented this with fundamental mathematical and physical aspects, forming the definitive text of the field. This work was conducted over 60 years ago, and the methods of measurement and analysis used by these key references predate computers and, in many cases, even general electronics in the field. Mechanical measurements analysed with ideal mathematical or empirical solutions were the primary source of data from experiments. Despite the current availability of sophisticated computers and measurement systems, much of this dated research is still relevant today, as even these more sophisticated methods now available are still constrained by the extreme environment of the UNDEX event.

2.2. UNDEX bubble interaction

At present, there remains a lack of consensus for a universal categorisation of UNDEX events in regard to their size and proximity to a platform. The following section discusses a variety of observations and theories that have attempted to define regimes of UNDEX events. Some of the most recent work in this field has also occurred from observations of bubble interactions with different boundaries. These works are reviewed and discussed, and current knowledge gaps are noted for further investigation.

2.2.1. Categorisation of UNDEX Events

UNDEX events may be generally categorised as occurring in either a near or far-field regime, depending on the proximity of the bubble to a boundary [8]. A dimensionless stand-off proximity γ, defined in Equation 2.1 as the ratio of the stand-off distance R to the maximum bubble radius A has been used by a number of authors [30-40] to describe UNDEX regimes and the influence of a boundary on a near-field bubble response.

$$\gamma = \frac{R}{A} \qquad\qquad 2.1$$

The generalised form of γ does not account for all variables of bubble-structure interaction, such as curvature and the degree of flexibility of the boundary, or the relative size of the bubble with respect to a finite boundary size. Because of this, there is currently no scientific consensus on an exact value of γ that may define the border between near or far-field regimes.

As a general definition, a far-field event is one where the bubble is essentially unaffected by the presence of a boundary. This is referred to as the free-field regime if there is absolutely no boundary present and the fluid flow field around the bubble remains undisturbed, shown in Figure 2-1. Under this regime the bubble generally remains spherical except for brief moments during the collapse phases. Only buoyancy forces will be present in the bubble motion, so the migration path will be directly towards the free surface. Bubble response models that utilise an ideal spherical assumption [24, 41, 42], consider a value of $\gamma > 2.00$ as far-field and consider this as a general limit of their applicability.
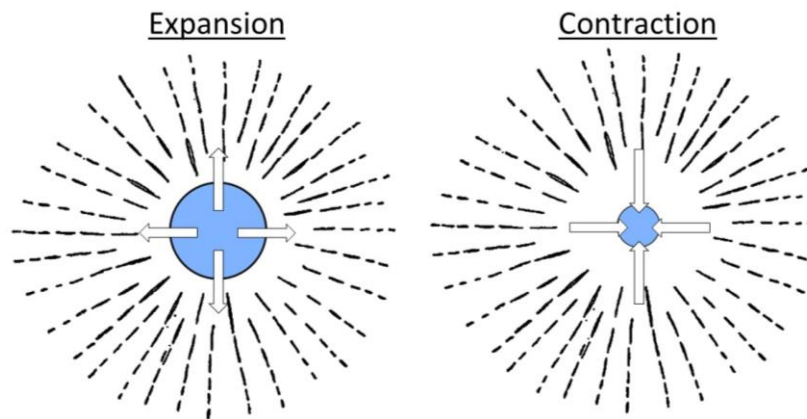
Figure 2-1   Free-field Bubble expansion and contraction flow fields

In contrast, a near-field bubble will experience interactions between its own pulsating fluid-flow field and the reflective fluid-flow field from a boundary. This interaction of flow fields appear as a force acting on the bubble in addition to buoyancy and are often referred to as Bjerknes forces [43] due to the similar responses seen in magnetic field interactions. Bjerknes forces can alter the bubble geometry, causing a non-spherical bubble shape during expansion phases, and modify the pulsation period. In extreme cases, Bjerknes forces may even overpower buoyancy forces, resulting in changes of the migration path, potentially in direct opposition of the buoyancy. How these Bjerknes forces influence the bubble shape and dynamics generally depends on the boundary geometry and its material properties [44].

2.2.2. Boundary effects on bubble dynamics

Studies on the interaction of bubbles and relatively rigid boundaries [30-34] have found that when $\gamma < 2.00$ the Bjerknes forces attract the bubble to the boundary and reduce the bubble's pulsation period. This occurs from the bubble "seeing" its reflection from the surface and generating reflection waves that are of the same phase as the source, as illustrated in Figure 2-2 and it physically behaves as if another real bubble is present in the field. An experimental investigation conducted by Zhang, et al. [34] which studied small UNDEX bubbles from detonators showed that a bubble migrating vertically towards the free-surface would experience limited attraction to a perpendicularly suspended flat rigid boundary when $\gamma = 1.40$, causing it to deform slightly. At this relative proximity the bubble was still able to undergo a complete set of pulsation cycles and maintain vertical migration without collapsing onto the boundary. In an additional experiment from Zhang, et al. [34] a horizontal plate was suspended below the bubble, parallel to the free surface representing a rigid floor. This arrangement demonstrated

that the Bjerknes forces were essentially balanced with the buoyancy forces when $\gamma = 1.20$, which prevented any significant migration during the early pulsation cycles. Values of $\gamma < 1.20$ caused the Bjerknes force to overpower the buoyancy force and resulted in the bubble collapsing on the plate. In a similar experiment from Krieger and Chahine [45], the incident pressure records from spark generated bubbles near a rigid boundary showed that as the bubble proximity approached $\gamma \leq 1.00$ the bubble was still able to undergo a pulsation cycles, and the peak pulse pressure from the subsequent bubble pulses reduced as energy was lost to the deformation of the bubble.

Near a relatively flexible boundary, the Bjerknes forces will repel the pulsating bubble and the pulsation period increases [34]. The flexible boundary alters the phase of the reflected waves and creates interference. There are few studies on the effects of bubbles near flexible boundaries, and it is difficult to distinguish to what degree the relative boundary flexibility influences the Bjerknes forces acting on the bubble. The repulsion effect is commonly observed when a bubble interacts with the free-surface [35, 36]. Gibson and Blake [46] conducted an experimental study on cavitation bubbles collapsing near a flexible rubber boundary and found that reduced relative proximity and different rubber material thickness had negligible effect on the repulse bubble response. This bubble interaction has also been explored in medical applications on human tissue material analogues [37, 38]. These medical studies identified that the Young's modulus of the boundary material was responsible for changes in the attraction and repulsion behaviour.

An experimental study by Tomita, et al. [31] demonstrated that curvature of the boundary also affected the Bjerknes forces, where convex curvature reduced the Bjerknes forces, while concave curvature increased them. It was observed that a bubble interacting with a solid sphere that had a similar radius to the bubble balanced the Bjerknes and buoyancy forces when $\gamma = 1.60$.
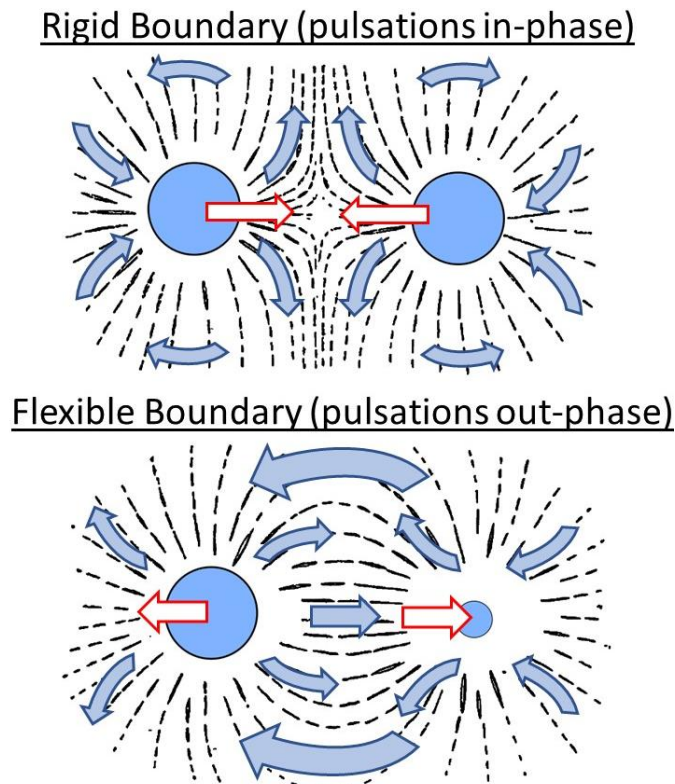
Figure 2-2   Bubble and image interactions near rigid and flexible boundaries

In close proximity (as γ approaches *1.00*), the bubble may collapse on the boundary [47]. In this case, a low pressure zone develops between the bubble and boundary. The bubble begins to flatten and the pressure difference on the boundary side and free side of the bubble cause the surrounding fluid to accelerate through the bubble, producing a toroidal form. The water accelerating through the bubble forms a distinct column, known as the bubble jet. The bubble's response while jetting can vary depending on the strength of the buoyancy and Bjerknes forces. Both Zhang, et al. [48] and Chahine [49] developed similar dimensionless buoyancy parameters to characterise how buoyancy forces affected the bubble response. Zhang's work also used this parameter to compare with the effects from Bjerknes forces, so this definition of the buoyancy force is adopted for the present work. This is expressed in Equation 2.2 where ρ_f and A were previously defined as the fluid density and maximum bubble radius respectively, δ is the buoyancy parameter, g is acceleration due to gravity, and ΔP is the difference between the ambient pressure and the saturated vapour pressure. A larger δ indicates a larger buoyancy force.

$$\delta = \sqrt{\frac{\rho_f g A}{\Delta P}} \qquad\qquad 2.2$$

Using this parameter and the previously noted proximity parameter γ from Equation 2.1 as a dimensionless comparison of Bjerknes force, Zhang, et al. [48] explored a broad range of buoyancy forces (*0.034 ≤ δ ≤ 0.950*) and proximities (*0.30 ≤ γ ≤ 3.00*), and characterised many different bubble responses near free and rigid surfaces. For a free-field bubble with a buoyancy force of $\delta = 0.451$ the bubble collapse caused a jet which splits the bubble into a toroidal form, before collapsing further into a cloud of smaller bubbles that reforms every subsequent cycle. Increasing δ decreased the jet velocity and this energy went towards a larger bubble radius and increased migration. Near the free-surface three behaviours were identified:

1. The bubble jetted away from the free-surface when the Bjerknes force was dominant.

2. The bubble jetted towards the free-surface when the buoyancy force was dominant.

3. The bubble either split if buoyancy was low or deformed when buoyancy was large, if both the buoyancy and Bjerknes forces were balanced, referred to as neutral collapse.

Three near-identical behaviours were also identified for a bubble above a horizontal rigid wall, except the outcome is reversed for behaviours 1 and 2, where jetting occurred towards the surface when Bjerknes was dominant, and away when buoyancy was dominant. The relationship of these forces are described in more detail in Figure 16 for interactions near the free-surface and Figure 20 for interactions near a rigid surface by Zhang, et al. [48].

It is noted by many authors [46, 49-51] that visual examination of the jetting phenomenon is difficult due to the opacity of UNDEX bubbles. For large UNDEX weapon sized bubbles, the force from the bubble jet can also be large enough to pierce through hull plate and multiple decks of a surface platform [23]. Due to both the destructive force of jetting and the complications in analysing it for UNDEX bubbles, the jetting phenomenon is not considered within the scope of this work.

2.2.3. Scale and scalability

All the interaction studies discussed were conducted at substantially smaller scales than even a small UNDEX bubble, which raises a question of how these responses might be influenced by the relative scale of the bubble and structure in a similar fluid. There is surprisingly very little information regarding how the relative size of the bubble to a structure will affect the response

of each, although three broad scenarios of interaction (shown in Figure 2-3) may be interpreted from the literature:

1. The first scenario considers a small bubble near a relatively large structure. Here the bubble will itself deform but the structure is unlikely to experience any significant global motion due to the bubble interaction. Such a situation is often the focus of cavitation bubble collapse studies near relatively rigid boundaries [52-54], while bubble interaction with the free-surface can be considered as the equivalent scenario for a highly flexible boundary.

2. The second scenario considers a large bubble against a relatively small structure. Here the bubble will not experience any significant deformation itself or be influenced by any Bjerknes forces between itself and the structure. The structure will likely experience a global motion response from the bubble. For example, Zhang, et al. [51] noted a spark-generated bubble was relatively undisturbed by the presence of the small electric ignition probes used in their experiments, while the report of the Crossroads Baker underwater nuclear explosion test [5] detailed how a ship momentarily floated atop the dome of the large bubble at the surface before disintegrating as it burst. This is of course an extreme scenario for UNDEX case and is not considered as a survivable scenario.

3. The final scenario considers a bubble and structure to be of similar size, this may be measured by some control length of a structure (e.g. a hull diameter). Here it is suggested that both the global and local dynamics of the structure and bubble are dependent on each other [31]. There is limited understanding on exactly what relative size limits apply to this scenario, other than that they are "comparable". This scenario is of significant importance in assessment of the UNDEX threat and platform response as it presents the most complicated bubble-structure interaction scenario. It is currently unknown what the relative proximity and size limits are required for a bubble-structure coupling to occur, and how this coupling may affect the UNDEX induced whipping response. How the bubble "sees" the platform is of equal importance for this investigation, and relative bubble proximities of $\gamma < 2.00$ remain largely unexplored for UNDEX weapon sized bubbles (scaled or full-size) and its interaction with a platform.
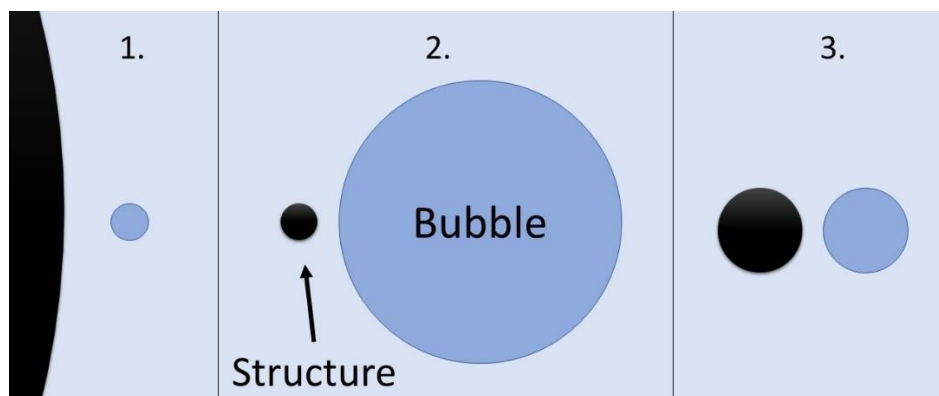
Figure 2-3   Scenarios of bubble- structure interaction

Snay [55] provided an incredibly detailed report on the methods of model testing and scalability (going so far as to provide comprehensive definitions of both these terms and their usage) where the challenges scalability were noted, and it is even further complicated through the use of different explosives and equivalents. Snay made a broad conclusion in this report on the usage of scaling for UNDEX, stating that:

> *"Since the fact remains that many underwater explosion phenomena of importance, in particular those which are connected with the behaviour of the pulsating bubble, often cannot be appropriately scaled, one has to investigate possibilities other than scaling in order to use small explosions to obtain the desired full scale results."*

Snay later stated that consideration of all scalable phenomena is "unattainable, even unreasonable" but model testing and scalability is suitable with appropriate validation of individual scalable items that are the focus of their relevant investigations. Snay also noted that due to the complexity of the UNDEX environment there will always be some compromise in these methods. Because of these additional complications the present investigation will seek to avoid direct scalability and the assumptions that come with it.

2.3. Analysis methods

A variety of analysis methods have been employed for the structural responses of platforms due to UNDEX loading. These may be broadly considered as experimental, standardised and spectral, analytical, and numerical methods. In this section relevant research work for each of these methods is discussed for the application to an UNDEX induced whipping response of a submerged platform. Appropriate methods for analysis of a submerged structure in response to UNDEX loads are identified to proceed with further investigation into this problem.

2.3.1. Experimental analysis

De Candia, et al. [56] reported on several key experiments that have been published for benchmarking purposes and noted that few of them considered whipping responses in their assessment. Furthermore, the reported experiments offer limited data, with shock loading and response being the primary focus of these experiments.

Chertock [57] performed some of the earliest experimental observations using small scale test platforms consisting of a floating barge and a submerged cylinder. The 2.510 m long, 0.206 m diameter cylinder was stiffened, and sealed by end plates. The cylinder was subjected to UNDEX events ranging from 1.2 to 8.2 grams of TNT, at depths of 3.66 to 275 m, and stand-off distances of 0.30 to 1.52 m; with all events considered far-field ($\gamma > 2.00$). This experiment also explored the effect of the longitudinal stand-off point on the whipping response, but only for the case of the surface barge. The submerged experiments showed how the variation of depth and charge size could excite BM1 and BM2 responses in the cylinder.

Outside of Chertock's work, most experimental analysis has primarily focused on the response of internal equipment and the extent of localised hull damage. A combined effort of the Defence Nuclear Agency, the Office of Naval Research, and the Naval Sea Systems Command produced the DNA/ONR 33.6 test model which consisted of a submerged 6.43 m long, 0.845 m diameter, ring stiffened cylinder that was subjected to a series of UNDEX events for numerical analysis benchmarking purposes [58]. This vessel was tested under three configurations: no internal equipment, symmetrical mass distribution, and asymmetrical mass distribution of internal equipment. However, the published measurements [58] and analysis conducted on this experiment only considered the early time shock response, resulting in an insufficient time history to determine whether whipping occurred.

The shock response of small submerged cylinder sections has been explored, specifically looking at far-field response and modelling techniques [59], close-in bubble collapse contact responses [32, 60], and the response of internal decks and their modelling [61, 62]. However,

none of the above experiments were able, or designed to consider, any significant whipping effects on the structural response. van Aanhold, et al. [63] conducted experiments on a floating stiffened cylindrical hull that was 17.5 m long and 3.1 m in diameter. This platform briefly displayed a whipping response; however, the authors did not discuss the whipping in any significant detail and the reported data ranges were sanitised, making it unsuitable for validation or benchmarking studies by a third-party.

A limited number of full-scale experiments have been conducted but were not as well documented as the generic tests discussed above. The shock response of full-scale submarines and onboard equipment has been documented from tests during the Second World War in [64], but the measurement and data acquisition equipment used at the time was in its infancy, and the data was case specific to the submarine vessels tested. The 'Steel Mosquito' from Hellqvist [65] was an 11 m long, 5.7 m diameter scale submarine section that investigated the localised panel damage, and the response to UNDEX events of structure and equipment such as ballast tanks, batteries, hull penetrations, and resiliently mounted decks. However, this low length to diameter ratio section did not exhibit any notable whipping response. Recent work from Liu, et al. [66] presented two experiments on complex water and double hull structure interfaces. The more complex of these experiments consisted of a liquid oxygen tank, resiliently mounted within a large stiffened pressure hull. This hull was surrounded by an elliptical sectioned light casing that was free-flooded. Two smaller independent pressure hulls were positioned port and starboard side of the large pressure hull, separated by the free-flooded area of the light casing. While no whipping response was predicted or observed by the outer hull, it was predicted that the resiliently mounted tank would exhibit an oscillatory response that would be amplified by the periodic bubble pulse loads. However, the experimental results showed much heavier damping of this cylindrical tank response with lower amplification resulting from the bubble pulse load.

From this overview of experimental work, it can be appreciated that the whipping response is not normally given primary focus. However as noted in Chapter 1, a submarine can be especially susceptible to this and even a minor UNDEX event could potentially induce severe damage to equipment through a whipping response. There is justifiable cause to conduct further experimental investigation with a focus on the whipping response to determine what parameters of the platform's design and the UNDEX might affect this, and to determine if existing assessment methods are appropriate for determining if a platform can undertake its operational requirements.

2.3.2. Shock standards and spectral analysis

Shock standards are the current and most practical methods of defining and assessing a platform's requirements. Many of these consider a spectral response as the requirement and this may be defined directly by a response plot, or through the classification of a threat by its explosive energy and potential to do damage. All these methods are based on prior experimental observations and at times broad assumptions to simplify the assessment process. They also tend to strongly favour the direct shock responses over that from the bubble loading and it is sometimes difficult to determine whether whipping is considered by these methods.

Shock Factor (SF)

As previously noted in Chapter 1, the UNDEX event severity depends on the charge mass (W) and stand-off distance (R), often combined in a measurement of EFD. A simplified relationship of these variables is considered as the Shock Factor (SF) [11, 23, 67]. Depending on the

platform and/or response of interest, the SF can be expressed as the Hull SF (HSF) as Equation 2.3, or the Keel SF (KSF) in Equation 2.4. As shown in Figure 2-4, for submerged platforms the HSF is the only consideration, while for surface platforms the HSF and KSF are applicable. The KSF considers the angle of incidence on the keel (Φ), the primary structural member in most surface platforms, where for an angle of 90° $KSF = HSF$. For a surface platform, the KSF is known to be proportional to the heave motion kick-off velocity [11]. The shock factor can be used for immediate threat assessment if the mass and stand-off of the threat is known. Levels of shock factors are indicators of the damage potential, and the classification of these levels remain confidential due to platform vulnerability risks.

$$HSF = \frac{\sqrt{W}}{R} \qquad\qquad [\text{kg}^{1/2}/\text{m}] \qquad\qquad 2.3$$

$$KSF = \frac{\sqrt{W}}{R}\left(\frac{1 + \sin\Phi}{2}\right) \qquad [\text{kg}^{1/2}/\text{m}] \qquad\qquad 2.4$$
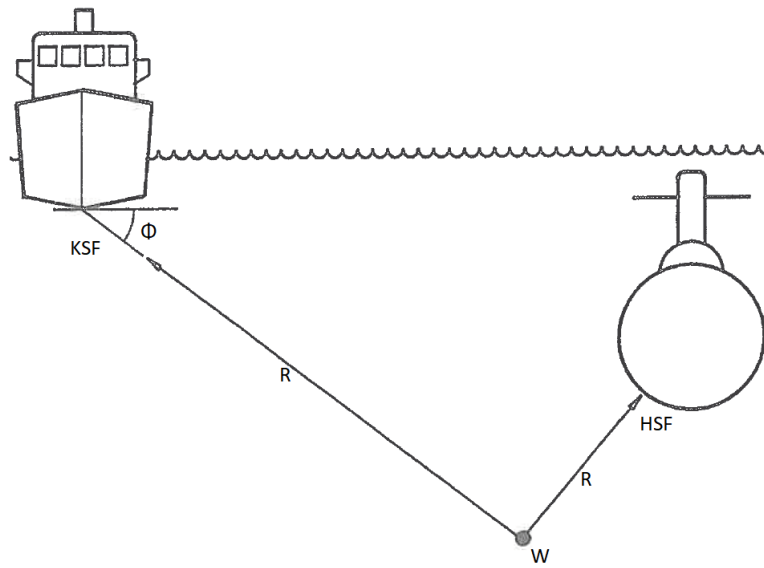
Figure 2-4   Shock factor definitions [67]

As the shock factor is based on the shock wave EFD, it inherently does not consider the effects of bubble loading. However, it remains unclear as to whether the shock factor may also be appropriate for assessing potential damage from a whipping response, and if there are limitations to applying the theory for this application.

Shock classes

Empirical standards consider platform and equipment response under different shock classes [67]. These shock classes are determined from UNDEX experiments conducted on real world platforms [64] or model analogues that represent key features of platform structure [65]. Shock classes are determined by general layouts of a platform. The specifics of classes vary for individual standards but in general they consist of three broad definitions of decreasing severity:

1. Components mounted on structure in direct contact with the shock load (e.g. hull)

2. Components mounted on structure off direct contact areas (e.g. stiffeners, bulkheads, and decks below the water line)

3. Components mounted on structure off secondary class components and above the waterline (e.g. ship superstructure)

From these definitions it is apparent that for a submerged platform, only the two most severe class definitions are applicable.

Bishop [67] compared two extremes of shock standards from the Swedish [68] and United States (US) [69] approaches. The common approach of these methods is to simplify the loading and analysis inputs from an UNDEX event, with particular focus on the shock wave component. The Swedish approach was developed from specific experiment analogues [65] and is applicable only for submarine structures. A shock response spectra (SRS) class was developed for specific areas of the submarine. This makes for more efficient designs but is also a more involved analysis process [67]. In contrast, the US approach is based on a larger number of experiments and observations since WWII [70] that were used to develop shock testing machines and testing procedures, detailed in the current revision of the MIL-S-901D standard [71]. These shock machines produce similar acceleration loads to an UNDEX event. The US shock qualification is more broadly applicable for equipment at any location in a platform, but due to this is considered a more severe requirement to meet [67].

The shock standard and class qualification methods have an inherent limitation, in that they are entirely based on previous design testing. This can make it difficult to apply these methods to new platform designs and equipment systems, particularly if these deviate greatly from anything that was considered by previous tests. As noted in Section 2.3.1, the whipping response has not generally been the focus of many experimental observations, so it is uncertain whether this has also been considered within existing requirements, or whether the requirements are even capable of considering the effect that a significant whipping response may have on the platform and equipment.

Shock response spectra (SRS)
Spectral analysis methods utilise the frequency domain to assess the response of a platform and/or mounted equipment from shock wave loading, often in terms of acceleration. Considering the individual frequency components of the shock wave and the measured response of a target, allows for characterisation of an event and susceptibility to given loading frequencies [72]. Scavuzzo and Pusey [73] note that shock spectra methods are popular for analysis firstly because the magnitude and frequency terms are common to all engineering fields, and secondly because the frequency components are independent of each other and may be assessed in relation to specific criteria. Shock spectra treat equipment responses as simple single DOF mass-spring-damper systems [72]. The responses for these are typically obtained through spectral decomposition of an experimental measurement [73]. These responses are presented in the frequency domain and may be used to assess potential equipment responses and failures. SRS are generally developed from acceleration frequency responses, where the peak acceleration from a given frequency response is taken and this is summarised as an acceleration frequency or SRS plot. The analysis is simple and has the inbuilt confidence of empirical knowledge. However, like shock standard procedures, this empirical basis may also arise as a limitation if the assessed design or equipment is drastically different from prior experiments, or if the analysed system does not easily conform to a single spring-mass-damper assumption. It is also nearly impossible to distinguish what phenomenon has caused the final response, so while SRS are an efficient assessment method, they are difficult to use for an investigative study into the underlying cause.

Pseudo Velocity Shock Spectrum (PVSS)

Gaberson [74] pioneered a spectral analysis method using a Pseudo Velocity (PV) to develop the Pseudo Velocity Shock Spectrum (PVSS). PV is determined by the peak displacement (z_{max}) of a given frequency response (ω), as expressed in Equation 2.5. Gaberson and Chalmers [75] demonstrated with this method that analysis of this pseudo velocity response was a better representation than acceleration for the potential damage and failure modes in structures and materials, as the maximum modal velocity is directly proportional to the maximum stress. It considers that "high g" accelerations act for only a short time during a shock event and thus result in small changes in velocity (and displacement causing the deformation), while "lower g" accelerations that act longer may induce higher velocities and larger displacements in certain items and areas of a platform.

$$PV = \omega z_{max} \qquad [\text{m/s}]$$

$$2.5$$

The PVSS response is best expressed using a four-coordinate log scale plot of the PV, acceleration, and displacement in the frequency domain. An example for the response of an equipment piece from a 800 g half sine shock wave is shown in Figure 2-5 [74]. The response is characterised by the presence of a low and high frequency asymptotic responses of displacement and acceleration respectively, and the plateau response of the velocity. The low frequency response causes the peak displacement of 50 inches (1.27 m) in this scenario. This response is due to the late-time free vibration of the equipment piece after the initial shock load. The 800 g peak acceleration is present in the high frequency response that is a direct result from the initial shock to the equipment piece. The plateau response corresponds to the peak velocity, approximately 196 inches per second (4.98 m/s), that is induced in the equipment piece from the initial shock load.
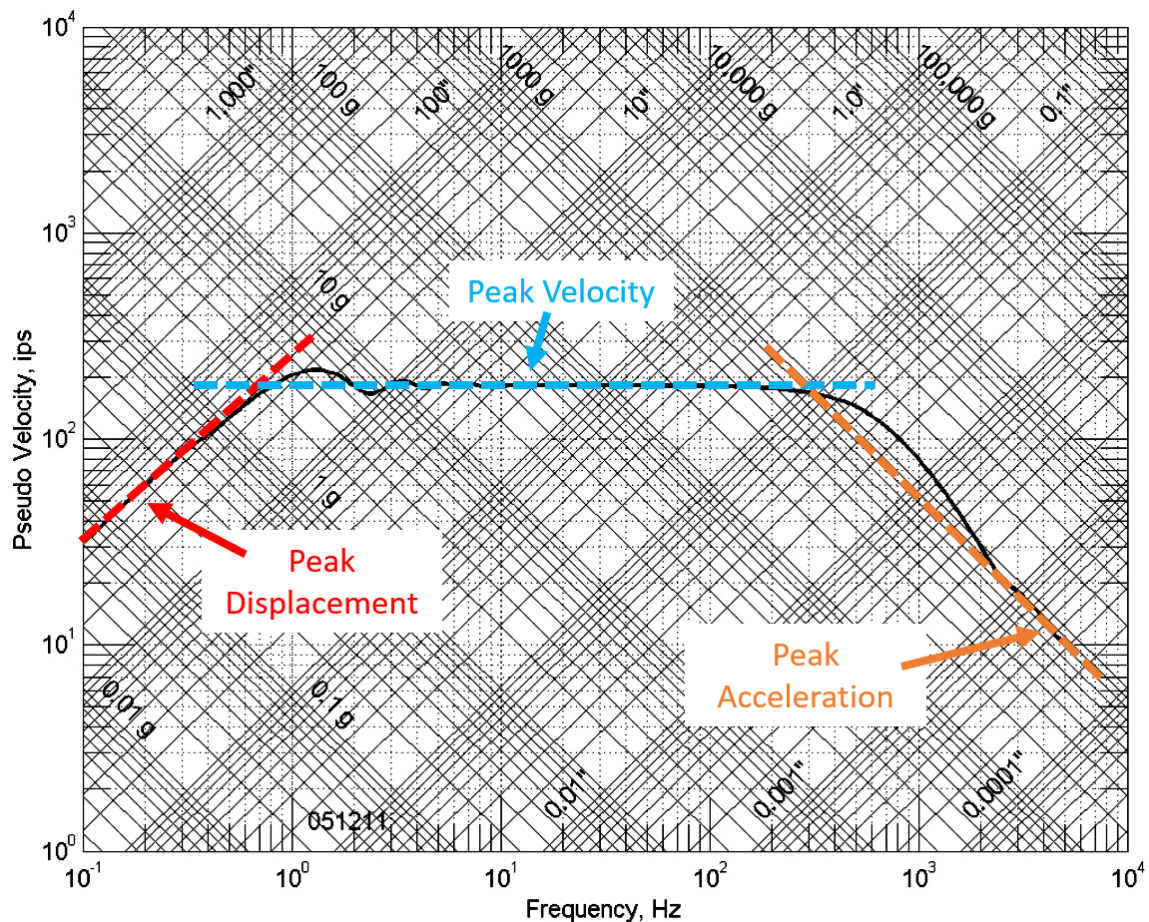
Figure 2-5   PVSS of a 800 g, 1 ms half sine shock wave [74]

24

The PVSS plot can be used as a comparative analysis tool, where the response at a given location on a platform can be assessed for a shock load, and mounted equipment can be assessed under the same shock load. Comparison of the PVSS responses will determine if the equipment is likely to survive the shock threat in this area. These can also be applied to whipping analysis if the response considers the subsequent bubble loading. However, issues from this may arise as it is not immediately clear if bubble loading and response has been considered on these plots. Like the SRS method, it is difficult to determine what phenomena caused the final response, so while PVSS are an effective assessment method, they are not suitable for an investigative study into the underlying cause.

Dynamic Design Analysis Method (DDAM)

The Dynamic Design Analysis Method (DDAM) is an analytical assessment process developed by the US Navy for equipment assessment in response to UNDEX [76]. DDAM utilises shock spectra of UNDEX to determine a Shock Response Spectra (SRS) that may be used to apply simplified loads to equipment that yield the equivalent response to real shock loads [77]. DDAM was first implemented in the 1960's, prior to adoption of numerical analysis and the computational power required for this. NAVSEA [76] noted a number of limitations due to this analysis method:

1. The analysis assumes that the equipment analysed is representative of a linear elastic system with discrete modes.

2. The analysis assumes no damping, which while valid for some shock response analyses, is not so for the longer duration whipping response.

3. The data behind DDAM specifications was obtained from many different full-scale platforms, and there is no distinction between the response of different platforms.

4. A single point spring-mass system is assumed which may not be applicable to large distributed items (e.g. a torpedo tube).

It has been noted that some, if not all, of these limitations are applicable to every standard or spectral assessment method. In the event that these limitations arise during assessment, NAVSEA [76] recommends that alternative assessment methods such as experimental trials and transient analysis should be employed. As it is uncertain if the whipping response is considered by these methods, the suggested alternatives are the most promising candidates for further investigation.

2.3.3. Analytical Methods

Analytical analysis of surface and submarine platform whipping responses was first considered by Chertock [78] who derived analytical solutions using a method of modal superposition of the structural response frequencies, based on the contributions from the pulsating bubble. Chertock derived this solution from the previously discussed experiments [57]. It must be noted that Chertock's method was developed prior to the availability of the modern computer, and the simplicity of the models and experimental setup resulted in limitations to the method's applicability and accuracy. A review of whipping analysis techniques by Bannister [79] noted four major simplifications that were considered in the solution:

1. The structure was considered as a uniform section, and the mass distribution was idealised as uniform across the length of the structure. This is rarely the case for a real platform.

2. The method is based on modal superposition, so only linear responses can be considered.

3. The effects of bubble migration to the surface are neglected, so the bubble is assumed to be stationary in space.

4. A spherical bubble is assumed, so this method may only be accurate for a far-field UNDEX scenario.

While Chertock noted good correlation on the surface barge events, the analysis overpredicted the response of the submerged pressure hull model due to the third BM response by 30 % when charges were detonated away from amidships. The error was attributed to the non-uniform mass distribution in the experimental model. Bannister [79] noted that there was no indication of how well this analytical theory would scale when applied to a full-sized platform and questioned how well it would apply to near-field bubble-structure interaction.

Geers [80] summarised a number of analytical solutions for the response of an infinitely long, elastic, cylinder submerged in an infinite fluid medium. Carrier [81] first derived modal response equations for the response of an elastic cylindrical shell, and Lax, et al. [82] presented solutions for the first circumferential and translational modal responses. Additional modal responses were presented by Murray [83], Forrestal [84], and Forrestal and Alzheimer [85]. Early-time response solutions of shock wave interactions with a cylinder were presented by Mindlin and Bleich [86] who treated the wave as planar. Haywood [87] improved on this solution by incorporating afterflow effects which allowed the shock wave to be treated as cylindrical in the two-dimensional analysis. Geers [80] noted that the responses from Mindlin and Bleich [86] and Haywood [87] were accurate for the early-time responses but were questionable for analysis of the late-time, low frequency, free vibration response.

All analytical modal analysis methods discussed thus far have the inherit limitation of only being able to assess elastic whipping responses, and generally require an idealised geometry to do so. Essentially all these methods were developed prior to the wide availability of computers and were limited to what could realistically be achieved through hand calculations.

2.3.4. Numerical Analysis

Numerical analysis methods were able to overcome computational hurdles in previous attempts to analyse structural responses due to complexities of Fluid Structure Interaction (FSI) for the UNDEX event [80]. Numerical techniques such as Finite Element Analysis (FEA) utilise two distinctive methods to approximate complex problems: implicit and explicit. Details on these methods are provided by Hughes [88]. In relevant summary, implicit methods follow an iterative convergence solution that resolves a global stiffness matrix for every timestep in response to imposed loads and boundary conditions. This method is unconditionally stable and provides a high degree of accuracy. However due to the convergence checks that must occur for the solution, it is extremely inefficient or ultimately unable to solve complex non-linear dynamic problems that require fine outputs over a very short duration, such as shock wave propagation. Explicit analysis forgoes the need to resolve a global stiffness matrix and iterative convergence checks by assuming minimal change in a short duration on an element-by-element solution basis. To ensure the analysis remains stable, a minimum timestep (ΔT) is generally determined by the smallest ratio of the element size (L_e) and the speed of sound (c) in that element (Equation 2.6), though some element formulations have different criteria and are best described by an analysis code manual [89]. As shock waves need to be tracked through each element and travel near the speed of sound, explicit codes are generally preferred for shock analysis. For whipping there is justification to use either method. The efficiency of implicit for

the longer duration is beneficial, but as the shock wave is always present in UNDEX it is also important to capture this response.

$$\Delta T \leq \frac{L_e}{c} \qquad\qquad \text{[s]}$$

2.6

Hicks [24] first demonstrated a numerical analysis approach for surface platform whipping analysis, with a beam model that used a geometric transform based on the added mass expressions from Lewis [20] to account for the non-uniform mass distribution of a typical surface ship hull form. Hicks also developed a spherical migrating bubble model that accounted for the first bubble pulsation cycle, which was coupled to the beam model. It was noted that due to the assumption of a spherical bubble, the model was only accurate for applications where the bubble is not distorted by the interaction with the vessel. This is generally considered applicable only for far-field UNDEX events, though Hicks provided no absolute value of a bubble proximity that may constitute this limit. These contributions went on to be consolidated into the MSWHIP analysis code [90] in 1971. While real world validation of this code is kept inside confidential reports, the fact that it was still in use as of 2006 [91] is some testament to its capability.

Numerical analysis of the elastic excitation of a submerged cylindrical shell due to a transient acoustic plane wave was first presented by Geers [80], using a two-dimensional numerical approach based on an earlier analytical method of the early-time shock response from Haywood [87]. Geers [92] later expanded this method into a three-dimensional analysis and noted that the approximate solutions from the developed asymptotic equations were suited to the shock wave impact problem, in which a structure undergoes short duration high-frequency response from the initial shock wave impact followed by a comparatively slower, low frequency free vibration response. This method was later referred to as the Doubly Asymptotic Approximation (DAA) [93], and treated as a Boundary Element Method (BEM) for the FSI of a submerged flexible structure. Geers demonstrated that the DAA method was applicable to transient [93] and vibration [94] analysis.

The USA code

The DAA method was utilised by DeRuntz [95] to develop the Finite Element (FE) Underwater Shock Analysis (USA) code. This application benefited from the significant computational efficiency of the DAA BEM, as fluid elements and responses did not need to be physically modelled. The commercialised version of the USA code is typically bundled with the Livermore Software Technology Corporation (LSTC) explicit LS-Dyna FE code [89] to conduct the full FEA. The analysis between the implicit USA and explicit LS-Dyna codes consists of a coupled feedback loop. Because of the substantial computation efficiency difference between an implicit and explicit code, a staggered feedback system is sometimes used, described by the analysis flowchart in Figure 2-6.
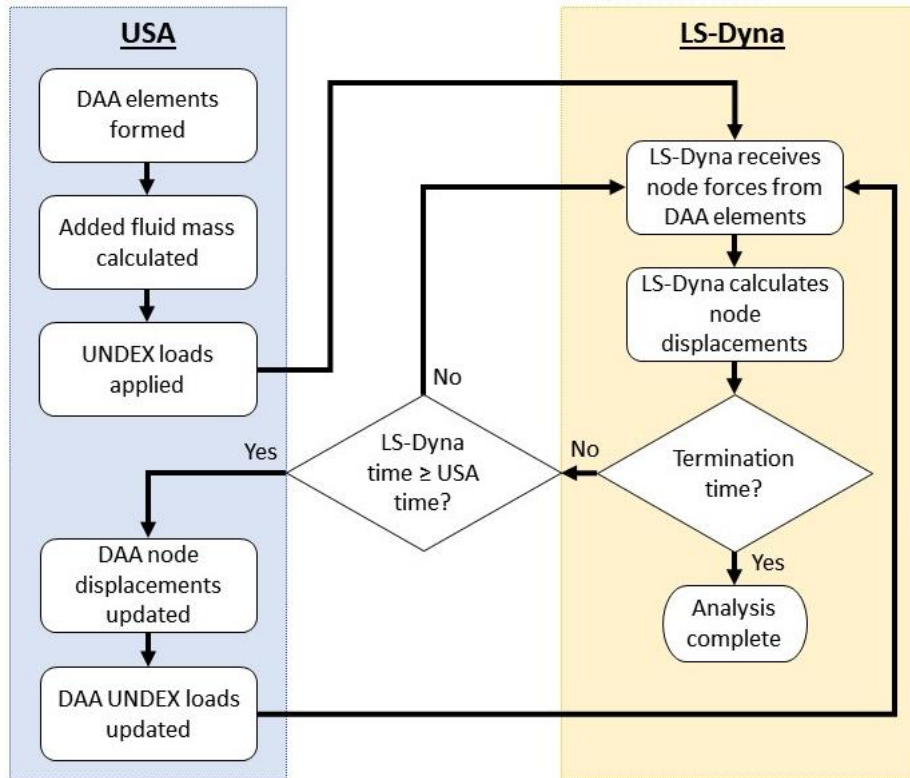
Figure 2-6   FEA process using the USA and LS-Dyna codes

The USA code can use a variety of different shock wave and bubble loading models to perform an UNDEX analysis. Shock waves based on the exponential decay assumption from the similitude equations [6] are the standard models. The USA code assumes incompressible flow theory and a spherical bubble shape and therefore only far-field bubble models can be used by the DAA BEM. The bubble model from Hicks [24] is implemented without a shock wave and is considered accurate for only one bubble cycle due to its lack of a decay function [96]. A more advanced shock wave and bubble model was developed by Geers and Hunter [42] and this was refined by Hunter and Geers [41]. Both these models contain decay functions and were validated up to three bubble pulsation cycles. The decay function was implemented through a user defined drag term, which is not directly representative of actual drag effects on the bubble. Optimisation of this drag term for different UNDEX bubble environments was analysed by Geers and Park [97]. The current R7.5.3 release of the USA code [96] contains a unique shock wave and bubble model that utilises an exponentially decaying shock wave fitted to empirical pressure data from Price [98] and the bubble from Hicks [24] with a decay function based on the Geers and Hunter [42] model. This is referred to as the Price-Hicks Shock Bubble (PHS-BUB) model [96]. In a previous benchmark application of these models for a surface ship whipping analysis by De Candia, et al. [99], the combined PHS-BUB model was found to best replicate the bending moment responses from an experimental whipping study, though no validation was made against the incident pressure.

While the USA code and its implemented shock wave and bubble models should be applicable to only far-field whipping analysis, there is limited validation beyond the assumed far-field limit of $\gamma \geq 2.00$ in these models. As previously noted in Section 2.2, this limit has some validity, but there is also justification for far-field conditions to apply at closer bubble proximities, and additional variables of the bubble structure interaction (such as relative size to the platform) are not considered by this bubble proximity limit. It is also unknown what level of error can result from an analysis if scenarios of $\gamma < 2.00$ are analysed with the DAA BEM and the USA implemented shock wave and bubble models.

Physical FSI modelling

The even greater availability of computation power since the development of the USA code now also allows for FSI modelling with structure and fluid elements. The benefits of this method are that restrictions inherent to the DAA, shock wave, and bubble models can be negated by the physical modelling of each phenomenon. This comes at the significant cost of computational power, but this is becoming more justifiable option for full-scale platform analysis as computing power costs continue to decline.

A hybrid approach using the DAA BEM on a fluid mesh is possible with the USA code and LS-Dyna. For this application part of the fluid around the structure is physically modelled assuming acoustic propagation properties. The DAA boundary elements are then applied to the outside of this mesh. This method has the advantage of being able to consider the effects of cavitation near the structure. The acoustic shock wave can also be modelled through the fluid for tracking purposes. This approach was demonstrated by Shin [100] for a full scale surface ship model, and it was noted that the numerical results compared well with experimental measurements. Shin also concluded from this approach that full scale ship shock assessment could be achieved with this method but noted the computational power constraints as a hurdle for adoption. It was also suggested that a whipping assessment would be possible through this approach, but this was not tested.

A different hybrid approach was presented by Zhang, et al. [101] who formulated a non-spherical bubble BEM that was capable of producing the jetting response. This was applied against a partially rigid cylinder and a full scale dimensionless surface ship model. The bubble was located in the far-field regime and thus the model did not consider the effects of the ship response on the bubble. Zhang's analysis noted that the jetting load was the most significant of these events, exceeding the damage potential of the shock wave and whipping motion. It was concluded that the application of this model for near-field scenarios was not practical due to the significant cavitation effects which were not captured by the bubble BEM. Zong, et al. [102] expanded on Zhang's method and developed a deformable bubble model that was coupled with the response of structural deformation.

Computational Fluid Dynamics (CFD) generally utilise a Eulerian mesh which remains static as the material flows. In contrast, most FEA methods utilise Lagrangian mesh which deforms as the material does. A combination of these methods known as the Arbitrary Lagrangian-Eulerian (ALE) method [103], allows for a deformable Lagrangian structure mesh to be modelled within a Eulerian fluid mesh and for the Eulerian mesh to be updated to account for the structural deformation. Barras, et al. [104] successfully demonstrated this method for modelling the UNDEX bubble from detonation to the second bubble cycle. It was noted that a 2D axisymmetric model had to be used as 3D would have greatly exceeded any reasonable CPU time costs for the analysis, but should these CPU costs be overcome this would be a promising analysis method. Prompted by the sinking of ROKS Cheonan, a joint investigation conducted a full analysis of the platform subjected to UNDEX using the ALE method [105]. The final ship damage from this model compared well with the 3D scans of the damaged hull, providing a rare real world and full scale validation, albeit at a significant cost. To date this is likely the most detailed model of UNDEX induced whipping available in open literature, though this was only conducted under the exceptional circumstances of the event and is not likely to be replicated in industry until computational power and the expertise to drive these analyses become more readily available. It is also worth considering that this significant effort only assessed one event, while industry would be expected to demonstrate survivability for many scenarios.

Zhang, et al. [106] applied the Smooth Particle Hydrodynamics (SPH) method from Gingold and Monaghan [107], using an axisymmetric model to analyse the detonation of UNDEX. A

BEM was also applied to produce a pulsating bubble and resolve a jetting response. This compared well to experimental results and highlights that combined numerical methods possess the capability to complete more of the UNDEX analysis as CPU time becomes more readily available. de Graaf [108] also used SPH to explore the complex interaction of the gas-water interface between the bubble produced by an underwater seismic airgun. She also noted computational power and time as limitations to the method and this ultimately meant the simulation was not capable of reproducing experimental results.

Modelling of the individual components in an UNDEX event (detonation, shock wave propagation, pulsating bubble) and the structural response to these is possible for independent consideration. The combination of all in one is at present an idealistic scenario and is rife with challenges from FSI effects, material properties and the raw computational power and time requirements. While it is possible to achieve a full ship analysis using more advanced techniques, the current methods remain reasonably inaccessible for industrial applications at present and therefore, it was considered impractical to conduct further assessment with these advanced FSI methods.

2.4. Conclusion

From this review of UNDEX bubble interaction and platform response analysis methods a number of tasks have been identified to conduct further investigation into the UNDEX induced whipping response of a submerged platform.

The interaction of bubbles and boundaries is an ongoing area of investigation. Studies have defined a proximity parameter of the bubble which has been used to characterise interaction regimes and responses that may occur within these. The relative size of the bubble to a structure has not been directly considered and is often only informally reported in extreme circumstances, i.e. a very small bubble near a very large structure or vice versa. The effect of the relative bubble-structure size on their coupled interaction warrants further investigation.

Existing experimental investigations have primarily focused on the shock response with limited regard, if any, to the whipping response. Further experimental investigation into the whipping response is required to assess and validate analysis methods that can be used to determine a platform's suitability for operational requirements.

Standard, spectral, analytical, and numerical methods were reviewed for their applicability and potential to conduct a whipping analysis. Previous demonstrations of transient UNDEX shock response using numerical analysis are promising for use as assessment tools for an UNDEX induced whipping analysis of a submerged platform, but these have yet to be validated for this purpose. The DAA BEM in the USA code is the most promising numerical method for this application, with the more advanced hybrid and full physical FSI modelling methods still largely inaccessible for industrial applications. Validation of this tool with experimental data will provide confidence for its use as an assessment method on future platforms.

Chapter 3. Experimental investigation

3.1 Introduction

In the previous Chapter it was identified that no recent experiments focused on the whipping response of a platform due to UNDEX loading. The last experiment to report on the UNDEX induced whipping response for a submerged platform in significant detail was Chertock [57] who conducted a series of experiments in the early 1950's. Since this time there has been significant advancements in the knowledge of UNDEX and structural response. Measurement equipment is also far more sophisticated now compared to what was available to Chertock at the time. With these considerations and with the interest in developing further understanding of the whipping response and ways in which it can be assessed, it was decided that a new experimental investigation was required to explore the research questions raised in Section 1.2 of Chapter 1.

The following experimental investigation was conducted to measure the elastic whipping response of a submerged platform. The platform was subjected to a series of UNDEX events of different charge sizes W, and at different stand-off distances R and locations L along the platform's length. With these variables, the investigation considers how the bubble proximity γ and its relative size to the platform λ affect the UNDEX induced whipping response. Details of this work have been published as a Research Report (DST-Group-RR-0451) [109] through DST Group, who also provided the experimental facilities and technical expertise to conduct this investigation. At the time of this publication, this is the largest generic platform to have been purposely developed for analysing the UNDEX induced whipping response.

3.2 Methodology

3.2.1 Platform design

The experiments were conducted at the Defence Science and Technology (DST) Group Underwater Explosion Test Facility (UETF) in Epping, Victoria. The facility is a flooded quarry with approximate dimensions of 100 x 40 m, as shown in the overview in Figure 3-1, and water depth varying from 12 to 16 m. A nominal test depth of 5 m was specified to limit boundary interaction effects from the free surface and the quarry floor.

A new test platform was required to undertake these experiments. This would be subjected to UNDEX events detonated at horizontal stand-off locations from the platforms centreline to induce a whipping response. Horizontal stand-off locations were used to prevent the bubble migrating and collapsing on the platform, which would have caused an undesirable contact scenario for this experimental investigation into the near-field, non-contact UNDEX induced whipping response of a submerged platform.
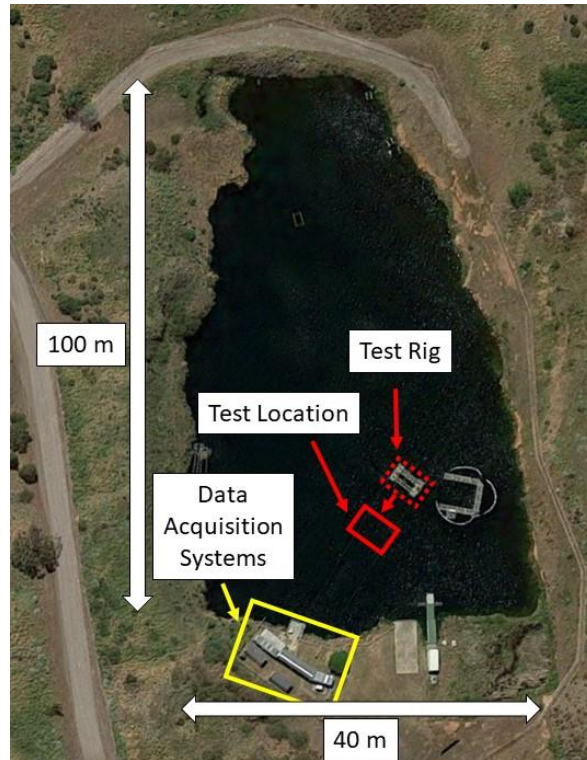
Figure 3-1   Overview of the DST UETF and test platform location

A design study for a free-free ended hollow cylindrical section beam structure (the platform) was conducted. The hull of the platform was constructed from a standard pipe size. It was determined that based on the test area size and depth, and the standard pipe sizes available, that a maximum charge size of 250 g[1] of Pentolite could be used and not pose a significant risk of yielding the platform hull. The design of the platform hull was primarily based on achieving a similar natural bending mode response frequency to the frequency of bubble pulsations from the 250 g pentolite charge detonated at a depth of 5 m, which was calculated to be 7.2 Hz from Equation 1.4. From these design constraints, a 12 m long, 400 mm nominal diameter (DN400), 6.35 mm thick (SCH10) standard pipe was selected for the platform hull. The high length to breadth ratio of this platform (12/0.4 = 30) is a largely unrealistic value however, this design produced a platform that could undergo the worst case whipping scenario, where the natural frequency of the platform bending response and bubble pulsation were similar. The simplicity of the platform also allowed for a simple numerical model to be developed for later comparisons and further investigation. Further details of tuning this design are described in Appendix 1.
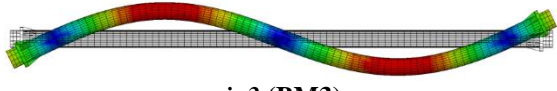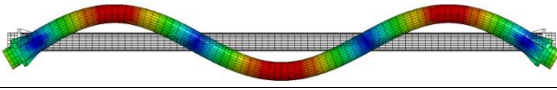
The platform hull was manufactured from C350 grade cold rolled steel according to standard AS1163 [110]. The platform hull was fitted with flat flanges at each end and flat endcap seals, constructed according to standard AS2129 Table E [111]. Each endcap had a purpose-built rack mount system to attach disk weights, which were used to control the platform's net buoyancy and to tune its bending mode frequency response to the bubble frequency. The overall design and additional structural features are shown in Figure 3-3. Each disk weight was approximately 25 kg and the final configuration utilised nine disk weights at each end, for a total additional mass of 450 kg. This provided a reserve buoyancy of approximately 80 kg.

A wet modal analysis was performed on this early stage design of the platform to predict the BM response shapes and frequencies when the platform was fully submerged at a centreline

---

[1] g is the mass unit of grams. To avoid confusion acceleration g units are not used within this thesis.

depth of 5 m. This was achieved using the implicit LS-Dyna solver [112] coupled with the USA code [113], which calculates the added fluid mass using the boundary integral method described by Deruntz and Geers [21]. The platform was expected to behave as a free-free ended beam, and therefore it was anticipated that the lowest BM responses would be dominant. The first three BM responses are considered sufficient to account for most of the response in naval platforms [17] and these mode shapes and frequencies are presented in Table 3-1, with longitudinal distances of the response shape node and anti-node positions measured from amidships. These shapes and locations were used to determine the explosive charge and instrumentation locations.

Table 3-1   Wet bending mode response frequencies and the longitudinal positions of the response shape nodes and anti-nodes, relative to amidships

Bending Mode	Frequency (Hz)	Anti-node positions (m)	Node positions (m)
j=1 (BM1)	6.8	0.00, ± 6.00	± 4.30
j=2 (BM2)	20.3	± 2.80	0.00, ± 5.25
j=3 (BM3)	41.6	0.00, ± 3.90	± 1.95, ± 5.62

Additional functional modifications were made to the early platform design. Three access portholes were constructed into cut-out sections that were welded back into the hull and reinforced to maintain the watertight integrity against UNDEX loading. These portholes were used to install and remove internal measurement transducers located at amidships and at 2.8 m forward and aft, as noted in Figure 3-3. A cable gland was inserted at the top of the pipe for running data cables to the on-shore data acquisition systems.

Six outriggers were used to suspend pressure gauges and position the explosive charge with respect to the hull. These were fixed by a clamped saddle design around the hull. The design also allowed these to be repositioned between each experimental event.

The locations of the portholes and outriggers corresponded to the anti-node locations for the BM1 and BM2 mode shapes, noted in Table 3-1. The total mass of the full platform outfit, including all modifications and measurement transducers, was measured as 1548±1 kg. A breakdown of the mass for major components, presented in Table 3-2, was calculated from CAD geometry and real measurements of the actual platform. An approximate mass distribution of the platform hull and end masses is shown in Figure 3-2.

Table 3-2   General breakdown of the platform structure and component masses

Component	Mass	Quantity	Total
Pipe Hull	735	1	735
End Flanges	36	2	72
Endcaps	65	2	130
End Masses (per end)	25	18 (9)	450 (225)
Outriggers	7	6	42
Access port inserts	6	3	18
Sealing caps	5	3	15
Transducers, cables, fixtures and weldments	86	1	86
Total			**1548 ±1 kg**
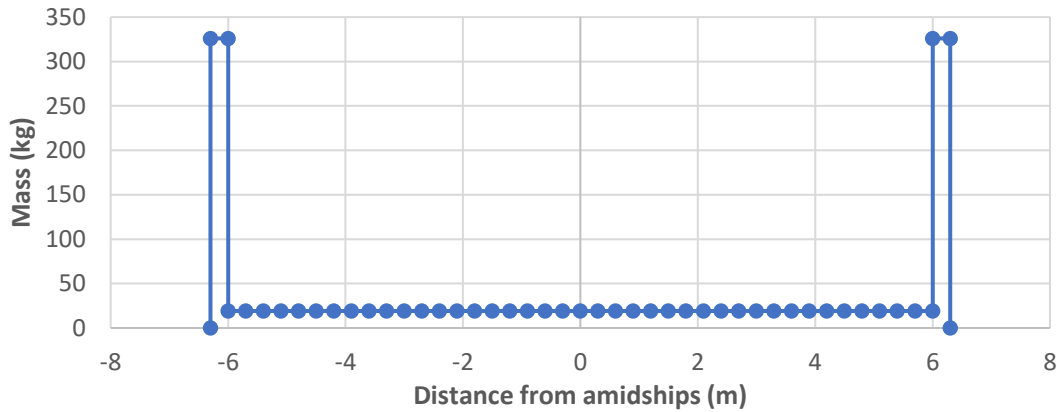
Figure 3-2   Approximate mass distribution per 0.3 m
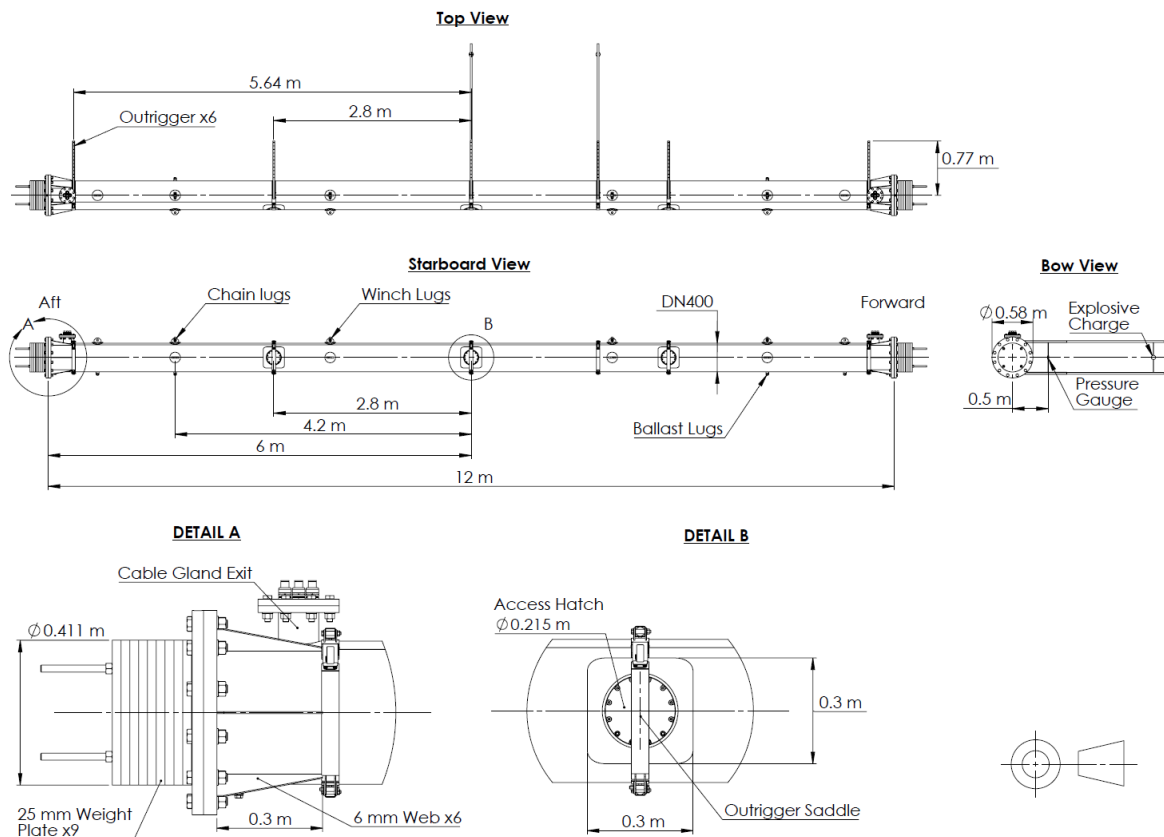
Figure 3-3   Schematic of the platform with detailed features of the end assembly and portholes

The platform was suspended from a floating test rig at a centreline depth of 5 m. A total of 100 kg of ballast mass was suspended by chains below the platform, split evenly between 4.2 m forward and aft of amidships as shown in Figure 3-4, to overcome the positive buoyancy. The location of the vertically suspended mass was at the expected nodal points of BM1 and thus it was judged that the mass would have negligible effect on the platform's horizontal response.
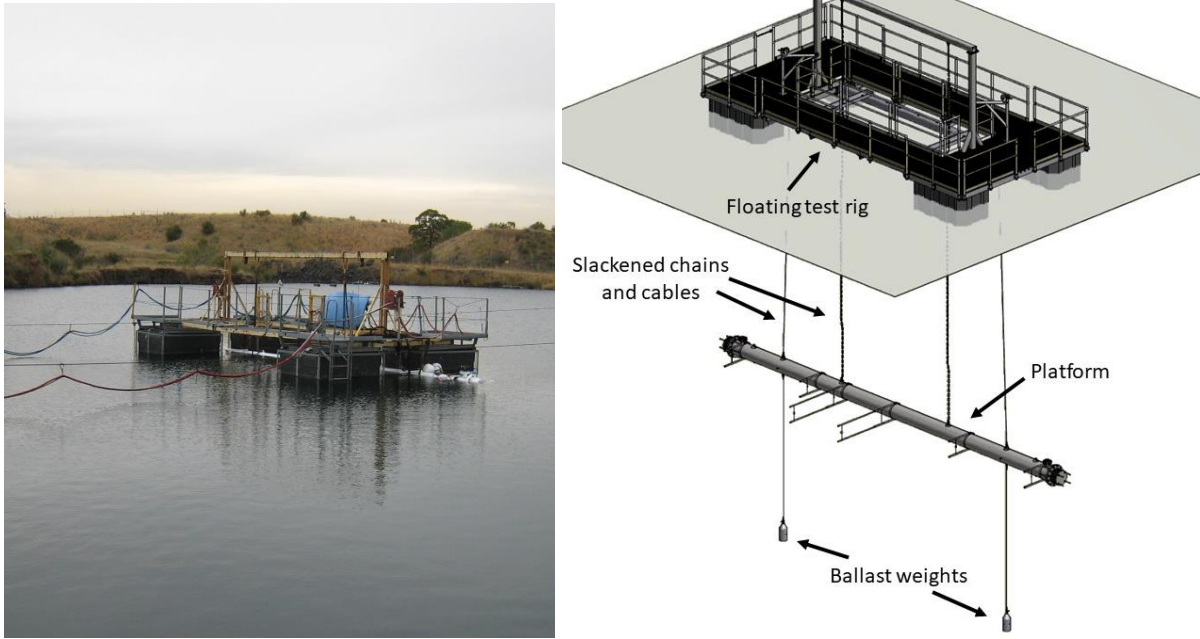
Figure 3-4   Floating test rig with platform suspended below

3.2.2 UNDEX event scenarios

Eight UNDEX events were performed on the platform using military grade Pentolite explosive charges (50/50 TNT/PETN). Each event considered the variables of the explosive charge mass W, and Stand-Off distance R, and the longitudinal stand-off position L. The R distance is taken from the platform hull surface to the centre of the explosive charge. The L distance is measured from amidships to the centre of the explosive charge, where forward is positive and aft is negative.

Two explosive charge sizes (250 g and 43 g) were used in this set of experiments, both detonated at the same depth of 5 m. The variables of each charge size are presented in Table 3-3. The maximum bubble radius (A) was calculated from Equation 1.3 for each charge size, using coefficient $J = 3.52$ from Table 10 of Swisdak [6]. The first T_1 and second T_2 bubble periods were calculated from Equation 1.4, using coefficient $K = 2.11$ from Table 10 of Swisdak [6] for the first bubble period and $K = 1.59$ for the second bubble period, based on an average value of the Pentolite data from Table XI of Swift and Decius [10]. It is worth noting that this Pentolite dataset for the second bubble cycle consists of only two results and the scenarios conducted in this experiment are outside the ranges of this dataset. Therefore, the predictions for the second bubble period may not be as accurate as those for the first bubble period. The pulsation frequency of the first f_1 and second f_2 bubble cycles was determined from the inverse of the period. The similar frequency of the 250 g bubble f_1 and the BM1 response of the platform was expected to induce a strong whipping response, while the mismatched frequencies of the smaller 43 g charge bubble were expected to induce a weaker whipping response. A dimensionless relative bubble size parameter λ was defined, taken as the ratio of the theoretical A, calculated from Equation 1.3, over the nominal platform hull radius R_H of 0.2 m, expressed in Equation 3.1. This parameter is used for the characterisation of the UNDEX events, considering the broad bubble structure interaction regimes that were discussed in Section 2.2.2 of Chapter 2.

$$\lambda = \frac{A}{R_H}$$

<div align="right">*3.1*</div>

Table 3-3   Explosive charge bubble variables

W	A$_{max}$	λ	T$_1$	T$_2$	f$_1$	f$_2$
(g)	(m)		(ms)	(ms)	(Hz)	(Hz)
250	0.9	4.5	140	106	7.2	9.4
43	0.5	2.5	78	59	12.9	17.0

The UNDEX events were arranged as shown in Figure 3-5 with the variables detailed in Table 3-4. All events were detonated on the port side of the platform. To characterise the bubble structure interaction effects of these events that were discussed in Chapter 1, the bubble proximity parameter γ was calculated using Equation 2.1. It is shown in Table 3-4 that *1.45 ≤ γ ≤ 2.00.* Given this proximity, it was expected that there would be a coupling of the bubble and platform responses, but sufficient distance to prevent direct collapse of the bubble on the platform. The Shock Factor (SF) is also provided in Table 3-4 for comparison, calculated from Equation 2.3. A placement tolerance for the *R* and *L* distances was defined as 0.04 m, accounting for a maximum misalignment of 10 % relative to the platform hull diameter.

Table 3-4   Details of event variables

Event	W	R	L	γ	SF
	(g)	(m)	(m)		(kg$^{1/2}$/m)
E1	250	1.8	0.0	2.00	0.28
E2	250	1.5	0.0	1.67	0.33
E3	250	1.3	0.0	1.45	0.38
E4	43	0.8	0.0	1.60	0.26
E5	250	1.3	-2.8	1.45	0.38
E6	43	0.8	-2.8	1.60	0.26
E7	250	1.3	-4.3	1.45	0.38
E8	43	0.8	-4.3	1.60	0.26
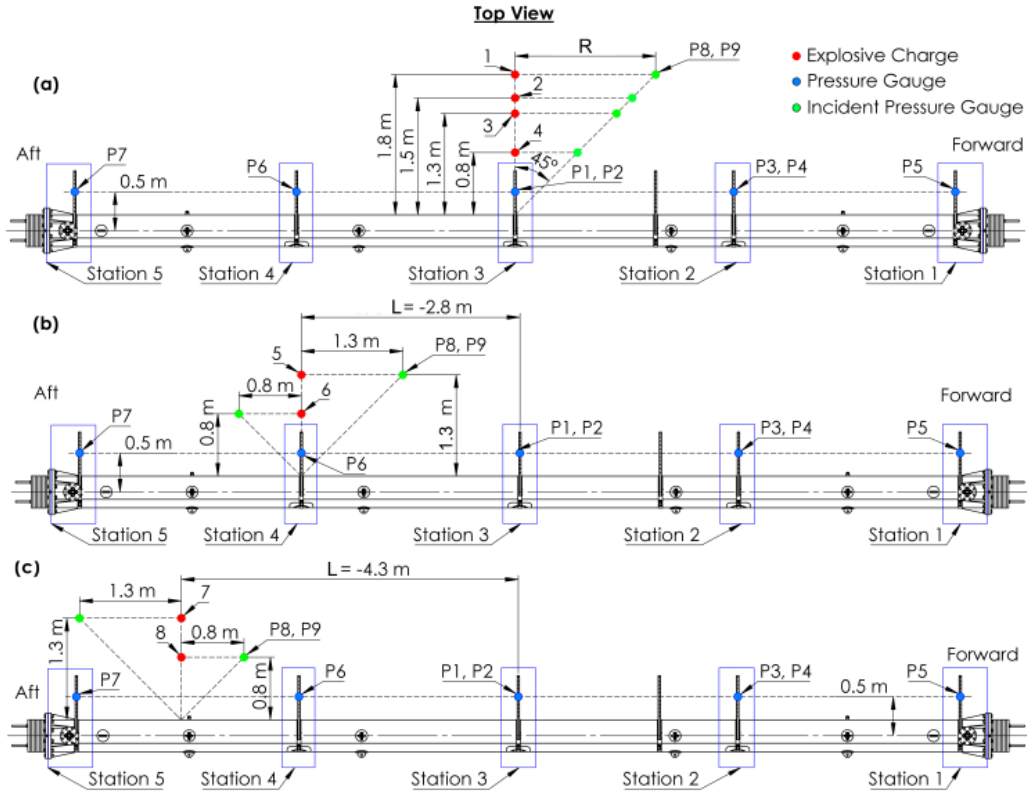
Figure 3-5   Topside view arrangement of charge location, external pressure gauges, and internal measurement locations for (a) E1 – E4, (b) E5 – E6, and (c) E7 – E8.

Events E1 – E3 used a 250 g charge at amidships ($L = 0.0$ m), decreasing the R distances for each successive event to establish the transition from the generally accepted borderline of far-field to near-field UNDEX regimes. Event E4 used a smaller 43 g charge at amidships to investigate the effects of reduced explosive energy and relative bubble size on the platform's response.

Events E5 and E6 repeated events E3 and E4 at a $L = -2.8$ m. These events were conducted to investigate BM2 of the platform. Events E7 and E8 also repeated events E3 and E4, at $L = -4.3$ m. It was expected that these events would excite BM2 and BM3 of the platform and reduce the contribution of BM1 as the L position was aligned with the node of the BM1 mode shape.

3.1.1. Measurement instrumentation

The full instrumentation outfit consisted of transducers for measuring the free-field water pressure, structural acceleration and velocity, and strain for each event. Measurements were taken at five measurement stations noted in Figure 3-5. This report only discusses the results of pressure and strain transducers to characterise the global whipping response from a structural perspective. Details of the additional data acquisition systems and transducers are discussed in Appendix 2.

An Elsys TraNET data acquisition system [114] was used to sample pressure and strain transducers. The data acquisition system was located on shore and suspended transmission lines were run out to the platform over the water. All measurements were taken for a duration of four seconds post trigger time.

Outside the platform, nine free-field pressure gauges (P1 – P9) were suspended from the outriggers at locations noted in Figure 3-5. Two types of pressure gauges were used: Six PCB 138A05 [115] and three Neptune T11 [116] gauges. All Neptune T11 gauges were paired with a PCB 138A05 for comparison. The designations of each gauge type are listed in Table 3-5. All pressure gauges were suspended between the outriggers at fixed positions along the platform length to measure the spread of the incident pressure. Gauges P8 and P9 were moved in relation to the charge position for each event, as shown in Figure 3-5 and detailed in Tables 3-4 and 3-5, to measure the effective incident pressure at the stand-off point on the platform. All pressure gauges were sampled at 5 MHz to track the rise time of the shock wave as close as possible, and calibrated to measure pressure relative to the ambient hydrostatic pressure of 0.05 MPa at the 5 m test depth ($P_{absolute} = P_{gauge} + 0.05$).

Inside the platform, 24 weldable strain gauges (S1 – S24) were used to measure the hull structural response and monitor for any permanent deformation between events. Strain measurements were taken at four locations at approximately 90° increments around the hull circumference, at each of the five measurement stations shown in Figure 3-5. The exact locations of each strain gauge are described using a polar coordinate system shown in Figure 3-6, with the coordinates detailed in Table 3-5. Two strain gauge models were used: Six VPG CEA06-W250-350 [117] gauges were used in two 45° rosette arrangements at amidships on the portside (S1 – S3) and bottom (S4 – S6) as shown in Figure 3-6, and 18 TML AW-6-350-11-01LT [118] (S7 – S24) gauges were aligned in the axial direction. All strain gauges were sampled at 1 MHz with the Elsys TraNET data acquisition system. All internal gauge transmission lines exit the platform hull through topside cable glands, shown in Figure 3-3, where gauges at the forward end exit through the forward gland and gauges at the aft end exit through the aft gland. In most cases strain gauges that make up a planar response (athwartships of vertically opposite pairs) were not able to be positioned directly opposite one another. This means there will likely be some differences when the responses of these planar pairs are compared.
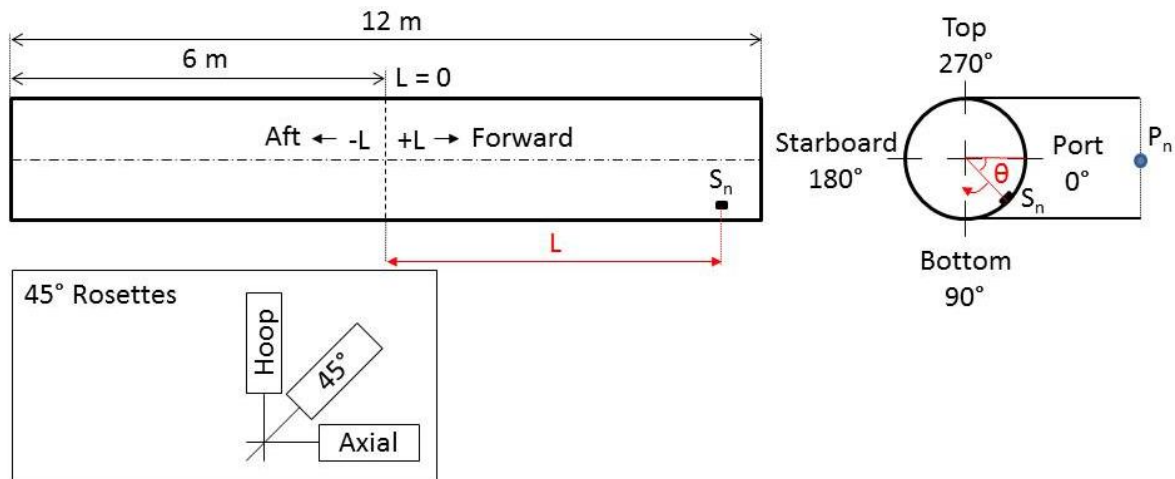
Figure 3-6   Internal arrangement of measurement transducers

Table 3-5   Strain and pressure gauge details and polar coordinates

Station	Gauge	L (mm)	θ	Orientation	Model
1	S13	5825	353		
	S14	5735	90	Axial	TML
	S15	5890	187		
(Bow)	S16	5890	270		
	P5	5640	0	-	PCB
2	S9	2750	0		
	S10	2850	90	Axial	TML
	S11	2500	180		
	S12	2800	270		
(Forward)	P3	2800	0	-	PCB
	P4	2800	0	-	Neptune
	S1	75	0	Hoop	
	S2	75	0	Axial	
	S3	75	0	45°	VPG
3	S4	-50	90	Hoop	
	S5	-50	90	Axial	
	S6	-50	90	45°	
(Amidships)	S7	300	180	Axial	TML
	S8	0	270		
	P1	0	0	-	PCB
	P2	0	0	-	Neptune
4	S17	-2750	0		
	S18	-2850	90	Axial	TML
	S19	-2500	180		
(Aft)	S20	-2800	270		
	P6	-2800	0	-	PCB
5	S21	-5825	353		
	S22	-5735	90	Axial	TML
	S23	-5890	187		
(Stern)	S24	-5890	270		
	P7	-5640	0	-	PCB
-	P8	L = R	0	-	PCB
-	P9	L = R	0	-	Neptune

3.3 Results and discussion

The results obtained during the experimental investigation are presented and discussed under two general aspects: the incident pressure loading and the structural response. The effects on the whipping response due to the different R distances and L positions, and the charge mass W are also discussed in further detail. Further discussion is made with the combined incident pressure and strain results for the L position variable.

3.3.1 Incident pressure

The incident pressures are representative of the pressure emitted by the explosive charge shock wave and bubble response at the measurement stand-off distance, where a positive pressure is defined as pushing away from the charge source and a negative pressure is pulling towards the charge source. Only one incident pressure gauge (P9) provided usable data from the experiments; all others suffered mechanical failure during the first few events. Failure of these gauges was largely due to compromised water integrity through by shock wave loads on the exposed gauge connecters. The shock wave itself was also likely to have damaged electrical

components over the repeated events. The combination of repeated usage, proximity of the bubble, and duration of the required measurements meant that these gauges were being operated at and above their limits during this experiment.

Gauge P9 was relocated between events to measure the effective pressure on the hull at the stand-off distance, as described in Section 3.1.1 and illustrated in Figure 3-5, which also corresponds to the bubble proximity parameter γ. Ultimately this gauge also failed during the shock loading from event E7. Due to this, incident pressure measurements are presented and discussed only for events E1 – E6 in this section. No comparison of the different pressure gauge models was possible due to the gauge failures.

The characteristic incident pressure for all events consisted of the shock wave, followed by at least two significant bubble pulse cycles. Differences in the frequency of bubble pulsations were purely dependent on the charge size, as all events were conducted at the same depth of 5 m in this experiment. An example incident pressure record for the 250 g charge size from event E1 is presented in Figure 3-7a. All 250 g events contained a minor third bubble response before the pressure record zeroed out, indicating the bubble had vented at the surface. The incident pressure for the smaller 43 g charge, example from event E4 shown in Figure 3-7b, contained a third and fourth minor bubble pulse before the signal zeroed out. The additional minor pulse from the 43 g events was due to the smaller bubble produced, which builds up a lower buoyancy force and reduces the migration rate to the surface.
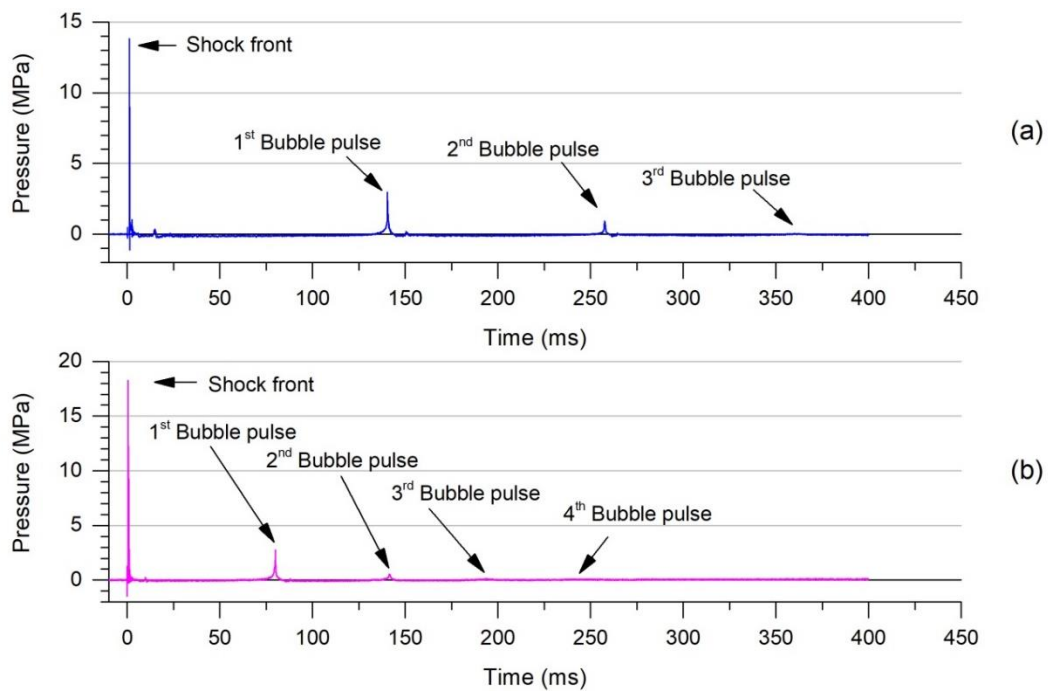
Figure 3-7 Characteristic incident pressures records for (a) W = 250 g from E1 (R = 1.8 m, L = 0.0 m), and (b) W = 43 g from E4 (R = 0.8 m, L = 0.0 m)

Shock wave

A detailed overview of the initial shock wave and reflection pressure loading is presented in Figure 3-8. The initial shock wave (Figure 3-8a) contained a small signal pulse almost immediately after the trigger time. This pulse was an artefact generated by the electric triggering mechanism and was present on all pressure and strain time histories and therefore, it was not considered to be representative of any mechanical loading from the UNDEX event itself. All pressure measurements of the initial shock wave contained large cavitation and

collapse effects during the initial front decay. From the Time of Arrival (TOA) of the cavitation pulses, the source was determined to be from the outriggers that gauge P9 was suspended from. The outriggers were comparatively flexible in the design, more so than what was initially anticipated. They also underwent some minor plastic deformation on post-event observations. The combination of these effects caused large cavitation loads from the initial shock wave to occur very close to the gauge. Fortunately, because these loads occurred so early in the decay of the shock wave, they did not obstruct any of the environmental reflections, noted in Figure 3-8b. Because of the source location, the measured cavitation loads are not representative of what would have been experienced on the platform. It is likely though that some cavitation would have occurred near the stand-off location on the platform.

The later shock wave loads in Figure 3-8b were determined to be reflection sources from the platform, free surface, and quarry floor and walls (noted and highlighted in Figure 3-8b), based on their TOA and relative distances from the gauge. The measured reflections from the platform are of course not representative of the direct loading experienced by the platform, but all other sources are considered to have contributed to the total shock loading of the UNDEX event.
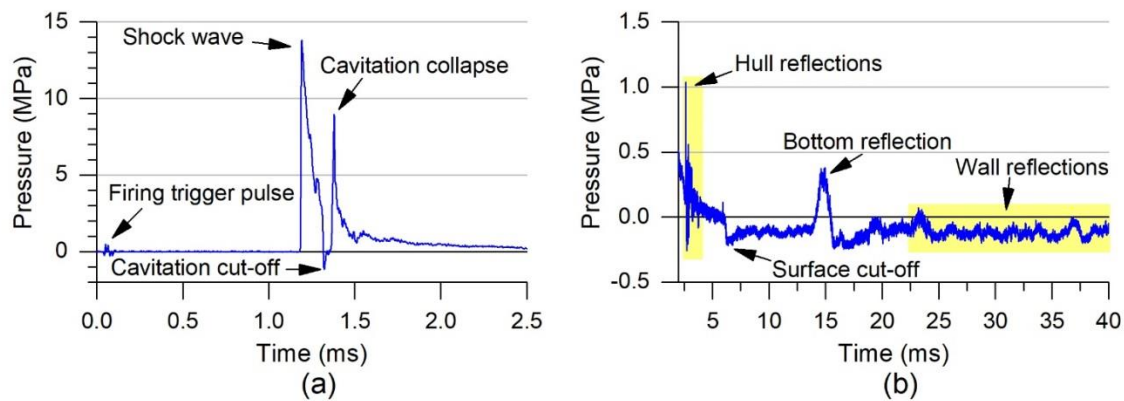
Figure 3-8   (a) Initial shock wave and (b) later shock reflection pressure measurements. Example from E1 (W = 250 g, R = 1.8 m, L = 0.0 m)

The initial shock wave incident pressure-time histories from events E1 – E6 are compared in Figure 3-9 for each charge size. The shock fronts from the 250 g charge events in Figure 3-9a show that the peak pressure increased when the R distance was reduced, as expected. The measured cavitation collapse loads from the outrigger in event E1 were much larger than those in other events. The variation in these loads can be attributed to variables in the outrigger design, such as bolt tension and fastening saddle position. Additionally, these outriggers did experience some minor plastic deformation from the first event which will have altered their response in subsequent events. Event E4 in Figure 3-9b also contained a more prominent cavitation loading from the outrigger than was seen in event E6, which may be due to further plastic damage occurring from this closer event.

There was a slight difference in TOA between events E3 (0.85 ms) and E5 (0.79 ms) which have the same R distance. There was a standard variation of 3.4% between their arrivals which can be accounted for within the charge placement tolerance. The similar 43 g charge events E4 (0.51 ms) and E6 (0.61 ms) also had a difference in TOA with a larger standard variation of 8.8%, which can also be accounted for in the charge placement tolerance.

The peak pressures between the similar events compared very well, with an average peak pressure of 21.8 MPa and standard variation of 0.1% for events E3 and E5 (W = *250 g, R = 1.3 m*), and average peak pressure of 18.1 MPa with a standard variation of 0.8% for the events E4 and E6 (W = *43 g, R = 0.8 m*). The similarity of the peak shock wave pressures in

these similar events show that the minor difference in TOA did not have a significant effect on the shock loading. Based on the similarity of these events, it can be assumed that the shock wave loads of events E7 (*W = 250 g, R = 1.3 m*) and E8 (*W = 43 g, R = 0.8 m*), which did not produce reliable measurements, would have been similar to events with the same *W* and *R*, namely E3 and E5, and E4 and E6 respectively.
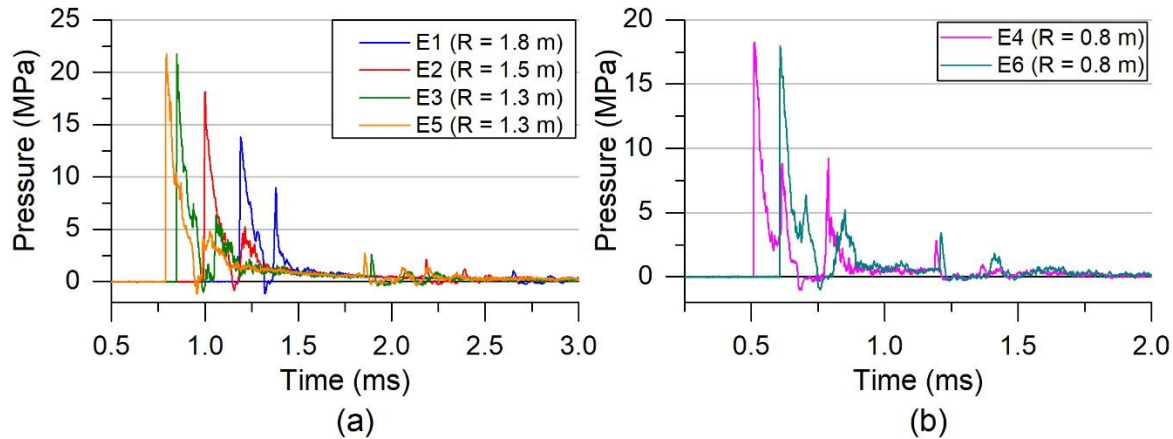
Figure 3-9   Comparisons of the initial shock wave for events E1 – E6 for (a) W = 250 g and (b) W = 43 g

Bubble response

The characteristic response of one bubble cycle (example from E1) is presented in Figure 3-10. Here it is shown that the gauge pressure was mostly negative during the quarry wall and floor reflections from the shock wave. The pressure record steadied and further reduced after these reflection sources, which is the characteristic response of the bubble under-pressure phase from its expansion. The lowest pressure, followed by a steady increase indicated when the bubble had reached its maximum radius, noted in Figure 3-10a by the dashed line at approximately 70 ms. The pressure steadily increased until it reached the hydrostatic pressure, and then it increased rapidly into the bubble pulse, highlighted in yellow. A close-up of the bubble pulse incident pressure in Figure 3-10b shows that the regular pulse shape had a sharp peak. The near instantaneous rise time of this peak indicates that a shock wave was emitted during the collapse phase of the bubble cycle and therefore this collapse partially occurred at supersonic velocity in the water. The highlighted bubble pulse rapidly decays and was followed by the arrival of its own surface cut-off reflection wave, and then the reflection from the quarry floor. The pressure then stabilised at the hydrostatic pressure until the bubble began to expand again, and the cycle was repeated.
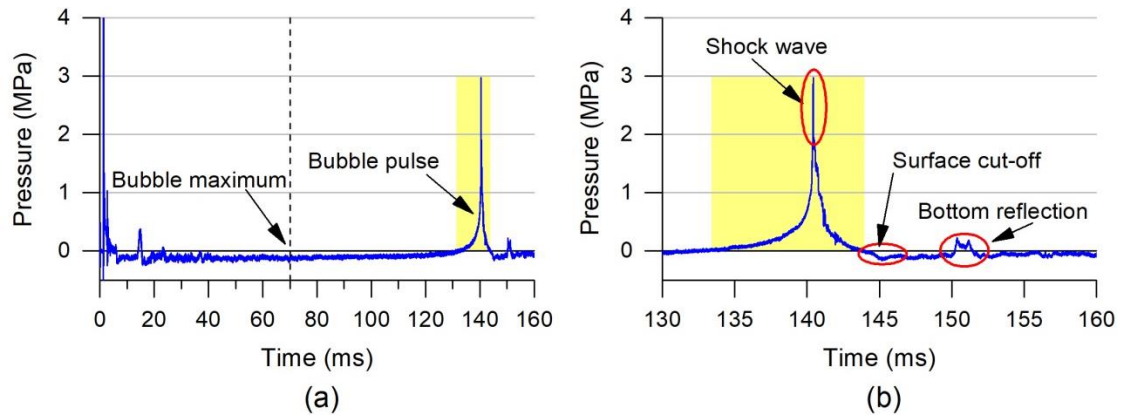
Figure 3-10 Incident pressure due to the pulsating bubble[2] noting (a) the bubble maximum and pulse, and (b) the loading from the bubble pulse. Example from event E1 (W = 250 g, R = 1.8 m, L = 0.0 m).

A comparison of the significant first and second bubble pulses from events E1 – E6 is presented in Figure 3-11 for each charge size. The periods and frequencies of each bubble cycle are listed in Table 3-6. The period of each cycle is taken as the time between the peak of the shock wave to the peak of the first bubble pulse for T_1, and from the peak of the first bubble pulse to the second bubble pulse for T_2. The plots in Figure 3-11 contain offsets for their transmission time from the charge to the platform and so the time values in Figure 3-11 are not a direct measurement of the period.

The first bubble pulse of events E1 – E3 and E5 (*W = 250 g*) presented in Figure 3-11a show that the pulse shape for all these events was very similar and all emitted a shock wave at the peak of the bubble pulse. The average period of these events was calculated as 138.5 ms with a standard variation of 0.2%, which compares very well with the predicted value from Equation 1.4 of 140 ms. Generally, the peak pulse pressure increased between events as the *R* distance reduced, but unexpectedly event E2 had the highest peak pressure due to its shock wave. This may be due to some variation in the expansion rate of the recompressed explosive gas. However, if the shock wave component of the bubble collapse is ignored, the overall pressure pulse from events E3 and E5 was larger. Similar events E3 and E5 (*R = 1.3 m*) had good correlation with their TOA and pulse magnitudes, where the average peak pulse pressure of these similar events was 3.9 MPa with a standard variation of 5.6%.

The first bubble pulse of the events E4 and E6 (*W = 43 g, R = 0.8 m*) presented in Figure 3-11b, also had very good similarity in their pulse shape and magnitude. The period of both events was measured at 79 ms, which corresponds to a pulsation frequency of 12.7 Hz. This compares well to the predicted pulsation frequency of 12.8 Hz from Equation 1.4. The average pulse peak pressure was 2.9 MPa with a standard variation of 4.5%. Unlike the 250 g events, these bubble pulses did not contain a shock wave component, which indicates the bubble collapse was entirely subsonic. The different response seen between charge sizes is likely due to the greater amount of energy that is contained in the 250 g charge compared to the much smaller 43 g charge.

The second bubble pulses are presented in Figure 3-11c for *W = 250* g, and Figure 3-11d for *W = 43 g*. Events E3 and E4 were found to have much smaller and flatter pulse shapes than their respective similar events E5 and E6. However, event E3 did contain a short spike right before the pulse begins to decay. While the pulse shapes varied, the spike in E3 meant that the peak pulse pressures of the similar events E3 and E5 (*W = 250 g, R = 1.3 m*) compared well,

---

[2] The peak incident pressure of shock front (13.83 MPa) has been cut-off the plot to improve clarity of bubble responses.

with an average of peak pressure of 1.1 MPa and standard variation of 3.1%. The similar events E4 and E6 ($W = 43$ g, $R = 0.8$ m) did not compare well, with a large standard variation of 24.9% between the two results. The flattened pulse shape of event E4 was unusual and the experimental setup did not provide a sufficient way to track the shape and motion of the bubble. Based on other experimental work discussed in Chapter 2, particularly the noted observations from Krieger and Chahine [45], a combination of interaction with the platform and migration of the bubble could be responsible for the distorted pulse profiles seen in events E3 and E4.

The average second bubble cycle period for the 250 g events was 116 ms with a standard variation of 0.4%, corresponding to a pulsation frequency of 8.6 Hz. For both 43 g events, the period was 61 ms, corresponding to a frequency of 16.4 Hz. A reduction in period between each pulsation cycle was expected, primarily due to the loss of energy that is emitted at the bubble pulse, which reduces the maximum size the bubble can reach. However, it was found that the periods did not reduce as much as predicted from Equation 1.4 in Table 3-3, where the 250 g and 43 g second bubble cycle periods were predicted at 106 ms and 59 ms respectively. The discrepancy is consistent between events of similar charge size, with the second cycle period being approximately 9% and 4 % longer than predicted for the 250 g and 43 g charges respectively. Two possible causes for this deviation have been identified: Firstly, the sample size for Pentolite UNDEX bubble data beyond the first bubble cycle from Swift and Decius [10] is limited to only two results, and the depth and charge sizes of the present investigation are outside of the ranges of the dataset. Secondly, if the predictions are accurate for free-field UNDEX, the apparent increase of the second bubble period may be taken as evidence of Bjerknes repulsion forces, which would indicate the bubble "sees" the whipping hull as a flexible boundary during the second cycle. Under the circumstances of this second possibility, the closer relative size of the bubble radius to the platform radius during the second cycle may have also increased the coupling strength of this bubble-structure interaction. However, the sample size of these results is insufficient to draw a conclusion to the exact cause.

The bubble period coefficients for the first K_1 and second K_2 bubble cycles have been calculated for all measured events and are presented in Table 3-6. An overall average of the first bubble period coefficient $K_1 = 2.12$ from these experiments compares well to the $K_1 = 2.11$ value from Swisdak [6]. Closer examination of individual events shows that the two furthest events 1 and 2 from the platform (250 g at 1.8 m, and 1.5 m) matched Swisdak's value, while the two 250 g Events 3 and 5 at 1.3 m stand-off had a lower value of $K_1 = 2.09$. The smaller 43 g charge Events 4 and 6 at the closer stand-off distance of 0.8 m had a larger value of $K_1 = 2.15$. These different values result from events outside of the general far-field assumption of $\gamma > 2.00$ which is considered as a limitation of the similitude equations. The results of the present experiment indicate that similitude predictions from Equation 1.4 were valid when $\gamma > 1.67$. Beyond this limit the predictions were unreliable and given the counteracting variation between the smaller and larger charge size scenarios, further work is required to understand the influence of charge size and stand-off distance variables on the fluid-structure interaction. Underwater imaging may greatly assist in future investigations of the bubble-structure interaction.

As previously discussed there was a large deviation of the expected second bubble period predictions and the present experimental results. Therefore, the overall average measured second bubble period coefficient of $K_2 = 1.73$ also varied significantly from the average Swift and Decius [10] value of $K_2 = 1.59$. For the second bubble period, only the charge size seems to have influenced the bubble period where for the 250 g charge an average $K_2 = 1.76$ was measured, while for the smaller 43 g charge an average $K_2 = 1.66$ was measured. This suggests that during the second bubble period the stand-off distance and therefore the relative proximity γ did not have a significant effect on the pulsation period. The same issue of different coefficients between the charge sizes is still present, and further work would be required to

establish the effects of charge size on the bubble-structure interaction where $\gamma < 1.67$. Migration of the bubble between pulses may also account for differences in the period and K factors. Without observation of the bubble response there was no way to determine the contribution of migration to this effect. Given the data from this experiment is of a larger sample size of pentolite explosives than what is present in Swift and Decius [10], the presented second bubble period coefficients from this investigation may be more suitable for use in similitude equations on similar scenarios. For future exploration, free-field UNDEX measurements as a baseline may provide insight on the bubble-structure interaction effects.

Table 3-6   Bubble pulsation periods for the first and second cycles of events E1 – E6. Predicted values from Table 3-3 are presented in red.

Event	γ	λ	T_1 (ms)	Table 3-3	T_2 (ms)	Table 3-3	f_1 (Hz)	f_2 (Hz)	K_1	K_2
E1	2.00	4.5	139	140	117	106	7.2	8.5	2.11	1.77
E2	1.67	4.5	139	140	116	106	7.2	8.6	2.11	1.76
E3	1.45	4.5	138	140	115	106	7.2	8.7	2.09	1.74
E4	1.60	2.5	79	78	61	59	12.7	16.4	2.15	1.66
E5	1.45	4.5	138	140	116	106	7.2	8.6	2.09	1.76
E6	1.60	2.5	79	78	61	59	12.7	16.4	2.15	1.66
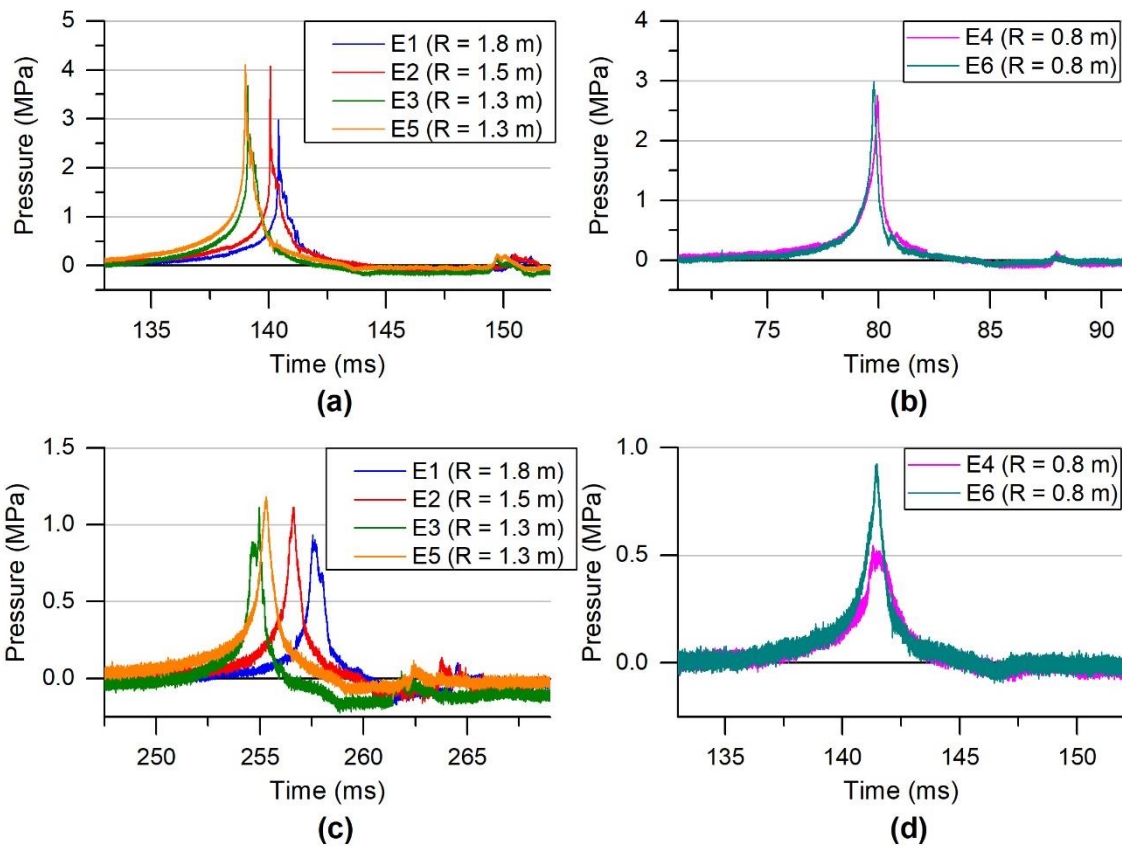
Figure 3-11 Comparison of (a) the first bubble pulse for W = 250 g, (b) W = 43 g, and (c) the second bubble pulse for W = 250 g and (d) W = 43 g from events E1 – E6

Pressure impulse

To assess the contribution of the shock wave and bubble components, the pressure impulse of each event was calculated from the pressure-time histories using Equation 1.5. An example of the first bubble cycle impulse from event E1 is presented in Figure 3-12. The total pressure

impulse of the event I_T (highlighted in yellow) is the sum of the maximum shock impulse I_S and the positive $+I_B$ and negative $-I_B$ portions of the bubble under-pressure impulse I_B. The start of the bubble pressure impulse is determined by a significant change in gradient after the shock wave reflection arrivals, denoted by the first dashed line in Figure 3-12. This point is noted for $W = 250\ g$ and $W = 43\ g$ in Figure 3-13. It is shown that there is a notable delay between the initial shock wave loading and the onset of the bubble under-pressure loading due to the comparatively slower response of the explosive gas expansion rate for the bubble.
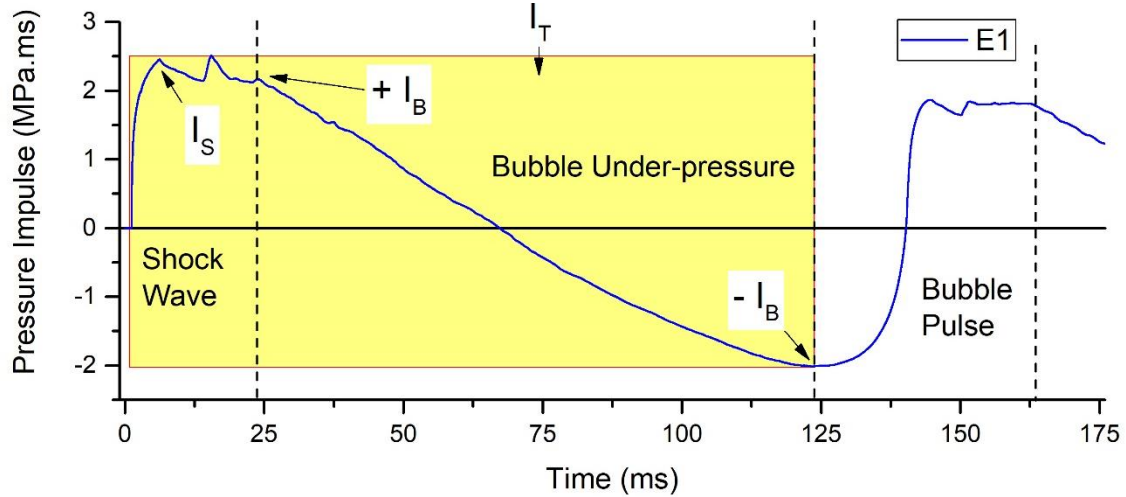
Figure 3-12 Example of pressure impulse produced by Equation 1.5 from event E1 incident pressure

From the identified delay between the shock front and first bubble expansion, a cut-off point between shock loading and bubble loading components was defined. For all 250 g charges, bubble impulse was insignificant on the structure for the first 24 ms, while for 43 g charges there was insignificant bubble impulse for the first 12 ms. Based on these observations, these times were taken as the points at which initial shock loading had ceased and the bubble loading became dominant. This point is noted for each charge size in Figure 3-13 by the dashed line.
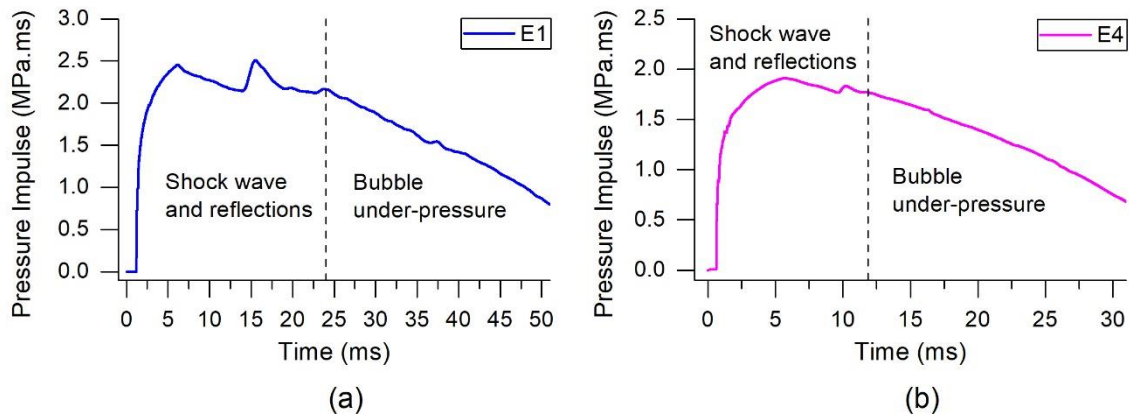
Figure 3-13 Pressure impulse from the shock wave and beginning of bubble loading for (a) W = 250 g, and (b) W = 43 g

The pressure impulse magnitudes for the I_S and I_B of each event are listed in Table 3-7. Assessing the relative contribution of I_S and I_B on the I_T it is shown that the average percentage of I_S and I_B is respectively 35.1% and 64.9% of I_T across all measured events, with a standard variation of 0.6%. Given the different W and R variables of each event, such consistency in these pressure impulse contributions between events indicates that this is likely a property of the explosive material.

For events with the same W and R, the standard variation of the I_T was 3% for $W = 250\ g$ at $R = 1.3\ m$ (E3, E5, and E7), and 1% for $W = 43\ g$ at $R = 0.8\ m$ (E4, E6, and E8). Based on the similarity of these pressure impulses and the previously noted similarity of the distribution of I_S and I_B, it was assumed that events E7 and E8 would have likely had similar incident pressure time histories for their respectively similar charge sizes and stand-offs. Calculated results of I_T for events E7 and E8 have been produced by the average values of similar events. The breakdown of I_S and I_B has been calculated assuming the previously noted average percentage contributions of I_T and these results are listed in Table 3-7.

Table 3-7   Pressure impulse magnitudes for shock and bubble components

Event	I_S	I_B	I_T	I_S/ I_T	I_B/ I_T
		(MPa.ms)		(%)	
E1	2.45	4.19	6.64	36.9	63.1
E2	2.88	5.23	8.11	35.5	64.5
E3	3.32	5.96	9.28	35.8	64.2
E4	1.74	3.64	5.38	32.3	67.7
E5	3.44	6.43	9.87	34.9	65.1
E6	1.91	3.55	5.46	35.0	65.0
Average				35.1	64.9
E7[3]	3.36	6.21	9.57	-	-
E8[3]	1.90	3.52	5.42	-	-

3.3.2 Structural response

The results and discussion of the structural response are categorised by whether the shock or bubble loading initiated the response. From the previous discussion of the pressure impulse loading, the cut-off point between shock and bubble loading was defined as 24 ms and 12 ms (dotted lines in Figure 3-13) from detonation for the 250 g and 43 g charge sizes respectively. Therefore, any structural response between detonation time and the defined cut-off time for each charge size is assumed to be due to the shock loading, while any response after this cut-off time is assumed to be predominantly due to the bubble loading.

For the presented strain records, positive strain is defined as a tensile response and negative strain is a compressive response. The sampling rate of the raw data was reduced by a common factor to reduce the overall file size and noise in the signal. This process is referred to as decimation [119]. The factor refers to the resampling size. A factor of 6 was used, meaning the raw data was sampled at 1 in every 6 points. A moving average filter was applied to smooth these values. Care was taken to ensure that the maximum values from the shockwave were not significantly affected, as a reduction to the peak value would indicate the resampling factor was too high. Plots of the shock fronts are presented unfiltered due to their large frequency content and short duration. Strain records presented for bubble loading responses were further filtered by the application of a low pass 10 kHz Fast Fourier Transform (FFT) filter to further reduce noise. As with the pressure measurements, all strain records contain a trigger signal pulse artefact shortly after the trigger time due to the electric trigger mechanism, which is not a mechanical response.

The first strain responses arise from the shock wave impact at the gauges closest to the stand-off point (SOP) on the platform. An example of this from the amidships rosette arrangement on the portside for event E1 is presented in Figure 3-14. The first measurement is a small and short duration compressive response from all gauges, indicating this is a local "dishing" reaction of the platform hull. This is followed by a rapid series of high magnitude tensile and

---

[3] Values estimated from similar events

compressive response cycles (highlighted in yellow), for an overall duration of approximately 0.25 ms. The early TOA and duration of this loading is likely due to cavitation formation and collapse around the SOP from the shock wave induced motion and elastic deformation of the platform hull, as well as the interaction of incident and reflection pressure waves in the surrounding fluid. In all events, this cavitation response cycle was the most severe response from the shock loading. After the cavitation loading, the platform began to undergo a global structural response, with the first bending response occurring around 0.25 ms after the cavitation response, noted in Figure 3-14.
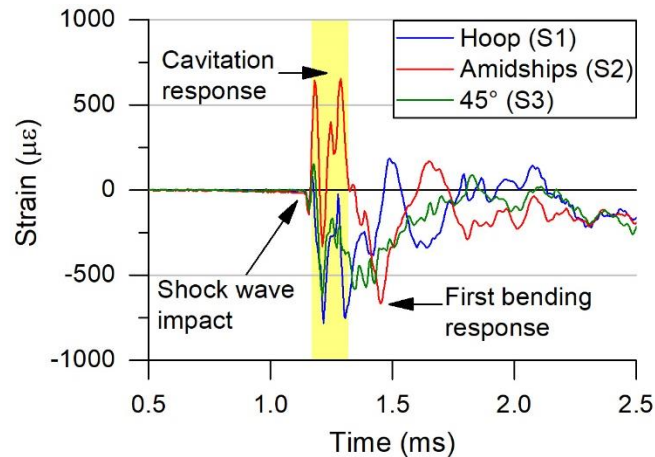
Figure 3-14 Strain measurements of the initial shock response from gauges S1 – S3 in a rosette arrangement at amidships. Example from event E1 (W = 250 g, R = 1.3 m, L = 0.0 m).

At measurement locations away from the SOP, the initial strain response was different. It was observed from strain measurements taken around the Station 4 (-2.8 m aft, strain gauges S17 – S20) in Figure 3-15a, that all four gauges contained a similar compressive pulse response at the same time. Based on this behaviour and the TOA, this first response was determined to be caused by the stress wave propagating down the cylinder from the initial SOP. This wave arrives before the water-borne shock wave travelling at 1500 m/s because it is travelling at a higher acoustic velocity of 5000 m/s through steel. This signal is followed a short time later by the arrival of the water-borne shock wave, noted in Figure 3-15a. Comparing the response as the shock wave moves down the hull length from gauges at amidships (S2), -2.8 m aft (S17), and -6 m aft (S21) in Figure 3-15b, it is shown that the water-borne wave response amplitude reduces at gauges further from the initial SOP. This is due to the greater distance the wave must travel, and therefore disperse, as well as the increased perpendicular angle of incidence of the shock wave interacting with the hull. In contrast, the steel-borne stress wave maintains a similar amplitude between strain gauges S17 and S21 as it moves along the hull length from the initial SOP, due to the absence of the larger dispersion area and angle of incidence that are present in the water environment.
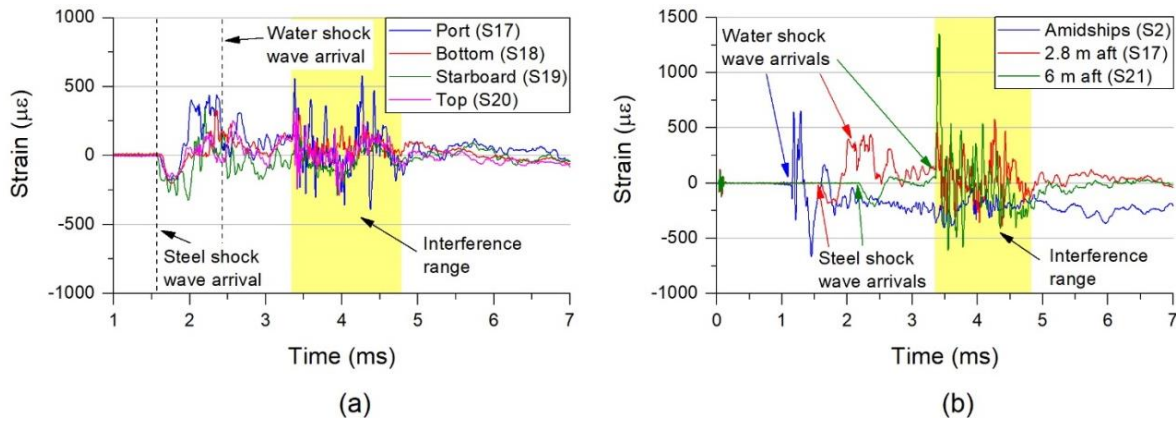
Figure 3-15 (a) Strain measurements for the shock response at Station 4 (-2.8 m aft, gauges S17 – S20), showing the simultaneous TOA for the steel and water acoustic waves, and interference range. (b) Strain measurements for the portside shock response at amidships (S2), -2.8 m aft (S17) and -6.0 m aft (S21), showing the different TOA for the steel and water shock waves, and the simultaneous arrival of interference. Example taken from event E1 (W = 250 g, R = 1.3 m, L = 0.0 m)

The arrival of the water-borne wave at bow and stern locations, noted when the water shock wave arrived at strain gauge S21 in Figure 3-15b, coincided with a significant high frequency anomaly (highlighted in yellow) that was found to be present in many of the strain records. This interference level greatly exceeded the initial shock wave response strain levels at the SOP on most gauges. In some cases, the increase in strain is greater than twice the yield strain limit of the material. Notably in Figure 3-15b, this interference has the same TOA on all affected strain gauges, regardless of their location from the initial SOP. Therefore, this interference cannot be due to a localised event around any one gauge but must be due to a disturbance in the transducer and data acquisition arrangement used by these gauges. Based on the TOA of the interference signal, it was determined that this interference is likely due to the shock wave impacting and reflecting amongst the measurement cables that protrude from the cable glands on the top side of the platform, shown in Figure 3-3. The rapid squeezing and release of the cable may have caused an unwanted change in the cable electrical resistance, acting in series with the desired signals from the strain gauges. The phenomenon has been observed and discussed by Walter [120] as a known problem in shock test measurements. This interference was greater at the aft cable protrusion, which may be attributed to a variation in the cable sealing process. On post-test examination, it was found the cables protruding closest to portside (the same side as charge detonation) were affected more than those closest to the starboard side, with the portside cables likely "shielding" those on the starboard side to some degree. For most strain measurements, the TOA of the interference was outside of any significant loading or structural response time ranges of interest and therefore, the interference response could be neglected. For measurements taken at the bow and stern of the cylinder (strain gauges S13 – S16 and S21 – S24) this was not the case, as these gauges were located near the cable gland protrusion and the shock wave reached these areas in the same time frame. To report the true maximum strain of the affected locations, it was assumed that due to the spherical spreading from the UNDEX source, the angle of incidence of the shock wave perpendicular to the hull at bow and stern locations was very large, and the bending strain in these areas was minimal due to the free-free beam structure. Therefore, it was assumed that the greatest strain response due to shock loading at these locations would be due to the strain wave travelling through the platform, and not the apparent maximum within the interference range.

For the strain response due to bubble loading and the damped free-vibration of the platform, the principal plane (vertical or athwartships) of the response was determined by comparing the

axial strain gauge measurements about a single measurement location. An example from event E1 taken at the amidships axial strain gauges (S2, S5, S7, and S8) and presented in Figure 3-16 demonstrates that the primary response was bending in the athwartships plane (strain gauges S2 and S7). This was also the primary response plane for all events in this experiment. It was found that all portside gauges measured slightly larger peak strain levels than their starboard counterparts, by an average of 91 με in all events. There are three main reasons why this was the case. First, the effective stiffness of the platform was slightly different for each side. The starboard side had the cut-outs and porthole inserts and additional welding as part of the manufacturing process, all of which will have affected the stiffness. The mass distribution between the port and starboard sides of the platform was also not equivalent as the starboard side porthole inserts were heavier than the portside mounted outriggers, which resulted in a noticeable angle of list of 7° to starboard. Second, the strain gauges on opposite sides (port – starboard, top – bottom) were not always directly opposite one another. For low frequency bending responses this was not as significant an issue due to the proportionally larger wavelength. However, when higher frequency bending responses where present, the strain gauge pair misalignments were more noticeable due to the shorter wavelengths. Larger differences were observed in these scenarios, but these were due to phase misalignment from the gauge measurements as opposed to different amplitudes. Finally, the presence of a bending response in the vertical plane, as seen in Figure 3-16 indicates that the platform response was three dimensional and therefore the measurements at each gauge will not be purely from axial strain due to in-plane bending. The vertical bending responses were found to be of a similar order of magnitude as the differences seen in the port and starboard measurements.
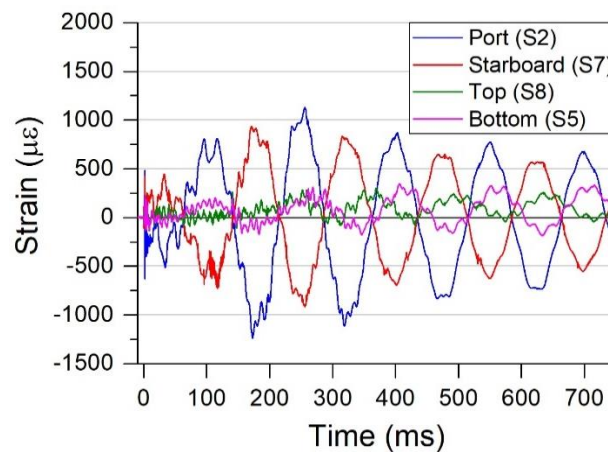
Figure 3-16 Strain measurements of the response from bubble loading at amidships (gauges S2, S5, S7 and S8) demonstrating the primary bending response in the athwartships direction. Example from event E1 (W = 250 g, R = 1.3 m, L = 0.0 m).

The effect of stand-off distance

To determine the effect that the *R* distance has on the structural response, the amidships stand-off events E1 – E4 (*L = 0.0 m*) were considered. A summary of the largest strain response magnitudes at each section of the platform for these events, due to shock and bubble loading, is presented in Figure 3-17.

The shock response was largest at amidships for all these events and was lower at measurement points further along the hull in both forward and aft directions, with the bow and stern locations exhibiting the lowest responses. This was expected due to the spherical spreading and increasing perpendicular angle of incidence to the hull of the shock wave.

For both shock and bubble loading, only minor strain responses were measured at the bow and stern locations, where the greatest strain of the four events was 232 µε measured during the shock response at the stern from event E3 (*W = 250 g, R = 1.3 m*). Given the free-free ended boundary condition of the platform, it was expected that these locations would naturally experience minimal strain during any bending response from whipping and would be more susceptible to the direct shock loading. All events demonstrated this to be the case, though the response from shock loading was only marginally higher than that from bubble loading. Low responses under shock loading are likely due to the dispersion of the spherically spreading shock wave by the time it reaches these ends and the substantial amount of mass at each end compared to the platform's cylindrical hull.
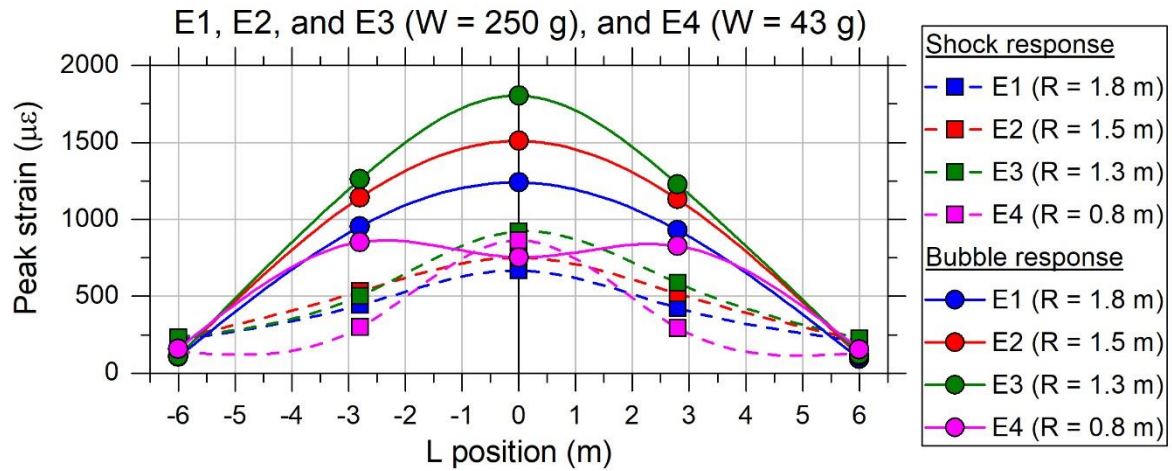
Figure 3-17 Largest strain response magnitudes due to shock and bubble loading at each measurement point for amidships SOP events E1 – E4.

For events E1 – E3 (*W = 250 g*), the largest strain response from bubble loading occurred at amidships on portside, and like the shock wave response the strain levels were lower at measurement points further along the hull in the forward and aft directions, with the lowest response seen at the bow and stern locations. The distribution of the response due to bubble loading indicated global bending of the platform as the dominant response. The most severe scenario of these three events, as well as overall of all events conducted, was E3 at a stand-off distance of *R = 1.3 m*. In this event, the peak strain response at amidships was measured as 1806 µε, which slightly exceeds the theoretical static yield limit of 1750 µε. However, all strain gauges at the amidships location had no indication of physical yielding occurring. Differentiation of the transient result for E3 at amidships (S2) revealed strain rates in the order of 10^5 s^{-1} at the time of the peak response, enough to cause dynamic yield limit effects which would increase the effective yield stress [121]. For all 250 g events at amidships SOP, the peak response from bubble loading was an average of 94% larger than the peak response from shock loading. Therefore, the bending response from the bubble loading was the dominant response of these UNDEX events.

Comparing the transient response of these three events at amidships from the strain gauge closest to the SOP (S2) in Figure 3-18a, it is shown that the bending response in the platform was amplified and the peak strain response occurred just after the first bubble pulse. This amplification of bending is a clear indication that a whipping response was induced by the UNDEX events and driven by the pulsating bubble loads. The bending strains were generally maintained up to the second bubble pulse, with an average reduction in strain levels of 11 %. Notably the closest event E3 (*R = 1.3 m*) had a significantly larger reduction of 308 µε, compared to 105 µε for E1 (*R = 1.8 m*) and 109 µε for Event 2 (*R = 1.5 m*). This larger reduction in event E3 did not continue in successive bending cycles, but was enough to make the bending

responses after the second bubble pulse for E2 and E3 almost equivalent. This unique behaviour in E3 suggests that the increased proximity of the bubble to the structure had a significant effect on the severity of the whipping response, and this severity was increased only when the bubble was driving the bending response in the platform over the first bubble cycle.

After the second bubble pulse, the platform demonstrated a damped vibration response, which suggests the bubble loading was no longer strong enough to have any significant effect on the platform's response. High frequency components from the shock wave loading were almost completely damped out by this time and the response was dominated by only a single modal frequency.

The frequency of the whipping response observed in these three events was determined by performing a FFT on the transient signals in Figure 3-18a to produce a frequency response plot, presented in Figure 3-18b. All frequency response plots presented in this paper were produced from an FFT performed on the full length and raw strain record, with a duration of 4 seconds at a sampling rate of 1 MHz. From this plot it was found that the whipping response was dominated by a single frequency of 6.7 Hz. Comparing this to the initial modal analysis from Table 3-1, the response was identified as the first bending mode (BM1) of the platform.
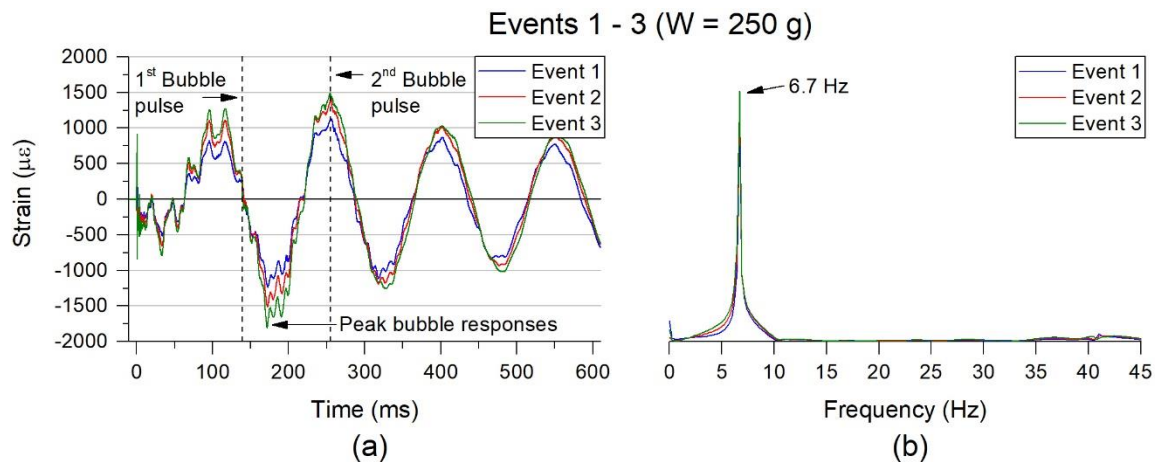
Figure 3-18 (a) Comparison of the strain response at amidships (S2) for events E1 (R = 1.8 m), E2 (R = 1.5 m), and E3 (R = 1.3 m), and (b) frequency response plot of these records.

Event E4 (*W = 43 g, R = 0.8 m*) differed in its bubble loading response from the other amidships events, where the greatest bubble response was measured at the portside locations 2.8 m forward and aft of amidships. The largest bubble response was also slightly lower than the shock response for this event. From the transient strain records on portside at the amidships (S2), 2.8 m forward (S9) and aft (S17) measurement locations, shown in Figure 3-19a, it was found that there was a higher frequency component in the whipping response. The frequency response of these signals, shown in Figure 3-19b, revealed that all these locations contained two significant frequency responses: a dominant response at 6.7 Hz, which was previously identified as the BM1 response of the platform, and another response at 41 Hz. From the modal analysis in Table 3-1, the 41 Hz response was identified as the third bending mode (BM3) of the platform. BM1 and BM3 share a mode shape anti-node at amidships and the alternating phase of these responses resulted in alternating constructive and destructive interference cycles between amidships and the 2.8 m forward and aft measurement locations. The arrival of the first bubble pulse coincided with the first peak of the BM1 response, as noted in Figure 3-19a, and the UNDEX induced whipping response amplified the interaction between BM1 and BM3. The timing of this bending mode interaction resulted in a constructive response occurring at the 2.8 m forward and aft locations for the maximum measured response due to the bubble loading, and a destructive response at amidships. Notably, this response only occurred under

the driving force of the first bubble cycle, and after the first bubble pulse the largest bending response consistently occurred at amidships. The amplified response during the bubble loading is again indicative of the bubble driving the whipping response. It is also worth noting that the bending responses at the 2.8 m forward and aft locations are in phase and have almost the same amplitude over the entire response duration which indicates the platform's response was symmetrical about amidships. Therefore, under this scenario the platform exhibited two independent zones of high severity while its response was driven by the first bubble cycle.

Figure 3-19 Event E4 (W = 43 g, R = 0.8 m, L = 0.0 m) (a) Strain response at portside amidships (S2) and 2.8 m forward (S9) and aft (S17), and (b) frequency response plot of these records.

The effect of longitudinal stand-off position

To examine the effect that different charge *L* positions had on the platform's response, events E3 – E8 are considered. These events are discussed according to their similar *W* and *R* variables. Initially the results of events E3, E5, and E7 (*W = 250 g, R = 1.3 m*) are considered. A summary of the largest peak strain response magnitudes along the platform length from shock and bubble loads in these events is presented in Figure 3-20.

The peak strain measured for the initial shock response of the platform was found to have a similar severity at the station closest to the SOP for each event, with a maximum shock response of 923 με in E3 (*L = 0.0 m*) and 816 με in E5 (*L = -2.8 m*). For E7 (*L = -4.3 m*), there was no strain gauge at the SOP. At -2.8 m aft a peak strain of 871 με was measured, while the closer proximity of the charge to the cable protrusion produced substantial interference on the signals of all strain gauges near the stern (S21 – S24) and no reliable measurement of the shock response could be obtained. The trend of the maximum shock response along the hull length for E7 indicates the peak response may have been higher than what was measured at 2.8 m aft, and would have occurred between the -2.8 m aft and stern measurement locations. However, the similarity of the peak strain level at 2.8 m aft compared to other events suggests that it would not have been significantly higher at other locations. The measured results have good correlation despite the issues with E7, with an average peak strain of 870 με and a standard variation of 3.5% over the three events. Therefore for these events, the shock response was not affected by the *L* position. The distribution of the shock response along the platform length for E5 and E7 was similar to what was observed in E3, with the peak of the distribution only being offset along the platform length by the change in *L* position for each of these events.

Similar to what was observed in events E1 – E4 in Figure 3-17, only minor strain responses were measured at the bow and stern locations for events E3, E5, and E7 in Figure 3-20, where the greatest strain measured was 467 με at the stern during the shock response of E5 (*L = -2.8 m*). It is worth reiterating that it is likely the shock response at the stern would have

been larger during E7 given the *L* position was the closest to this location in this event, but reliable measurements could not be obtained at this location due to signal interference. As previously discussed this general distribution was expected due to the charge proximity, mass distribution and free-free ended boundary condition of the submerged platform. Unlike the amidships events, the peak responses of E5 and E7 were larger at the stern than the bow for both the shock and bubble responses. This can be attributed to the closer proximity of the charge, and smaller perpendicular angles of incidence from the spherically spreading shock and bubble pulse waves for these events.
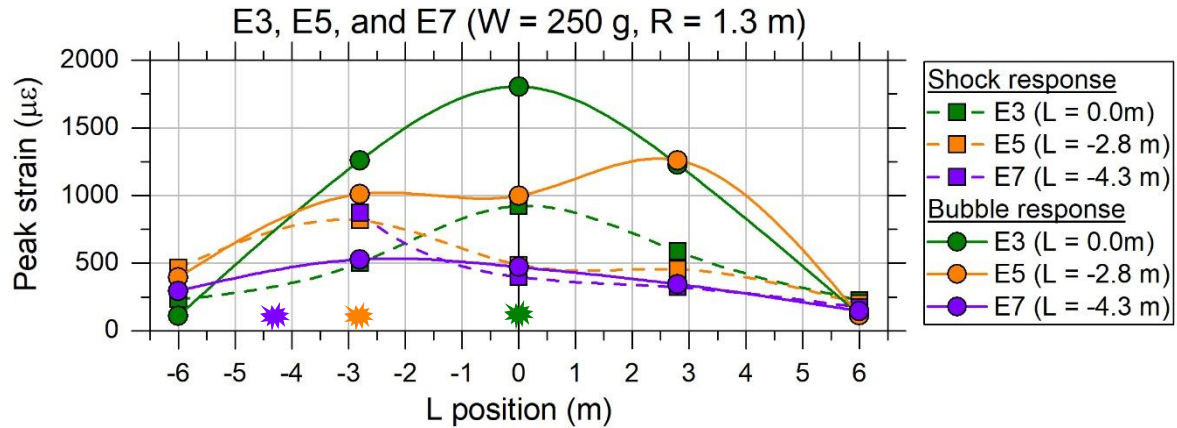
Figure 3-20 Summary of the peak strain response from shock and bubble loading at each measurement location for events E3 (L = 0.0 m), E5 (L = -2.8 m), and E7 (L = -4.3 m).

The peak responses due to bubble loading were substantially different for each event. As previously discussed, E3 (*L = 0.0 m*) exhibited the most severe bubble response out of all the events conducted, with a peak strain magnitude response of 1806 µε at the portside amidships measurement location.

The peak bubble response observed in E5 (*L = -2.8 m*) was one of the most noteworthy observations in this investigation. Here, the peak response from the bubble loading occurred at the 2.8 m forward location on the platform, measured at 1260 µε. A lower peak response of 1011 µε was measured at -2.8 m aft, closest to the charge SOP.

The unexpected response from E5 was further investigated through examination of the transient strain gauge records, on portside at amidships (S2), 2.8 m forward (S9), and aft (S17) in Figure 3-21a. The frequency response plot of these signals is shown in Figure 3-21b. The transient results in Figure 3-21a demonstrate an amplification of the bending response during the first bubble cycle, which demonstrates the bubble was driving the whipping response. Unlike the other 250 g events at *L = 0.0 m*, there were different bending mode responses occurring between each of the measurement locations. The amidships location (S2) was dominated by only one frequency response, the previously observed BM1 at 6.7 Hz, while the forward and aft locations contained a combined response of two dominant frequencies, the BM1 response and a response at 20 Hz. The transient measurements also show that the 20 Hz response was inverted between the 2.8 m forward (S9) and aft (S17) and had similar amplitude which indicates the 20Hz was antisymmetric about the amidships location. The absence of the 20 Hz response at amidships also indicates there was a node for this mode shape at this location. Based on this behaviour and the modal analysis from Table 3-1, the 20 Hz response was identified as the second bending mode (BM2) of the submerged platform.

The interaction of these two bending modes is the most likely cause of the peak response occurring at the forward end, despite the SOP at *L = -2.8 m*. While the BM1 response was symmetric about amidships, the BM2 response was antisymmetric, so BM responses in the

forward and aft ends of the platform were always in opposing constructive and destructive interference cycles. It is seen in Figure 3-21a that due to the phase of these response frequencies, the constructive interference of BM2 at the forward location coincided with the peak bending response of BM1 while under the driven whipping response from the bubble, which resulted in the maximum whipping response occurring at this location.

As with other 250 g events discussed in the previous section, the platform response began to undergo damped free vibration after the second bubble pulse. During this time, the phase of the response at the 2.8 m forward and aft locations shifts slightly which results in the forward and aft responses having similar amplitudes, with the response at the 2.8 m forward location still being marginally higher. The phase shift after the direct bubble loading is a strong indication that the vessel response was predominantly driven by the bubble pulsation frequency and the bubble and platform responses were decoupled after the second bubble pulse.

This result of the overall peak response occurring away from the SOP has important implications for assessment and recovery response of a real platform. It highlights that it is possible for a scenario to occur where the most susceptible part of the vessel is not at the location of the SOP. The change in the *L* position between E3 (*L = 0.0 m*) and E5 (*L = -2.8 m*) also reduced the overall severity of the response in E5 by 30%. Furthermore, it should be noted that the severity at the 2.8 m forward location was essentially the same for both events, i.e. while the overall severity reduced, the 2.8 m forward location saw the same severity from whipping between both events. To correctly identify similar vulnerable scenarios of a platform, the full response would need to be replicated and therefore the entire platform structure would need to be considered in the analysis method. A simplified compartment or symmetric model would not be sufficient to capture this response.
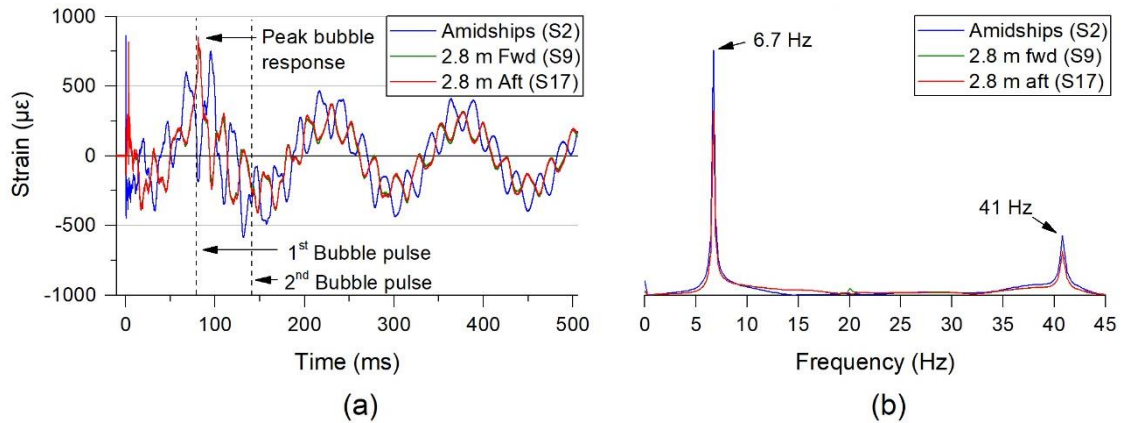

Figure 3-21 Event E5 (W = 250 g, R = 1.3 m, L = -2.8 m) (a) strain responses at portside amidships (S2), 2.8 m forward (S9), and aft (S17), and (b) frequency response plot of these records.

The peak response from bubble loading during event E7 (*L = -4.3 m*) was measured at only 528 µε, as shown in Figure 3-22. This was a significant reduction of 71% compared to E3 (*L = 0.0 m*) shown in Figure 3-20, despite the same charge size (*W = 250 g*) and stand-off distance (*R = 1.3 m*). This was also the only 250 g event where the response due to bubble loading did not exceed the response from the shock wave loading. This reduction in response from the bubble loading is a remarkable result given the only difference in this event was the charge *L* position.

The reduced response from the bubble loading observed in E7 was further examined in the transient strain gauge records taken at the portside amidships (S2) and 2.8 m forward (S9) and aft (S17), presented in Figure 3-22a. Here it is apparent that after the shock wave, there is no amplification of the bending response until the first bubble pulse. In fact, between the shock

wave and the first bubble pulse, the bending cycle amplitudes decayed. The same was true for the bending responses that occurred between the first and second bubble pulses. This behaviour indicates that unlike all other 250 g events, the platform's response was not being driven by the under-pressure of the first bubble cycle. Only the direct pulse loads from the bubble's collapse were able to induce a notable response after the shock wave. This event has demonstrated that the *L* position has a significant effect on the bubble-structure coupling and at this location (*L = -4.3 m*), which coincided with the theoretical position of a node in the BM1 mode shape, the bubble and platform responses were uncoupled. It is possible higher strains may have occurred at the SOP during the bubble loading, but no strain gauges were placed at this location. The lower responses measured at other locations along the platform length in Figure 3-20 suggest that it is unlikely the strains would have been significantly larger at the SOP.

Unlike all other 250 g events, the amplitude of the responses measured between the 2.8 m forward (S9) and aft (S17) locations was not equivalent. For every second cycle of the bending response at these locations, the peaks of each cycle at the aft end were on average 130 με larger than the forward end while under loading from the bubble. The frequency response plot from a FFT of the transient strain records, presented in Figure 3-22b, indicated that unlike all other 250 g events, the dominant bending response for E7 was the previously identified BM2 at a frequency of 20 Hz. Minor responses of the previously identified BM1 at 6.7 Hz and BM3 at 41 Hz were also present. The different amplitudes seen at every second cycle of the 2.8 m forward and aft locations can be explained by the superimposed interaction of the dominant, antisymmetric BM2 and minor, symmetric BM3 responses. The BM3 response frequency is approximately double the BM2 response frequency, resulting in every second BM3 cycle being in phase with BM2. The combination of the periodic phase alignment and the different symmetry conditions of these responses about amidships resulted in constructive and deconstructive interference cycles consistently occurring at the aft and forward ends of the platform respectively.

The results from E7 demonstrate that if the SOP is aligned with a node response of the primary bending mode shape of a platform, the severity of the platform's response from bubble loading can be greatly reduced, to the point that the initial shock response is of a greater concern.

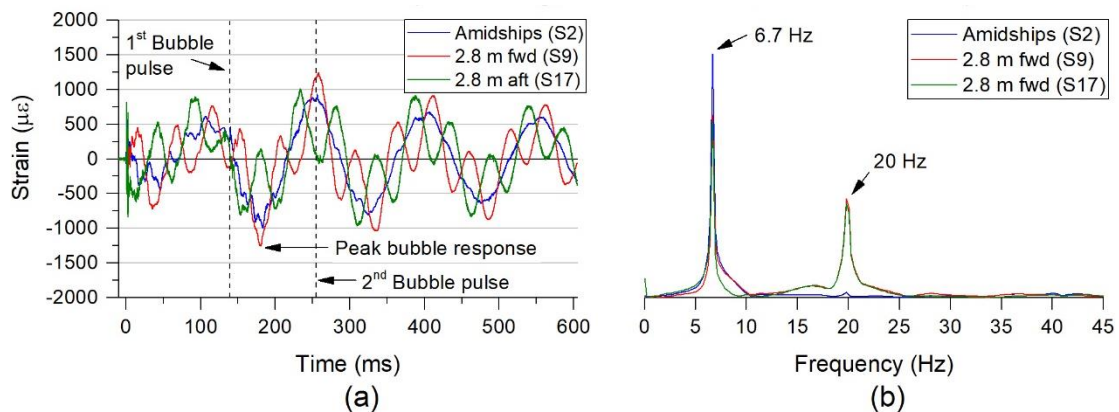*Figure 3-22 Event E7 (W = 250 g, R = 1.3 m, L = -4.3 m) (a) strain response at portside amidships (S2), 2.8 m forward (S9) and aft (S17), and (b) frequency response plot of these records.*

The results for Events E4, E6, and E8 (*W = 43 g, R = 0.8 m*) are now considered. The peak strain response magnitude from shock and bubble loads at each measurement location are summarised in Figure 3-23.

There was a noticeable disparity of the peak shock response between what should have been similar events E4, E6, and E8, shown in Figure 3-23. The peak response of E4 (*L = 0.0 m*) measured 863 µε, compared with just under 600 µε for E6 (*L = -2.8 m*) and E8 (*L = -4.3 m*). There are two explanations for why this was the case. First, the overall reduced energy of the 43 g explosive charge may have been insufficient to produce the same deflection of the platform when the *L* positions from E6 and E8 were closer to the ends, which contained a significant portion of the overall platform mass. Second, due to the interference that occurred at the stern measurement location, it is possible that the true maximum shock response for events E6 and E8 was hidden within the distorted signal. While a set of results was able to be determined at the stern for E6 and E8, these may not be as reliable as other locations due to the interference issues.

Once again, only minor responses were measured at the bow and stern locations for both shock and bubble loading, with the largest response of 360 µε measured at the stern in E6. Again, the peak responses at the stern were higher than at the bow, which can again be attributed to the closer proximity of the charge and the smaller perpendicular angles of incidence from the spherically spreading shock and bubble pulse waves.
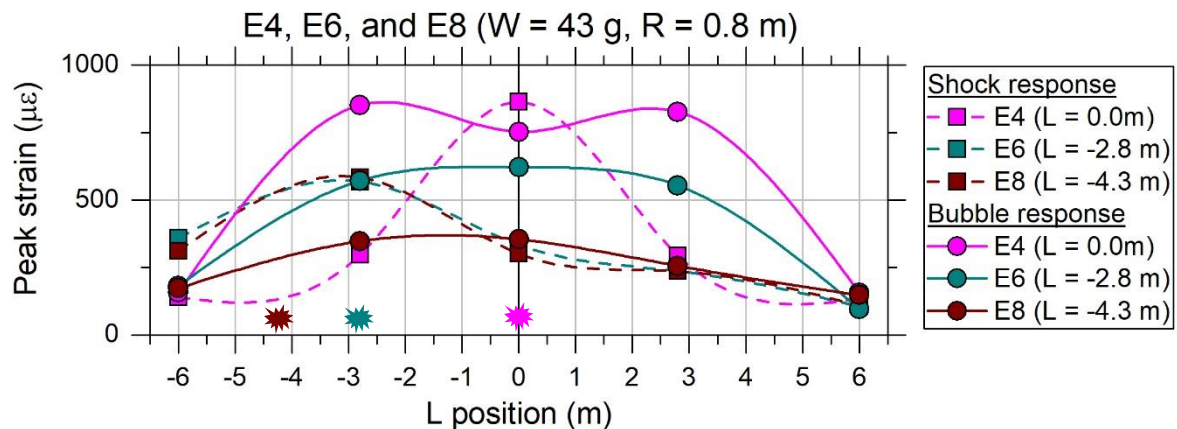
Figure 3-23 Summary of the peak strain response from shock and bubble loading at each measurement location for events E4 (L = 0.0 m), E6 (L = -2.8 m), and E8 (L = -4.3 m)

The overall severity of the bubble response in these events decreased as the *L* position was moved away from amidships. The previously described amidships E4 had the most severe bubble loading response of the 43 g charge events, measuring 852 µε at the - 2.8 aft location.

The peak bubble loading response from event E6 was 621 µε, measured at amidships despite the SOP at *L = -2.8 m*. This peak response was 27 % lower than the amidships event E4. This event did not have the same dip in the peak strain distribution along the hull length at amidships that was seen in E4, instead the severity at the amidships and 2.8 m forward and aft locations was very similar, with an average of 582 µε and a standard variation of 3.5% between the peak measurements at these locations.

The cause of similar peak strain levels measured at the amidships, 2.8 m forward and aft locations for E6 was further examined in the transient strain gauge records from the portside gauges at amidships (S2), 2.8 m forward (S9), and aft (S17), presented in Figure 3-24a. It was found that in this transient response, the amidships strain levels were generally much lower than the forward and aft locations. The only exception to this was at the time of the first bubble pulse, where a large spike was observed in the amidships response. This spike was also the overall peak in the platform's response from the bubble loading for this event. It is also shown that the bending response between the shock wave and the first bubble pulse was amplified, indicating an UNDEX induced whipping response.

Between the first and second bubble pulses, the response was not symmetric between the forward and aft ends of the platform. This non-symmetric behaviour could be due to the bubble locally forcing the aft end and because the lower energy of the 43 g event was insufficient to induce the same motion into the forward end. Additionally, there was a difference between the bubble pulsation frequency of 12.9 Hz for the 43 g charge compared to any of the bending mode frequencies of the submerged platform, which means the pulsating bubble was unable to excite a distinct response in the platform. While the bubble was capable of initiating a whipping response, it was not able to maintain a driving force over the full platform length beyond the first bubble pulse, and the platform's inertia appears to have dominated the motion after the first bubble pulse. Beyond the second bubble pulse the platform started to undergo damped free vibration, where the amplitude of the responses at the 2.8 m forward and aft locations was nearly always double that of the amidships response amplitude.

The frequency response of the three locations is determined by applying a FFT on the transient signals to produce a frequency response plot in Figure 3-24b. Three frequencies were noted, all of which have previously been observed and identified in this investigation. This event is one of the few that exhibited an UNDEX induced whipping response which was not dominated by BM1 at 6.7 Hz. Instead, BM2 at 20 Hz is the dominant response, which is apparent in the previously noted larger responses occurring at the forward and aft locations of the transient records in Figure 3-24a. A minor contribution of BM3 at 41 Hz was also present in all three records. This can be clearly seen interacting with BM1 on the superimposed response measured at amidships during free-damped vibration in Figure 3-24a. The BM3 response did not appear to have any significant interference with the dominant BM2 response at the 2.8 m forward and aft locations.

Like event E4, E6 has shown that when higher modal responses are excited by the UNDEX loads, there can be scenarios where there are multiple points of similar severity over the platform length. E6 also demonstrated that this can be the case even when the UNDEX event occurs away from amidships. Like event E5, it highlights that the most severe response from bubble loading may not always occur at the SOP.
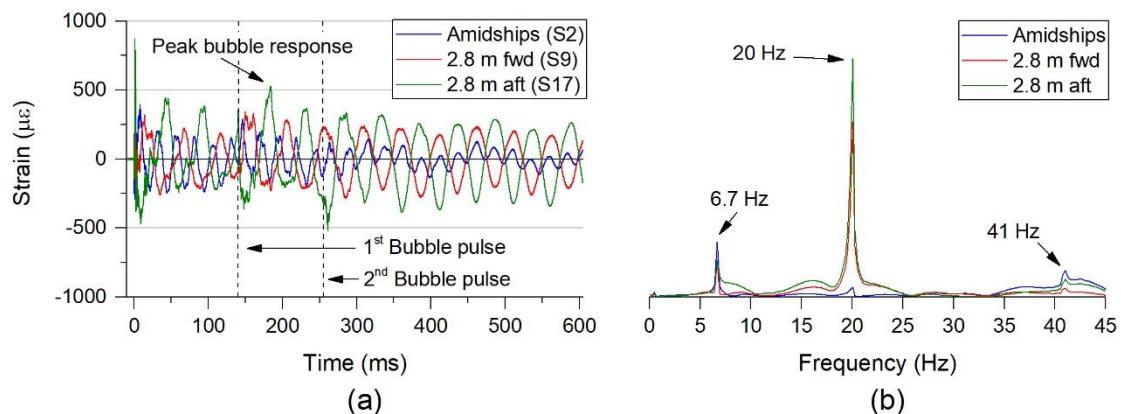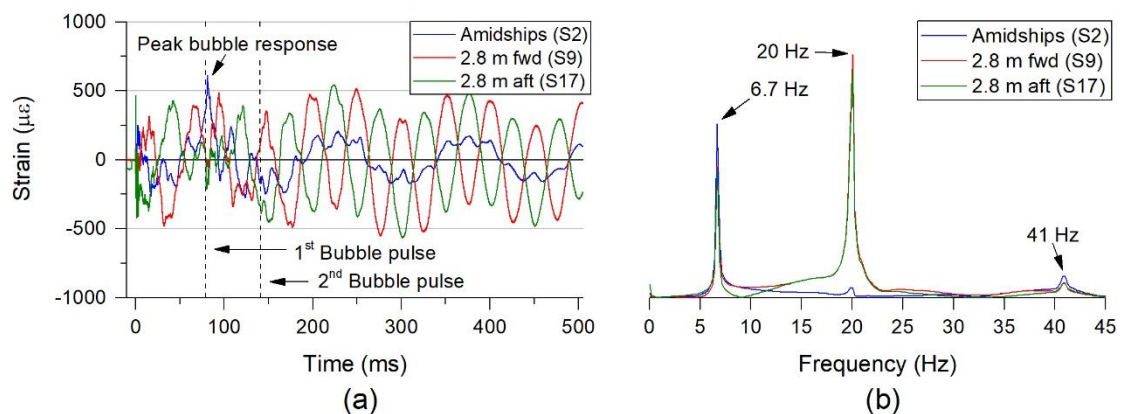

Figure 3-24 Event E6 (W = 43 g, R = 0.8 m, L = -2.8 m) (a) strain responses at portside amidships (S2), 2.8 m forward (S9), and aft (S17), and (b) frequency response plot of these records.

The peak bubble response from the event E8 (*L = -4.3 m*) measured 354 µε, a reduction of 58 % compared to E4 (*L = 0.0 m*). The bubble response in E8 was very similar to what was observed in E7 and while all other 43 g events had a similar severity between the shock and bubble responses, the peak bubble response from E8 was much lower than its peak shock response.

The greatly reduced response from bubble loading was found to be due to the same reasons discussed for E7. The transient strain gauge records from amidships (S2) and 2.8 m forward

(S9) and aft (17), presented in Figure 3-25a, show that like E7, the initial bending response of the structure prior to the first bubble pulse did not amplify. This behaviour combined with the overall reduced strain levels during the bubble loading indicate the bubble did not drive any significant whipping response. The peak responses due to bubble loading for this event are only due to the pressure pulse loading that was emitted during the first bubble cycle collapse. The different amplitudes between the forward and aft locations are also due to the symmetry conditions and phase alignment of BM2 and BM3 discussed for E7. The FFT frequency response results in Figure 3-25b, show that all previously identified frequency response components were present in this event, and like E7, the dominant bending response for E8 was due to BM2 at 20 Hz.

Given the similarity of the E8 response results to those in E7, the same conclusions may be drawn and extended to apply to this smaller charge size of $W = 43$ g. To reiterate, the results of both E7 and E8 have demonstrated that when the SOP was aligned with a node of the primary bending mode shape of the platform, the severity of the platform's response from bubble loading was greatly reduced, to the point that the initial shock response was of a greater concern. As this has been observed for two different charge sizes and R distances, it would appear that this is a function of the L position in relation the platform's primary bending mode shape. Because modal response shapes are a fundamental physical attribute of any structure, it is suggested that any similar structure could be inherently "hardened" against a whipping response if the UNDEX SOP can be influenced to coincide with the node of the structure's primary bending mode shape.
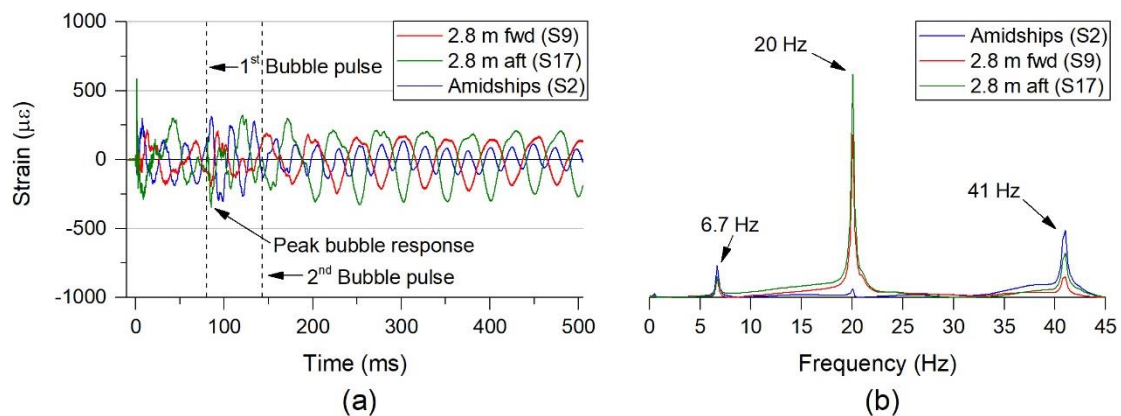
Figure 3-25 Event E8 (W = 43 g, R = 0.8 m, L = -4.3 m) (a) strain responses at portside amidships (S2), 2.8 m forward (S9), and aft (S17), and (b) frequency response plot of these records.

3.3.3 Comparison of bubble pressure impulse and peak strain response

The effect of the L position on the peak strain response magnitude is summarised in Figure 3-26. A linear regression on the shock peak strain data demonstrates that the L position had no effect on the severity of the shock response in these events (R^2 value of -0.05). For the bubble responses, there was a weak linear correlation R^2 value of 0.52, where the peak response was lower as the charge was positioned further from amidships ($L = 0.0$ m). The spread between the highest and lowest peak strain responses from bubble loading at each L position also reduced, despite the same W and R scenarios at each L position. This suggests that the bubble loading had a diminishing effect on the peak strain response after the shock wave, as the L position was moved further from amidships. While it was noted that the results for E7 may have been slightly larger due to the strain gauge locations, this would only result in a stronger correlation between the L position and peak platform response from bubble loading. However,

further data is required to quantitatively determine a relationship between the L position and the peak strain response on a submerged platform.
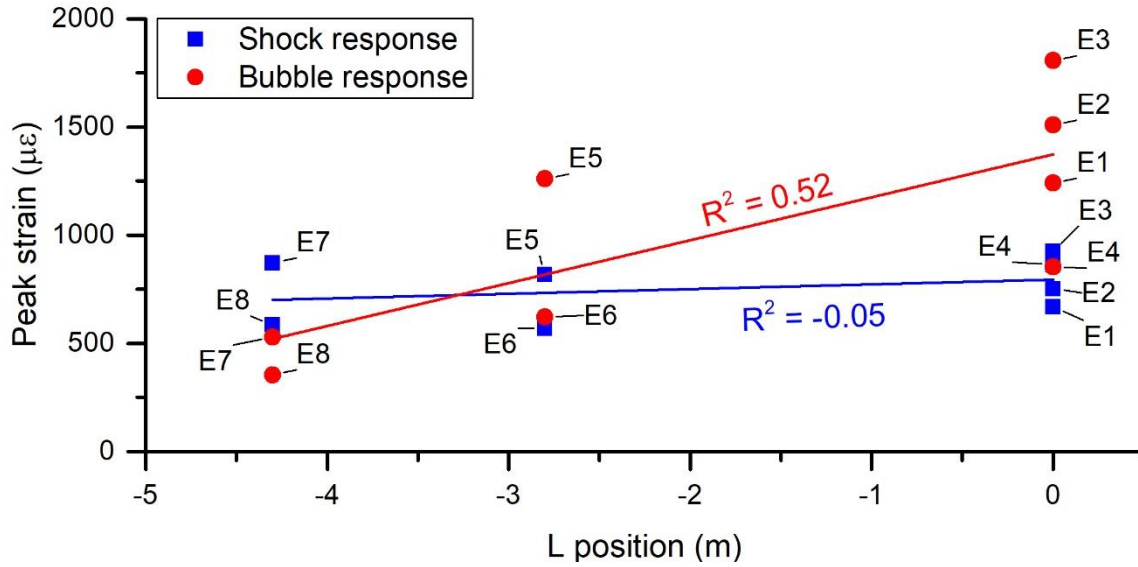
Figure 3-26 The effect of L position on the peak strain responses from shock wave and bubble loading for all events

The effects of the L position on the platform response from bubble loading are further examined by comparing the I_B from Table 3-7 and the peak strain measurements due to bubble loading in Figure 3-27. Here it is shown that while I_B was similar for events with the same W and R (event sets E4, E6 and E8 *(W = 43 g, R = 0.8 m)*, and E3, E5 and E7 *(W = 250 g, R = 1.3 m)*), the strain levels during the UNDEX induced whipping response varied significantly at each L position.

The cause of these differences was purely due to the L position as all other variables remained the same for each similar event set. Due to this, the differences were attributed to the proximity of the bubble to the nodes and anti-nodes of the primary distortional mode shape of the submerged platform, which for this case was BM1. Events closest to the anti-node of the BM1 mode shape at *L = 0.0 m*, E3 *(W = 250 g)* and E4 *(W = 43 g)*, induced the most severe whipping responses for their charge sizes, while those at the node of the mode shape at *L = -4.3 m*, E7 *(W = 250 g)* and E8 *(W = 43 g)*, were 71 % and 58 % lower compared to their respective *L = 0.0 m* events.

It is shown that the peak strain results follow a linear trend at each L position, as per the fitted lines in Figure 3-27, with an assumed intercept at point *(0 MPa.ms, 0 με)*. The trend is well characterised for the amidships *(L = 0.0 m)* events E1 – E3 *(W = 250 g)* while lacking for E4 *(W = 43 g)*. There is insufficient data to validate this trend for other charge sizes and L positions. However, it is clear from the limited results that the L position had a significant effect on the submerged platform's whipping response severity, where the gradient of the peak strain and I_B relationship decreased by approximately 100 με between each successive L position. This relationship suggests that the effects of the L position increase as I_B increases, for the investigated bubble proximity ranges of *1.45 ≤ γ ≤ 2.00* and relative sizes of *2.5 ≤ λ ≤ 4.5*.

Considering a comparison of each event's SF, previously noted in Table 3-4, this parameter is unable to differentiate between the three trends noted in Figure 3-27, most apparent by the large difference in the peak response from events E3, E5, and E7, which all have the same *SF = 0.38*. Furthermore, the shock factor would not be able to account for changes in the response due to depth of the event, while the pressure impulse is comparable at any depth, given it is a function

of it. For these reasons it is strongly suggested that the SF should not be used to predict whipping events on submerged platforms.

Equation	y = a + b*x		
Plot	L = 0.0 m	L = -2.8 m	L = -4.3 m
Weight	No Weighting		
Intercept	0 ± --	0 ± --	0 ± --
Slope	287.69904 ± 13.01614	191.06252 ± 8.8487	88.52135 ± 5.77943
Residual Sum of Squares	47613.88704	4224.05858	1713.58133
Pearson's r	0.99694	0.99893	0.99788
R-Square(COD)	0.9939	0.99786	0.99576
Adj. R-Square	0.99186	0.99572	0.99151
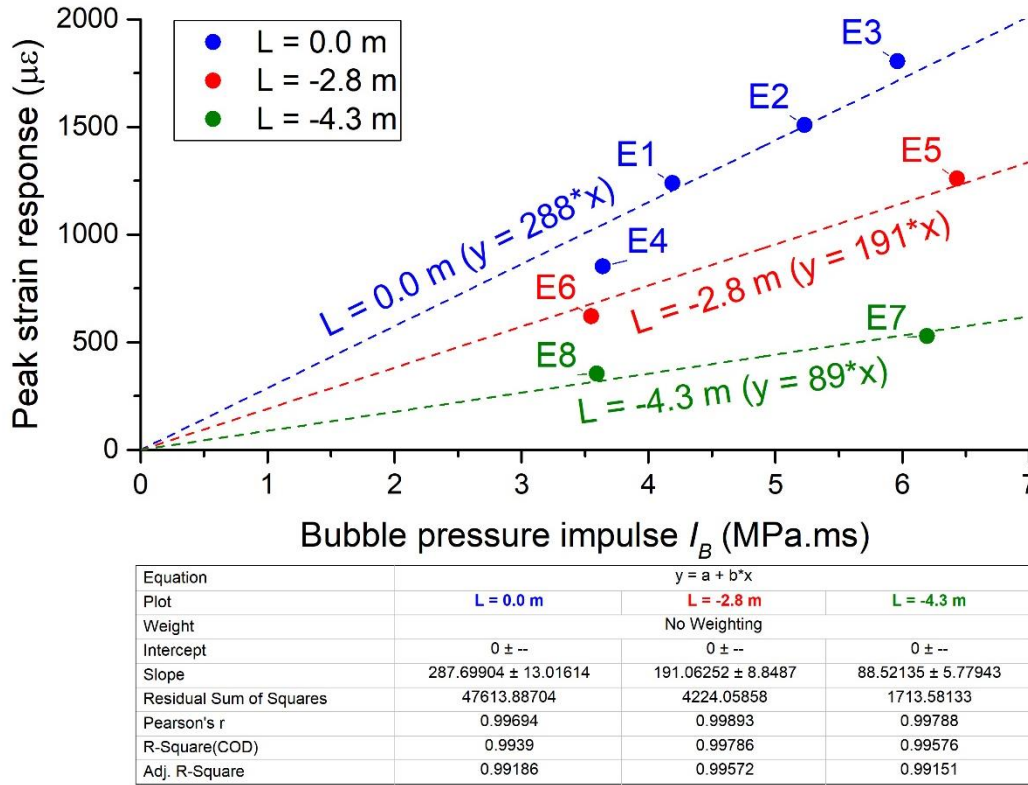
Figure 3-27 Peak strain responses from bubble loading compared to the bubble pressure impulse I_B

3.4 Conclusion

A set of eight underwater explosion experiments were conducted to investigate the whipping response of a submerged 12 m long, 0.4 m diameter cylindrical platform. Two Pentolite charge sizes (250 g and 43 g) at stand-off distances from 1.8 m to 0.8 m, and at different longitudinal positions along the hull length were used in this experiment. All UNDEX events were conducted with the charge and the platform at a depth of 5 m.

Measured incident pressures showed good correlation with theory for the first bubble cycle. Similitude equations for the bubble period compared well with experimental measurements for a relative proximity of $\gamma > 1.67$. Beyond this limit the similitude results under or over predicted the period depending on the charge size. New K coefficients for bubble period calculations were identified and presented from this experimental dataset. Due to the limited data sets available, further experimental analysis of different bubble proximities would be required to determine the cause of these differences at bubble proximities of $\gamma < 1.67$.

Through integration of the incident pressure-time data, it was found for both Pentolite charge sizes that 35.1% and 64.9% of the total pressure impulse was associated with the shock wave and bubble respectively. Given the consistency across all conducted events, this relative contribution is likely a property of the explosive material.

The severity of whipping induced bending responses was shown to depend on the relative contribution of the first three distortional bending modes for the submerged platform. The contribution of a mode increased with the proximity of the bubble frequency to the submerged platform's modal frequencies, and with the physical proximity of the UNDEX to the anti-node

of the primary distortional mode shape, which was the first bending mode for this platform. Charges of any size detonated in proximity to the anti-node of the first bending mode shape induced the most severe whipping responses. Charges detonated near the node of the first bending mode shape induced whipping response strains that were 71 % and 58 % lower than the respective 250 g and 43 g charge sizes detonated at the anti-node of the mode shape. It was observed that interaction of the multiple dominant mode shapes caused the peak bending response to occur at locations away from the charge stand-off point for some events. This generally occurred when the charge stand-off location was between the node and anti-node of the first bending mode shape.

It is suggested that if the stand-off location along the platform length can be influenced to occur at the node of the primary bending mode shape, the platform will be inherently hardened against a severe whipping response. Additionally, should a scenario occur where multiple bending modes are excited, the responses at locations away from the stand-off point may need to be assessed, as these can potentially undergo a more severe response than that at the stand-off point.

Comparison of the bubble pressure impulse to the peak strains measured during the whipping response suggest that as the impulse increases, the stand-off location in relation to the primary bending mode shape has a more pronounced effect on the whipping severity. This relationship appears valid for the 250 g charge size detonated at amidships for the investigated bubble proximity ranges of $1.45 \leq \gamma \leq 2.00$ and relative size of $\lambda = 4.5$. Further work is required to determine if this is also valid for other charge sizes and stand-off locations. This will be investigated in the following chapters using a validated numerical model.

Chapter 4. Numerical model development and validation

4.1. Introduction

Experimental analysis is a time consuming and expensive assessment method, particularly in the case of a full-scale naval platform UNDEX assessment. Failed assessments can result in significant cost to procurement programs, in terms of dollars and delays. In Chapter 2, numerical modelling was discussed as a potential alternative for an intermediate assessment method, to provide knowledge of a platform's performance prior to full scale assessment trials. To achieve this, a numerical model requires some form of experimental validation to provide confidence in its results, but this validation can be performed on scaled experimental scenarios which are cheaper to produce and easier to examine for specific details. As long as a numerical model is appropriately validated, it can be used to assess additional scenarios that may identify a platform's design limits or unexpected responses that can be addressed prior to full scale assessment and commissioning into service.

Using the incident pressure and strain measurements obtained from the experimental investigation discussed in Chapter 3, a numerical model for a submerged platform whipping analysis was developed and validated. The model and validation methodology are discussed in this chapter.

4.2. Numerical model methodology

Numerical modelling capability has always been dependent on the available computing power. Therefore, there is constant improvement in modelling capability as computing power increases and becomes accessible to more end users. From the previously discussed methods in Chapter 2, it was established that the implicit Underwater Shock Analysis (USA) R7.5.3 [96] Boundary Element Method (BEM) code coupled with the explicit LS-Dyna R10.1 [122] Finite Element (FE) code had the best potential to conduct further analysis for this investigation and to validate as a potential assessment tool in industrial environments. As a BEM, the USA code does not directly model the bubble response, so Bjerknes force effects are not accounted for. This validation will determine if this limitation has any significant effects on the accuracy of the USA code for modelling scenarios where the bubble proximity range is $1.45 \leq \gamma \leq 2.00$.

4.2.1. Finite element model

The FE model shown in Figure 4-1 was constructed in the explicit LS-Dyna environment, which limited the element selection to first-order functions. The model was defined using a cartesian coordinate system, where the origin (point 0, 0, 0) was at the centroid of the cylindrical hull. The X-axis was aligned with the longitudinal axis of the platform, where the forward end of the platform was defined as positive. The Y-axis was aligned with the transverse axis of the platform, where port was defined as positive. The Z-axis aligned with the vertical axis of the platform, where up was defined as positive.
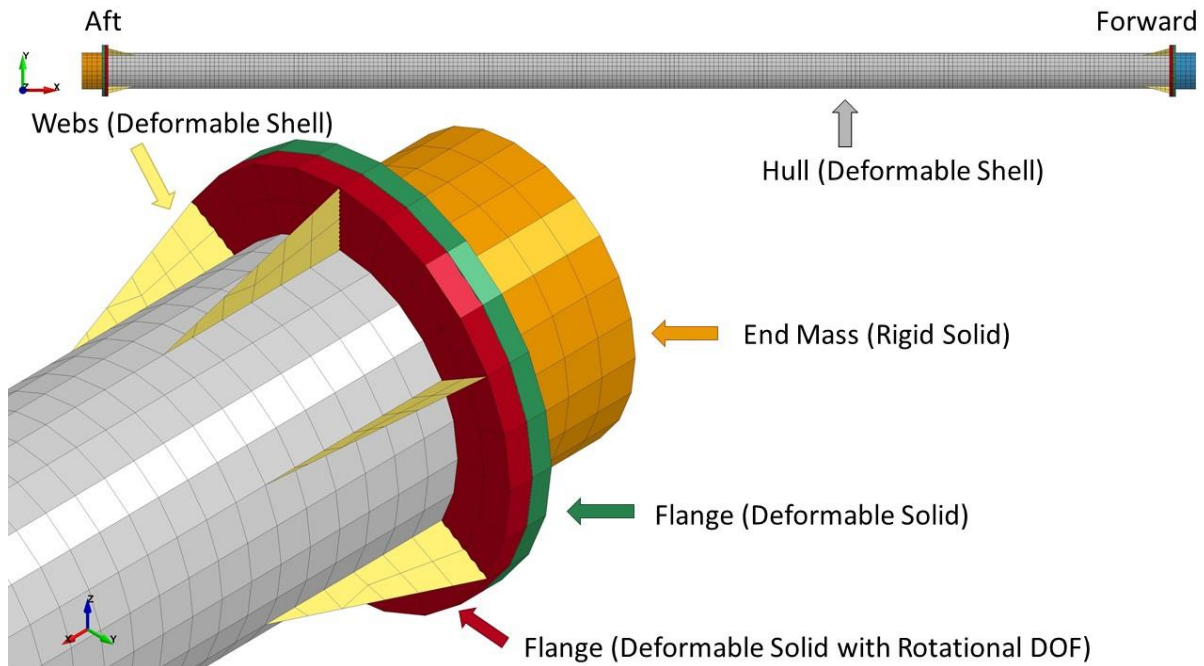
Figure 4-1   Finite element model of the test platform

A mesh refinement study was conducted to determine a mesh density that would efficiently represent the whipping response in the hull part. The study evaluated the FE mesh by the accuracy of the structural and added fluid mass, the time required to form the BEM equations, the accuracy of the modal frequency responses in a submerged environment, and the peak response from a simple shock wave impact. The findings of this study are summarised here, and further details are provided in Appendix 3. It was found that an arrangement of 24 elements about the circumference and 240 elements along the length provided the best trade-off between accuracy and analysis run-time. With this element arrangement, the hull part mesh consisted of 5760 fully integrated (Type 16) shell elements. The remaining FE model parts were built around the hull part arrangement.

The end mass and flange parts were modelled using 1272 solid elements. The solid element meshes were relatively coarse as only the mass and geometric properties of these components were required for this analysis. Beam and lumped mass models were also explored for these parts, but it was found this produced issues when attempting to apply damping models. A different USA formulation must also be used for these types of models, so for simplicity the solid elements were used. Most solid element parts used the default reduced integration formulation (Type 1). A single row of solid elements on the flange closest to the cylindrical hull and webs used a fully integrated formulation with rotational degrees of freedom at nodes (Type 3), as noted in Figure 4-1, which can receive rotational displacements and allowed for direct connection with shell elements. The stiffening webs that connect the flange and hull assemblies were modelled using 120 reduced integration (Type 1) shell elements. All parts were attached to each other by sharing common nodes at their borders.

For the hull and web parts, the shell mesh was defined at the mid-surface of the shell thickness. The thickness of the hull and web shells was 6.35 mm and 3 mm respectively. The mid-surface shell model for the circular hull section provided the best mass accuracy due to the faceted representation of the circular profile from the first-order elements[4]. However, this also induced a minor error in the USA boundary elements, which are also defined at this mid-surface mesh.

---

[4] Refer to Figure A2-1 in Appendix 3

This difference in stand-off distance of half the shell thickness (3.175 mm) results in an error of 0.4 % for the closest experimental event at 0.8 m, and was deemed to have a negligible effect on the fluid structure interaction of the model.

The web elements were the smallest in the model and significantly reduced the explicit stable timestep criteria from Equation 2.6, where the smallest web shell elements only permitted a timestep of 2.5E-6 s. As the response of the webs was not of interest, it was desirable to increase the timestep to an appropriate stable value based on other parts in the model. From the deformable flange part elements, a stable timestep of 5E-6 s was determined by Equation 2.6. A safety factor of 90% is automatically applied internally by LS-Dyna to improve analysis stability if the wave propagation should slightly exceed to material acoustic velocity [122], which resulted in a stable timestep of 4.5E-6 s. To increase the timestep of the small web elements, mass scaling was applied to all elements in the web parts. The total scaled mass to achieve a desired timestep of 4.5E-6 s was 1.7 kg, a negligible increase of the total mass. The application of mass scaling improved the estimated runtime by 80% and in addition, the use of a consistent timestep for the entire explicit analysis is useful for maintaining stability with the USA coupling.

Only the general external features of the platform (hull, flanges, endcaps, and disk weights) were explicitly modelled. The response of additional external features such pressure transducer outriggers, cable glands, and lifting lugs were assumed to not contribute substantially to the global whipping response and where not modelled. Internal features were predominantly made up of transducers and cables, with mounting plates and porthole inserts being the only significant structural members. However, the strain measurements used in this validation were assumed to not be affected by these features and therefore these were also not modelled. The final model mass was 1438 kg, compared to the measured 1548±1 kg of the experimental test platform. This missing mass was attributed to the previously noted un-modelled structure. This difference of 110 kg was accounted for by applying mass elements to the entire cylindrical hull part.

Only elastic and rigid material properties were used in the model, as the strain results from the experimental investigation in Chapter 3 indicated no plastic deformation had occurred. The material properties of the steel hull were provided by the manufacturer's nominal material specifications [123] and are listed in Table 4-1. Deformable elastic properties were assigned to all parts of the model except for the solid end mass parts, noted in Figure 4-1. Rigid material properties were assigned to the end mass parts to reduce computation times, as these were assumed to act as a rigid mass in the platform design and there were no experimental measurements at these locations. A wet modal frequency analysis initially found that the model was overly stiff, which was attributed to the un-modelled components and calculation of the added mass (discussed in the following section). To compensate for this, the Youngs modulus of the hull material was reduced from 200 GPa to 190 GPa, a difference of 5%. Further details of the FE model are provided by the keyword input file in Appendix 4.

Table 4-1   Nominal steel material properties

Youngs Modulus	200 (190) GPa
Yield Stress	350 MPa
Poisson's Ratio	0.25
Density	7850 kg/m^3

4.2.2. Boundary element method

The USA BEM was used to represent the surrounding fluid and initiate the UNDEX loading. The BEM uses the Doubly Asymptotic Approximation (DAA) from Geers [93] to calculate the transient loading and the coupled responses of the structure and fluid. All external element faces of the model, except for web parts, were assigned a DAA boundary element, as shown in Figure 4-2. Inclusion of the web parts prevented the implicit USA code from converging and forming its solutions. The absence of their added mass contribution was deemed negligible for this whipping analysis.
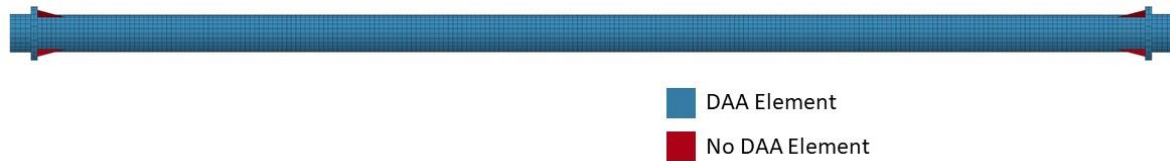
Figure 4-2   DAA elements

The USA BEM requires the free-surface location to be defined with respect to the FE model coordinate system, and also requires the material properties of the surrounding fluid. The free-surface was defined as 5 m above the FE model origin. As the test environment was small and reflections were noted on the incident pressure records during the experimental investigation in Chapter 3, the sea-floor location was also defined for these analyses at -11 m below the FE model origin, an approximate value of the quarry depth where the experiments were conducted. The respective locations of the free-surface and the sea floor to the FE model are shown in Figure 4-3. The water acoustic velocity and density were defined as 1500 m/s and 1000 kg/m^3 respectively.
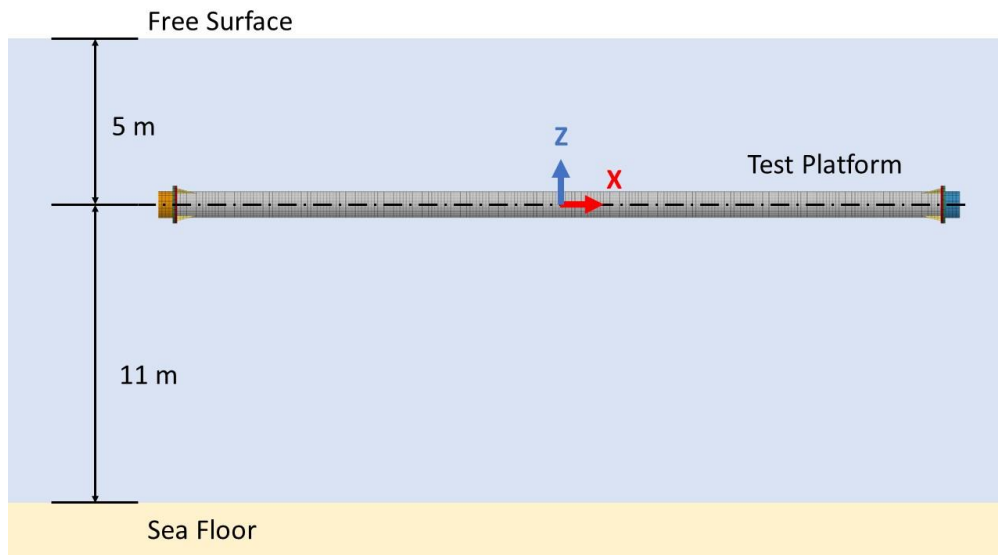
Figure 4-3   Free-surface and sea floor locations on port side view

The USA code utilises an infinite frequency added fluid mass for the DAA elements, calculated using the method described by Deruntz and Geers [21]. Rigid body added mass for sway, heave, and surge modes is output by the USA code, which was compared against analytical solutions from Blevins [18]. The USA code calculated the added fluid mass for heave and sway modes as 1548 kg, which compared well to the analytical solution of 1557 kg from Blevins's solution. Surge responses were not considered important for a whipping analysis, as the overall platform response was dominated by bending modes. The added mass values for specific distortional

frequency responses are not directly outputted by the USA code so no direct comparison of these can be made. However, the wet modal responses are compared to experimental results in Section 4.2.5.

A relative timestep of 1:1 LS-Dyna and USA solver timesteps offers the best stability and accuracy [96]. However due to the high computing cost of the implicit USA solution, a reasonable trade-off between analysis efficiency and accuracy may be obtained by increasing the USA timestep. The USA code manual [96] advised that ratios between 1:1 and 1:5 timesteps are generally appropriate. In the present investigation, a USA timestep of 4.5E-6 s (1:1 timestep ratio) was required to maintain analysis stability during the initial shock wave loading and early structural response between 0 – 30 ms of analysed time. The USA timestep was increased to 9.0E-6 s (1:2 timestep ratio) for the remaining analysis (31 – 1000 ms), with linear ramping of the timestep between 30 – 31 ms, to improve the overall analysis efficiency. Larger USA timesteps were attempted but resulted in analysis instability.

4.2.3. UNDEX model

The USA code generates incident pressure loads for the shock wave and bubble based on empirical datasets and user defined inputs of the explosive charge mass and location. The author has performed whipping analysis benchmarking studies of the USA code for surface [99] and submerged [124] platform's, and has previously determined that the Price-Hicks Shock Bubble model (PHS-BUB) in the USA code provided the most accurate UNDEX incident pressure. The PHS-BUB model consists of the shock wave similitude pressure data from Price [98], combined with the bubble model from Hicks [24], and is fitted with a bubble decay function developed by Geers and Hunter [41, 42]. The PHS-BUB model is considered accurate for up to three bubble pulse cycles, but it is recommended to cut the model off at a point of zero particle velocity to prevent instabilities occurring after the cut-off point [96]. The experimental measurements indicated that each charge only produced two significant bubble pulses so the models were cut during the third bubble cycle at 300 ms and 164 ms for the 250 g and 43 g charges respectively.

Previous analysis [99, 124] with the R7.5 release of the USA code [113] required the user to manually input a TNT equivalent mass of the explosive. The current R7.5.3 release of the USA code [96] introduced a Pentolite explosive charge material, which is controlled by a user definable TNT equivalence factor. The default TNT equivalence factor for Pentolite is 1.10, but there is a known variation in this equivalence based on the charge size. Swisdak [6] offers alternative TNT equivalents ranging from 1.06 – 1.19, which consider different charge sizes and variables of the UNDEX environment. These equivalence factors were investigated, and the resulting incident pressures compared to measurements from the experiment in this numerical validation.

An additional update of the R7.5.3 release of the USA code, allows for bubble loading models to account for the sea floor influence on the bubble response. Typically, this should increase the bubble period, depending on the bubble size and relative proximity to the sea-floor [34]. The inclusion of these effects is also investigated.

4.2.4. Model outputs

To validate the numerical model, high-resolution strain outputs were taken from elements at locations corresponding with strain gauge locations, shown in Figure 4-4. These results allow for direct comparison with the experimental measurements. Only the amidships, forward, and

aft locations were considered as the bow and stern did not demonstrate significant responses due to whipping in the experimental investigation. Lower resolution outputs were obtained for all elements in the hull part to monitor the peak strain locations. All outputs were taken for a duration of 1000 ms. The notation for discussion of these gauge locations is simplified to their general location along the hull length, as noted in Figure 4-4.
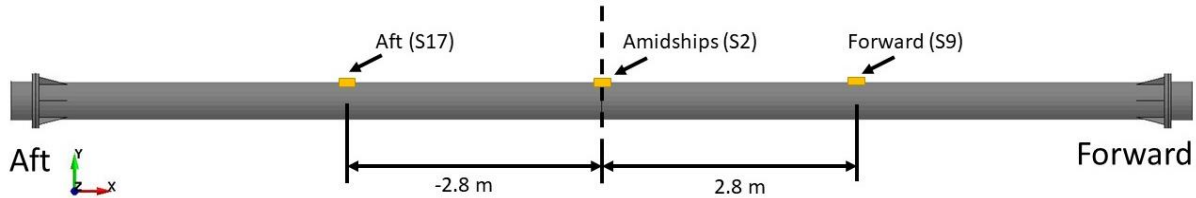
Figure 4-4   Top view of platform locations for high resolution strain outputs and the corresponding experimental strain gauges

All strain outputs were taken with reference to the element coordinate system, where the element X-axis is defined by the vector of nodes 1 to 2, the Y-axis is the vector of nodes 1 to 4, and the Z-axis is normal to this plane (through the shell thickness) [89], as shown in Figure 4-5. At the initial state, all hull part elements had their Y-axis aligned with the global X-axis and their Z-axis pointing away from cylindrical cross-section centroid. The element X-axis follows a tangent of the circumference defined by the vector of nodes 1 to 2 and is clockwise looking in the forward direction.
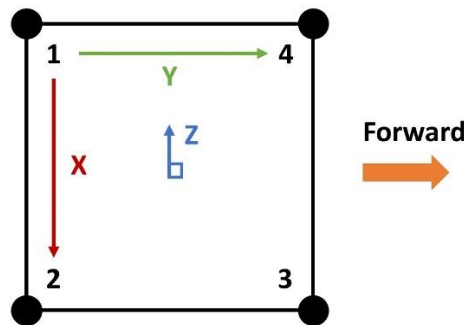
Figure 4-5   Hull part shell element coordinate system

The incident pressure is calculated at the node closest to the charge source and directly output by the USA code. These outputs were retrieved for comparison against the measured incident pressure from the experiment.

4.2.5. Modal responses

To determine the accuracy of the structural FE model and the implementation of the USA BEM, a modal analysis was performed. The experimental investigation in Chapter 3 identified that the dominant responses of the submerged platform were the first three bending modes (BM1 – BM3). These are reiterated in Table 4-2. The resulting bending modes and circumferential modes of the platform from the USA results are listed in Table 4-3 and Table 4-4 respectively, using the notation from Blevins [18]. Deformable responses up to approximately 100 Hz were considered relevant for this global structure response problem, as the experimental measurements identified minimal effects of any frequency response beyond this.

The model demonstrated an excellent comparison of the first three BM responses, with all results within 1 Hz of the experimental observations. This provided good confidence for the additional frequency response results obtained by this model. From this analysis, it was concluded that the structural FE model and application of the USA BEM provided an appropriate representation of the submerged whipping hull's modal responses and was suitable for further numerical analysis.

Table 4-2   Bending mode responses measured from the experimental investigation

Mode	Frequency
BM1	6.7 Hz
BM2	20.0 Hz
BM3	41.0 Hz

Table 4-3   Bending mode responses from the numerical model
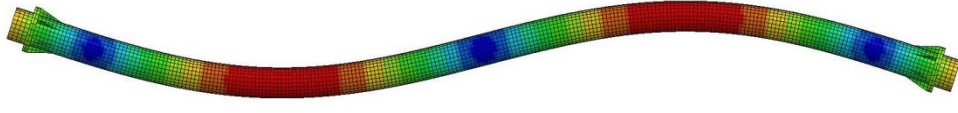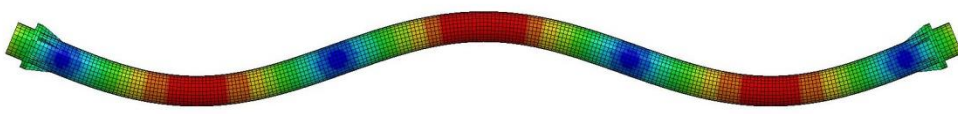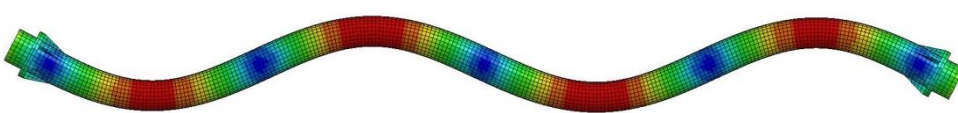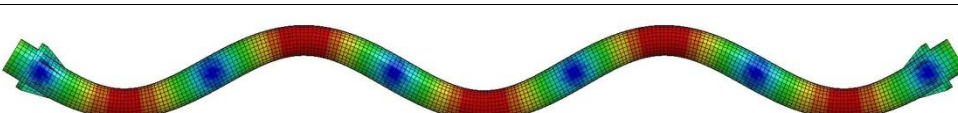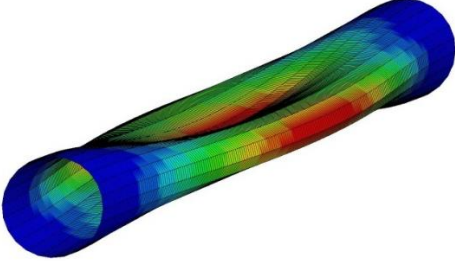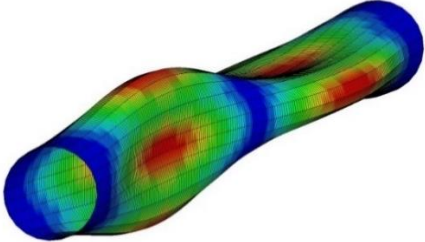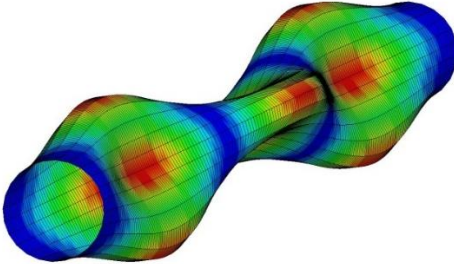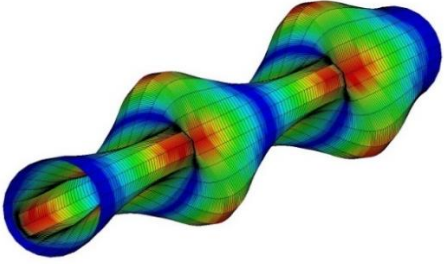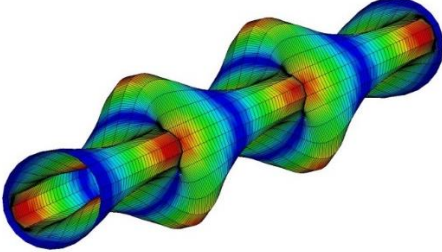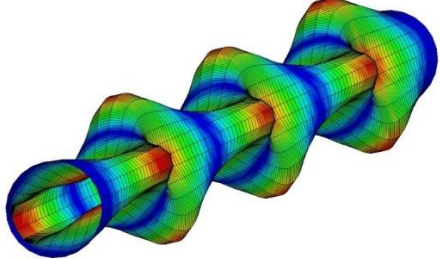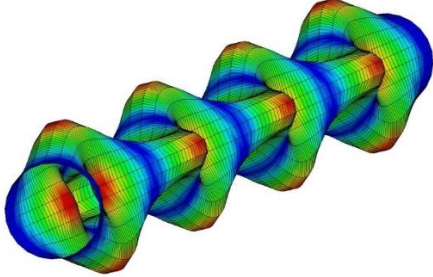
Mode Shape	f
	BM1 $j = 1$ 6.7 Hz
	BM2 $j = 2$ 19.9 Hz
	BM3 $j = 3$ 40.5 Hz
	BM4 $j = 4$ 68.2 Hz
	BM5 $j = 5$ 102.5 Hz

Table 4-4   Circumferential mode responses from the numerical model (ends hidden)

f	Mode Shape	f	Mode Shape
CM1 $i = 2$ $j = 1$ 63.3 Hz		**CM2** $i = 2$ $j = 2$ 64.1 Hz	
CM3 $i = 2$ $j = 3$ 66.2 Hz		**CM4** $i = 2$ $j = 4$ 70.7 Hz	
CM5 $i = 2$ $j = 5$ 78.4 Hz		**CM6** $i = 2$ $j = 6$ 89.7 Hz	
CM7 $i = 2$ $j = 7$ 104.8 Hz			

4.2.6. Damping models

Damping is normally required in any transient analysis to simulate the effects of energy dissipation sources present in any mechanical system such as friction, heat, and sound. For shock analysis, damping is often negligible due to the short duration of these events. A whipping response has a much greater duration and therefore damping is an important consideration. Stettler [125] comprehensively covered damping mechanisms that are important for the whipping response of a submerged submarine, summarising three main contributors to the overall damped response as hull, internal, and external damping.

Hull damping results from energy loss due to friction and heating within the structural material (hysteresis damping) and friction between connecting joints (dry friction damping). Internal damping occurs due to the transmission of vibrational energy from the global hull response

into resiliently mounted equipment and the sloshing of fluids in tanks, such as ballast and fuel. These additional responses can be described by their own equations of motion and solved in a set of multiple Degree of Freedom (DOF) systems that interact with the global model. Finally, external damping arises from the loss of vibrational energy into the surrounding medium, which in this case is water as a near-incompressible fluid. Two primary energy losses from this are wave radiation (particularly if the platform is near the free-surface) and viscous drag friction.

The challenge of performing an accurate whipping analysis can be largely due to the consideration of all these damping mechanisms. Two primary numerical damping models are considered for application in a whipping analysis: Rayleigh and Frequency Range damping.

Undamped (UD)

An UD analysis was conducted to act as a baseline for the other damped numerical analyses. It was found in the experimental investigation that the peak whipping response always occurred after the first bubble pulse, which was relatively early in the analysis and where damping effects are minimal. Therefore, it was anticipated that the UD numerical model may provide a reasonably accurate result for the peak whipping response.

Rayleigh damping (RD)

The RD method considers a combination of mass weighted and stiffness weighted damping terms to construct a resultant damping factor across multiple frequencies [122], as shown in Figure 4-7. This is expressed numerically though the resultant damping matrix C from the mass M and stiffness K matrices in Equation 4.1. The mass α and stiffness β proportionality constants for a desired damping factor ζ_n can be determined for a single frequency response ω_n using the relationship in Equation 4.2. As these constants are independent, they can be fitted between two frequency responses (ω_a and ω_b) to achieve the desired damping factors (ζ_a and ζ_b) using Equation 4.3.

$$[C] = \alpha[M] + \beta[K] \tag{4.1}$$

$$\zeta_n = \frac{\alpha}{2\omega_n} + \frac{\beta\omega_n}{2} \tag{4.2}$$

$$\begin{bmatrix} \alpha \\ \beta \end{bmatrix} = 2\frac{\omega_a\omega_b}{\omega_b^2 - \omega_a^2} \begin{bmatrix} \omega_b & -\omega_a \\ -1/\omega_b & 1/\omega_a \end{bmatrix} \begin{bmatrix} \zeta_a \\ \zeta_b \end{bmatrix} \tag{4.3}$$

The experimental investigation indicated that all whipping responses were within the elastic limit of the material and therefore RD can be applied to represent the internal damping of the platform [125]. With two damping terms, the mass α and stiffness β constants of proportionality, two independent frequencies can be damped by this method. The experimental investigation identified the first three bending modes as the primary contributors in the platform's whipping response. The experimental strain measurements were filtered using a band pass FFT filter for each of these bending modes to identify their individual contribution and damping. An example of this process is shown in Figure 4-6, which analysed the BM2 and BM3 responses of Event 6. From these records, the logarithmic decrement δ for each isolated mode was obtained from the free-vibration portion of the response, and the critical damping factor ζ was calculated using Equation 4.2. The δ and ζ for each BM are presented in Table 4-5.
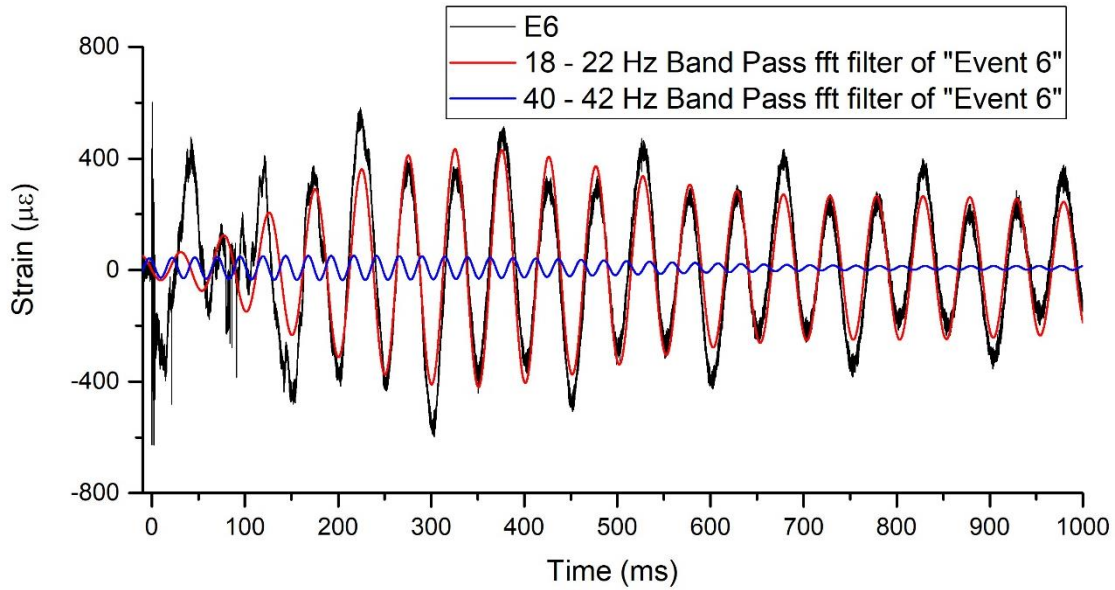
Figure 4-6   Breakdown of frequency components of event E6 to calculate δ

Table 4-5   Critical damping factors from experimental data

Mode	f_n (Hz)	ω_n (Rad/s)	δ	ζ
BM1	6.7	42	0.185	0.029
BM2	20.0	126	0.069	0.011
BM3	41.0	258	0.075	0.012

From this analysis it was established that the critical damping ratio for BM2 and BM3 was similar and therefore it was desirable to aim for a constant damping ratio between these frequencies. BM1 was in most cases found to be the dominant response, so it was just as important to ensure this mode was sufficiently damped. Therefore, BM1 and BM3 were selected as the damped frequencies for Equation 4.3 to calculate the proportionality constants, where:

$$\begin{bmatrix} \alpha \\ \beta \end{bmatrix} = \begin{bmatrix} 2.33375 \\ 5.7963 \times 10^{-5} \end{bmatrix} = 2\frac{42(258)}{258^2 - 42^2}\begin{bmatrix} 258 & -42 \\ -1/258 & 1/42 \end{bmatrix}\begin{bmatrix} 0.029 \\ 0.012 \end{bmatrix}$$

The critical damping factors for this range of frequencies are plotted in Figure 4-7, where it is shown that the fitted critical damping factors achieved the desired damping ratio, while the ratio between ω_2 and ω_3 remained approximately constant.
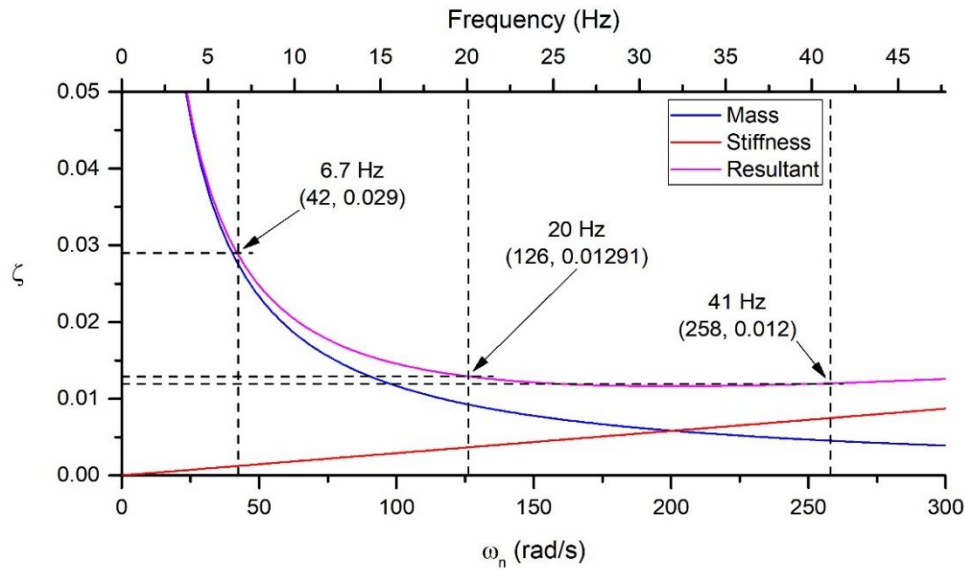
Figure 4-7   Critical damping factors for RD model

Frequency Range damping (FR)

The frequency range damping method was developed by Arup Group Ltd. and is implemented in LS-Dyna. Its exact details remain proprietary information but a limited overview is provided by LSTC [126, 127]. It is designed to be used in situations where controlled damping of more than two critical frequencies is required.

FR damping applies an approximate constant damping over a defined range of frequencies. An initial analysis of this submerged test platform by De Candia, et al. [124] used LS-Dyna R9 [128] to perform a whipping analysis on the submerged test platform, and identified that the FR damping method became increasingly inaccurate when the platform response consisted of multiple dominant bending modes, particularly when BM3 had a significant presence. Since that analysis, there has been a significant accuracy advancement in LS-Dyna R10 release of the FR damping model [127, 129] that allows the critical damping to be applied across a much larger frequency range. The greater frequency range may overcome the noted shortfalls of only being able to damp small frequency ranges when using this method.

The FR model requires some estimation to refine the frequency window and critical damping factor [122, 126, 127]. It was found through initial trial and error analyses that different damping factors and frequency windows were required based on the charge L position and mass W, detailed in Table 4-6. Furthermore, these parameters can modify the natural frequency of the model through an effective decrease in stiffness. To compensate for this, the model stiffness was increased from 190 GPa to 195 GPa for 250 g events, and to 200 GPa for 43 g events.

Table 4-6   FR damping model variables

L	0 m		-2.8 m	-4.3 m		
W	ζ	F_1	F_2	ζ	F_1	F_2
43 g	0.02	5 Hz	25 Hz	0.01	15 Hz	25 Hz
250 g	0.04	5 Hz	8 Hz	0.02	15 Hz	45 Hz

The resultant critical damping factors for these FR model parameters are plotted in Figure 4-8, noting that the frequency scale is logarithmic. These plotted values are approximate, based on technical advice provided by the LSTC support note [127].
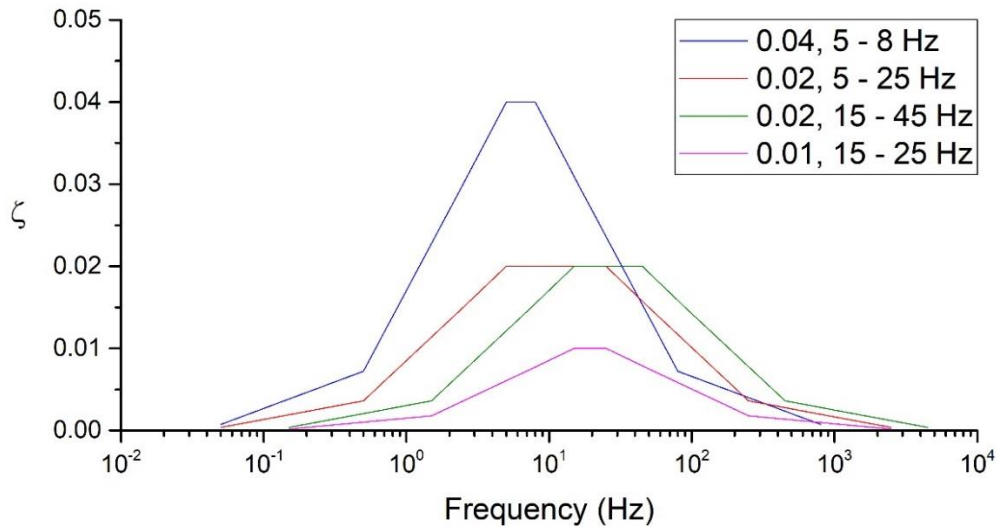
Figure 4-8   Approximate critical damping factors for FR models

Combined Rayleigh and Frequency Range damping (RDFR)

The FR model itself is limited as only one critical factor can be applied to a part in the numerical model. However, the RD and FR models can be used in conjunction to partially control the critical damping at additional frequencies. This combined method of the RD and FR damping models (RDFR) was implemented by using the mass proportional term of the RD model to damp the lowest frequencies (BM1 to BM3) and using the FR model to damp frequencies above this. The same RDFR damping model was applied to all analyses, where the RD mass proportionality term $\alpha = 2.52$, and the FR critical damping factor $\zeta = 0.01$ across a frequency range of 40 – 120 Hz. Damping up to 120 Hz was introduced to remove higher frequencies that occur from the large bandwidth of the explicit analysis environment. The resultant critical damping factors through the combined RDFR damping are plotted in Figure 4-9. The plotted FR and resultant RDFR values are approximate, based on technical advice provided in the LSTC support note [127].
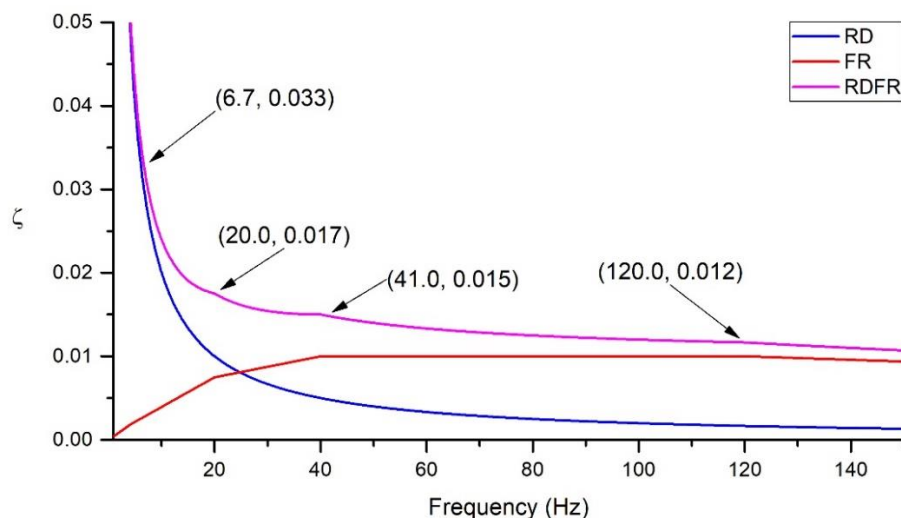
Figure 4-9   Approximate critical damping factors from combined RDFR damping model

4.2.7. UNDEX Scenarios

The experimental investigation consisted of eight UNDEX events, discussed in Chapter 3. The general layout of these events is reiterated in Figure 4-10 and the variables of each event are detailed in Table 4-7. Experimental results used for comparison are denoted as E, while the numerical results of these scenarios are denoted as EN. The bubble proximity factor γ for each event is listed in Table 4-7.

Table 4-7   UNDEX experiment variables

Event	W (g)	R (m)	L (m)	γ	SF $(kg^{1/2}/m)$
1	250	1.8	0.0	2.00	0.28
2	250	1.5	0.0	1.67	0.33
3	250	1.3	0.0	1.45	0.38
4	43	0.8	0.0	1.60	0.26
5	250	1.3	-2.8	1.45	0.38
6	43	0.8	-2.8	1.60	0.26
7	250	1.3	-4.3	1.45	0.38
8	43	0.8	-4.3	1.60	0.26
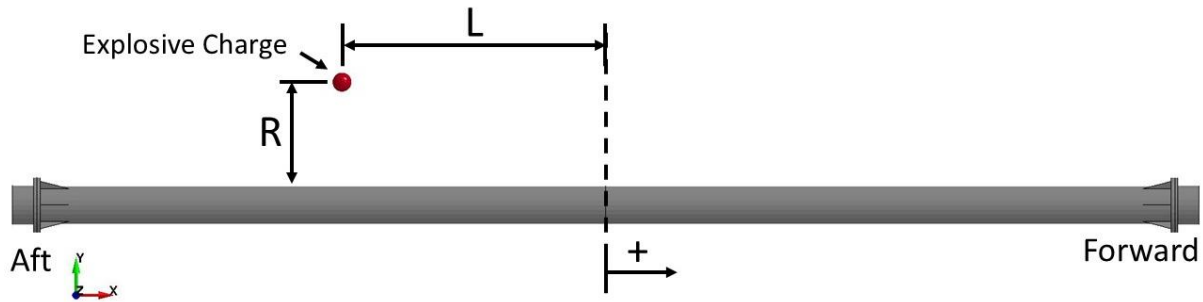
Figure 4-10 UNDEX scenario setup (Top side view)

4.3. Model validation

The accuracy of the numerical model was validated according to two criteria: pressure loading (the input) and structural response (the output). The pressure loading validation was performed by comparing the incident pressure inputs calculated by USA against the experimental pressure measurements. The structural response was validated by comparison of the transient FE and experimental records, and the frequency response. Differences between the time and location of the peak whipping response in the FE results are qualitatively validated through comparison of the strain contours at the relative times and locations for each event.

4.3.1. Pressure loading

The incident pressure loading produced by the PHS-BUB model of the USA code was compared against the experimental measurements with consideration of the shock wave and bubble pulses. Pressure impulse comparisons are made to validate the effective loading contribution of the shock wave and bubble, with the late-time transient impulse response comparing well with experimental measurements.

The shock wave

The shock wave incident pressures from the PHS-BUB model using TNT equivalents of 1.10 – 1.19 are compared to their respective experimental pressure time histories in Figures 4-11 to 4-14 and the peak pressures are compared in Table 4-8. Models that contain the boundary effects of the sea floor are denoted with "bottom" in these figures. Those without assume a free-field bubble response. From the comparison in these figures it is clear that the TNT equivalence factors and bottom effects did not have a significant effect on the shock wave, as each numerical result is virtually indistinguishable from each other. All numerical results overpredicted the peak pressure by 9 – 17 %. Cole [8] and Hunter and Geers [41] note similar over-predictions due to the use of Pentolite TNT equivalents in calculations. It is shown in the first (a) figure of each scenario that the TNT equivalence factor had minimal effect on the pressure decay rate and all models had good accuracy for the shock wave decay profile. Early reflective sources from the test platform, previously noted in Chapter 3, are not calculated by the BEM and do not appear in the resulting incident pressure time histories. The surface cut-off and ground reflections in Figure (b) of each event were accurate for all 250 g charge events, confirming the defined depth from the surface of 5 m and the depth of sea floor from the platform of 11 m were appropriate for these scenarios. The surface cut-off response also compared well for the 43 g charge events in Figure 4-14b, but there was a significant difference between the time of arrival of the ground reflection between the PHS-BUB model and the experimental measurements. For the 43 g events, the experimental measurements suggest a depth of approximately 7 m, despite the testing depth arrangements being identical for all events, regardless of charge size. Sonar surveys of the quarry floor were assessed but no variation in the quarry floor depth could account for this discrepancy. At present the cause of this inconsistency remains unknown. However, it was previously identified in the experimental investigation that the ground reflections did not have a major contribution to the overall UNDEX loading, and the sea floor definition of 11 m was maintained for further analysis for consistency with the test environment.

It is clear in Figures 4-11b to 4-14b that the ground reflection profiles are different between the experimental and numerical measurements. This difference is caused by the image reflection assumption used by USA, where the reflected wave is assumed to be a perfect shock wave initiated at an image source, described in Chapter 1. In reality, the direct wave radiates and makes contact with the bottom on multiple occasions, which produces a number of reflections that combine to form the final reflection profile.

Table 4-8   Comparison of experimental and numerical peak pressure

Event	E (MPa)	EN (MPa)	Δ (%)
1	13.83	15.98	16
2	18.15	19.86	9
3	21.78	23.71	9
4	18.28	21.00	15
5	21.75	23.71	9
6	18.00	21.00	17
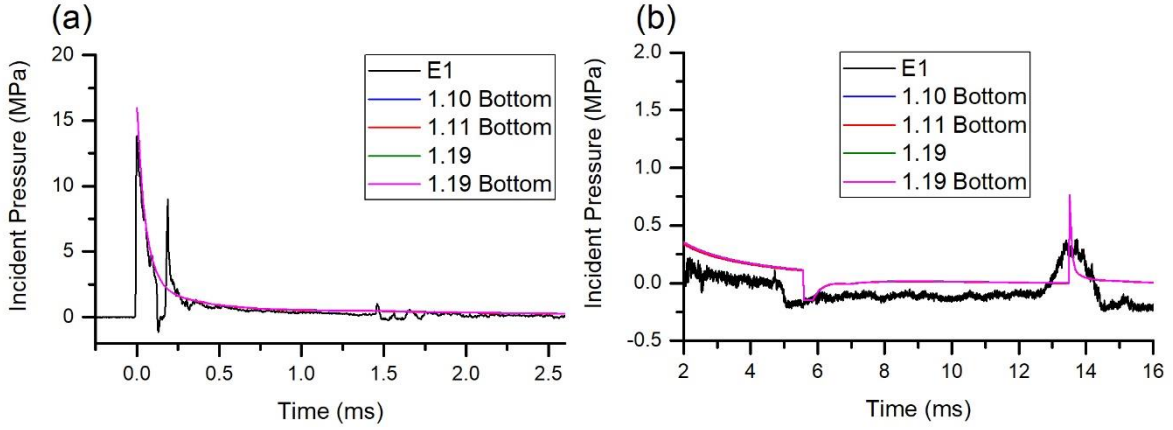
Figure 4-11 Comparison of experimental and numerical (a) shock wave and (b) reflection incident pressures of different TNT equivalent factors for Pentolite (W = 250 g, R = 1.8 m)
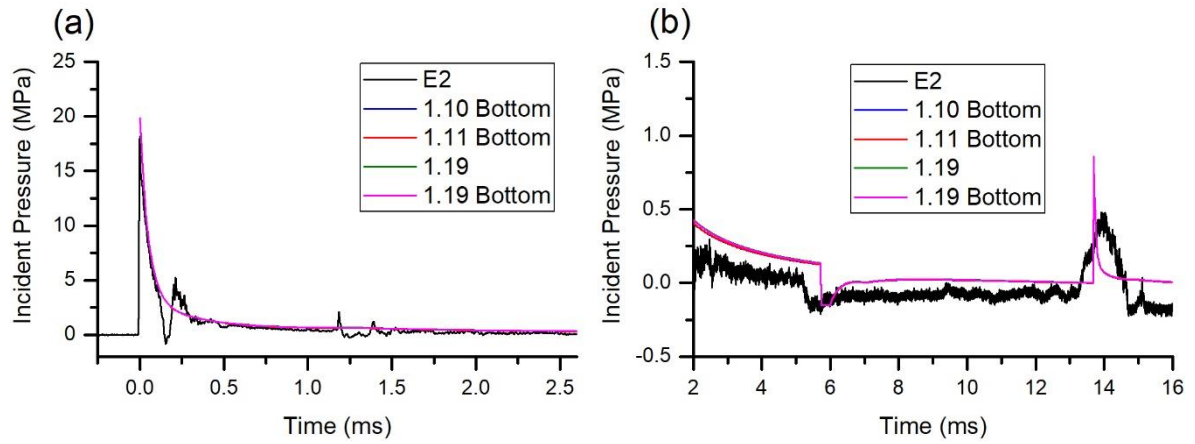
Figure 4-12 Comparison of experimental and numerical (a) shock wave and (b) reflection incident pressures of different TNT equivalent factors for Pentolite (W = 250 g, R = 1.5 m)
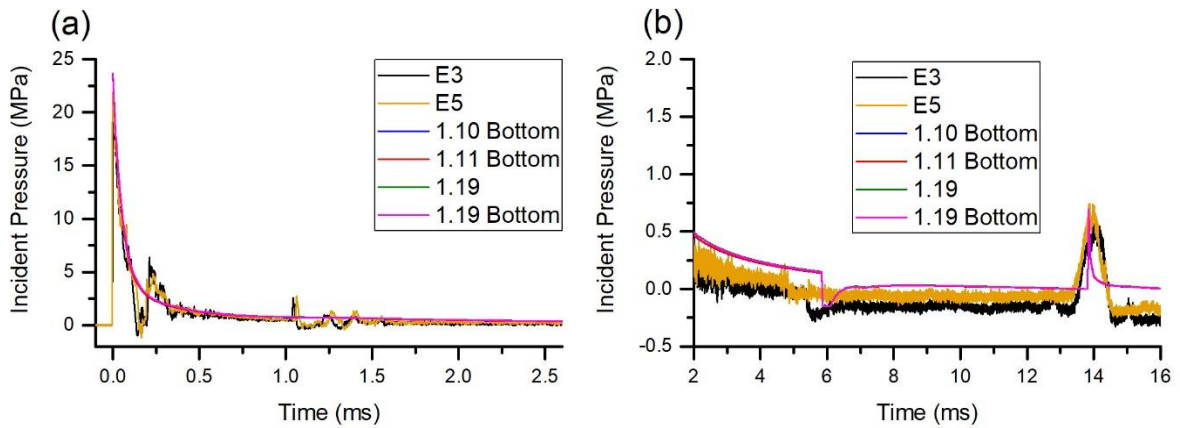
Figure 4-13 Comparison of experimental and numerical (a) shock wave and (b) reflection incident pressures of different TNT equivalent factors for Pentolite (W = 250 g, R = 1.3 m)
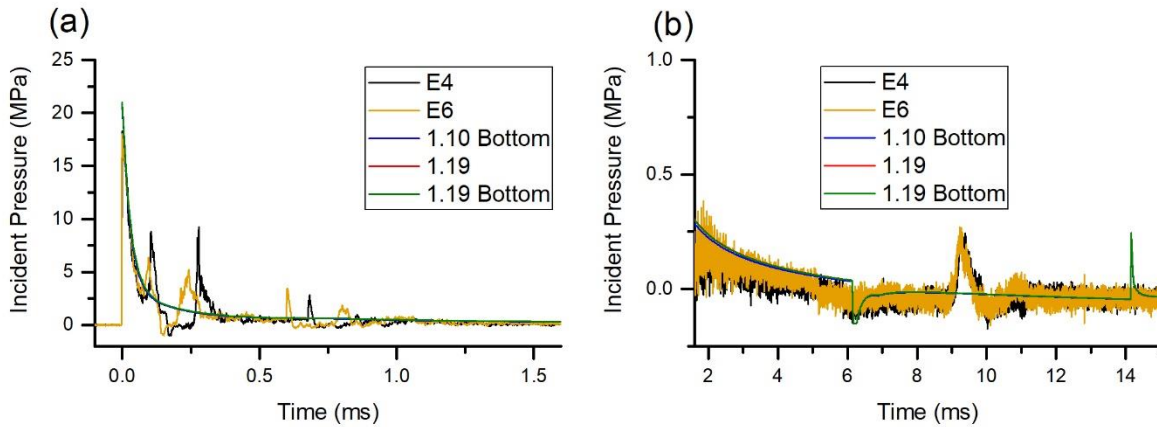
Figure 4-14 Comparison of experimental and numerical (a) shock wave and (b) reflection incident pressures of different TNT equivalent factors for Pentolite (W = 43 g, R = 0.8 m)

Bubble pulses

The bubble pulse incident pressures for the first (a) and second (b) pulses are compared for all events in Figures 4-15 to 4-18. It is clear in these comparisons that the TNT equivalence and bottom presence factors had a more significant effect on bubble pulse periods. It should be noted that the PHS-BUB model does not account for the propagation time in its bubble model, while all experimental measurements contain this by default. Events with the smallest stand-off distance offer the best comparison for the bubble period, while in other events the pulse magnitude is compared.

Initial results from earlier work [124] utilised a Pentolite TNT equivalence of 1.19, which was obtained from Swisdak [6] and manually entered as the equivalent charge mass for the USA analysis. It is shown for all events that the inclusion of bottom effects increased the bubble period for all charge sizes when using this equivalence factor. Comparing the closest 250 g events E3 and E5 (*R = 1.3 m*) in Figure 4-17, the increased period from the bottom effect reduced the accuracy of the USA results when using the 1.19 TNT equivalence. The default 1.10 TNT equivalence with bottom effects was found to have better representation for the first bubble pulse, but slightly under-predicted the first bubble period. A study of additional equivalence factors between these limits was conducted and found that a TNT equivalence of 1.11 gave the best representation for the first bubble period. The second bubble period of the 250 g charge events was less accurate with a 1.11 TNT equivalence. However, since the findings of the experimental investigation in Chapter 3 suggest that the first bubble cycle is the primary cause of the whipping response, and that the first pulse is the largest load after the initial shock wave, it was chosen to prioritise greater accuracy of the first bubble cycle over general accuracy of the entire UNDEX loading event. In the E1 (Figure 4-15) and E2 (Figure 4-16) 250 g events it would appear that larger TNT equivalence factors are required; however when accounting for the additional period in these further events due to the propagation time of the bubble pulse, the 1.11 equivalent factor provided the best representation of the bubble period, measuring 138.2 ms compared to the average experimental measurement of 138.5 ms.

The numerical model did not recreate the sharp peaks recorded during the 250 g bubble pulses. These peaks are due to shock waves emitted by a supersonic collapse phase in these bubbles. The PHS-BUB model assumes the fluid is incompressible for the bubble phase, and therefore is unable to replicate compressible effects, such as these shock wave emissions. Later comparisons of the transient pressure impulse in Figures 4-19 to 4-21 show that these small

shock waves had minimal contribution in the bubble loading, and their absence in the numerical model was considered to have negligible effect on the whipping response analysis.
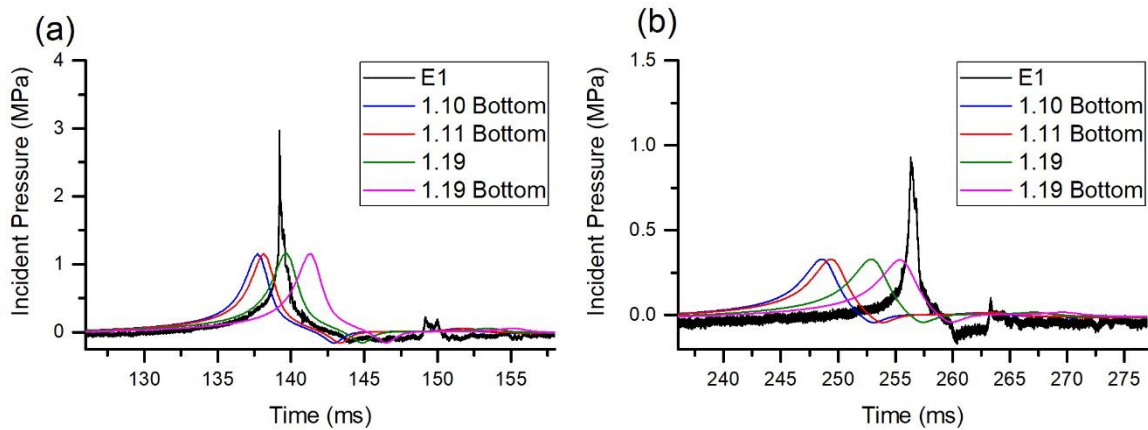
Figure 4-15 Comparison of the first (a) and second (b) experimental and numerical bubble pulse incident pressures of different TNT equivalent factors for Pentolite (W = 250 g, R = 1.8 m)
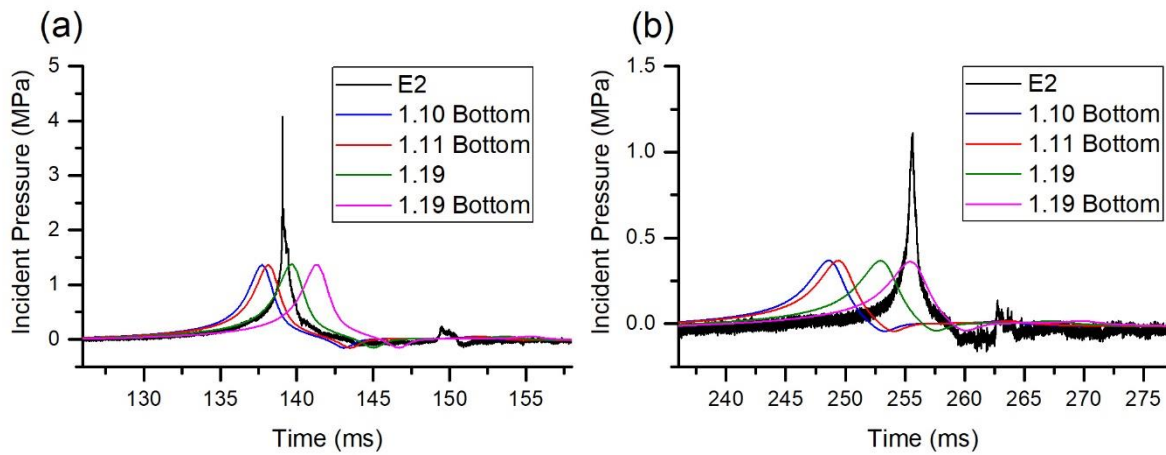
Figure 4-16 Comparison of the first (a) and second (b) experimental and numerical bubble pulse incident pressures of different TNT equivalent factors for Pentolite (W = 250 g, R = 1.5 m)
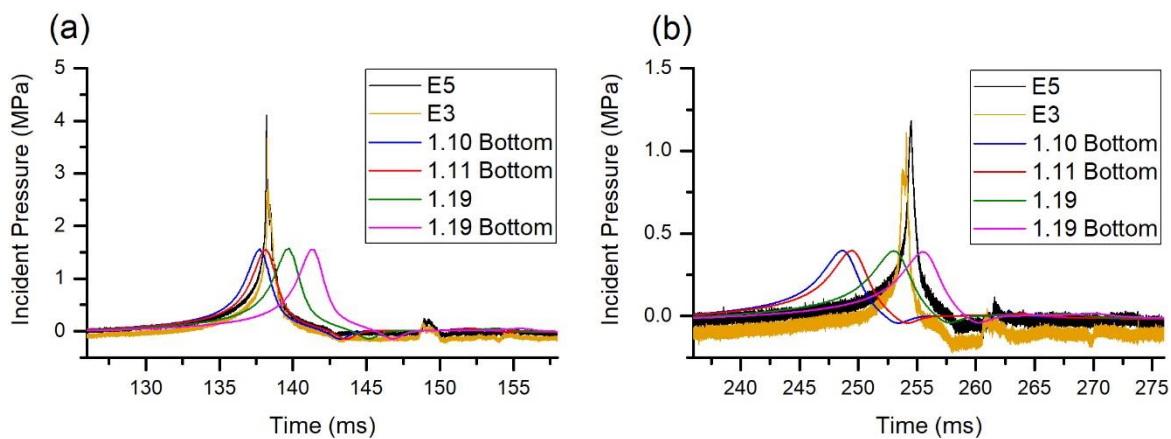
Figure 4-17 Comparison of the first (a) and second (b) experimental and numerical bubble pulse incident pressures of different TNT equivalent factors for Pentolite (W = 250 g, R = 1.3 m)

For the 43 g charge events, it was found that the increased period from the bottom effects improved the accuracy of both the first and second bubble period when using a TNT equivalence factor of 1.19. where the model matched the first experimental bubble period of 79 ms. Using the default TNT equivalence of 1.10 with bottom effects under-predicted both

bubble periods. Swisdak [6] notes that charges in this size range can have different equivalence factors. Unlike the 250 g comparisons in Figures 4-15 to 4-17, the peak pulse values from the PHS-BUB models compare well with the experimental measurements. As the USA code does not model supersonic collapse, the closer approximation of the peak shape by the code may be taken as additional evidence that the 43 g charge bubbles did not have a supersonic bubble collapse.
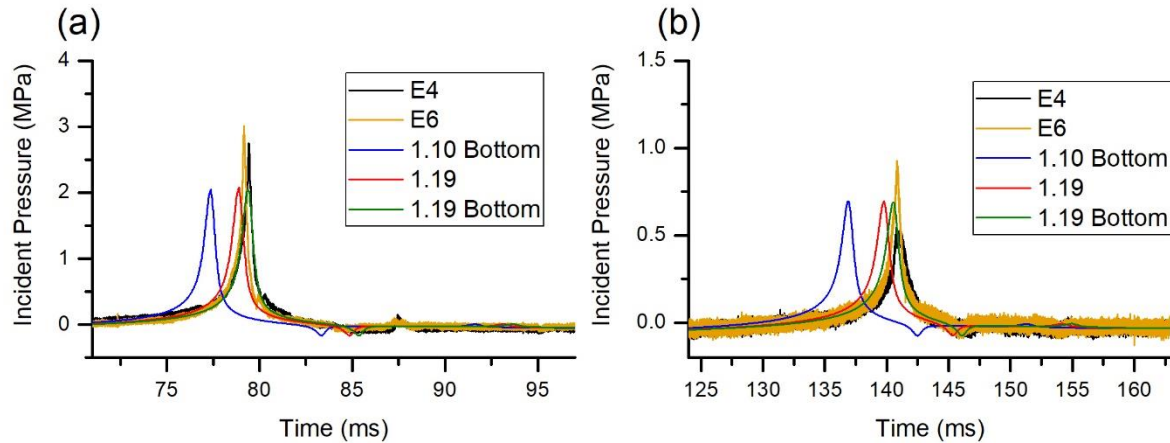
Figure 4-18 Comparison of the first (a) and second (b) experimental and numerical bubble pulse incident pressures of different TNT equivalent factors for Pentolite (W = 43 g, R = 0.8 m)

Pressure impulse

It has been discussed previously that the pressure impulse provides a better comparison of explosive loading contributions than peak pressure comparisons [14, 15]. The pressure impulse for each event was computed from the integral of the numerical incident pressure time history using Equation 1.5. The computed numerical impulses for the shock wave (I_S), bubble expansion (I_B), and total (I_T), along with differences (Δ) from the experimental measurements in Table 3-7 are presented in Table 4-9. This comparison shows that the numerical model overpredicted the pressure impulse by 13 – 29 %. Cole [8] remarked upon similar errors when comparing the impulse quantity of pentolite to the equivalent weight of TNT, noting that similitude equations over-predicted the peak pressure by 4 %, while the integral of shock wave pressure was over-predicted by 29 %. Cole noted these large differences result from the different decay rates of the shock wave and bubble pulsations for different explosive materials. Hunter and Geers [41] also remarked upon this over-prediction for Pentolite explosives. If it is assumed that the TNT equivalent energy is used, the over-predicted pressure should correspond with a lower particle velocity in the PHS-BUB model. A thorough validation of this phenomenon would require particle velocity measurements for bubble responses, which were not obtained during the experimental investigation, and which Hunter and Geers also noted as a difficult measurement to achieve [41]. Hunter and Geers made comparisons with other numerical models and found similar discrepancies for impulse and particle velocity and concluded that this over-prediction was an acceptable error.

Table 4-9   Comparison of pressure impulse from USA/LS-Dyna and experimental measurements

Events	W (g)	R (m)	I_S (MPa.ms)	Δ (%)	I_B (MPa.ms)	Δ (%)	I_T (MPa.ms)	Δ (%)
E1	250	1.8	2.97	21.2	5.29	26.3	8.26	24.5
E2	250	1.5	3.59	24.7	6.51	24.4	10.10	24.5
E3, E5	250	1.3	4.17	23.4	7.01	13.1	11.18	16.7
E4, E6	43	0.8	2.36	29.3	4.17	15.9	6.53	20.4

From the transient pressure impulse records in Figures 4-19 to 4-21, it can be observed that while the PHS-BUB model over predicted the total pressure impulse, it provided good approximations of both bubble pulses. As previously stated, greater accuracy of the first bubble loading cycle was preferred to an overall accuracy of the UNDEX loading, as the whipping response severity was dependent on this loading. The cut-off time for the PHS-BUB model also resulted in a shorter duration of the loading impulse than what was observed in the experiment. While PHS-BUB model produced a greater initial impulse, the experimental loading lasted and "drove" the response for longer. Due to the previously described cut-off criteria for bubble loading models [96], it was not possible to extend this loading duration without inducing additional errors.
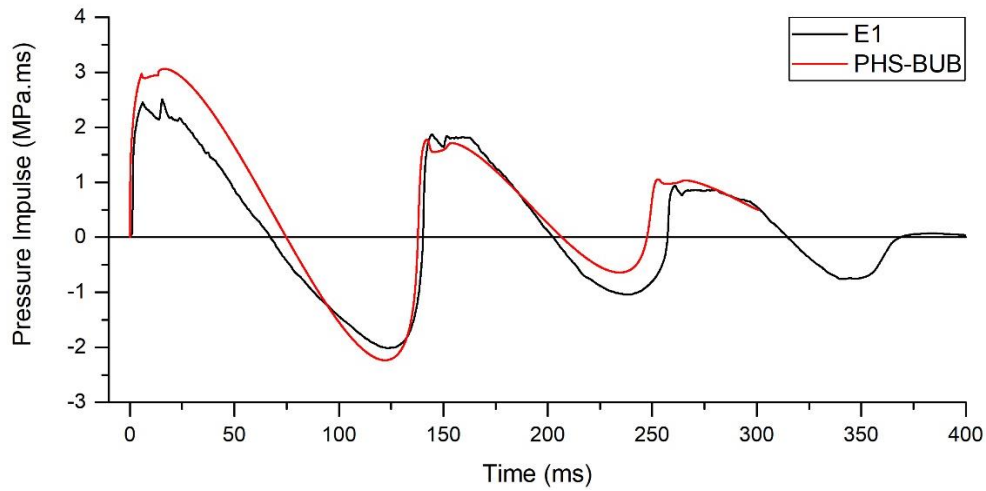
Figure 4-19 Comparison of experimental and numerical pressure impulse (W = 250 g, R = 1.8 m)
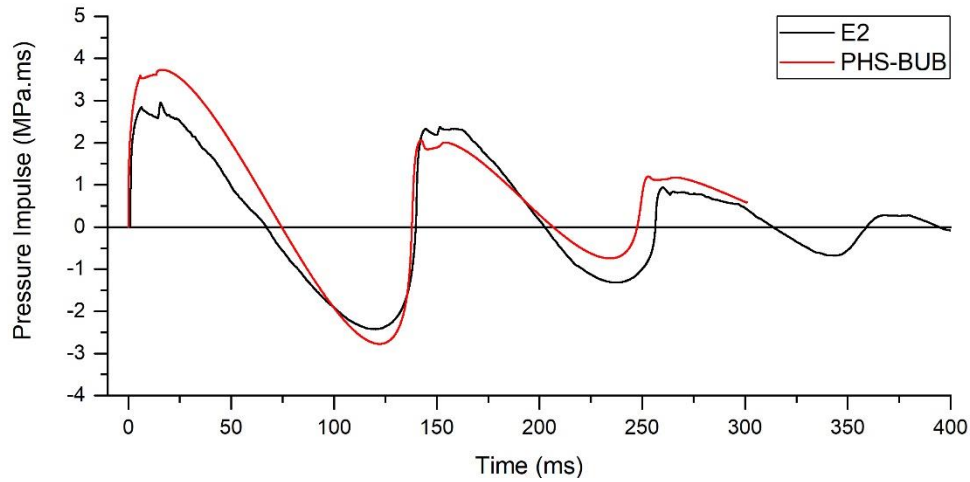
Figure 4-20 Comparison of experimental and numerical pressure impulse (W = 250 g, R = 1.5 m)
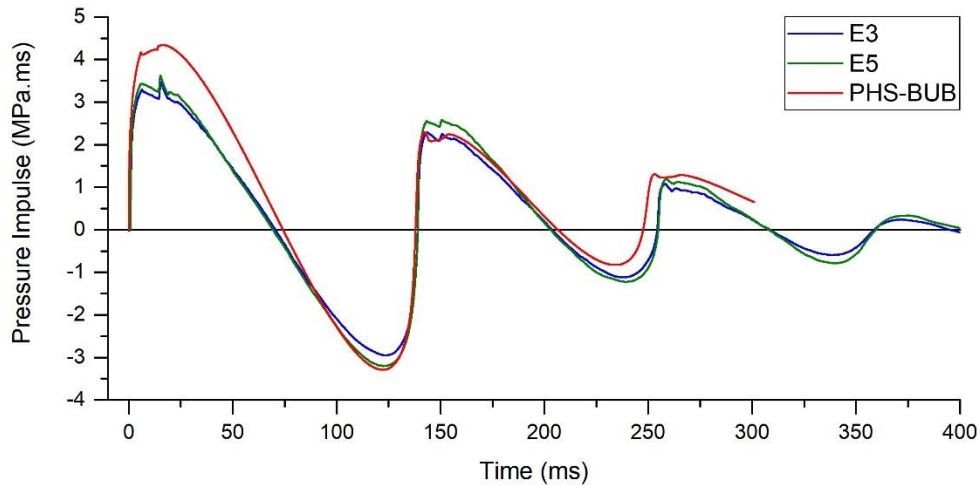
Figure 4-21 Comparison of experimental and numerical pressure impulse (W = 250 g, R = 1.3 m)

While most PHS-BUB results had the same trend of initially over-predicting the shock wave impulse but comparing well with the later bubble responses, it is shown in Figure 4-22 that E4 was quite different. This is despite the similar event E6 demonstrating the same trends as all other events. The sharp and larger rise during the shock wave pressure impulse suggest that this pressure gauge may have experienced some damage from the shock wave loading. This offset affects the transient comparison but when considering the summation of positive and negative bubble impulse components the bubble pressure impulses are similar. Based on this and the better comparison from the similar event E6, the PHS-BUB loading was still considered as appropriate for conducting a whipping analysis.
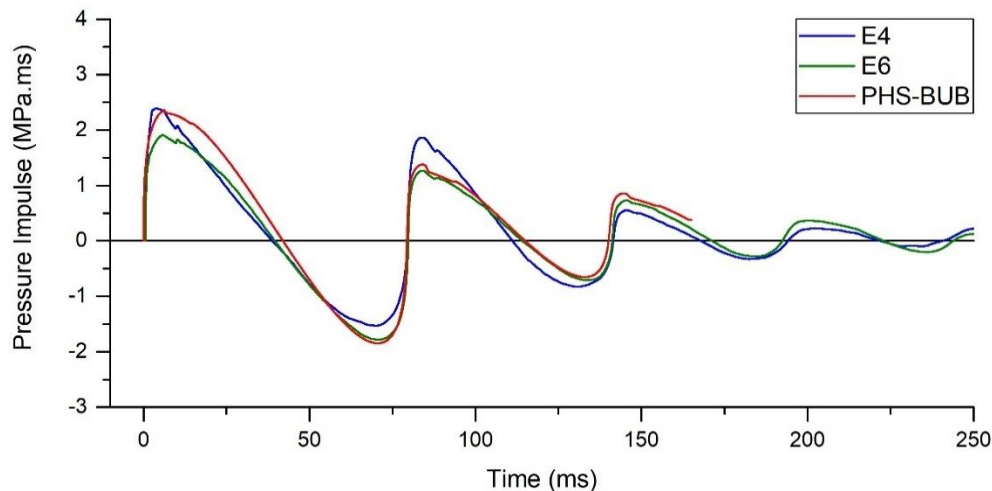
Figure 4-22 Comparison of experimental and numerical pressure impulse (W = 43 g, R = 0.8 m)

From these comparisons, it was concluded that the PHS-BUB model provided an appropriate representation of the UNDEX loading for these experimental events and was suitable for conducting further numerical studies. While different TNT factors did not have a significant effect on the shock wave, they had a noticeable effect on the bubble responses. An equivalence factor of 1.11 was used for $W = 250$ g scenarios and 1.19 was used for $W = 43$ g scenarios.

4.3.2. Structural response

The structural response of the model was validated by the comparison of the numerical and experimental strain responses. Experimental and numerical results are designated as E and EN respectively. The damping methods discussed in Section 4.2.6 were assessed to determine the

best method for achieving an accurate transient response over an analysis duration of 1000 ms. The peak result contour plots are presented to qualitatively determine the modal responses and peak response locations during whipping.

Damping models

Events E1 – E3 (*W = 250 g, L -= 0.0 m*) all demonstrated similar modal responses, shown in Figure 4-23, dominated by BM1 at 7 Hz, with the highest strain levels occurring at amidships. The difference in the response frequency from these results is due to rounding, as the analysis was only analysed for a 1 s duration, compared to 4 s in the experimental measurements, resulting in a larger frequency step size. The EN damping model results for amidships, forward, and aft locations on portside are compared against the experimental responses from Section 3.3.2 of Chapter 3 in Figures 4-24 to 4-26. Here it is shown that no EN model captured the initial peak shock wave response. This is also the case for all other results. It was expected that the shock wave would not be captured accurately as the mesh size is quite large and not capable of effectively tracking the shock wave response. To capture this response, smaller and solid elements would be better choice as the wave would need to be tracked both longitudinally and through the thickness of the platform's hull. It would have been possible to create an appropriate mesh, even for a localised area, however this would have significantly reduced the stable timestep and increased the analysis runtime. As the focus of this investigation is on whipping, it was decided that the mesh should be appropriate for that response and not refined for the shock wave.

Beyond the initial shock wave response, the whipping response was reproduced well by all damping models for the first 200 ms, during which the experimental peak response occurred at 168 ms, as noted in Figures 4-24b to 4-26b. After the initial 200 ms, differences in the damping effects of each model became noticeable. Without damping, the UD model results became more inaccurate over subsequent whipping cycles as these steadily decreased, therefore this model was not appropriate for transient analysis of the later whipping responses. The RD model was able to provide some damping but always under-damped the response, compared to the experimental measurements. As the RD model is only based on internal damping responses, it is likely the insufficient damping was due to external damping effects in the experiment which are not considered by the RD model. The FR model results correlated better with the experimental results over the entire duration of the analysis. However, the error this model introduced to the natural frequency become apparent at all locations for the last few whipping cycles of EN1 FR results in Figure 4-24, where the response became delayed to the E1 measurements. The EN2 (Figure 4-25) and EN3 (Figure 4-26) FR results did not have a significant delay compared to their respective experimental measurements E2 and E3. All FR results in Figures 4-24 to 4-26 contained a superimposed response of BM5 at approximately 102 Hz. While this was a minor contribution for these events, this response was not observed in any of the equivalent experimental results. The response frequency is likely real, but the experimental measurements show that this was heavily damped out by the later whipping cycles, which suggests that there was insufficient damping at this frequency in the UD, RD, and FR models. The combined RDFR model provided the best transient results for these events, with similar accuracy over all whipping cycle peaks to the FR model but did not contain any error in the natural frequency response. The frequency response from this model for these three events in Figure 4-23 also demonstrates that the BM5 response was greatly reduced which shows that the RDFR model was also able to damp out most of the BM5 response.

The RDFR model generally overpredicted the peak response of each whipping cycle but marginally under-predicted the overall peak response at 168 ms. A comparison of the

experimental peak responses against those predicted by the RDFR models is presented in Table 4-10. The RDFR models under predicted the peak experimental responses by $4 - 7$ % for events E1 – E3. From the EN3 results in Figure 4-26 it is seen the RDFR model over-predicted the response at all locations more than any other events. It was noted in experimental results from Chapter 3 that this scenario could have been susceptible to stronger interaction from the bubble, which is not accounted for in the DAA solutions.

The overall peak response from all damping models occurred at 252 ms, during the subsequent whipping peak of the overall peak response seen in the experimental measurements. For the RDFR results, this peak was only marginally higher than the experimental peak at 168 ms. The difference in response levels was considered negligible and the qualitative accuracy of the different peak response times is considered further in the following sections.
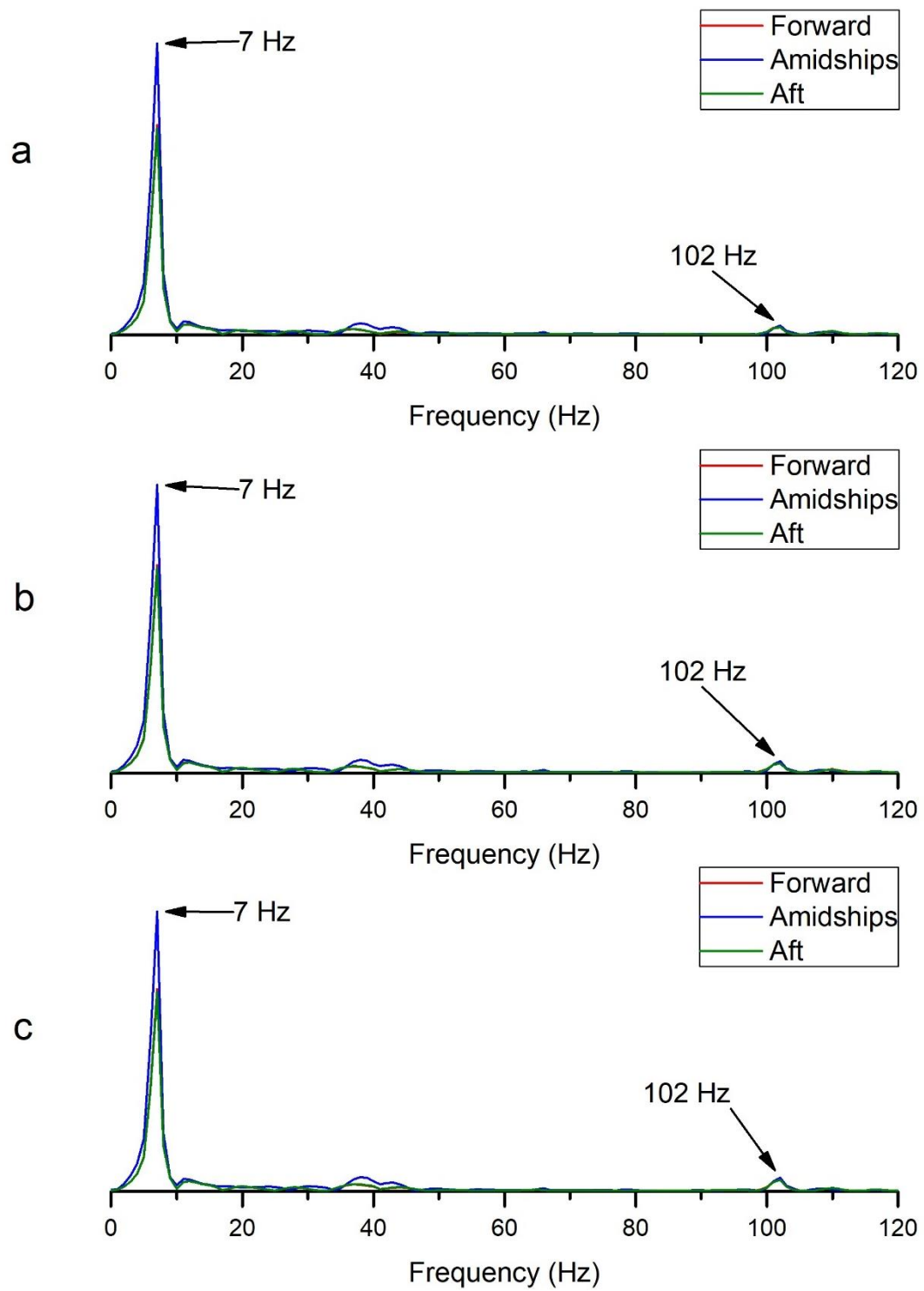
Figure 4-23 Frequency response of RDFR model for (a) EN1, (b) EN2, and (c) EN3

Figure 4-24 Comparison of EN1 damping models at (a) forward, (b) amidships, and (c) aft for E1 (W = 250 g, R = 1.8 m, L = 0.0 m)

*Figure 4-25 Comparison of EN2 damping models at (a) forward, (b) amidships, and (c) aft for E2
(W = 250 g, R = 1.5 m, L = 0.0 m)*

Figure 4-26 Comparison of EN3 damping models at (a) forward, (b) amidships, and (c) aft for E3 (W = 250 g, R = 1.3 m, L = 0.0 m)

For event E4 (*W = 43 g, R = 0.8 m, L = 0.0 m*), the UD and RD models performed well for the initial 100 ms. The experimental peak response occurred within this time at 81 ms, noted in Figure 4-28. Both the UD and RD models slightly over-predicted the peak. After this time, a significant contribution of higher frequency response from BM3 at 41 Hz and BM5 at 102 Hz caused both these damping models to be largely inaccurate for both the strain levels and modal responses.

The FR and RDFR models presented in Figure 4-29 compared better, exhibiting good accuracy over the first 100 ms, while also damping out the higher frequency components in the late time whipping response. The EN4 FR model contained a similar natural frequency error that was

observed in EN1, which caused the FR model response to become delayed compared to the E4 measurements. The EN4 RDFR model did not have this issue and maintained good accuracy over the entire duration. The RDFR model under-predicted the experimental peak by 4 %, compared in Table 4-10, and subsequent whipping peaks after 400 ms were also slightly under-predicted by this model. The frequency response from the RDFR model in Figure 4-27 shows that while BM1 at 7 Hz and BM3 were dominant, there was still a large component of BM5 at 102 Hz.
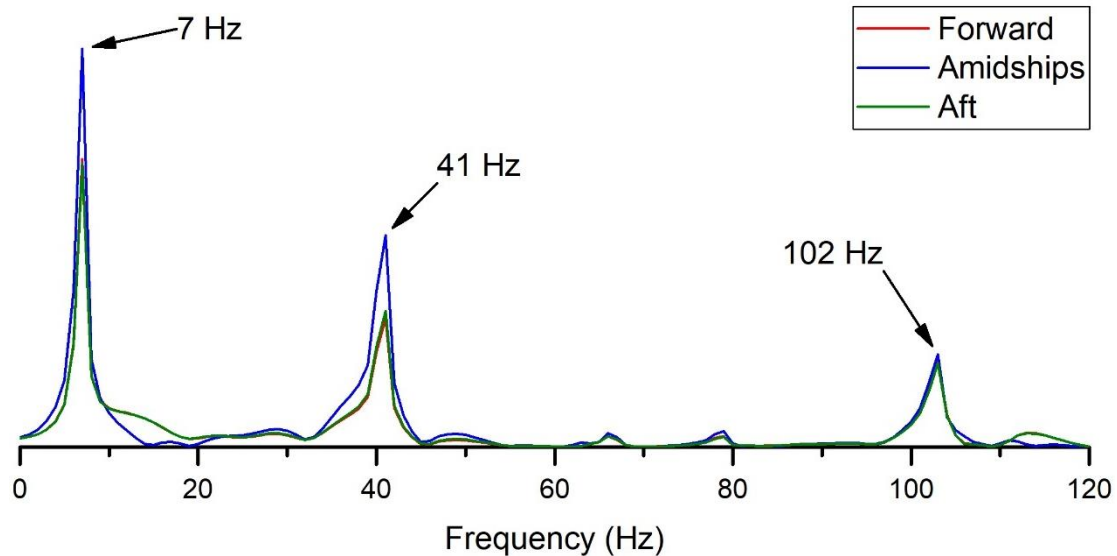
Figure 4-27 Frequency response of EN4 RDFR model

The overall peak response for EN4 RDFR occurred at amidships at 94 ms, compared to the overall peak response from E4 peak at the aft location at 81 ms, noted in Figure 4-29. Both peaks occurred after the arrival of the bubble pulse at each location, so this variation may be due to a difference in the bubble pulse energy from the PHS-BUB loading model. As noted in Chapter 3, event E4 had a noticeable presence of the BM3 response and saw similar peak whipping strain levels at the amidships, forward, and aft locations. This may also account for the difference in the peak response location if the combined contribution of BM1 and BM3 is slightly larger in the numerical model. However, as with the differences between experimental and numerical peak whipping values from the *W = 250 g, L = 0.0 m* events, there was only a minor difference in the peak values.

Figure 4-28 Comparison of EN4 UD and RD damping models at (a) forward, (b) amidships, and (c) aft for E4 (W = 43 g, R = 0.8 m, L = 0.0 m)

Figure 4-29 Comparison of EN4 FR and RDFR damping models at (a) forward, (b) amidships, and (c) aft for E4 (W = 43 g, R = 0.8 m, L = 0.0 m)

In Figure 4-30 it is shown that all EN5 damping models compared well to E5 (*W = 250 g, R = 1.3 m, L = -2.8 m*) for the first 300 ms. The overall peak response from E5 occurred during this time at 181 ms. As with previous results, the UD and RD models became more inaccurate for later whipping response peaks, after 300 ms. The FR and RDFR models maintained a good representation of the whipping response for the entire analysis duration. Overall, the RDFR model performed marginally better by damping out the higher frequency responses in the late time whipping response, which matched better with the whipping behaviour observed in E5 measurements. The RDFR model peak response occurred at the subsequent whipping peak at 254 ms, noted in Figure 4-30a, but as with other events, this peak was only marginally higher than the E5 overall peak response at 181 ms. The experimental peak response was perfectly

predicted by the EN5 RDFR model, noted in the comparisons made in Table 4-10, while subsequent whipping peaks were slightly over-predicted. The frequency response from the RDFR model in Figure 4-31 shows that while BM5 was present at 102 Hz, it was minor compared to the dominant BM1 at 7 Hz and BM2 at 20 Hz.
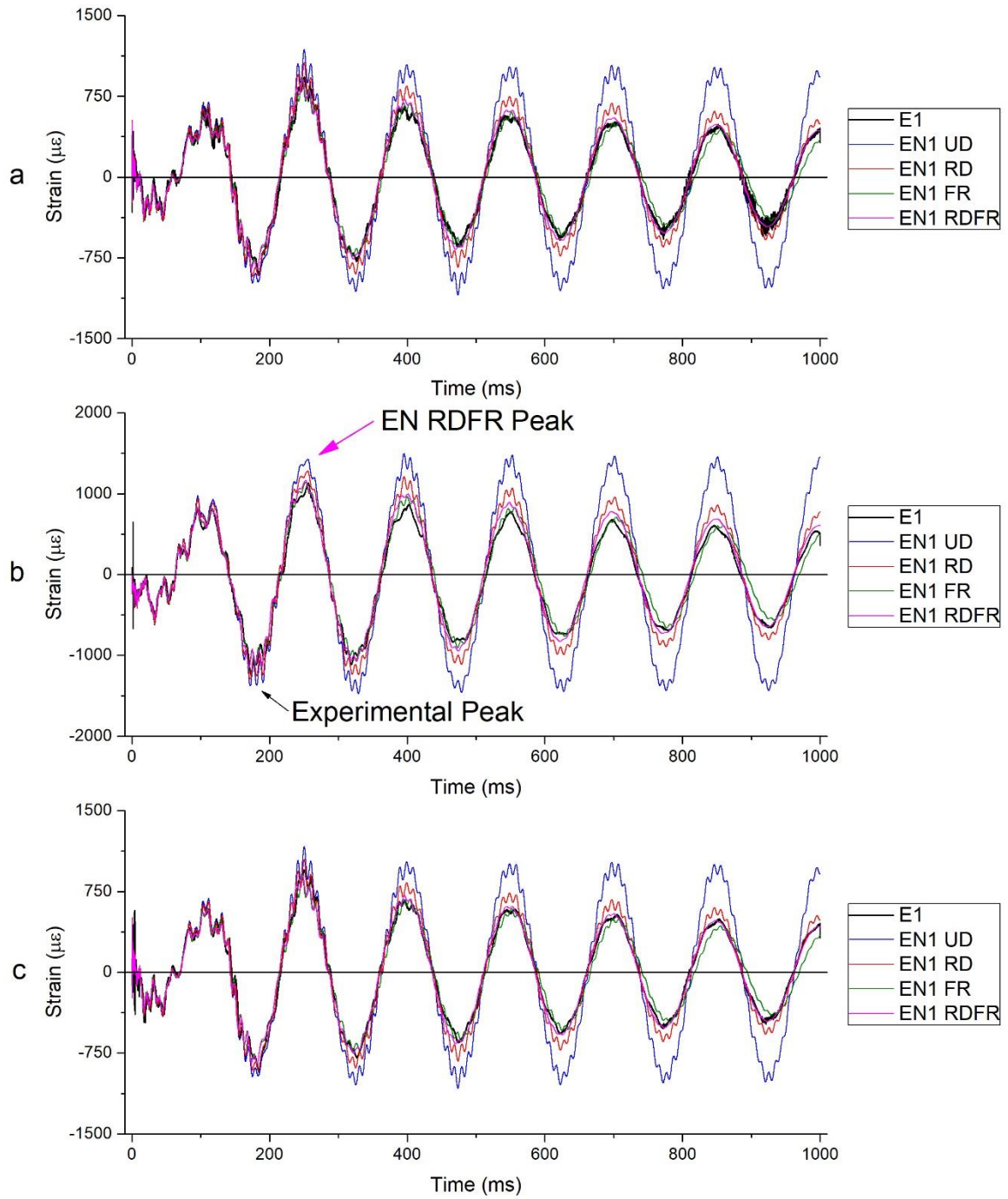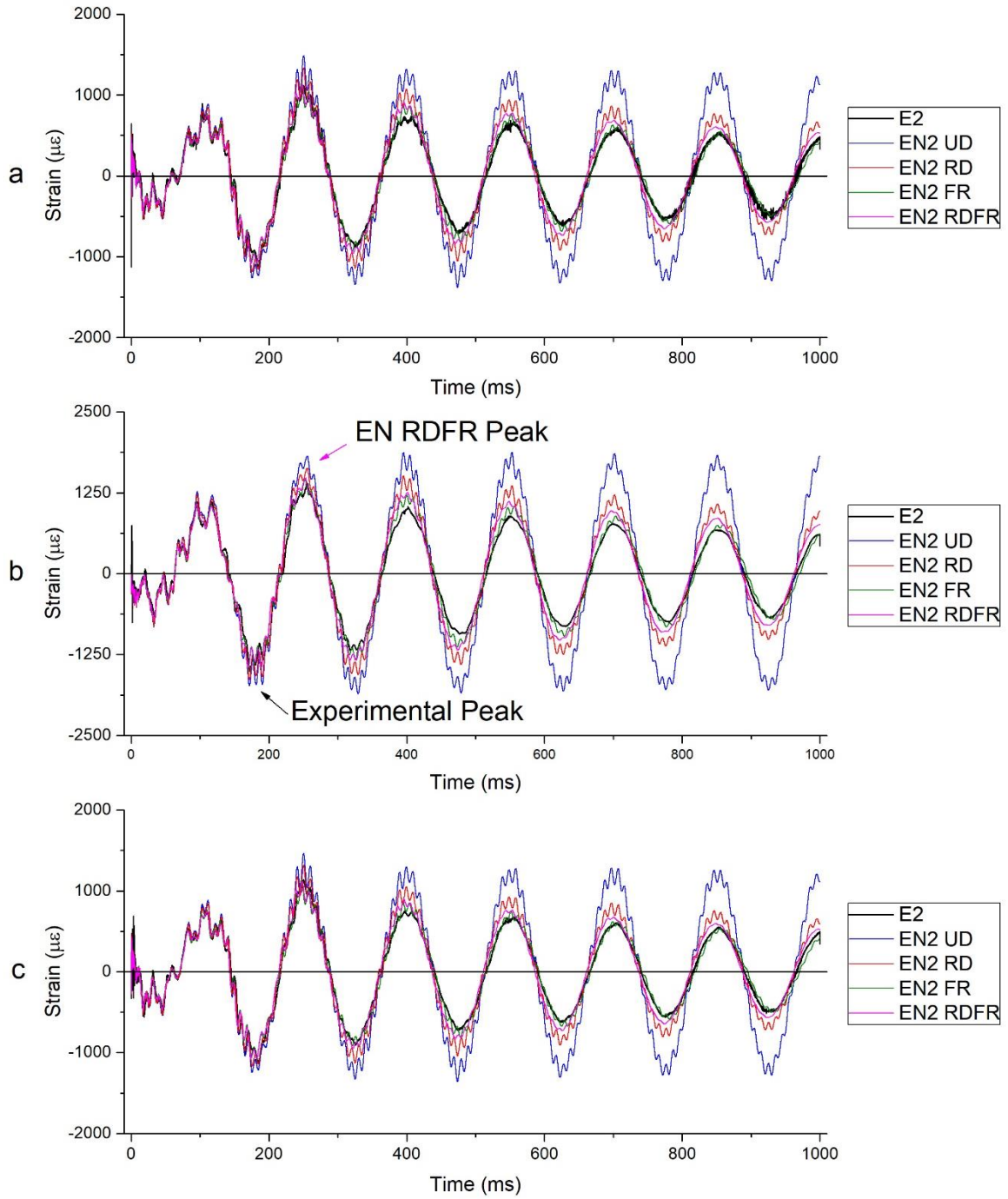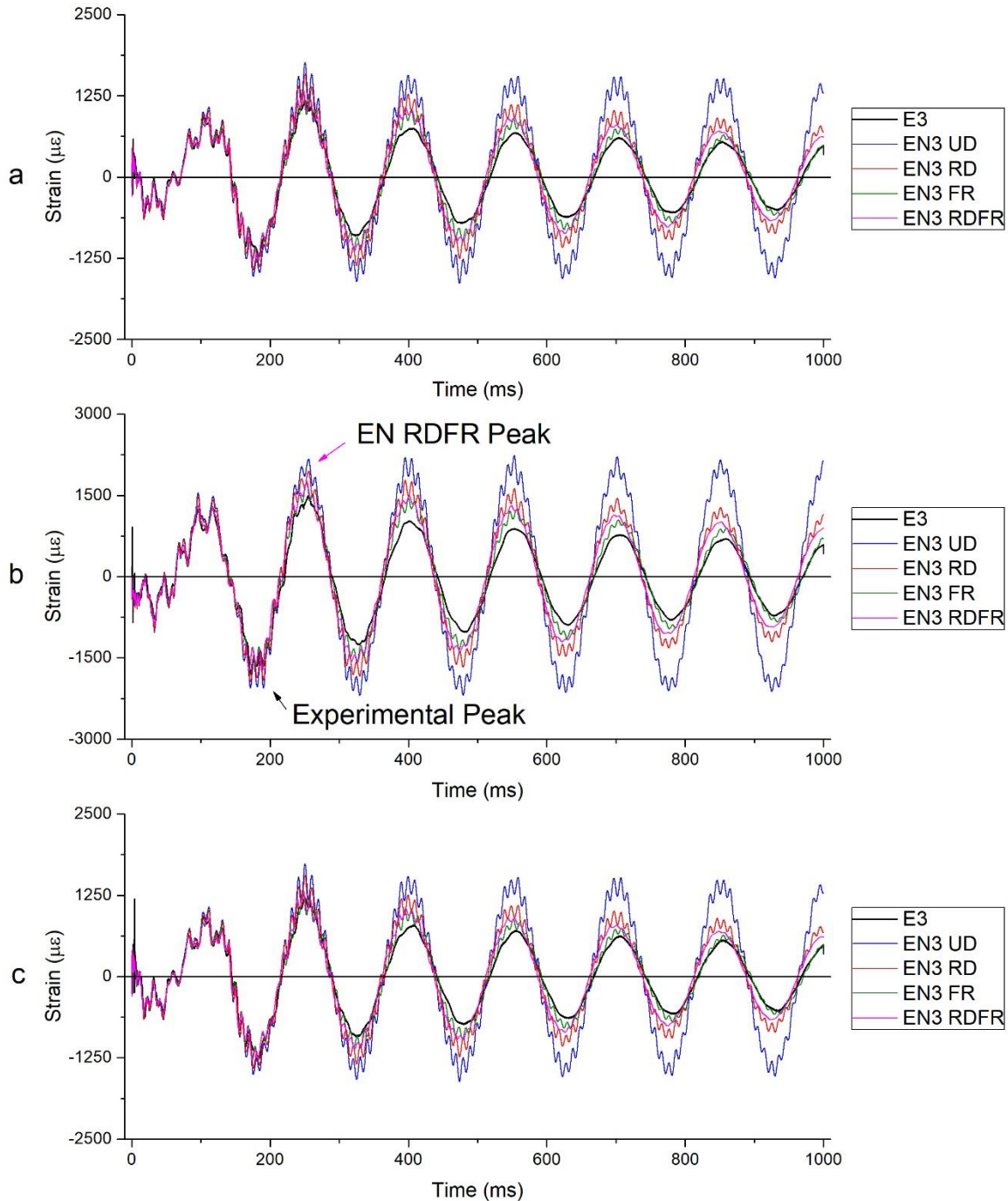

Figure 4-30 Comparison of EN5 damping models at (a) forward, (b) amidships, and (c) aft for E5
   (W = 250 g, R = 1.3 m, L = -2.8 m)
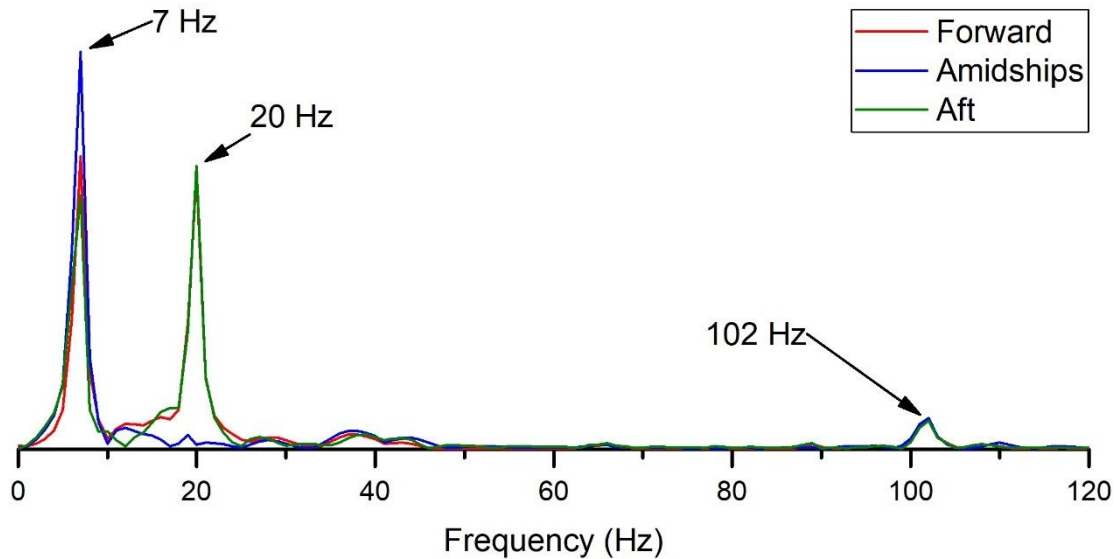
Figure 4-31 Frequency response of EN5 RDFR model

The UD and RD models for EN6 (*W = 43 g, R = 0.8 m, L = -2.8 m*) only performed well for the very early shock induced whipping response, and greatly over-predicted the peak experimental response at 81 ms, shown in Figure 4-32. Reponses after this were also largely over-predicted due to a significant presence of the higher frequency BM3 and BM5 responses, similar to what was observed from these models in the similar event E4 in Figure 4-28. Consequently, the UD and RD models were not considered suitable for whipping analysis of this scenario.

The EN6 FR and RDFR model results, shown in Figure 4-33, compared much better. Both these models over-predicted the whipping response for the initial 400 ms, but by a far smaller degree than the UD and RD models. This over-prediction appeared to be due to contributions of BM5 that were still not sufficiently damped out by this time. The frequency response of the RDFR model in Figure 4-34 show that BM5 at 102 Hz still had a relatively large contribution, particularly when compared to BM3 at 41 Hz. However, it is shown that both models did ultimately damp these out in the late time whipping response and the subsequent peaks were slightly under-predicted by both models. The FR model contained the natural frequency error, causing the response to be delayed from the E6 response during the late time whipping, particularly in the amidships response in Figure 4-33b. This was the only scenario where the numerical and experimental peak occurred at the same time and location. However, the EN6 RDFR model over-predicted this peak response by 15 %, noted in Table 4-10. It was noted in the experimental investigation that while the peak response in E6 occurred at amidships, the whipping response after this was larger at the forward and aft locations. These locations in Figure 4-33a and c compared much better to the E6 measurements.
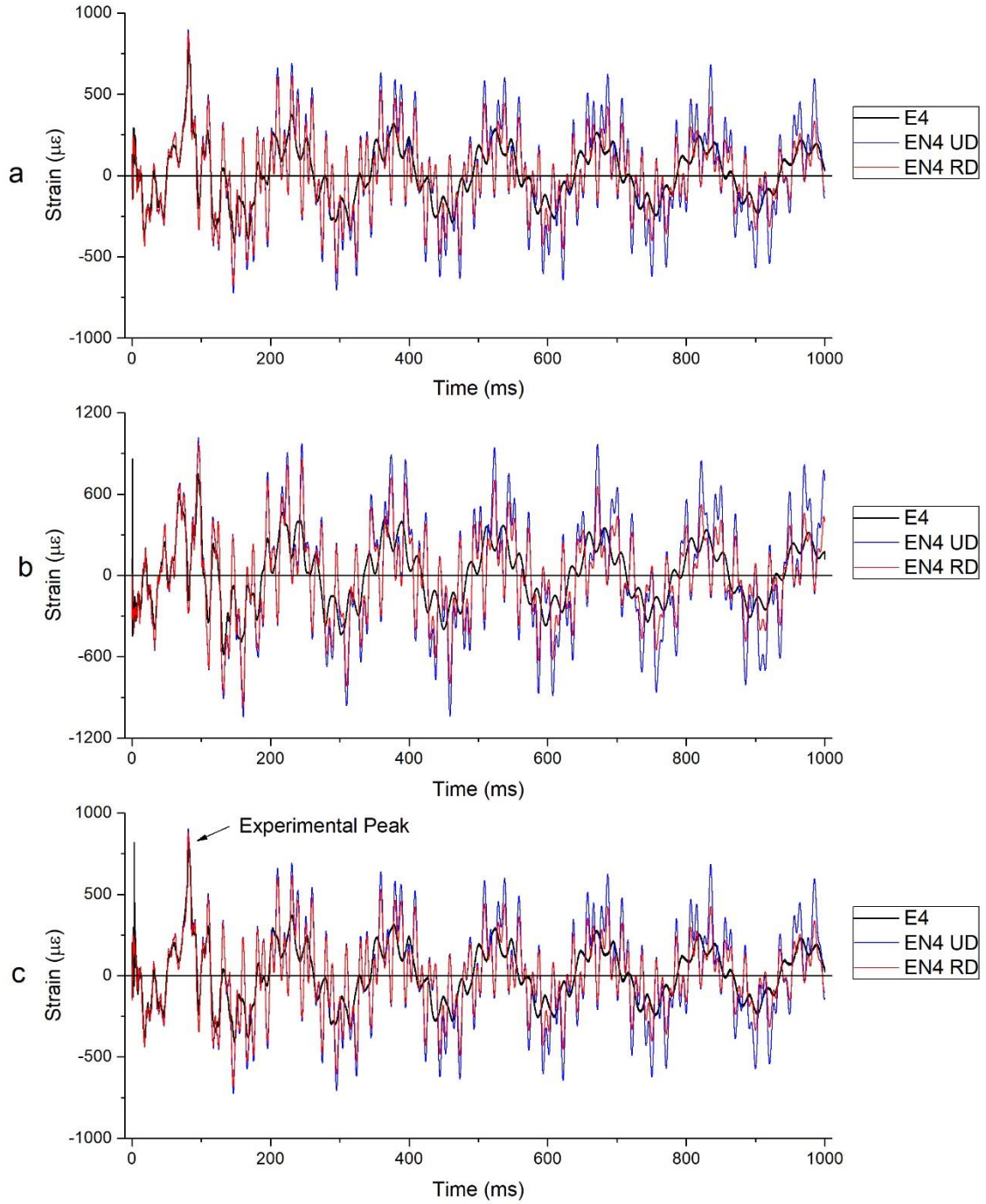
Figure 4-32 Comparison of EN6 UD and RD damping models at (a) forward, (b) amidships, and (c) aft for E6 (W = 43 g, R = 0.8 m, L = -2.8 m)
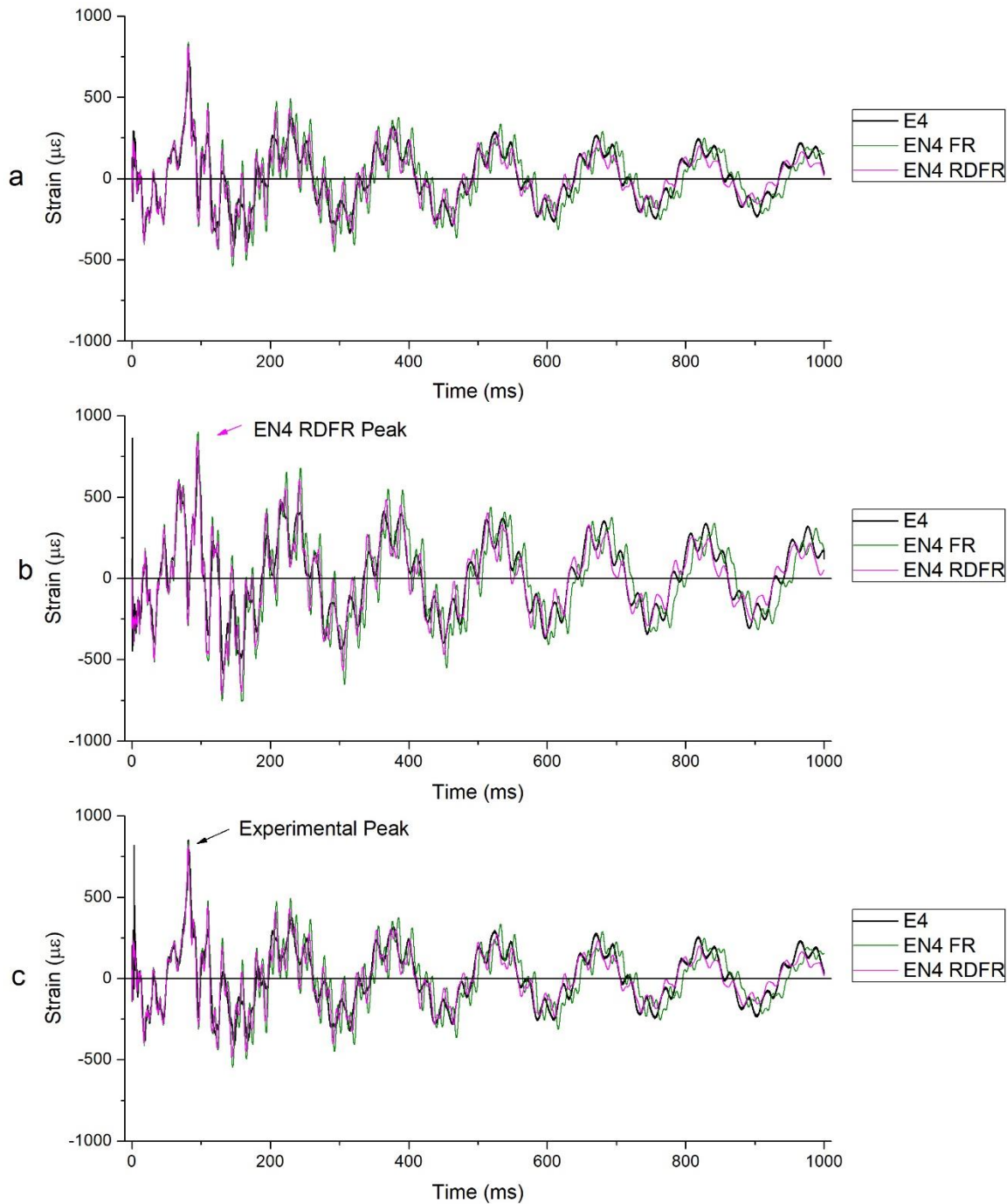
Figure 4-33 Comparison of EN6 FR and RDFR damping models at (a) forward, (b) amidships, and (c) aft for E6 (W = 43 g, R = 0.8 m, L = -2.8 m)

Figure 4-34 Frequency response of EN6 RDFR model

EN7 model comparisons to E7 (*W = 250 g, R = 1.3 m, L = -4.3 m*) in Figure 4-35 and Figure 4-36 show that all damping models compared well over the initial 200 ms. The experimental peak response occurred during this time frame at 184 ms. The UD and RD models in Figure 4-35 became increasingly inaccurate for subsequent whipping peaks, while both the FR and RDFR models in Figure 4-36 performed well for the entire analysis duration. Between these two, the RDFR model compared marginally better, by damping out high frequency content in the late time whipping response. The EN7 RDFR model response compared very well with the overall peak response from E7, with a difference of only 1 %. Both the FR and RDFR models had an error in the natural frequency response for the last few whipping cycles. The frequency response from the RDFR model in Figure 4-37 shows that BM1 was essentially absent and the response was dominated by BM2 at 20 Hz.

The aft responses compared very well, and this was the most severe location from this scenario. Other locations were less accurate. The response from the EN7 RDFR model at the forward location in Figure 4-35a over-predicted all whipping peaks for the first 600 ms, although the model accuracy did improve after this time. At amidships, shown in Figure 4-35b, the RDFR model over-predicted the E7 measurements for the initial 300 ms. There was also a significant amount of high frequency response in the EN7 model between 200 and 400 ms that was not observed in the E7 measurements. After 400 ms, the EN7 model results were overdamped, and under-predicted the responses from E7 measurements. The response at amidships was the least severe, compared to the other location in Figure 4-35. Despite these discrepancies, the model was able to predict the peak response within an accuracy of 1 % and compared extremely well with the most severe response at the aft location in Figure 4-35c. Therefore, the RDFR model was considered the most suitable for obtaining this information in further numerical studies, with consideration for the inaccuracies at other locations.
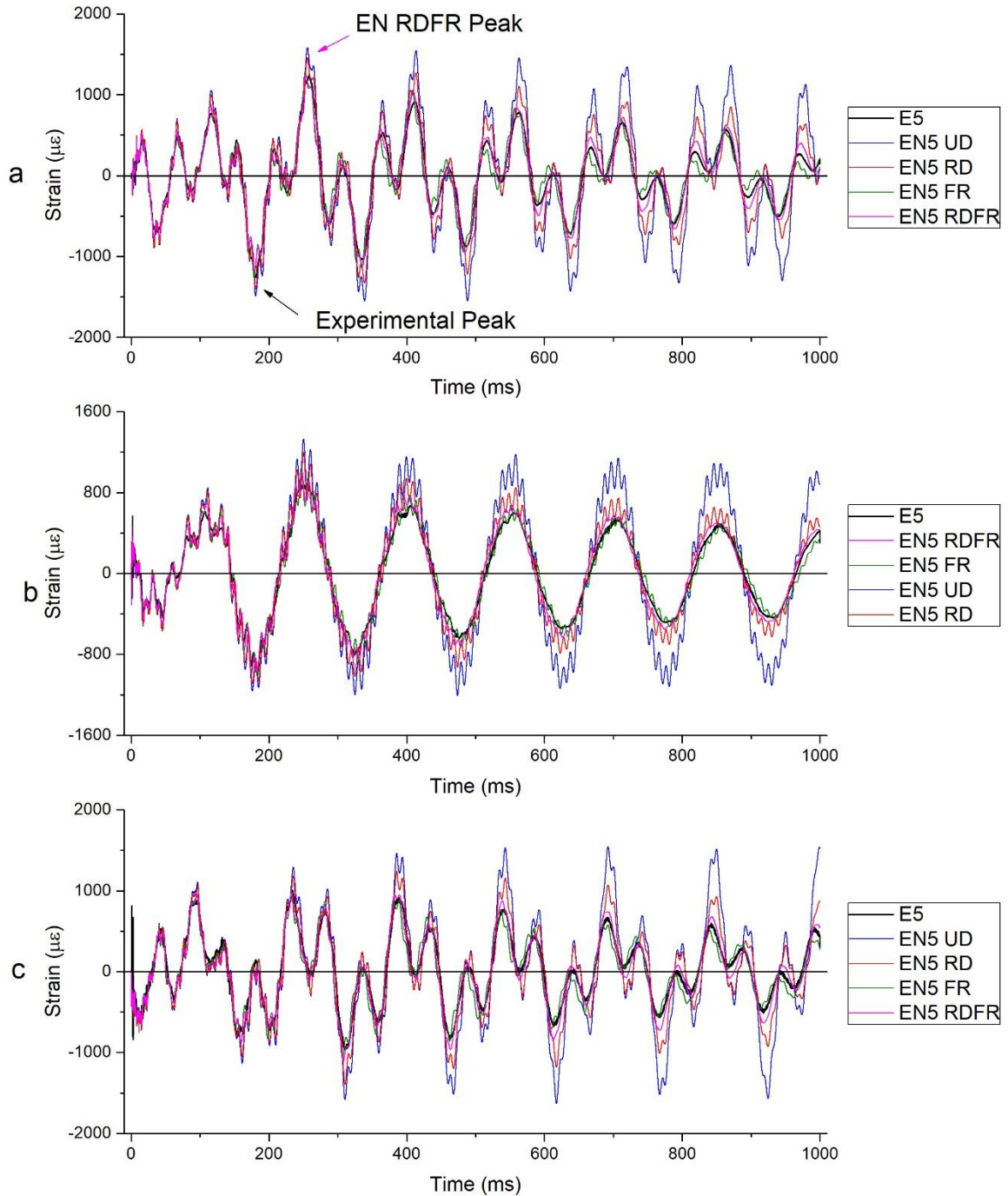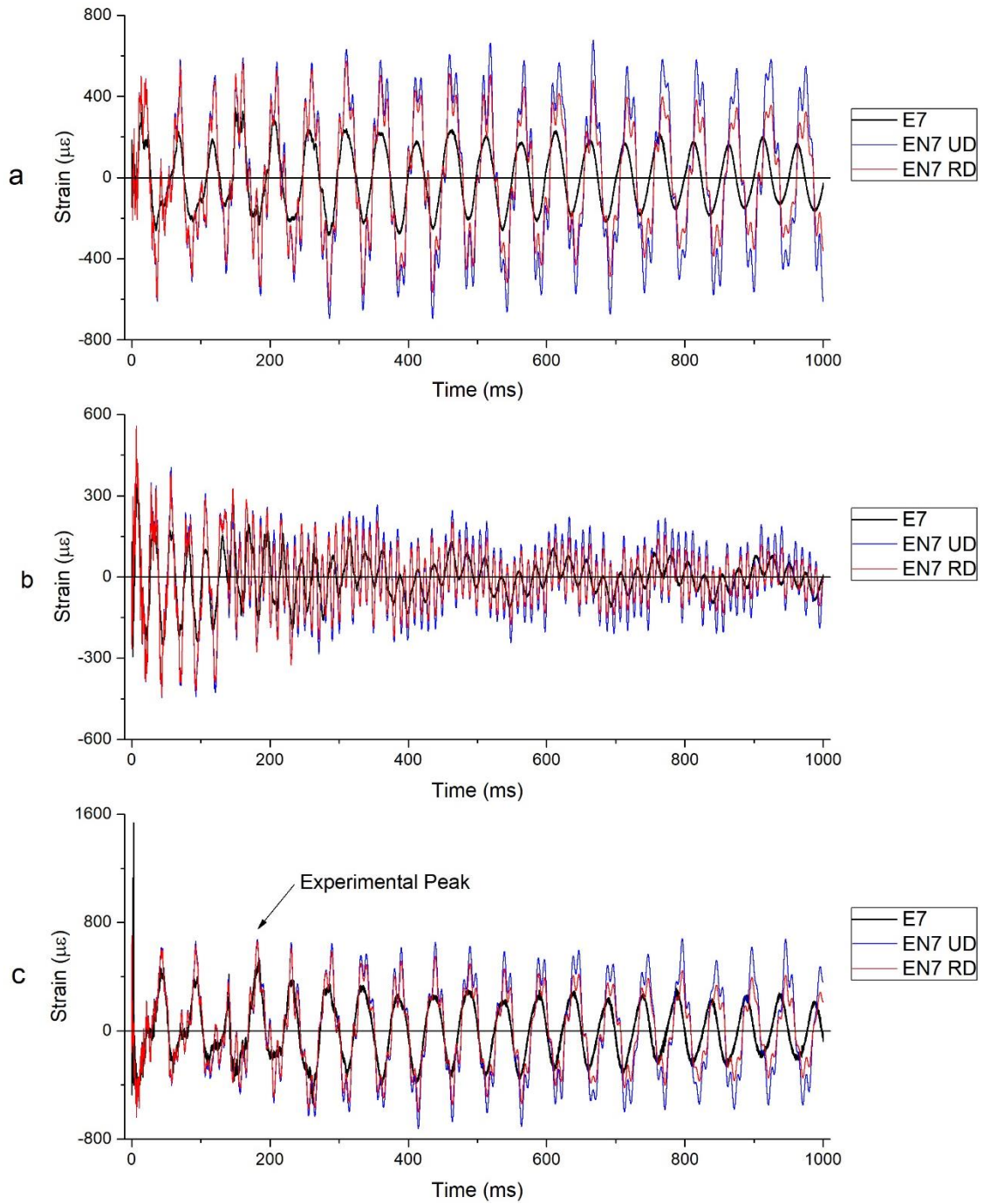
Figure 4-35 Comparison of EN7 UD and RD damping models at (a) forward, (b) amidships, and (c) aft for E7 (W = 250 g, R = 1.3 m, L = -4.3 m)
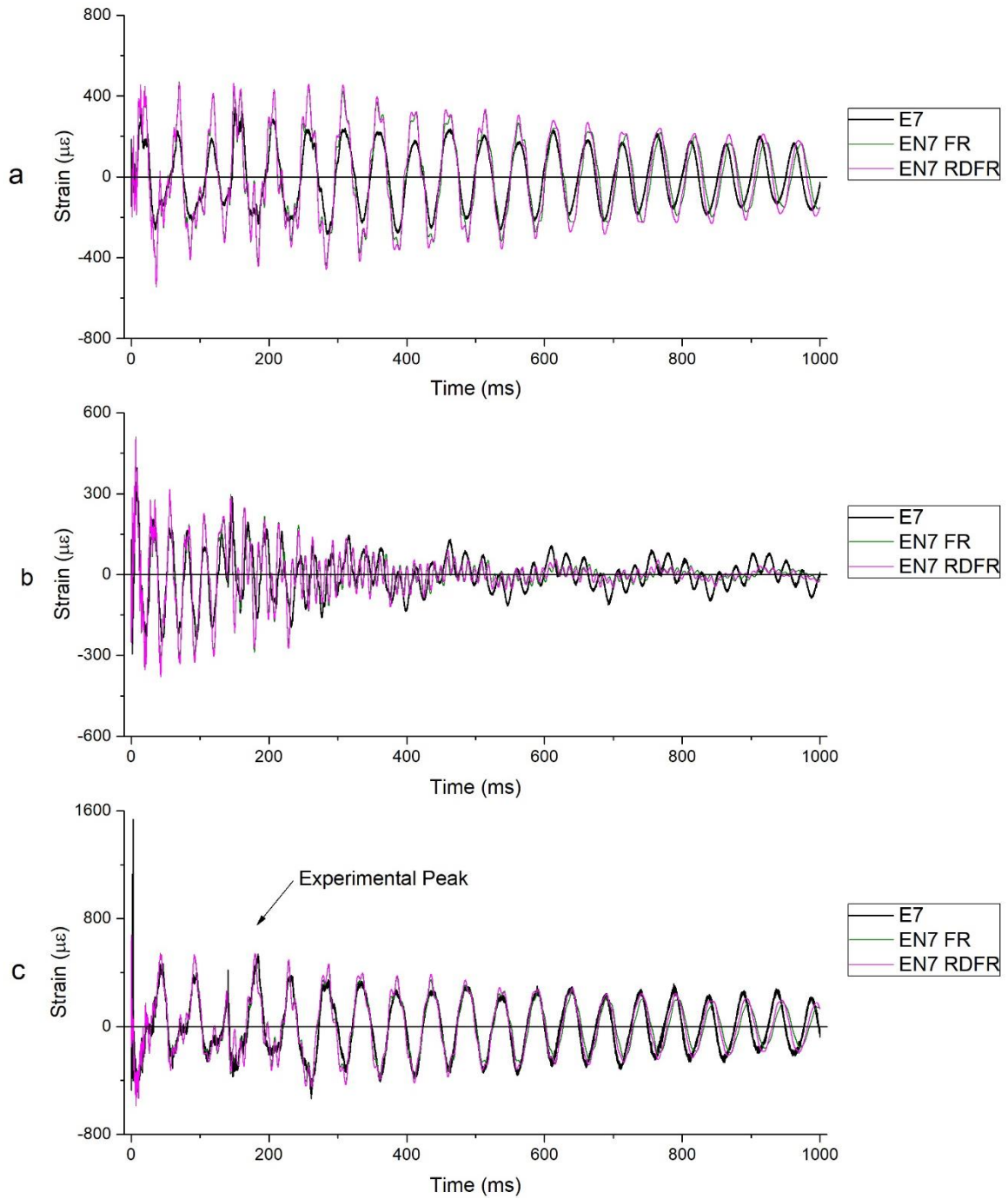
Figure 4-36 Comparison of EN7 FR and RDFR damping models at (a) forward, (b) amidships, and (c) aft for E7 (W = 250 g, R = 1.3 m, L = -4.3 m)
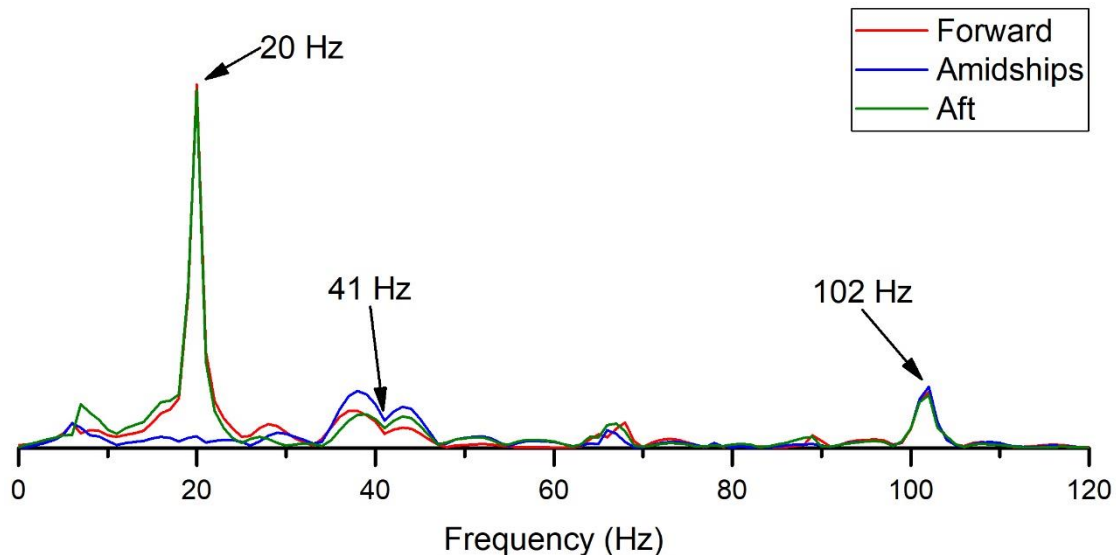
Figure 4-37 Frequency response for EN7 RDFR model

The EN8 UD and RD models compared well with the initial 80 ms of the E8 (*W = 43 g, R = 0.8 m, L = -4.3 m)* measurements but significantly over-predicted the response after this, including the overall peak whipping response, noted in Figure 4-38. All whipping peaks after the initial 80 ms contained large spikes which appear due to a substantial presence of the BM5 response, which was not observed in the E8 measurements. These models were not considered suitable for whipping analysis in this scenario.

The FR and RDFR models, shown in Figure 4-39, compared better to E8 in the late time whipping response but still over-predicted the early whipping responses between 80 and 350 ms. The maximum experimental response at 86 ms was over-predicted by the EN8 RDFR model by 36 %, noted in Table 4-10, and subsequent whipping peaks from these models even exceeded this value. This was the only scenario were there was a clear distinction between the FR and RDFR results, particularly at the amidships location in Figure 4-39b.

These errors from the early whipping response made it difficult to obtain an accurate value for the maximum whipping response from the EN models in this scenario. These spikes occur during the bubble loading of the UNDEX analysis, where the bubble pulse arrives at 79 ms. All comparisons show the EN8 RDFR model results compared well with the late time experimental whipping response, from 500 ms onwards. Based on this long-term accuracy the EN8 RDFR model was considered appropriate for further whipping studies, but caution was taken when assessing the peak responses during bubble loading for similar scenarios.
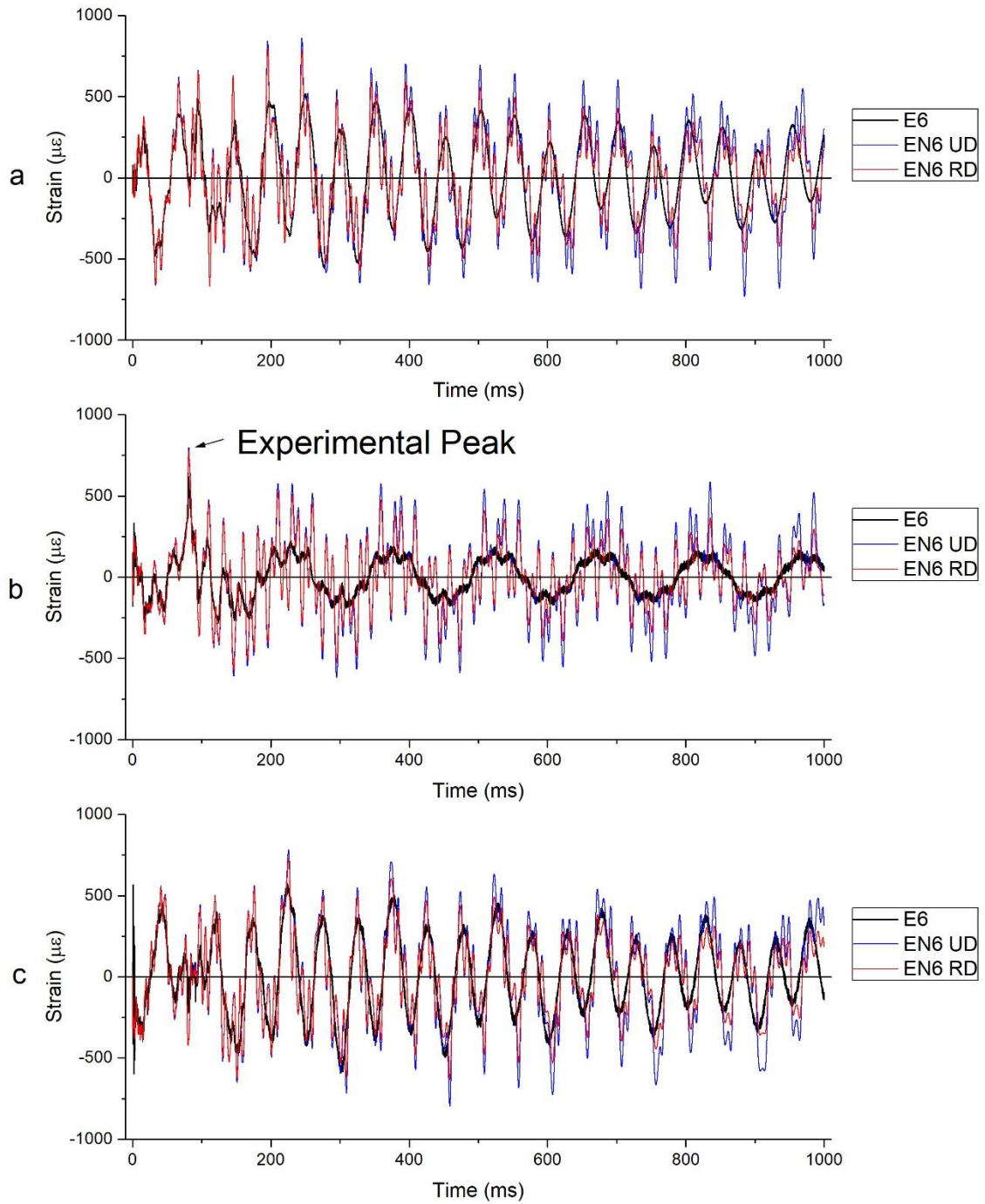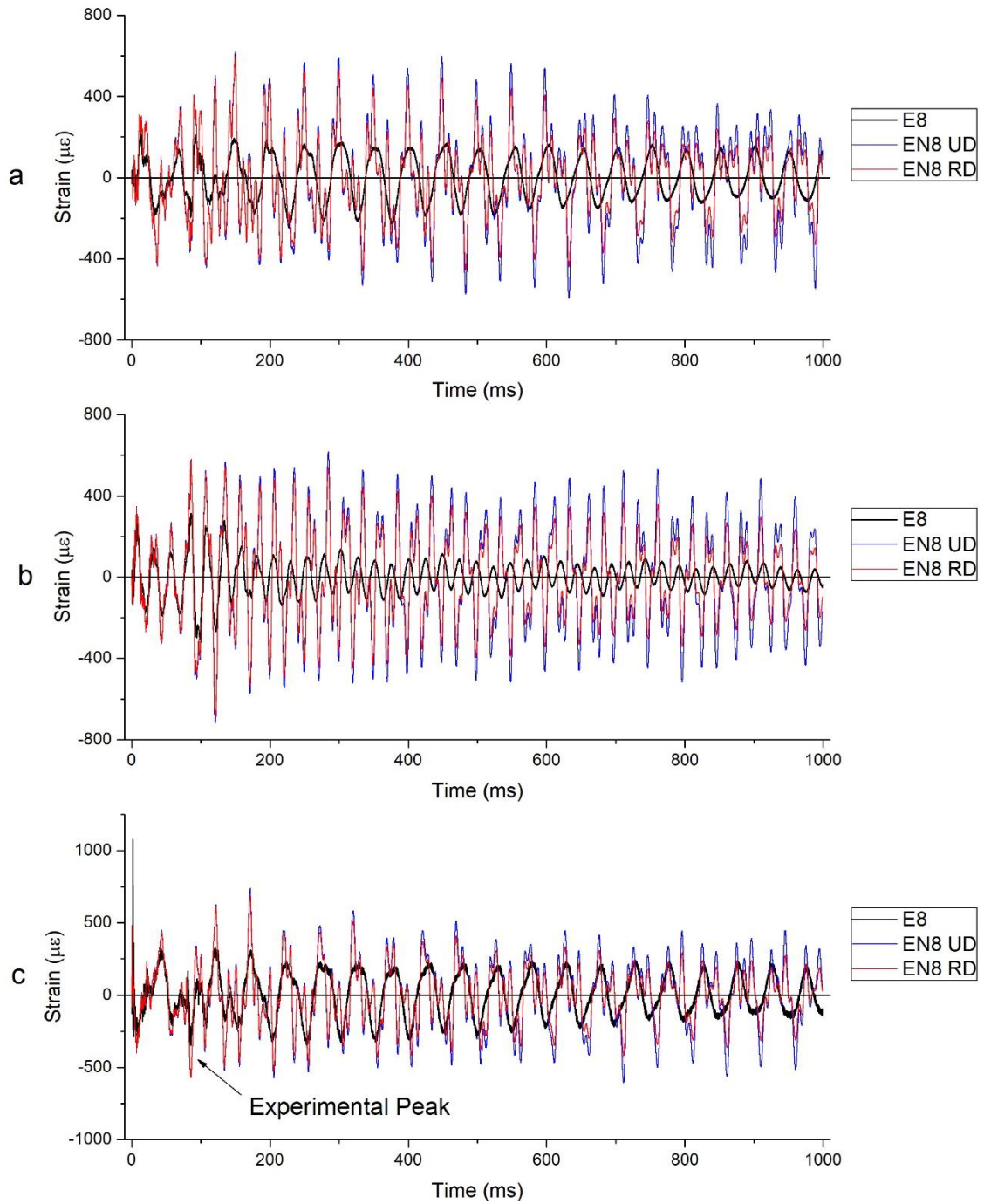
Figure 4-38 Comparison of EN8 UD and RD damping models at (a) forward, (b) amidships, and (c) aft for E8 (W = 43 g, R = 0.8 m, L = -4.3 m)
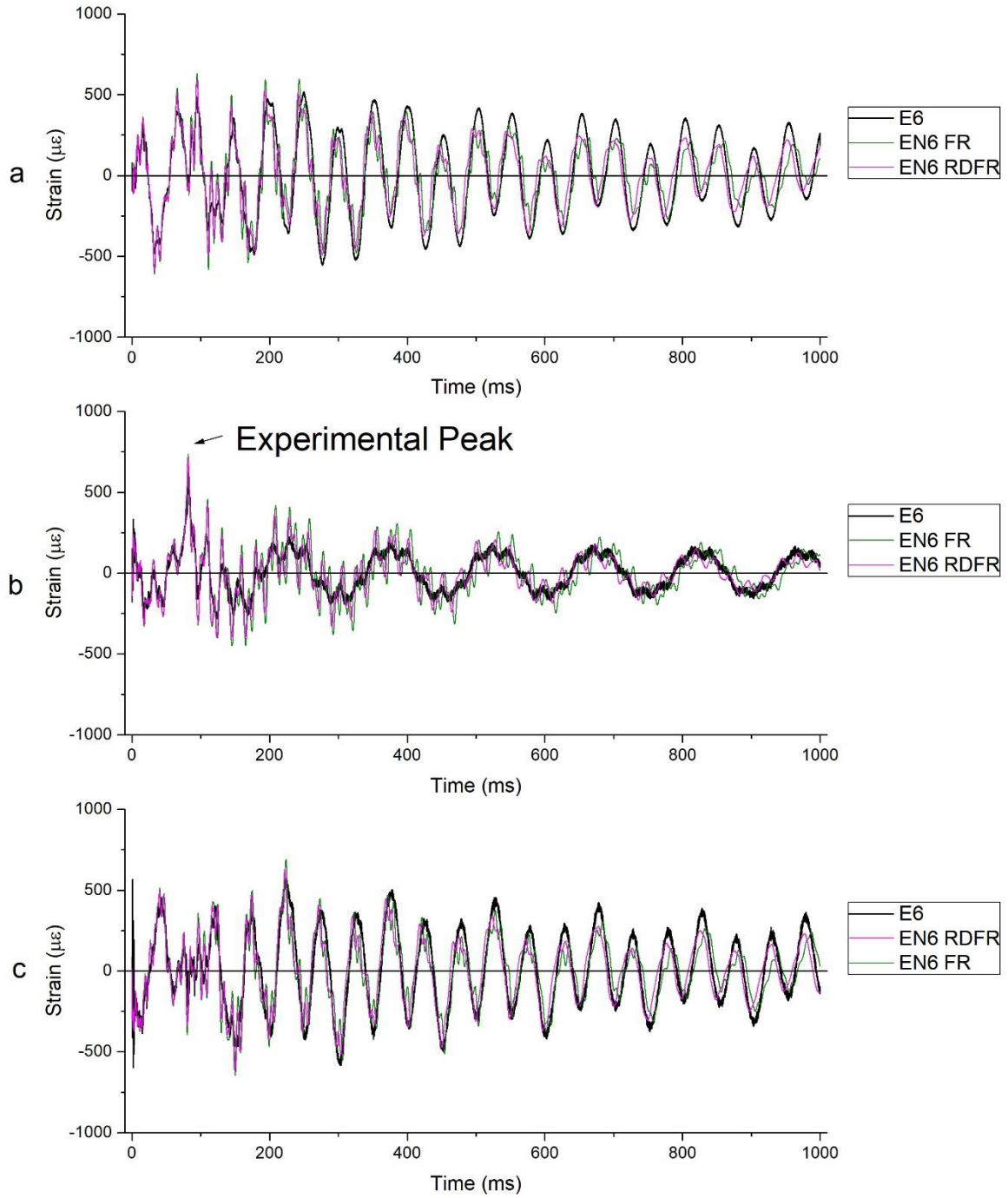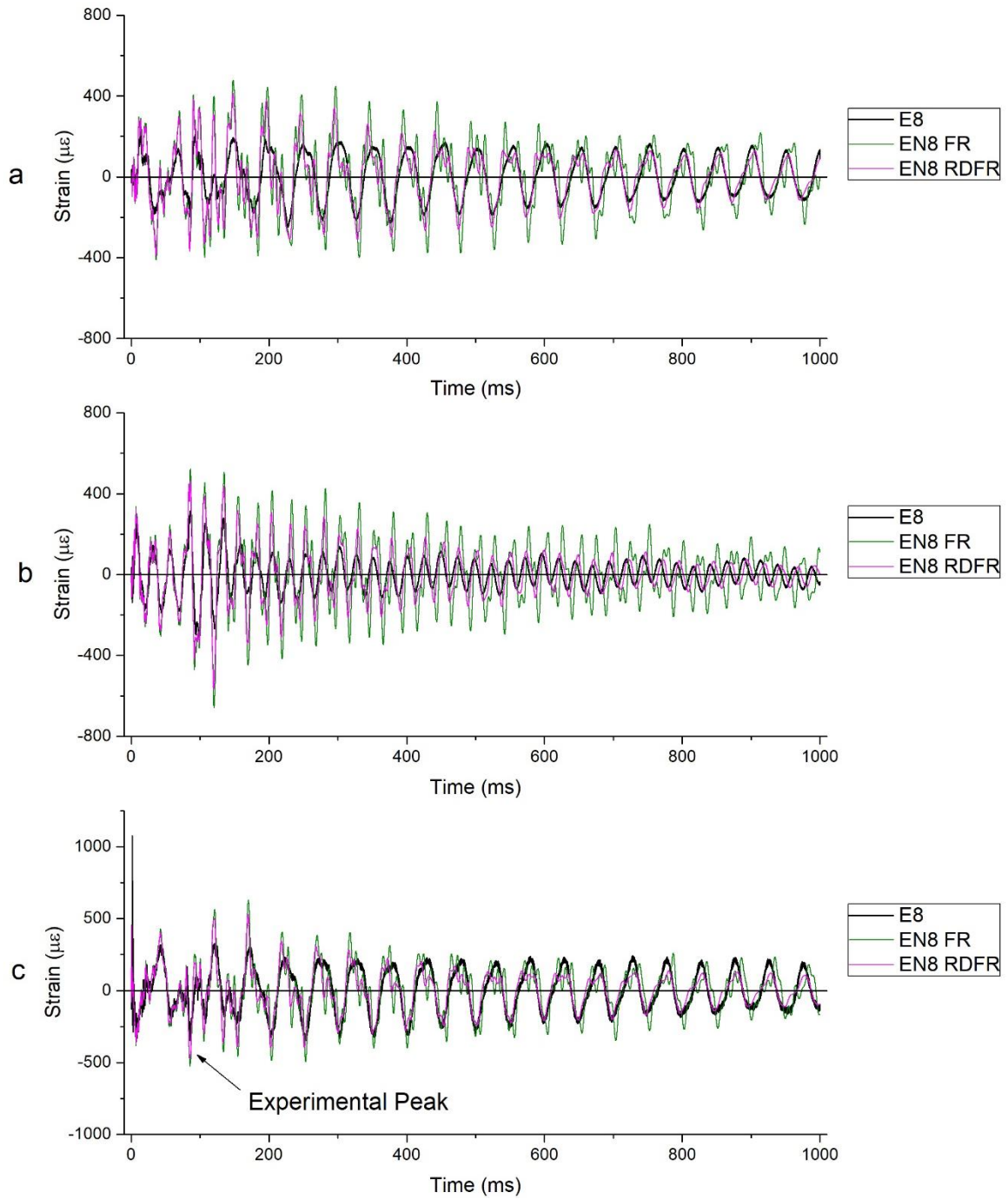
Figure 4-39 Comparison of EN8 FR and RDFR damping models at (a) forward, (b) amidships, and (c) aft for E8 (W = 43 g, R = 0.8 m, L = -4.3 m)
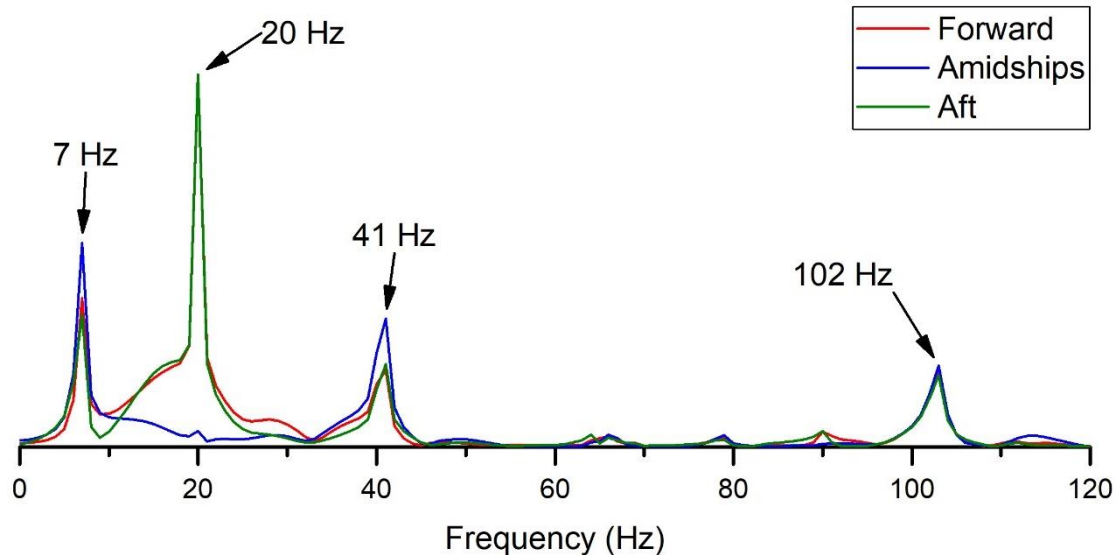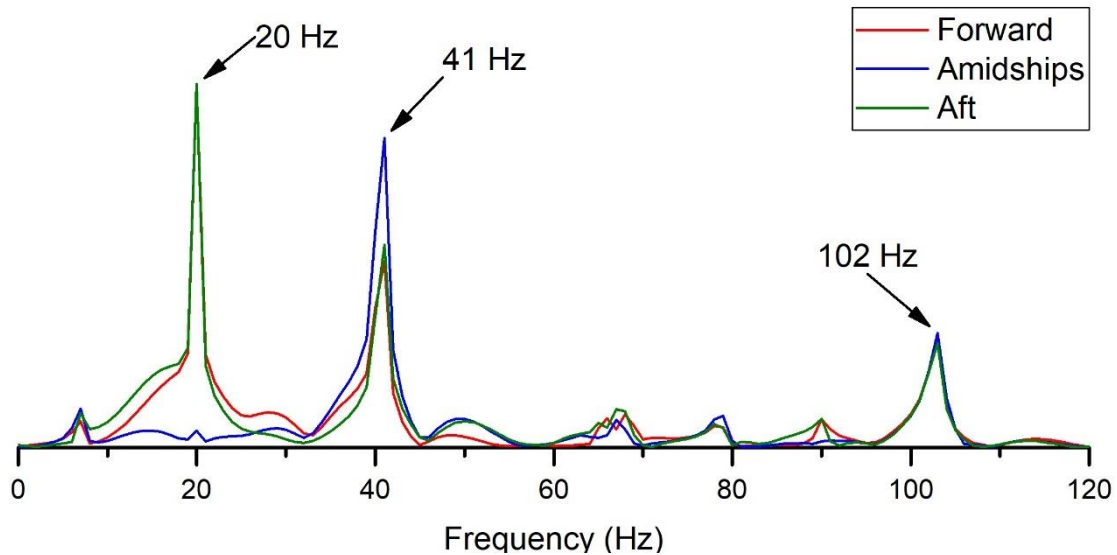
Figure 4-40 Frequency response for EN8 RDFR model

The peak strain from the whipping response is of interest for comparison to the bubble loading and therefore, the numerical model needs to accurately represent this value. As noted in the comparisons above, the peak whipping response from the numerical models often occurred at a different time than the experimental results and the numerical peak was generally larger than the experimental values. For a one-to-one comparison the peak responses from each experimental event E is listed in Table 4-10 and the numerical results at the same moment in time and location are also presented from each damping model with the percentage difference to the E results Δ also listed. This comparison shows that the FR and RDFR models tended to slightly under-predict the peak experimental value. From this quantitative comparison, it is clear that the UD and RD models do not provide acceptable results, particularly with the E8 scenario (*W = 43 g*, *R = 0.8 m*, *L = -4.3 m*). The FR and RD models compared better, and both had similar discrepancies from the experimental results in most scenarios. However, the FR model was still largely inaccurate for the E8 scenario, as demonstrated in both the transient comparison in Figure 4-39 and the 51 % difference to the experimental value in Table 4-10. The RDFR model also had a large difference in peak response for E8, with a difference of 36 %; however, it was shown to perform far better in the transient comparison in Figure 4-39. Therefore, the RDFR model was selected as the preferred numerical damping method to conduct further whipping analysis, with consideration of the aforementioned discrepancies in any similar scenarios.

Table 4-10   Comparison of EN responses at the largest E response time and location

Event	E (με)	UD (με)	Δ (%)	RD (με)	Δ (%)	FR (με)	Δ (%)	RDFR (με)	Δ (%)
1	1239	1375	11	1296	5	1160	-6	1150	-7
2	1509	1734	15	1638	9	1468	-3	1454	-4
3	1806	2058	14	1943	8	1764	-2	1727	-4
4	852	904	6	884	4	842	-1	820	-4
5	1259	1490	18	1407	12	1263	0	1183	-6
6	621	798	29	780	26	734	18	715	15
7	535	677	27	655	22	528	-1	542	1
8	347	573	65	568	64	525	51	473	36
Average[5]			23		19		10		10

---

[5] Calculated using the absolute Δ value

Platform response

With the numerical model it was now possible to visually demonstrate the modal responses of the platform and compare these with the modal responses that were interpreted from the strain records in the experimental investigation. As noted previously, most numerical results had their peak response occur at a different time, and in some cases a different location, than what was observed in the experimental investigation. Contour plots of the longitudinal strain response at the time of both the experimental and numerical peaks are presented, to validate if the maximum responses from the numerical model were qualitatively similar to the experimental responses for each scenario. **All contour plots present Y-strain values, which refer to the shell element coordinate system (defined in Figure 4-5) and <u>NOT</u> the global coordinate system Y-axis**. The units of the following plots are presented in meters-kilograms-seconds (MKS) and the longitudinal strain contours are dimensionless strain values.

For events E1 – E3 (*W = 250 g, L = 0.0 m*), the experimental and numerical maximums occurred at 168 ms and 252 ms respectively. The longitudinal strain contour plots for the EN3 peak responses from the experimental (Figure 4-41) and numerical (Figure 4-42) peak times show that the dominant response was bending, with peak deflection occurring at amidships, a characteristic property of BM1. The difference between experimental and numerical events was simply the absolute minimum and maximum peaks of the same whipping cycle. Therefore, the model responses are qualitatively the same as the experimental observations for these scenarios.

Figure 4-41 Longitudinal strain at element integration points at the time of the experimental peak response from EN3 RDFR (t = 168 ms). View from top of platform.

Figure 4-42 Longitudinal strain at element integration points at the time of the numerical peak response from EN3 RDFR (t = 252 ms). View from top of platform.

For event E4 (*W = 43 g, L = 0.0 m*) there was a difference in the time and location of the peak responses between the experimental (Figure 4-43) and numerical (Figure 4-44) results. At the experimental peak, the maximum tensile and compressive strains occurred on the same sides

at both the forward and aft ends, a characteristic feature of the symmetric BM3. The absence of the amidships peak can be explained by the superposition of the BM1 response, cancelling out the peak contribution at the amidships location. The EN4 peak occurred at amidships, slightly after the E4 peak at the aft location, and demonstrated a bending strain distribution only at the amidships location. However, the bending response was more localised in this scenario compared to the BM1 response in Figure 4-42. Therefore, this is also likely due to the BM3 response, with the superposition of BM1 cancelling out any significant contribution in the forward and aft ends. Based on these observations, the different E4 and EN4 peak responses are from the same whipping cycle and are qualitatively the same result for this scenario.

Figure 4-43 Longitudinal strain at element integration points at the time of the experimental peak response from EN4 RDFR (t = 82 ms). View from top of platform.
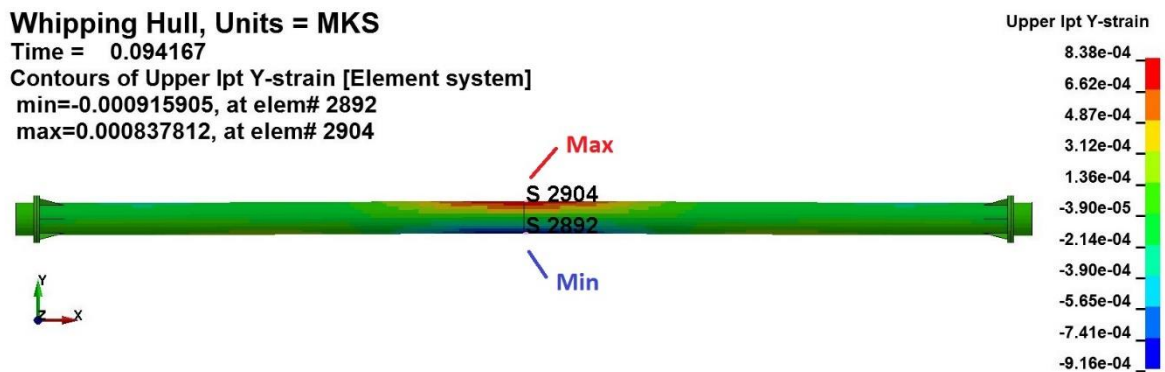
Figure 4-44 Longitudinal strain at element integration points at the time of the numerical peak response from EN4 RDFR (t = 94 ms). View from top of platform.

The peak response for E5 (*W = 250 g, L = -2.8 m*) occurred at the forward end in both the experimental (Figure 4-45) and numerical (Figure 4-46) results. The strain response is a characteristic bending response, and its location for both experimental and numerical peaks corresponds with the BM2 shape. The absence of a similar magnitude response in the aft end of anti-symmetric BM2 is likely due to the superimposed BM1 in the response. The EN5 peak response shows the same distribution with opposing tensile and compressive responses. Due to this behaviour and the time at which these responses occurred, the E5 and EN5 peak responses are from the same whipping cycle and therefore these results are qualitatively the same for this scenario.
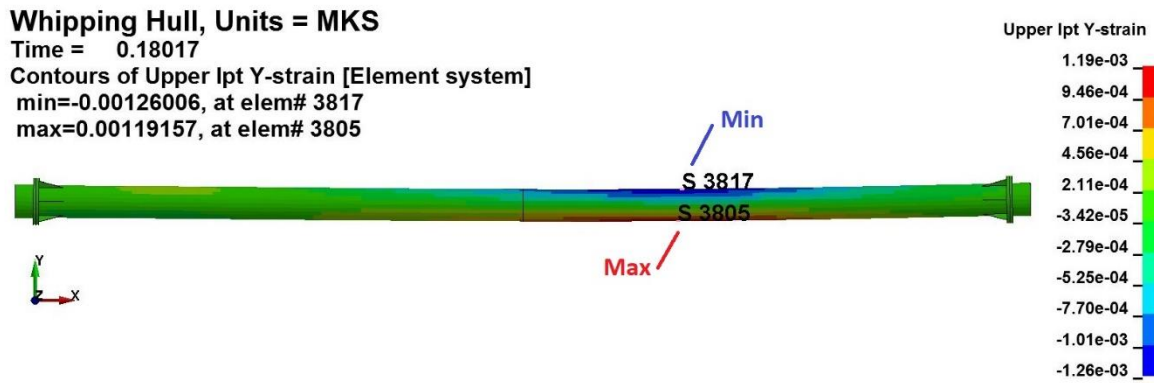
Figure 4-45 Longitudinal strain at element integration points at the time of the experimental peak response from EN5 RDFR (t = 180 ms). View from top of platform.
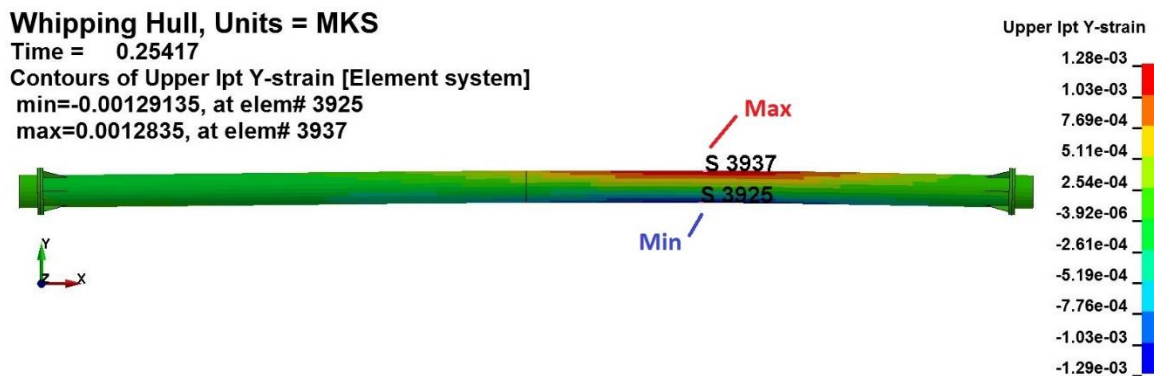
Figure 4-46 Longitudinal strain at element integration points at the time of the numerical peak response from EN5 RDFR (t = 254 ms). View from top of platform.

Both the experimental and numerical peak results occurred at the same time and location for E6 (*W = 43 g, L = -2.8 m*), shown in Figure 4-47. The peak response was slightly offset from amidships and demonstrates a bending response. The distribution of the bending strain was similar to that seen from E4 in Figure 4-44, and therefore is likely due to the BM3 response. The absence of additional peaks is due to the superimposed BM1 response, cancelling out the BM3 responses at these locations.
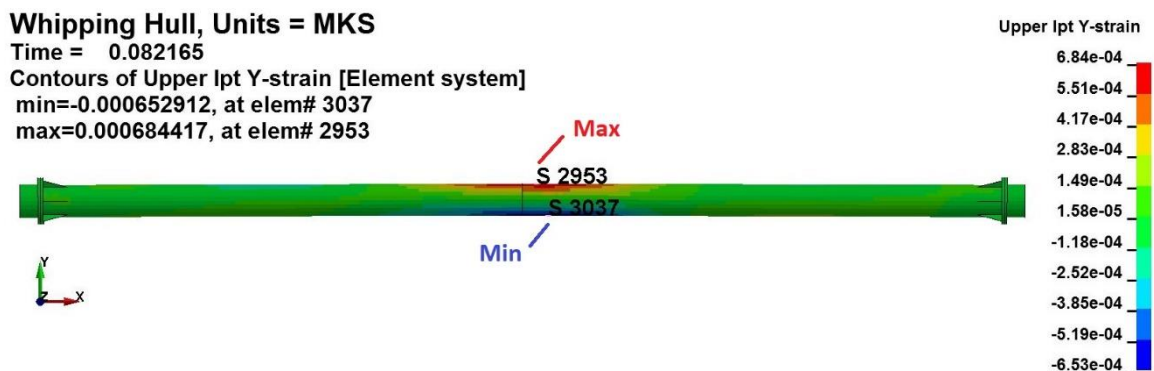
Figure 4-47 Longitudinal strain at element integration points at the time of the peak response from EN6 RDFR (t = 82 ms). View from top of platform.

The peak responses from the E7 (*W = 250 g, L = -4.3 m*) in Figure 4-48 and EN7 in Figure 4-49 were completely different. The E7 peak demonstrated a bending response at the aft end, with a lower magnitude and opposite bending response at the forward end. This is characteristic

of the BM2 response. In contrast, the EN7 peak occurred much earlier at 18 ms. It also demonstrated a bending response, however this occurred at the forward end and the smaller strain distribution suggests this was due to BM3. It is indeed possible that this was the true peak response of this event, as it demonstrates the similar whipping behaviour that was seen in E5. It is however unlikely that strain levels were as high as the numerical model suggests, given it was previously noted that the numerical model over-predicted the early whipping responses for this scenario. Based on this response comparison, the peak responses were qualitatively different. However, it was previously demonstrated that the long-term transient response was accurate for this scenario. This model is considered suitable for further numerical studies, but caution was taken for any early time peak responses in similar scenarios.
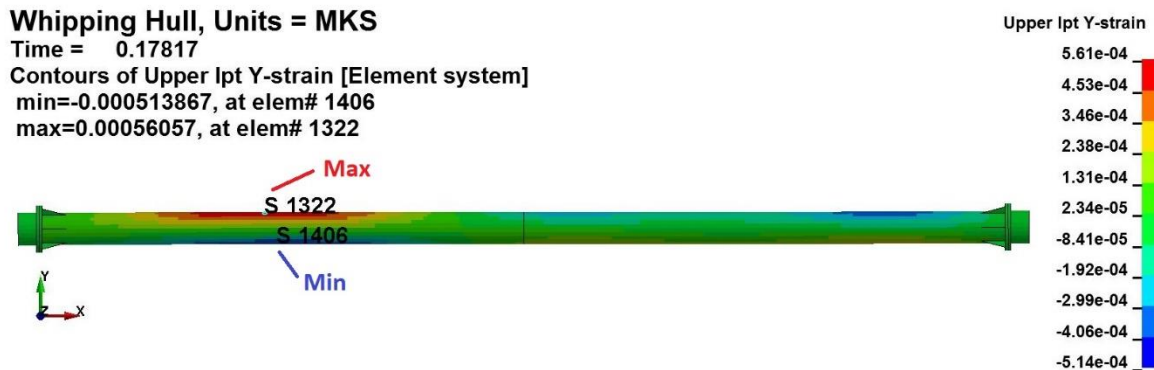
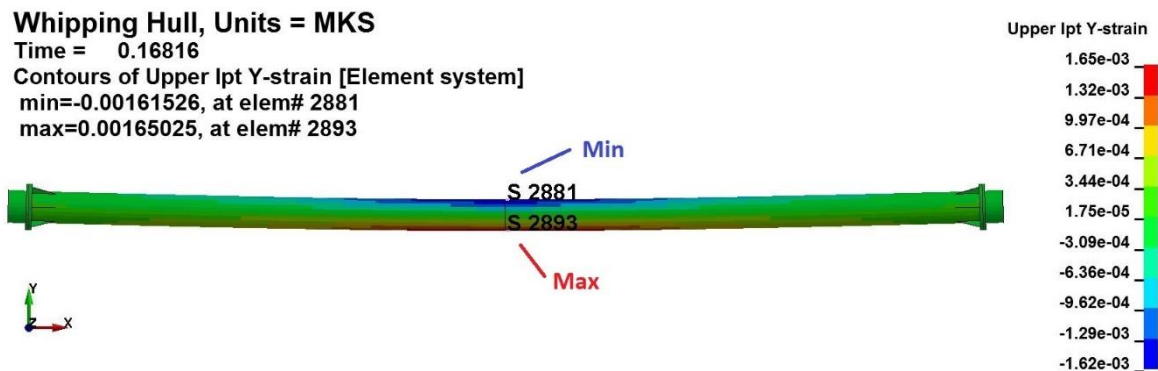*Figure 4-48 Longitudinal strain at element integration points at the time of the experimental peak response from EN7 RDFR (t = 178 ms). View from top of platform.*
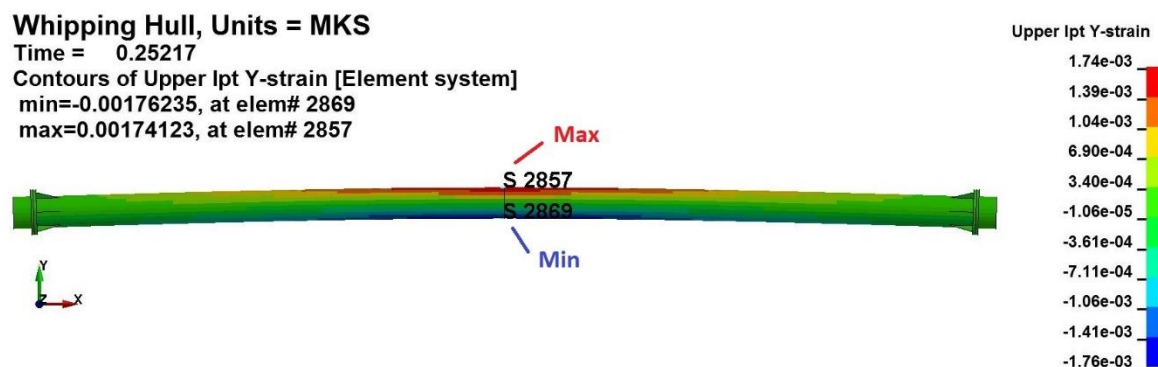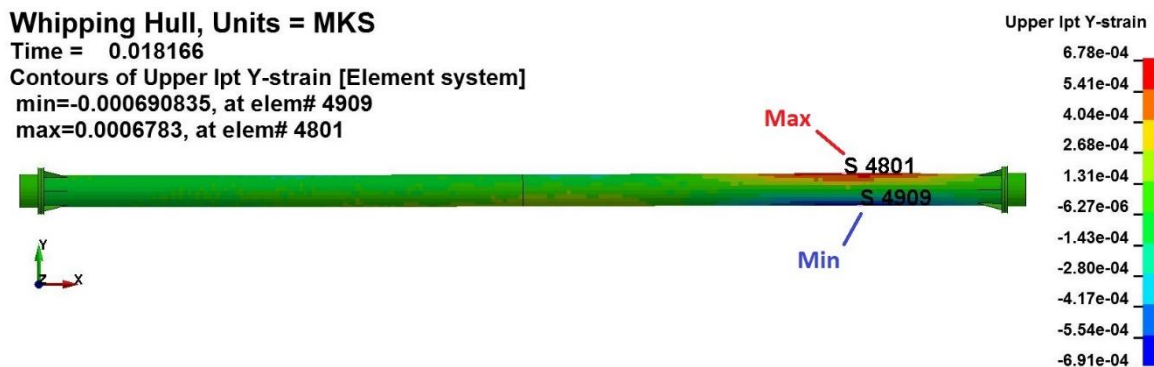

Figure 4-49 Longitudinal strain at element integration points at the time of the numerical peak response from EN7 RDFR (t = 18 ms). View from top of platform.

The platform response at the time of the peak experimental response for E8 (*W = 43 g, L = -4.3 m*), shown in Figure 4-50, demonstrated the characteristic three alternating peaks that are symmetric about amidships for the BM3 response. The peak responses occurred at the aft end closest to the charge stand-off location. The numerical peak response, shown in Figure 4-51, occurred later at 96 ms and also demonstrated the BM3 response, but the peak occurred at the forward end and the peaks were the inverse of the experimental response shape. From this behaviour, these responses were determined to be from the same whipping cycle but there was a substantial difference in the response magnitude. The response shape is likely real but given the significant over-prediction that was noted in this scenario during the timeframe of 80 – 350 ms, and the behaviour from other 43 g charge events, it is unlikely the numerical response peak is accurate. Based on this comparison, the whipping response results were qualitatively the same for this scenario, but the magnitude was not. Caution will be taken when assessing similar responses from numerical study scenarios.
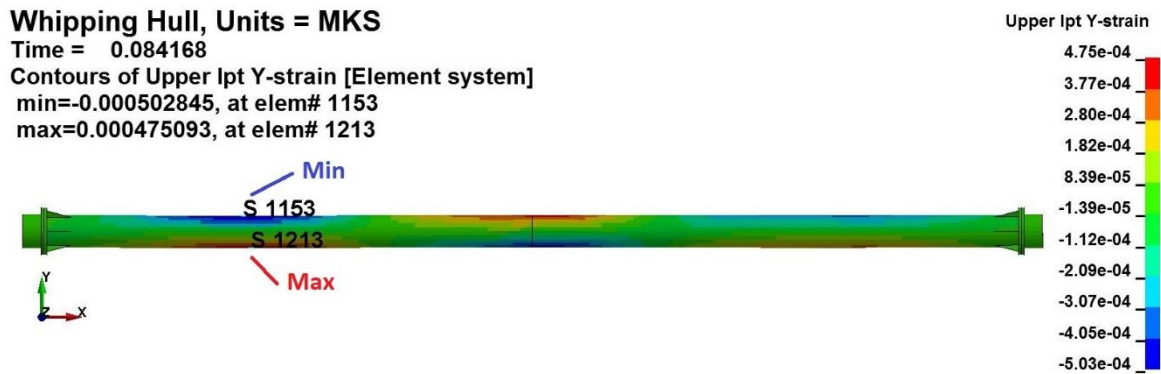
Figure 4-50 Longitudinal strain at element integration points at the time of the experimental peak response from EN8 RDFR (t = 84 ms). View from top of platform.
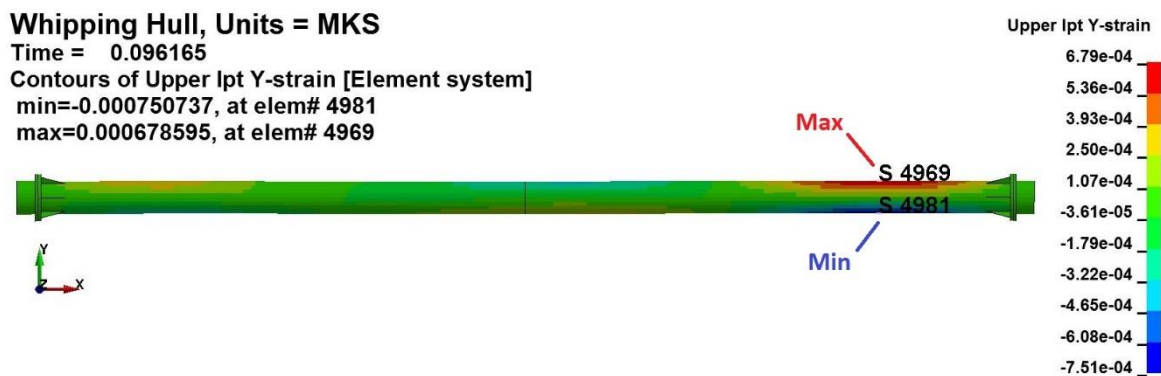
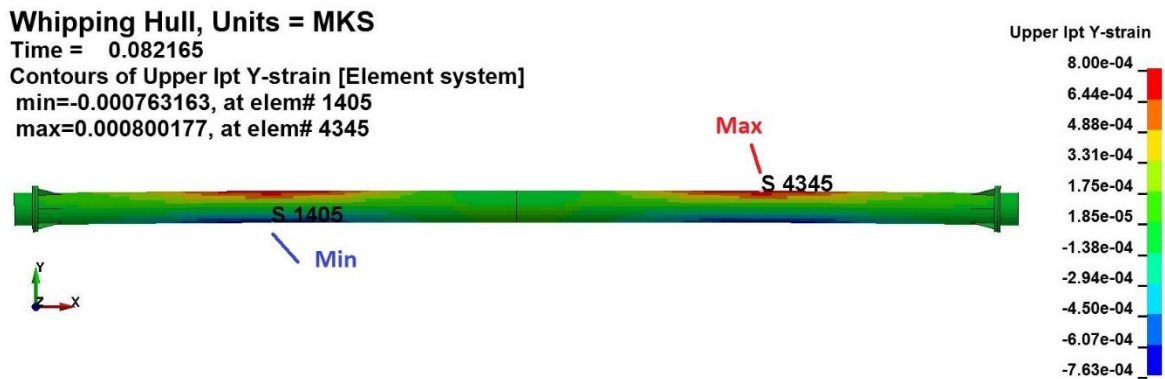*Figure 4-51 Longitudinal strain at element integration points at the time of the experimental peak response from EN8 RDFR (t = 96 ms). View from top of platform.*

## 4.4. Conclusion

A finite element model of an experimental submerged platform was created and validated against experimental scenarios. The finite element structure was built using LS-Dyna and the underwater environment and UNDEX loading was implemented using the boundary element method of the USA code. The empirical PHS-BUB model was used to simulate the UNDEX loads and incident pressure time histories compared well with the experimental measurements.

A modal analysis was performed on the numerical model. The first three BM compared well with those measured in the experimental investigation. This indicated that the FE model structure and added mass calculation of the USA BEM provided a suitable representation of the experimental test platform. Additional bending and circumferential modal responses of the submerged platform were identified and presented from the numerical model.

UNDEX loads were calculated by the USA code using the PHS-BUB model. Updates to the USA code since previous analysis of the submerged platform have improved its accuracy. Comparisons of the incident pressure from different TNT equivalence factors found that the 250 g and 43 g charge sizes required different equivalence factors of 1.11 and 1.19 respectively. Comparisons of the integrated incident pressure time histories found that the PHS-BUB model overpredicted the total pressure impulse by 13 – 29 %, but accurately replicated the transient pressure impulse of the first bubble cycle.

Four damping methods were assessed for a transient whipping analysis: undamped, Rayleigh damping, frequency range damping, and a combination of Rayleigh and frequency range damping. All models compared well with the initial whipping response and in most scenarios were able to capture the peak whipping response. For scenarios where the charge stand-off was located at the node of the first bending mode shape (E7 and E8), these early responses were over-predicted by all damping models.

For transient whipping responses the undamped model largely over-predicted the peaks of all whipping cycles, demonstrating that some form of damping was required for a transient whipping analysis. On its own, Rayleigh damping did not provide sufficient damping for any scenario. This was likely due to the absence of any external damping mechanism in the numerical model. Frequency range damping was applied as a surrogate for both the internal and external damping and compared well with most experimental results. However, this method occasionally introduced errors in the natural frequency response of the platform, which made it inaccurate for some long duration transient whipping analyses, particularly for frequency response assessment comparisons. This model was also unable to damp out higher frequency responses that were exaggerated by the explicit modelling environment, which caused some scenarios to be over-predicted.

A combined damping method was implemented using the mass damping term from the Rayleigh model to damp the first bending mode frequency, combined with a lower critical damping factor in the Frequency Range Damping model across a spectrum of 40 – 120 Hz. This method provided similar accuracy to the FR model for early time responses but performed better for late time responses and produced the best comparison for all scenarios. Due to the accuracy of this combined damping model, it was selected for use in further numerical studies, with caution taken for noted inaccuracies of specific scenarios.

Chapter 5. Further numerical studies

5.1 Introduction

The experimental investigation reported in Chapter 3 identified that the charge size W, stand-off distance R and location along the platform length L all influenced the whipping response of a submerged platform. In Chapter 4 a fluid-structure interaction numerical model capable of simulating these whipping responses was developed and validated using the experimental data. In the present chapter the validated numerical model is used to perform a numerical investigation, to explore further iterations of these variables in a set of numerical studies.

These studies also explore the absolute contribution of the shock wave and bubble loading on the whipping response. This is demonstrated by using an idealistic shock-only loading model. The assumed shock-only loading demonstrates an inherent assumption of analysis methods that focus on the shock response which may neglect the bubble loading contribution and under predict the severity of the whipping response.

5.2 Numerical study methodology

The validated numerical model from Chapter 4 was used to conduct the three numerical studies, detailed in the following sections. The combined Rayleigh and Frequency Range damping (RDFR) model was applied to all analyses of these numerical studies.

The previously validated PHS-BUB model was used with updated parameters as required by each study. From the numerical validation in Chapter 4, it was determined that different TNT equivalent factors were required for each charge size. A TNT equivalence factor of 1.11 was used for 250 g events and 1.19 was used for 43 g events.

5.2.1 Stand-off distance study

From the original eight experimental UNDEX scenarios that were reported in Chapter 3 and numerically modelled in Chapter 4, 10 additional numerical scenarios (N1 – N10), listed in Table 5-1, were selected to examine the effect on the whipping response from different R distances at each of the L positions. In the original scenarios, only the 250 g charge at $L = 0.0\ m$ explored the effects on the whipping response from different R distances. It was found that different R distances did not affect the whipping response behaviour, only the severity.

Here, using the validated numerical model, both the 250 g and 43 g charge sizes were simulated at three R distances at each of the previously studied L positions (amidships, -2.8 m aft and -4.3 m aft). The additional stand-off distances were selected to provide a similar bubble proximity factor γ for each event. Bubble proximity limits of $2.00 > \gamma > 1.40$ were enforced to maintain assumptions that the bubble would not collapse on the boundary, so the USA BEM could still be used. SF values are also listed for comparison, calculated by Equation 2.3.

Table 5-1   Experimental gap study variables

Event	W (g)	R (m)	L (m)	γ	SF (kg$^{1/2}$/m)
N1	250	1.8	-2.8	2.00	0.28
N2	250	1.8	-4.3	2.00	0.28
N3	250	1.5	-2.8	1.67	0.33
N4	250	1.5	-4.3	1.67	0.33
N5	43	1.0	0.0	2.00	0.21
N6	43	1.0	-2.8	2.00	0.21
N7	43	1.0	-4.3	2.00	0.21
N8	43	0.7	0.0	1.40	0.30
N9	43	0.7	-2.8	1.40	0.30
N10	43	0.7	-4.3	1.40	0.30

The 250 g numerical events N1 – N4 were conducted at the same experimental *R* distances as the *L = 0.0 m* experimental events E1 – E3, but were relocated to *L = – 2.8 m* for N1 and N3, and *L = -4.3 m* for N2 and N4. These scenarios were selected to determine if the linear trend of the bubble pressure impulse and peak strain response from bubble loading identified in Figure 3-27 was valid at other *L* positions. The 43 g events N5 – N10 introduced additional *R* distances at the same *L* positions used in the experiment. Events N5 – N7 investigate a further stand-off distance of *R = 1.0 m*, while events N8 – N10 investigate a closer stand-off distance of *R = 0.7 m*. These events were selected to determine how the *R* distance affected the whipping severity for the 43 g charge events, and to also determine if the linear trend of the bubble pressure impulse and peak strain response from bubble loading from Figure 3-27 was also valid for the 43 g charge size.

5.2.2 Intermediate charge study

The original eight experimental UNDEX scenarios used a relatively large 250 g and a smaller 43 g charge in relation to the test platform's size. From these experimental results reported in Chapter 3, there were some significant differences between the whipping responses for each charge size. The larger 250 g charge generally excited lower BM and was usually dominated by the BM1 contribution, while the smaller 43 g charge always contained a large contribution from BM3. To further explore the effect that the charge size has on the whipping response, nine additional numerical scenarios (N11 – N19) were conducted using an intermediate 150 g charge size. The intermediate charge size introduces new bubble response parameters. The maximum radius *A*, relative size to the platform *λ*, first bubble period T_1 calculated from Equation 1.4 and the resulting frequency f_1 are listed in Table 5-2, with the previous charge size bubble properties from Table 3-3 also listed for comparison.

Table 5-2   Bubble parameters

W (g)	A (m)	λ	T_1 (ms)	f_1 (Hz)
250	0.90	4.5	140	7.2
43	0.50	2.5	78	12.9
150	0.76	3.8	117	8.5

For consistency with the other charge sizes, the 150 g charge was analysed at three *R* distances at the three previous *L* positions (amidships, -2.8 m aft and -4.3 m aft), detailed in Table 5-3 and arranged according to Figure 4-10. The stand-off distances were selected to provide similar

$γ$ to the original $W = 250$ g, $L - 0.0$ m events E1 – E3. The SF was also calculated using Equation 2.3, for comparison.

Table 5-3   Intermediate charge study variables

Event	W (g)	R (m)	L (m)	$γ$	SF ($kg^{1/2}$/m)
N11	150	1.5	0.0	1.98	0.26
N12	150	1.5	-2.8	1.98	0.26
N13	150	1.5	-4.3	1.98	0.26
N14	150	1.3	0.0	1.71	0.30
N15	150	1.3	-2.8	1.71	0.30
N16	150	1.3	-4.3	1.71	0.30
N17	150	1.1	0.0	1.45	0.35
N18	150	1.1	-2.8	1.45	0.35
N19	150	1.1	-4.3	1.45	0.35

As no experimental data was available to determine a TNT equivalence factor for the 150 g event, the calculated period of the first bubble cycle from Equation 1.4 (listed Table 5-2) was used to determine an appropriate TNT equivalence factor. Bottom effects were considered in all 150 g pressure models as the numerical validation in Chapter 4 found this affected the period for both of the original experiment charge sizes. A comparison of the incident pressures from different TNT equivalent factors is presented in Figure 5-1 and shows that the first bubble period of the 150 g charge was best represented by a 1.11 TNT equivalence.
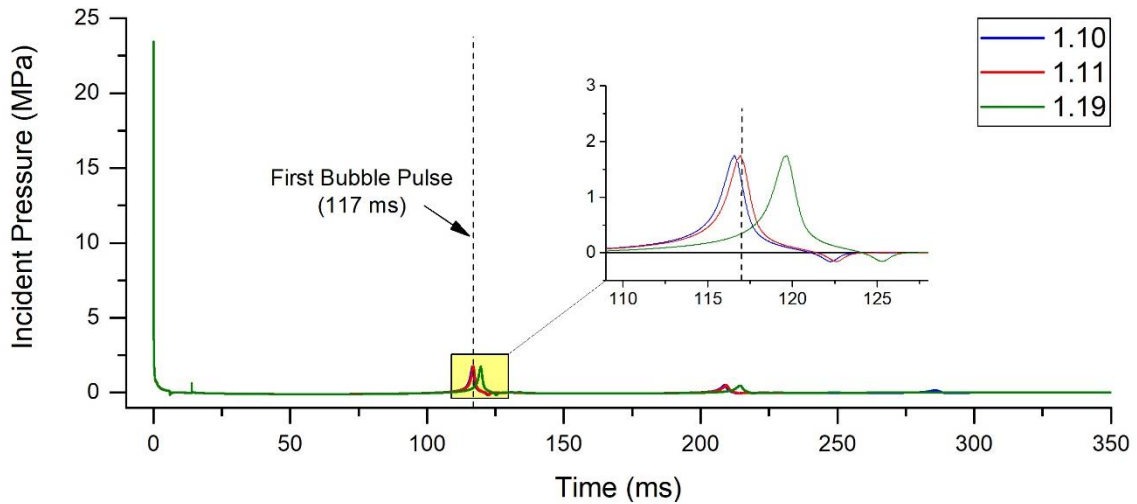
Figure 5-1   Comparison of incident pressures for different TNT equivalent factors for Pentolite (W = 150 g, R = 1.1 m)

5.2.3 Shock-only loading study

From the experimental investigation in Chapter 3 and the numerical validation in Chapter 4, it was observed that when the UNDEX event was located near the node of the BM1 shape the platform did not respond significantly to the bubble loading, and had a less severe whipping response. To demonstrate if this was the cause of the reduced whipping severity in events at the node of BM1 ($L = -4.3$ m), the three most severe events at each L position E3, E5, and E7 ($W = 250$ g, $R = 1.3$ m), were analysed using a shock-only loading model. It was assumed that with the absence of bubble loading, any whipping response from this could be attributed entirely to the shock wave loading. This shock-only loading scenario is also representative of any analysis method that only considers the shock response in a platform's assessment. Should

results from this loading under-predict the whipping response, it will demonstrate that assessment methods based on shock response methodologies are not suitable for conducting a whipping analysis. The details of the three numerical shock-only analyses (NS1 – NS3) are listed in Table 5-4 and arranged as shown in Figure 4-10.

Table 5-4   Shock induced whipping study variables

Event	W (g)	R (m)	L (m)	SF
NS1	250	1.3	0.0	0.28
NS2	250	1.3	-2.8	0.28
NS3	250	1.3	-4.3	0.28

These three events were selected as E3 (*L = 0.0 m*) demonstrated the most severe whipping response overall, E5 (*L = -2.8 m*) demonstrated the unique example of the peak whipping response at the opposite end to *L* position on the platform, and E7 (*L = -4.3 m*) did not appear to have any significant response due to the bubble loading. It was expected that NS1 and NS2 would not reach the same whipping severity as their respective bubble loaded counterparts E3 and E5, while NS3 would have a similar whipping response to E7.

For this study, the USA loading was applied using the previously validated PHS-BUB model described in Chapter 4. The PHS-BUB model was cut-off after the initial shock wave and reflection loads, as shown in Figure 5-2, to create the idealistic shock-only loading.
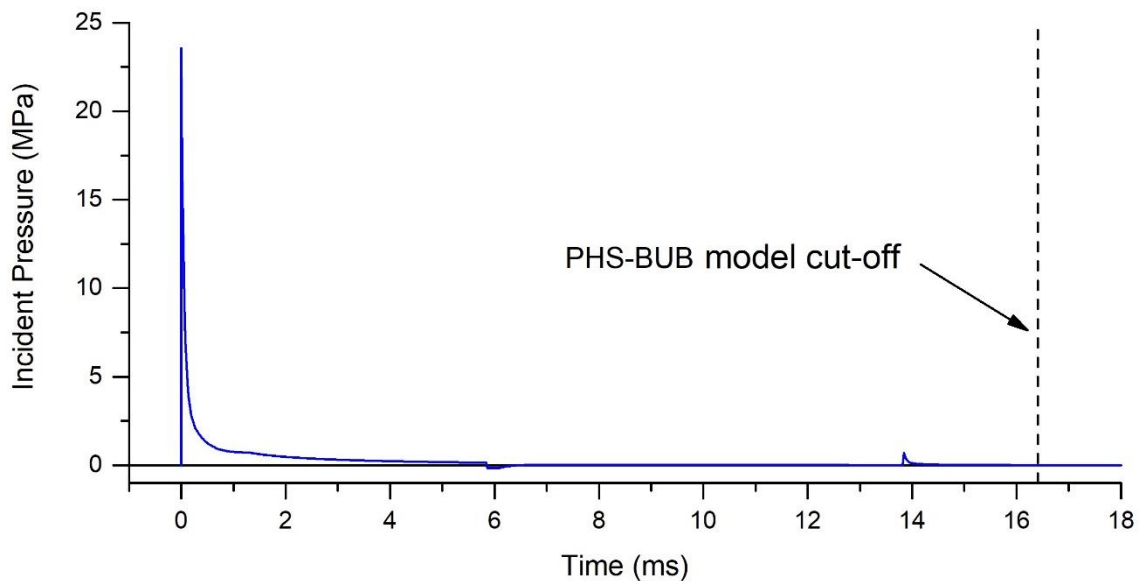
Figure 5-2   Shock-only loading study incident pressure (W = 250 g, R = 1.3 m)

5.3 Study results

5.3.1 Stand-off distance study

From the experimental investigation it was shown that the reduced *R* distance between events E1 – E3 (*W = 250 g, L = 0.0 m*) only affected the whipping strain levels, and that the modal responses were qualitatively the same. The following results discuss the effects of R distance for each charge size and *L* position at the most severe locations on the platform.

The most severe response of events EN5, N1, and N3 (*W = 250 g* at *L = -2.8 m*) occurred at the forward location, which is compared in Figure 5-3. From this comparison it is clear that the

modal responses were qualitatively the same for all these events, demonstrating that like the experimental $L = 0.0$ m events, the R distance had no effect on the modal response. The peak response of all events also occurred at the forward location despite the aft L position, similar to what was previously identified in E5 during the experimental investigation in Chapter 3. This indicates that this form of whipping is not dependent on the R distance for the bubble proximity range of $1.45 < \gamma < 2.00$ and relative size of $\lambda = 4.5$.

The furthest event N1 ($R = 1.8$ m) had the least severe whipping response. The intermediate event N3 ($R = 1.5$ m) was 27 % larger than N1, while the closest and most severe event EN5 ($R = 1.3$ m) was 51 % larger than N1. There was little difference between N3 and EN5 peaks during the later whipping responses, where N3 was only marginally lower, while the furthest event N1 was always noticeably lower.
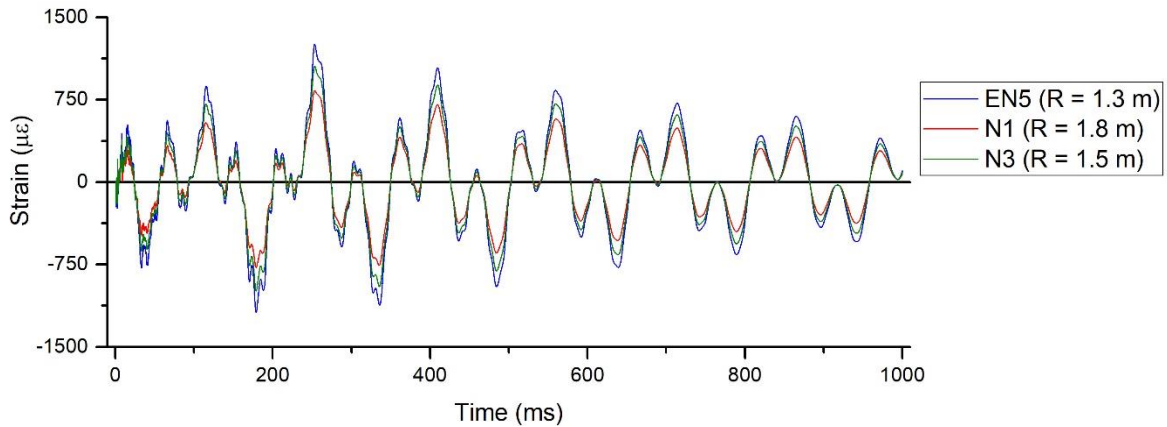
Figure 5-3   Forward whipping responses from events N1, N3, and EN5 (W = 250 g, L = -2.8 m)

The aft responses were the most severe for events EN7, N2, and N4 ($W = 250$ g, $L = -4.3$ m), which are compared in Figure 5-4. From this comparison not only were the modal responses qualitatively similar, but there was also only a small variation in the peak responses. This comparison suggests that the bubble loading does not seem to significantly influence the whipping in the proximity range of $1.45 < \gamma < 2.00$ and for a relative size of $\lambda = 4.5$.

In relative comparison, the least severe event was N2 ($R = 1.8$ m) at the furthest R distance. The peak response from the intermediate event N4 ($R = 1.5$ m) was 25 % larger than N2, while the closest event EN7 ($R = 1.3$ m) was 53 % larger. Outside of these peak responses, there was little variation between each R distance for $W = 250$ g at $L = -4.3$ m.
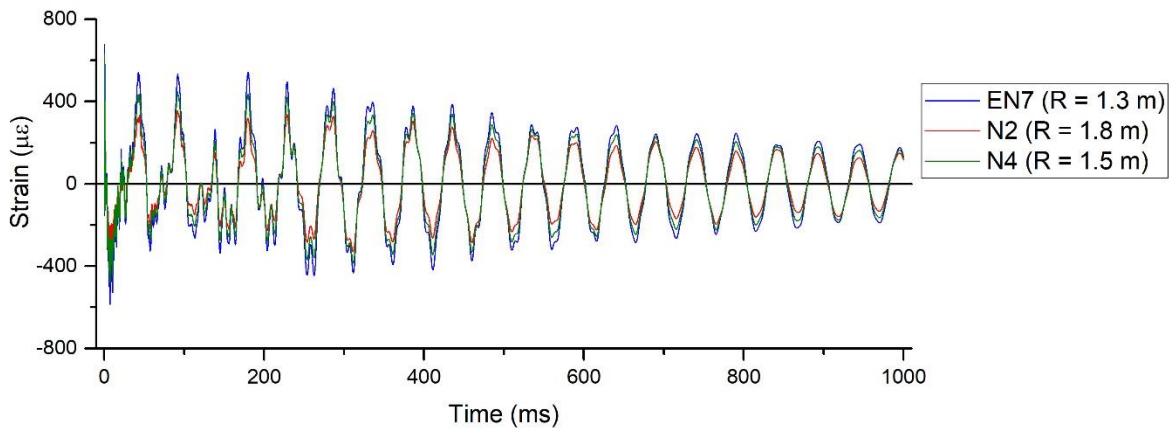
Figure 5-4   Aft whipping responses from events N2, N4, and EN7 (W = 250 g, L = -4.3 m)

The amidships responses were the most severe for events EN4, N5, and N8 ($W = 43$ g, $L = 0.0$ m) which are presented in Figure 5-5. The modal responses of all events were found to

be qualitatively the same, indicating that for a bubble proximity of *1.40 < γ < 2.00* and for a relative size of *λ = 2.5*, the *R* distance had no effect on the modal response. This suggests that the noticeable contribution of BM3 for *W = 43 g, L = 0.0 m* events, that is absent in *W = 250 g* events, is likely due to the charge and relative bubble size.

As with previous comparisons, the furthest event N5 (*R = 1.0 m*) produced the least severe whipping response. The intermediate event EN4 (*R = 0.8 m*) was 33 % larger than N5, while the closet event N8 (*R = 0.7 m*) was 55 % larger.
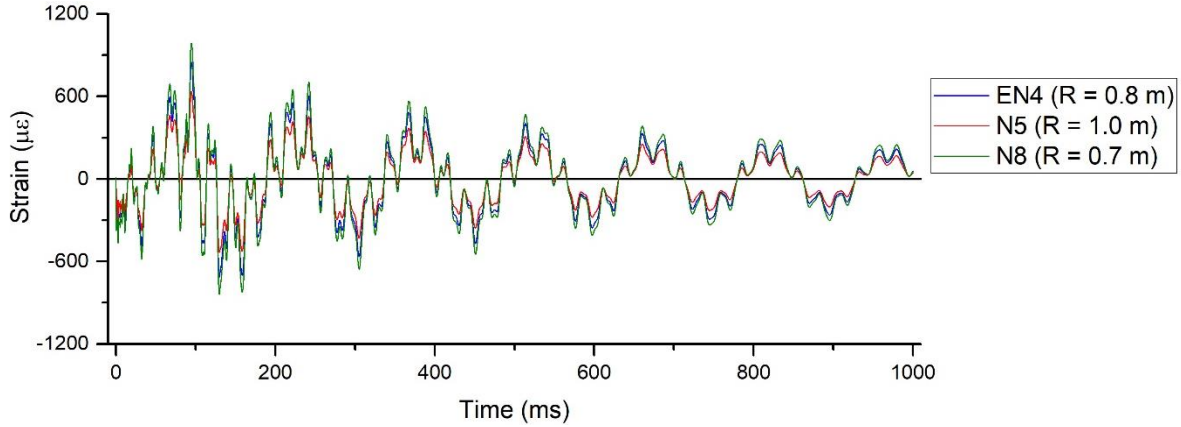
Figure 5-5   Amidships whipping responses from events N5, N8, and EN4 (W = 43 g, L = 0.0 m)

The aft responses were the most severe from events EN6, N6, and N9 (*W = 43 g, L = -2.8 m*) events and are compared in Figure 5-6. The furthest event N6 (*R = 1.0 m*) produced the least severe whipping response. The intermediate event EN6 (*R = 0.8 m*) was 27 % larger than N6, while the closet event N9 (*R = 0.7 m*) was 45 % larger.
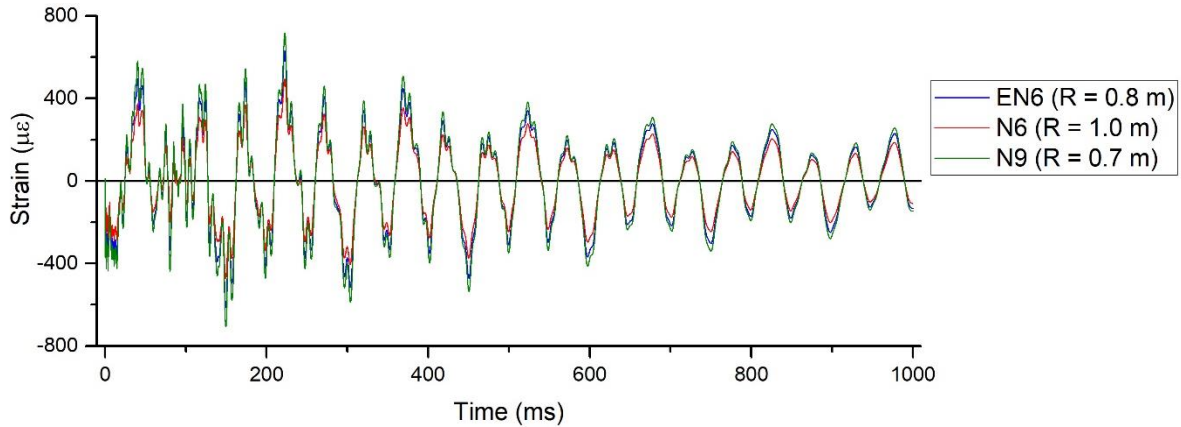
Figure 5-6   Aft whipping responses from W = 43 g, L = -2.8 m events

For events EN8, N7, and N10 (*W = 43 g*, *L = -4.3 m*) the aft response was the most severe. Comparing the response at this location from these events in Figure 5-7 it is shown that the late time response from this scenario was very similar for all *R* distances. From the validation of the model in Chapter 4, it was found that the early time response was over-predicted, and the quantitative values should be taken with caution. However, the relative difference of these numerical events still holds qualitative value. As with all previous events, the furthest event N7 (*R = 1.0 m*) produced the least severe whipping response. On comparison, the intermediate event EN8 (*R = 0.8 m*) was 32 % larger than N7, while the closet event N10 (*R = 0.7 m*) was 54 % larger.
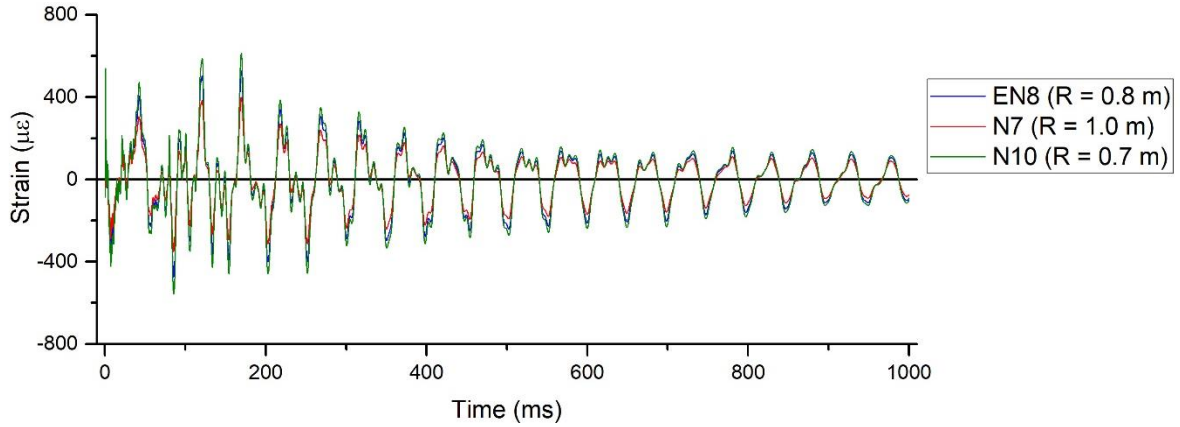
Figure 5-7   Aft whipping responses from W = 43 g, L = -4.3 m events

The comparisons made in Figures 5-3 to 5-7 demonstrate that the *R* distance did not affect the modal responses during whipping for the studied bubble proximity range of *1.40 < γ < 2.00* and relative size of $2.5 \leq \lambda \leq 4.5$. Considering the relative increase of the peak whipping strain levels, for events with the same *W* and *L*, as the *R* distance was reduced, comparison can be made in regard to the bubble's relative proximity *γ*. Taking a reference point at *γ = 2.00*, a common point for both experimental charge sizes and commonly considered as the cut-off point between near-field and far-field bubble interaction, the peak whipping response was normalised as the percentage of increased peak strain for a given reduction in *γ*. These results are presented in Figure 5-8 for *W = 250 g and 43 g*. This dimensionless analysis suggests that within the explored bubble proximity range of *1.40 < γ < 2.00* and relative size of $2.5 \leq \lambda \leq 4.5$, the relative increase in the peak strain of the whipping response from a closer bubble proximity is similar at all *L* positions. In summary, for this platform, the peak response at *γ = 1.40* was approximately 55 % higher than the peak response at *γ = 2.00* for all comparisons with the same charge size and *L* position.
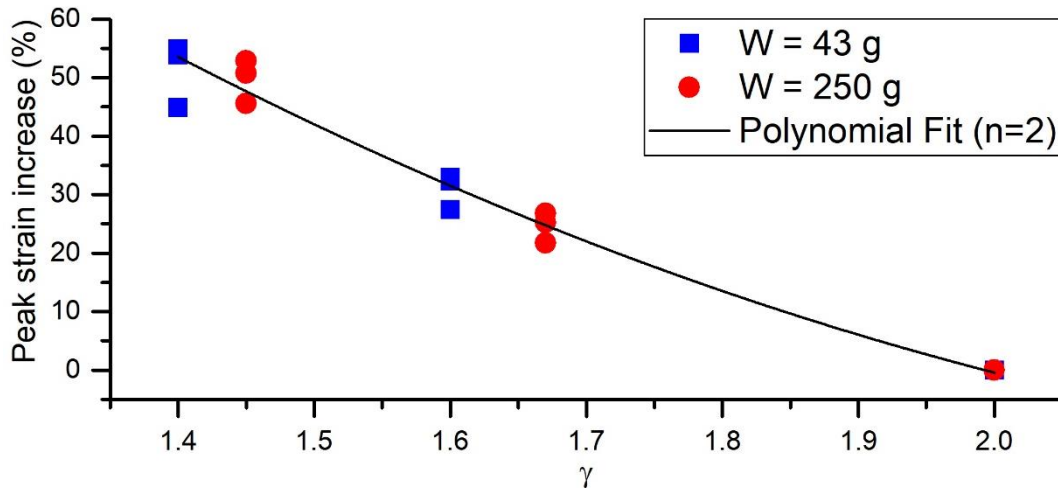
Figure 5-8   Increase in peak strain whipping response compared to the bubble proximity (γ), with baseline at γ = 2.00 for events EN1 – EN8 and N1 – N10.

5.3.2 Intermediate charge study

The whipping behaviour from all 150 g events was found to be largely similar to their comparative 250 g events at the same *L* locations. Comparisons are made between events at each *L* location and the closest 250 g event (*R = 1.3 m*) at the same *L* location is also presented for comparison of the transient whipping response behaviour. FFT response plots contain a

component of BM5 at 102 Hz. It is likely the contribution of this BM is overestimated by the numerical modelling environment, as previously discussed in Section 4.3.2 of Chapter 4. Based on its absence in experimental observations, the contribution of BM5 was not considered as a real response in this investigation.

Events N11, N14, and N17 (*W = 150 g, L = 0.0 m*) all produced similar whipping responses on the submerged platform. The whipping response at the forward, aft, and amidships locations from the closest event N17 (*R = 1.1 m*) is presented in Figure 5-9a. The whipping response was greatest at amidships and the responses at the forward and aft locations were essentially the same as each other, and marginally lower than the amidships response. An FFT response plot of these results in Figure 5-9b demonstrates that BM1 at 7 Hz was the dominant response at all locations. A minor contribution of BM3 at 41 Hz was also present at all locations.

Figure 5-9   (a) Whipping response at amidships, forward, and aft locations and (b) the frequency response at these locations for numerical event N17 (W = 150 g, R = 1.1 m, L = 0.0 m)

The amidships response of all 150 g events at *L = 0.0 m* are compared in Figure 5-10. The experimental amidships response from event E3 (*W = 250 g, R = 1.3 m, L = 0.0 m*) is also shown for transient comparison. Comparing the 150 g events, it is shown that the decreased *R* distance increased the whipping response strain levels, but the whipping response behaviour was qualitatively the same for all events. Between the furthest event N11 (*R = 1.5 m*) and the closest event N17 (*R = 1.1 m*) the peak whipping response strain level increased by 43 %.

Comparing 150 g events to the 250 g event E3, it is shown that the early time UNDEX induced whipping response behaviour was essentially the same for both charge sizes, while the later whipping response under the bubble loading and damped free vibration was larger for event E3. Although the 150 g events were dominated by the same BM1 frequency as the 250 g event, it is clear from the transient comparisons that the phase of this response was different. The peak whipping response occurred 15 ms earlier in the 150 g events. This is most likely due to the smaller bubble from the 150 g events, which also has a shorter bubble cycle period, and therefore drives the whipping response for a shorter amount of time, compared to the larger 250 g bubble and its longer pulsation cycles. It is unlikely this delay would have a significant effect on equipment responses, given the structural whipping frequency was the same for both charge sizes. It is however notable that the smaller charge and bubble did amplify the whipping response earlier than the larger one.
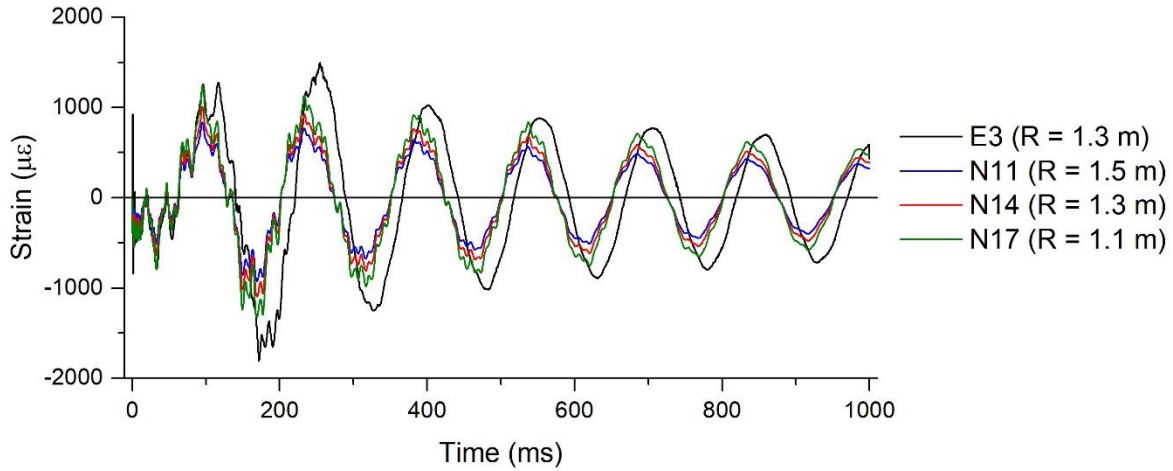
Figure 5-10 Comparison of the whipping response at amidships from events N11, N14, and N17 (W = 150 g, L = 0.0 m) and E3 (W = 250 g, L = 0.0 m)

The whipping response from events N12, N15, N18 (*W = 150 g, L = -2.8 m*) were all similar to each other, where the overall peak response occurred at the forward end, and the whipping responses were always larger at the forward and aft ends than the amidships location, as shown for the closest event N18 (*R = 1.1 m*) in Figure 5-11a. From the FFT response plot of these results in Figure 5-11b, it is shown that the amidships location was dominated by the BM1 response, while the forward and aft locations dominated by the BM1 and BM2 at 20 Hz. Minor contributions of BM3 at 41 Hz were also observed at all locations.

The whipping behaviour of these 150 g events was very similar to that of the 250 g events at the same *L* location, where the responses at the forward and aft ends were larger than amidships and consisted of a significant BM2 component. The peak response also occurred at the forward end for all these events, despite the aft end stand-off at *L = -2.8 m*, which indicates that this whipping behaviour was not unique to the 250 g charge size. This would also suggest that any *W* and *R* combinations occurring at the aft end will likely cause a more severe response at the forward end, and vice versa, so long as there is sufficient explosive energy to induce the global whipping response. From this study, the exact energy threshold for this behaviour on the investigated test platform could not be quantified. However, it has been demonstrated that Pentolite charges of *W = 250 g and 150 g*, at the proximity ranges of *1.40 < γ < 2.00*, and relative bubble sizes of *3.8 ≤ λ ≤ 4.5*, were sufficient to induce the response, while Pentolite charges of *W = 43 g*, at the proximity ranges of *1.40 < γ < 2.00*, and relative bubble size of *λ = 2.5* were not.
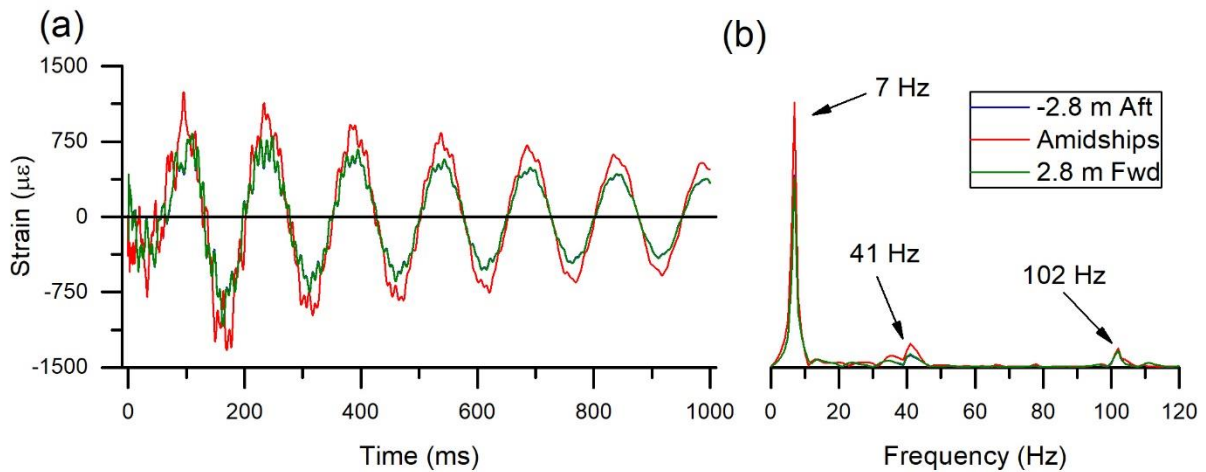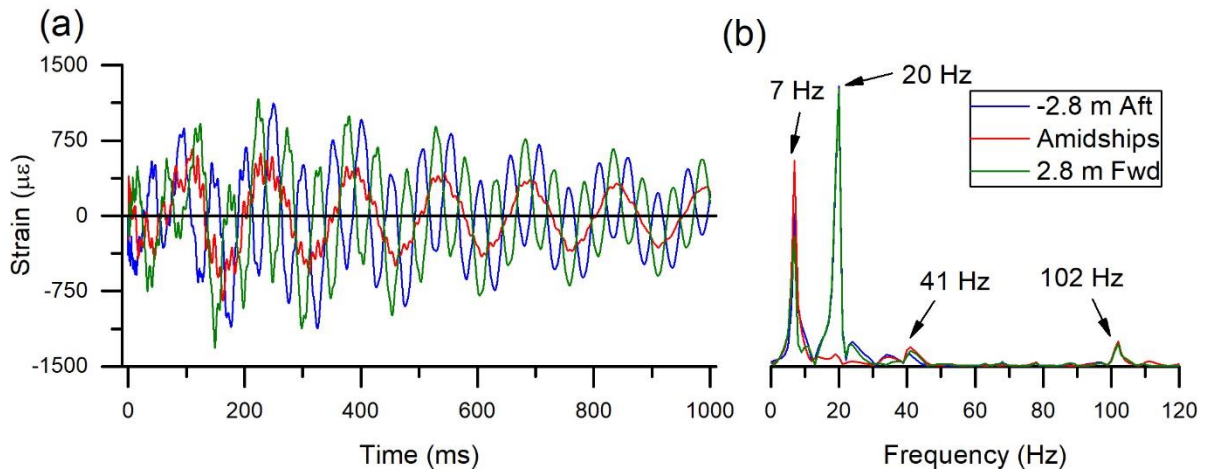
Figure 5-11 (a) Whipping response at amidships, forward, and aft locations and (b) the frequency response at these locations for numerical event N18 (W = 150 g, R = 1.1 m, L = -2.8 m)

The forward responses from these events, which were the most severe, are compared in Figure 5-12. The forward experimental result of event E5 (*W = 250 g, R = 1.3 m, L = -2.8 m*) is also shown for comparison, as it exhibited a similar whipping behaviour. It is shown from the comparison of the 150 g events that the whipping behaviour was qualitatively the same, and the reduced stand-off distance only resulted in an increase of the whipping strain levels. The closest event N18 (*R = 1.1 m*) induced a peak whipping response that was 52 % larger than the furthest event N12 at *R = 1.5 m*.

The early UNDEX induced whipping response behaviour was similar for all these events, even when compared with the 250 g event E5. Once again, there was a difference in response during the bubble loading, where the peak whipping response from the 150 g events occurred 30 ms earlier than E5, which may again be attributed to the shorter loading period of the smaller 150 g bubble. From this comparison it can also be seen that during the late time whipping responses, the 150 g events had a similar severity to the 250 g response, despite the reduced explosive energy.
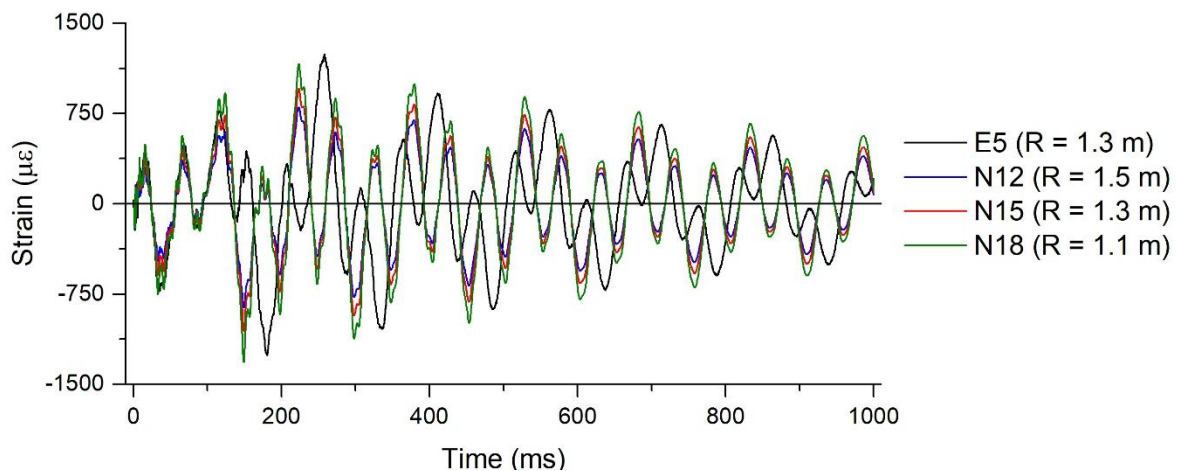
Figure 5-12 Comparison of the whipping response at the forward end from events N12, N15, and N18 (W = 150 g, L = -2.8 m) and E5 (W = 250 g, L = -2.8 m)

The 150 g events N13, N16, and N19 (*L = -4.3 m*) also demonstrated very similar whipping behaviour to each other. From the example of the amidships, forward, and aft responses of event N19 (*R = 1.1 m*) in Figure 5-13a, which was the most severe, it is shown the forward and aft responses were always much larger than the amidships response. The overall peak response

occurred at the aft end, after the arrival of the first bubble pulse. The behaviour of these 150 g events was similar to that observed in the 250 g events conducted at the $L = -4.3$ m location, rather than the 43 g events at $L = -2.8$ m, which always had similar peak responses at all locations. The FFT response plot of these results, presented in Figure 5-13b, show that BM2 at 20 Hz was the dominant response at the forward and aft locations. Minor contributions of BM3 at 41 Hz were also present. An additional response at 68 Hz was also present which was identified as BM4 based on the frequency responses identified in Table 4-3 and examination of the response shape in the transient numerical results.
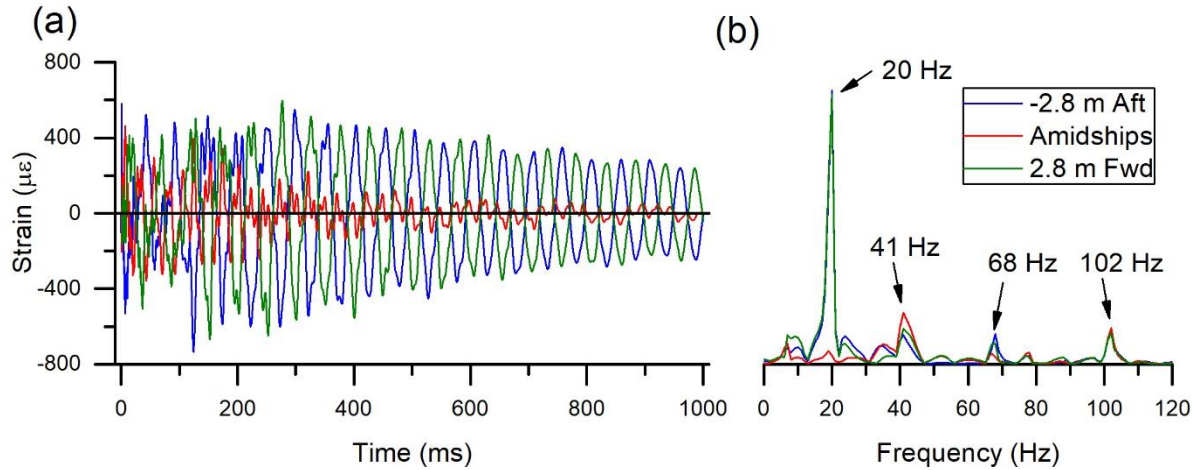
Figure 5-13 (a) Whipping response at amidships, forward, and aft locations and (b) the frequency response at these locations for numerical event N19 (W = 150 g, R = 1.1 m, L = -4.3 m)

The aft responses of all 150 g events at $L = -4.3$ m are compared in Figure 5-14. The experimental aft response of event E7 ($W = 250$ g, $R = 1.3$ m, $L = -4.3$ m) is also shown for comparison due to the similar whipping behaviour. It is shown that the early UNDEX induced whipping response was similar for all events. After the first bubble pulse of each respective charge size, the responses differed, and like previous comparisons the shorter bubble period of the 150 g charge resulted in the peak response occurring earlier than the 250 g event. The late-time whipping strain levels were similar between all events in Figure 5-14, despite the different W and R variables. The whipping response appears to be larger for the numerical 150 g events; however, it was noted during the validation in Chapter 4 that the numerical model tended to over predict the whipping response strains for events at $L = -4.3$ m, so it is likely these would be lower in reality. As with previous comparisons of events with the same W and L, the R distance only affected the peak whipping response level, where the peak strain level for the closest event N19 ($R = 1.1$ m) was 51 % larger than the furthest event N13 ($R = 1.3$ m). Despite the noted over-prediction of these events, this relative comparison is similar to that observed for the other L locations and was assumed as a valid result for further consideration.
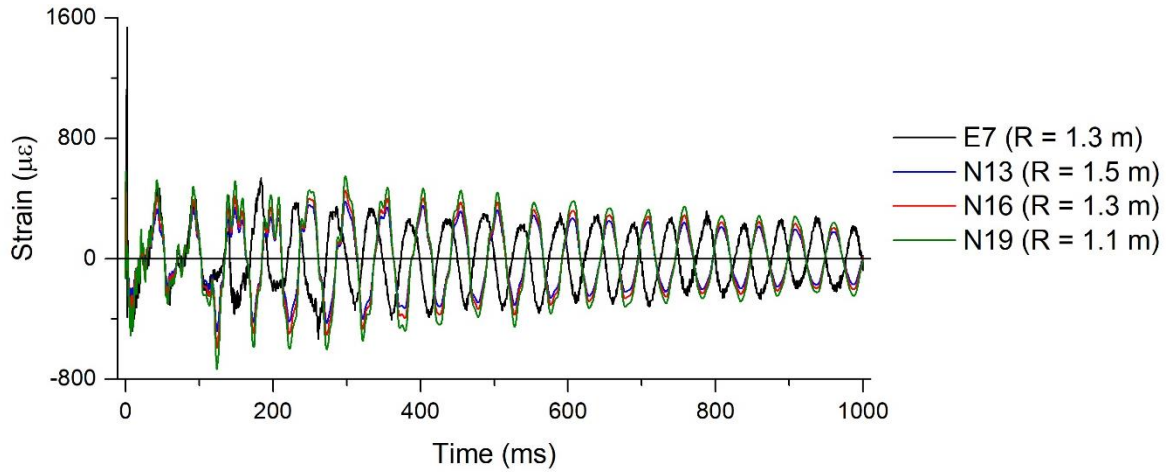
Figure 5-14 Comparison of the whipping response at the forward end from events N13, N16, and N19 (W = 150 g, L = -4.3 m) and E7 (W = 250 g, L = -4.3 m)

Applying the same approach from Section 5.3.1, the peak whipping response strain from each event was normalised as a percentage increase compared to the responses at a bubble proximity of $\gamma = 2.00$ of similar W and L. These results of $W = 150$ g were added to the plot from Figure 5-8 to produce Figure 5-15. The inclusion of the additional charge size responses was found to fit with the existing trend, which further suggests that for this explored bubble proximity range of $1.40 < \gamma < 2.00$ and relative size of $2.5 \leq \lambda \leq 4.5$, the increase in peak strain during a whipping response is proportional to the relative bubble proximity, regardless of the charge L position. The additional results in this comparison also suggest that the peak response from an UNDEX induced whipping response at different R distances can be predicted from a known R distance response for each charge size W and L position. In other words, it has been shown for this platform that the peak response from UNDEX induced whipping from a given charge size W and L position will be approximately 55 % larger at $\gamma = 1.40$ than at $\gamma = 2.00$. Characterisation of this response for a particular platform could potentially improve an operator's ability to assess the UNDEX threat in the field.
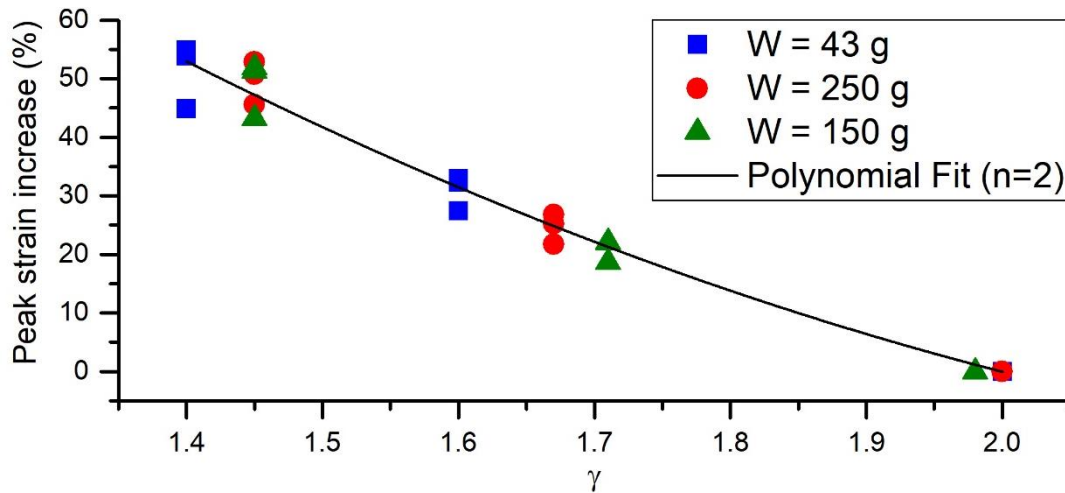
Figure 5-15 Increase in strain compared to the bubble proximity (γ), with baseline at γ = 2.00 for events EN1 – EN8 and N1 – N19

5.3.3 Shock-only loading study

The whipping responses for each event of the shock-only loading study are presented at the forward, aft and amidships locations, along with FFT response plots of these results. As with the previous study, all presented FFT response plots contained a component of BM5 at 102 Hz. It is likely this component is an error of the numerical modelling environment, previously discussed in Chapter 4, and is not considered as a real response from this investigation. Each shock-only loading event is compared to its equivalent experimental event to qualitatively demonstrate the effects of bubble loading on the whipping response of this submerged platform.

The results of NS1 ($L = 0.0$ m) are presented in Figure 5-16a. The whipping response was greatest at the amidships locations and the responses at the forward and aft locations were essentially the same. In a notable departure from previous amidships events, the overall peak response occurred earlier, during the first whipping peak. In addition, the whipping response does not amplify on any subsequent peaks beyond the first bending cycle. Both of these effects were attributed to the complete absence of any bubble loading to continue driving the whipping response. From the FFT response plot of these results in Figure 5-16b, it is shown that all locations were dominated by almost equal contributions of BM1 at 7 Hz and BM3 at 41 Hz, which was unlike any other 250 g event at $L = 0.0$ m, where the responses always consisted of only BM1 as the dominant contribution.

Figure 5-16 (a) Whipping responses and (b) frequency contribution of these responses from shock-only loading study NS1 (W = 250 g, R = 1.3 m, L = 0.0 m)

The amidships response from NS1 and the experimental equivalent E3 are compared in Figure 5-17. The early shock induced whipping response compared well, where the shock-only NS1 response was only slightly larger. However, the absence of bubble loading in the NS1 results is apparent in the comparison, as no amplification of the whipping response occurred in subsequent cycles. Direct comparison of the NS1 amidships response at the time of the experimental E3 peak whipping response shows that the shock-only loading response was 39% lower, with a peak response of 703 με. This comparison demonstrates that using any assessment method that prioritises shock response methodology for UNDEX survivability, could substantially under-predict the platform's whipping response due to a charge at $L = 0.0$ m, which was the most severe scenario for any given W and R combination investigated.
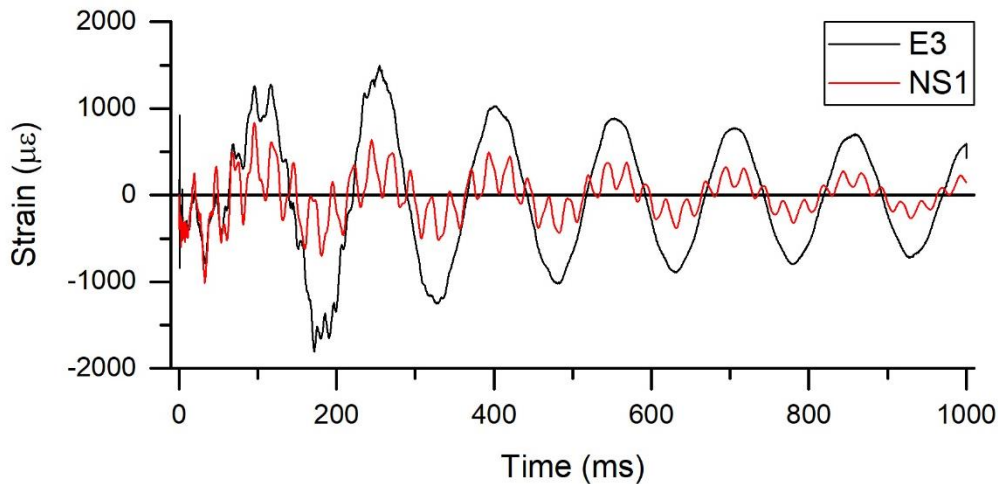
Figure 5-17 Comparison of amidships responses from E3 and shock study NS1

The results of the NS2 are presented in Figure 5-18a. As with other 250 g events at $L = -2.8$ m, the responses at the forward and aft locations were larger than the amidships response, and the peak whipping response occurred at the forward end, despite the aft end L position. This is notable as this occurred in the absence of any bubble loading, and this would suggest that this type of whipping response can be initiated by the shock wave loading alone. The FFT response plot of these results in Figure 5-18b shows that BM2 at 21 Hz was the dominant contribution in the forward and aft locations, and all locations had responses from BM1 at 7 Hz and BM3 at 41 Hz.
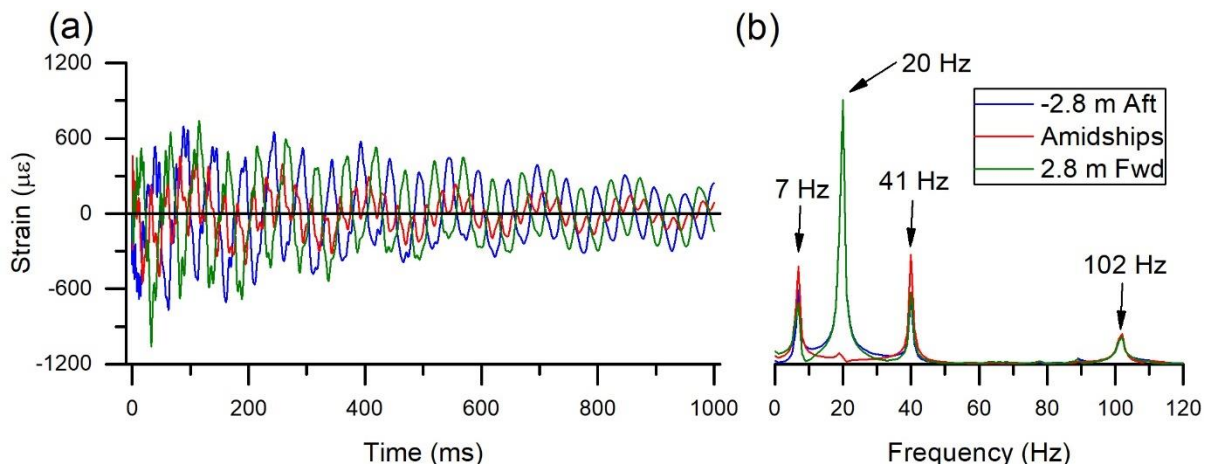
Figure 5-18 (a) Whipping responses and (b) frequency contribution of these responses from shock-only loading study NS2 (W = 250 g, R = 1.3 m, L = -2.8 m)

Comparing the response at the forward location from NS2 with the equivalent experimental event E5 in Figure 5-19, it is shown that the initial whipping responses were larger under the NS2 shock-only model and its overall peak response also occurs in this time. In contrast, the E5 responses were initially lower but its overall peak was larger and occurred later, after the first bubble pulse. The initial larger responses from NS2 are likely due to the absence of the bubble expansion under-pressure loading, which pulls the platform back towards the source location and effectively unloads some of the initial shock response. As with the NS1 shock-only loading scenario, there was no amplification in the NS2 whipping response and its peak occurs during the first whipping cycle. Comparing this response at the time of the experimental peak, NS2 was 54 % lower. This comparison has again demonstrated that using any assessment method that prioritises shock response methodology for UNDEX survivability could substantially under-predict the platform's whipping response.
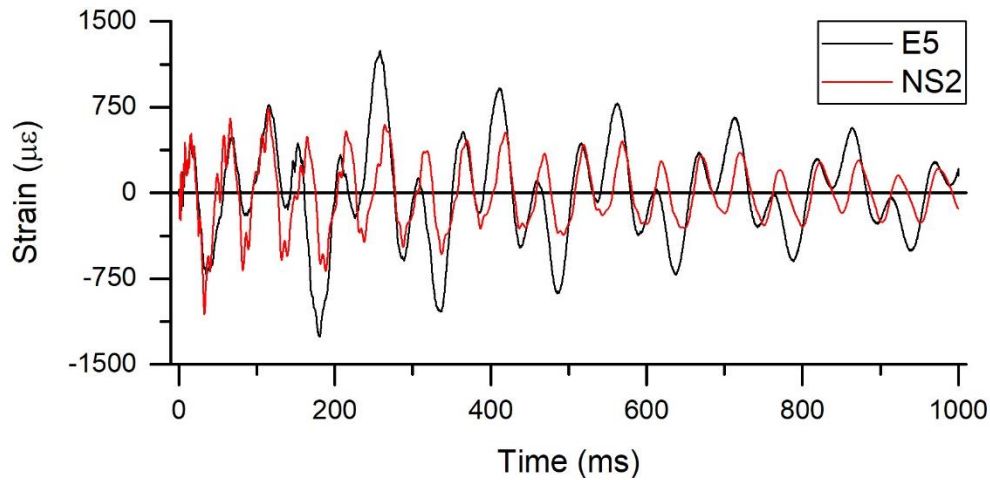
Figure 5-19 Comparison of forward responses from experimental E5 and shock study NS2

The responses from NS3 (*L = -4.3 m*) are presented in Figure 5-20a, and it can be seen that there were similar strain levels during the whipping response at all locations, with the forward and aft locations being marginally higher than amidships. Like the other shock-only loading scenarios, the peak response occurred during the early whipping response, with the overall peak response at the aft location. The FFT response plot of these results in Figure 5-20b shows that the whipping response was dominated by BM2 at 20 Hz on the forward and aft ends with a minor contribution of BM3 at 41 Hz. Amidships was purely dominated by the BM3 response, and unlike all other investigated events there was no significant excitement of BM1 at any location.
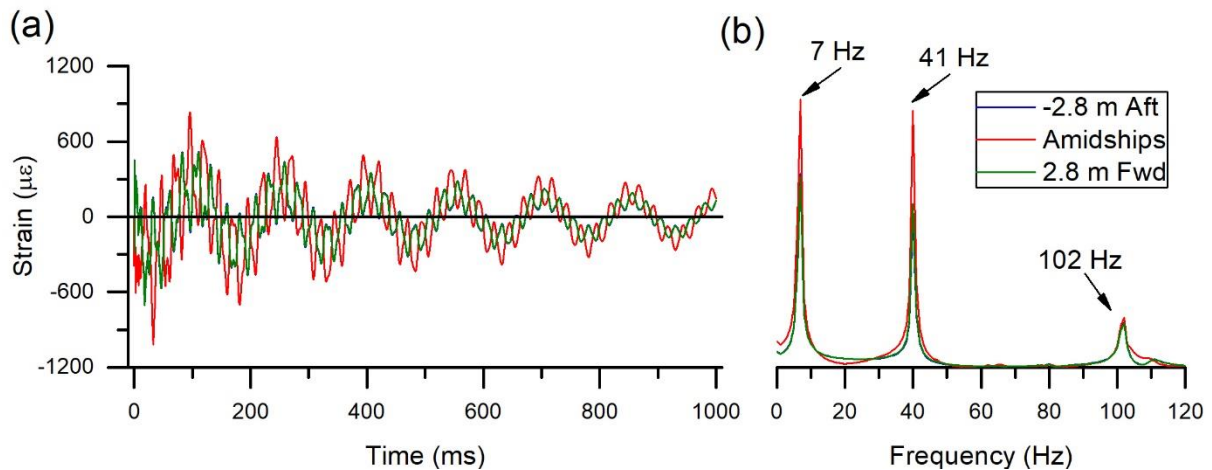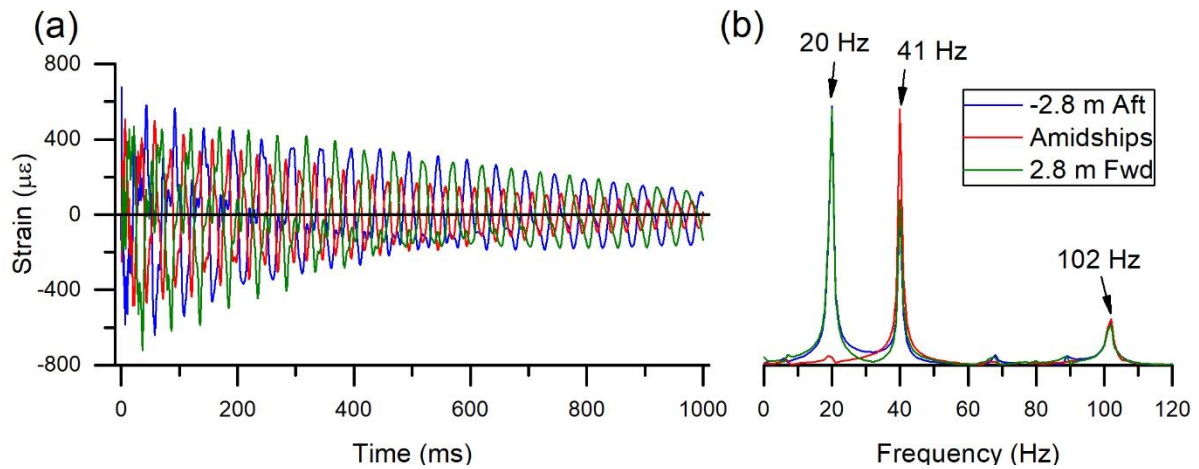

Figure 5-20 (a) Whipping responses and (b) frequency contribution of these responses from shock-only loading study NS3 (W = 250 g, R = 1.3 m, L = -4.3 m)

Comparing the aft responses of NS3 with its equivalent experimental event E7 in Figure 5-21, it is shown that unlike previous comparisons in this study, the whipping responses were very similar. Early time responses appear to be larger from the NS3 results; however, it was previously described in Chapter 4 that the numerical model tended to over predict the responses of scenarios at *L = -4.3 m*. As previously noted from the experimental investigation in Chapter 3, the bubble appeared to have minimal effect on the whipping response when the UNDEX events occurred at *L = -4.3 m*, corresponding with the node of the BM1 mode shape. The close similarity from the shock-only NS3 results appear to confirm this to be the case and demonstrate that the shock wave loading was the primary cause of the whipping response for this scenario. This also means that an assessment method that prioritises shock response methodology for UNDEX survivability could be used for such a scenario. However, it is

important to reiterate that by only considering the shock response there is a significant risk that the whipping response could be largely under predicted for other scenarios, such as those demonstrated by NS1 and NS2.
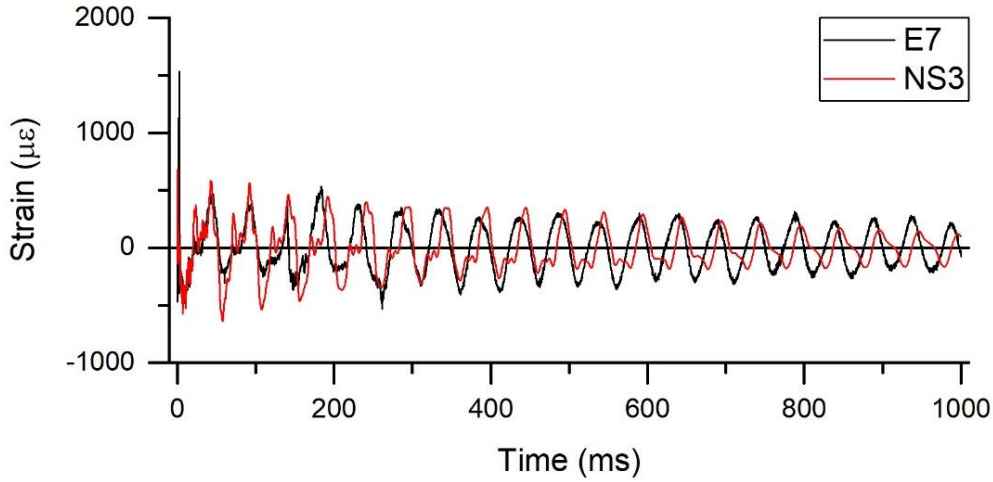
Figure 5-21 Comparison of aft responses from experimental E7 and shock study NS3

5.4 Categorisation of whipping responses

It has been shown that the whipping responses of the investigated experimental scenarios in Chapter 3 and the present studies demonstrated different whipping behaviours, depending on the *L* position in reference to the primary distortional mode shape, which was BM1 for the investigated test platform. For generalised comparison and further discussion of all results, the *L* position of each event is normalised (L_n) to the platform length (L_P) using Equation 1.1, where $L_n = 0.00$ is located at the stern and $L_n = 1.00$ is located at the bow of the cylindrical hull of the platform.

$$L_n = \frac{L + (L_P/2)}{L_P}$$

5.1

As the platform was symmetrical about amidships, the normalised event responses can also be assumed to be symmetrical about amidships. With this assumption, the investigated responses can be considered for L_n locations shown in Figure 5-22, where the BM1 shape displacement contour is shown for reference.
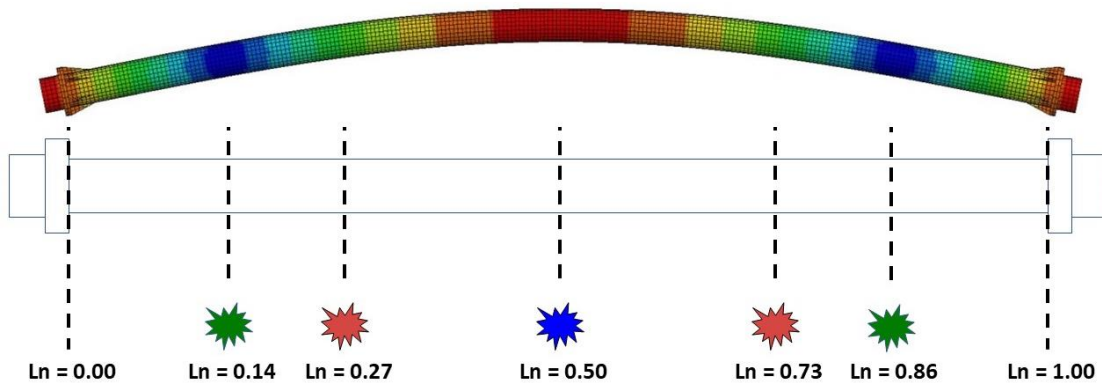
Figure 5-22 Normalised charge locations (L_n) compared to the BM1 shape displacement contour

Using the same comparison method from the experimental investigation in Figure 3-27, the peak responses from all numerical results (excluding those from the shock-only loading study)

at each L_n position are plotted against the bubble impulse I_B (summarised for each event in Table 5-5) in Figure 5-23.

Table 5-5   Bubble pressure impulse and shock factor from all numerical scenarios

Events			W (g)	R (m)	I_B (MPa.ms)	SF ($kg^{1/2}$/m)
EN1,	N1,	N2	250	1.8	5.29	0.28
EN2,	N3,	N3	250	1.5	6.51	0.33
EN3,	EN5,	EN7	250	1.3	7.01	0.38
N11,	N12,	N13	150	1.5	4.59	0.26
N14,	N15,	N16	150	1.3	5.38	0.30
N7,	N18,	N19	150	1.1	6.46	0.35
N5,	N6,	N7	43	1.0	3.26	0.21
EN4,	EN6,	EN8	43	0.8	4.17	0.26
N8,	N9,	N10	43	0.7	4.79	0.30

With additional data points from the numerical investigation, 2nd order polynomial trends were fitted to each set of L_n positions to confirm if the previous linear trends from Figure 3-27 were valid for other L positions and charge sizes. The fitted trends were forced to intercept point (*0 με, 0 MPa.ms*), assuming that an absence of any impulse would not induce any response in the platform. From these fitted relations, the following trends were found for each L_n position:

UNDEX stand-off locations near the anti-node of the BM1 shape ($L_n = 0.50$) produced the most severe whipping responses and the severity increased in a nonlinear trend as the bubble impulse increased, which demonstrates that the linear trends previously identified from the experimental comparisons in Figure 3-27 were only valid for the smaller dataset. To better define different UNDEX induced whipping responses, this may be considered as a "critical whipping response", as this was always the most severe outcome from the UNDEX scenarios investigated.

Stand-off locations near the node of the BM1 shape ($L_n = 0.14$ and 0.86) demonstrated that the whipping response severity also followed a nonlinear trend but for these scenarios it tended to plateau, despite larger bubble impulses. It was previously recognised that these events saw minimal effect from the bubble loading and their whipping responses were primarily due to shock loading. Notably it appears from the results at this location that the events with smaller charges (EN8, N7, and N10) seemed to produce a larger whipping response, a counterintuitive outcome to previous results. However, it should be reiterated that the numerical model over-predicted scenarios involving smaller charges at this location by 36 %, and the peak responses from these results are likely much lower in reality. Results from the intermediate charge size (N13, N16, and N19) also appear larger than the largest charge size events (EN7, N2, and N4). This is again likely due to the known inaccuracy of the numerical model for events at this stand-off location. The numerical model over-predicted the EN7 response by 7 % and it is likely the responses from the intermediate charge events are also over-predicted by 7 to 36 %. Even with these modelling accuracy considerations, the trend indicates that the peak whipping response was remarkably lower from UNDEX stand-offs at this location. Based on this trend, this type of whipping response may be defined as a "resilient whipping response" of a platform, due to its resistance against the bubble loading that would have otherwise amplified the whipping. For a platform's overall survivability, this would be the most desirable outcome from a potential UNDEX event.

It can be seen from the diverging nonlinear trends from UNDEX stand-offs at the node and anti-node L_n positions of the BM1 shape, that a linear severity trend must exist between them. Responses at $L_n = 0.27$ and 0.73 demonstrated an approximate linear trend of severity as the

bubble pressure impulse increased. Hypothetically, this trend may exist for a broader range of L_n positions, as this will affect the relative contribution of other distortional mode responses. Therefore, this whipping behaviour may be defined as the "general whipping response" of a platform. Given this could hypothetically occur at many L_n positions, it is suggested that this is the most likely whipping response to occur from a potential UNDEX event.

It is reiterated that if shock-only loading is assumed in the analysis, it is unlikely a general or critical whipping response would be accounted for, as only the resilient response compared well with results from the shock-only loading study.
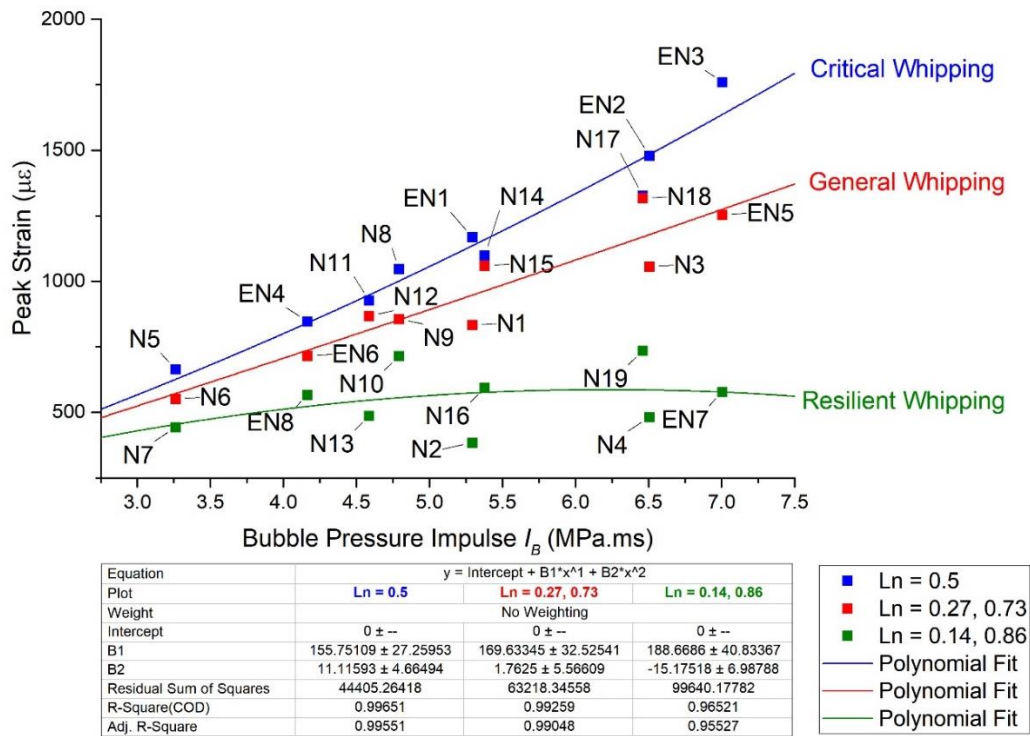
Figure 5-23 Characterisation of whipping responses

With limited extrapolation of these trends, as demonstrated in Figure 5-24, theoretical regimes of submerged platform response have been suggested, that warrant further investigation to validate and quantify.

At low bubble impulse levels, it is suggested that the trends are essentially linear for all L_n positions. This suggests that as the bubble is further away, and/or a smaller charge is used, the bubble does not have as significant an effect on the platform's whipping response and the bubble and structural responses may be assumed to be uncoupled. This theoretical regime may be defined as the far-field elastic whipping regime, noted in Figure 5-24. The limits for this regime were not explored in the present investigations, and further experimental work would be required to quantify a definition of this regime.

The present investigations have demonstrated that the type of whipping response induced (critical, resilient, or general) is dependent on the location of the UNDEX L_n position to the primary distortional mode shape. When these diverging whipping responses are observed, they may be collectively defined as the near-field, non-contact elastic whipping regime. Under this regime the bubble and structural responses may be coupled, in the case of critical and general whipping, or uncoupled in the case of resilient whipping.

Extrapolation of peak strain responses suggest eventually the material yield limit ε_y would be exceeded and a plastic whipping response would occur. So long as the bubble does not make

direct contact with the platform, this may be defined as the non-contact plastic whipping regime. This is denoted by the ε_y limit projection in Figure 5-24. The most severe event from the present investigations (EN3) reached the theoretical ε_y but did not exhibit any yielding behaviour. Therefore, the effects that material plasticity have on the whipping response were not observed, and these were not considered in the initial scope of this investigation. Further investigation may be required to quantify the non-linear material effects for a plastic whipping response.

Finally, based on bubble interaction with boundaries discussed in Section 2.2.2 of Chapter 2, there must be a limit where the bubble will make direct contact with the platform, through either its expansion or migration phases. This would introduce bubble jetting and damage responses, which could be defined as the contact damage regime, noted in Figure 5-24. The damage mechanics at this point would be vastly different from the whipping response and beyond the scope of the present investigations. The definition of this regime is also complicated by variables that affect the interaction of bubbles in proximity to structures, discussed in Chapter 2. This regime would be the most difficult to quantify with further work, as the current knowledge of bubble-structure interaction is limited for this scenario.

All regimes discussed and presented in Figure 5-24 are also dependent on the relative size of the bubble to the platform. As discussed in Chapter 2, current knowledge of how the relative bubble size affects any response in a platform is limited. Through these investigations it has been shown that the discussed regimes and whipping response behaviours are valid for a relative bubble size of $2.5 \leq \lambda \leq 4.5$. For relative sizes outside this range, it remains uncertain if these regimes and behaviours are applicable, as the absolute limits were not identified in the present investigation. As a final note, the stated values should not be taken as absolute figures or limits in regard to analysis on any other platform. However, this work has demonstrated an underlying methodology to obtain these.

Figure 5-24 Categorisation of whipping response regimes[6].

---

[6] Note that far-field elastic and contact damage limits were not explored in this investigation and are shown only as hypothetical regimes.

5.5 Conclusion

The numerical model developed and validated in Chapter 4 was used to conduct three numerical studies. These studies explored the effects on the whipping response from different stand-off distances at positions along the platform length, an intermediate charge size, and the contribution of the bubble loading by using a shock-only loading model.
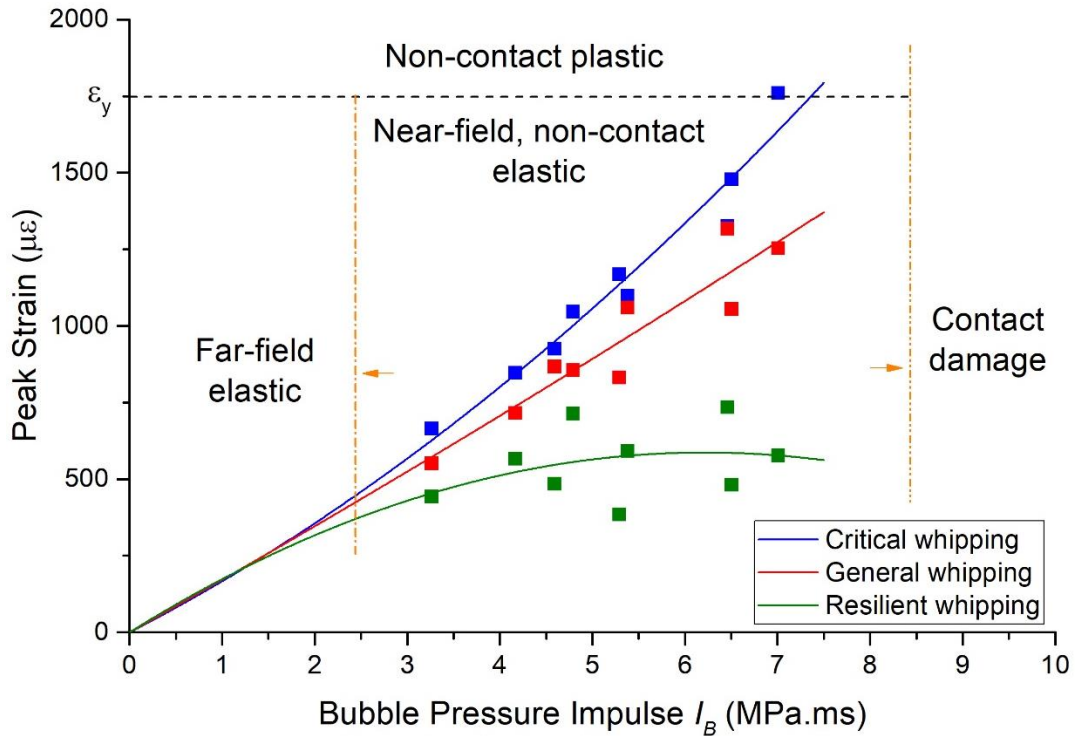
From the stand-off distance study, it was found that the stand-off distance did not affect the modal responses during whipping and that this was dependent only on the charge size and stand-off location for the studied bubble proximity range of $1.40 \leq \gamma \leq 2.00$ and relative size of $2.5 \leq \lambda \leq 4.5$. The whipping strain levels increased as the stand-off distance decreased, where events at $\gamma = 1.40$ had peak strain levels approximately 55 % larger than their $\gamma = 2.00$ counterparts at the same stand-off location. Comparison of the peak whipping responses from the intermediate charge results to those from the stand-off study found there was a similar increase in strain levels for a decrease in bubble proximity, fortifying the identified trend. These figures may be a specific property of the platform, but this general characterisation of the whipping response could be utilised as a rapid threat assessment for a platform's survivability of known UNDEX threats.

From the intermediate charge study, it was found that the 150 g charge size induced similar whipping responses as the 250 g charge. This suggests that there is an energy threshold for inducing the global whipping behaviour seen from the 250 g and 150 g events, compared to the more localised behaviour from the smaller 43 g charge events. This explosive energy threshold was not directly identified from this study. However, it was observed that Pentolite charges of $W = 250\ g\ and\ 150\ g$, with a relative bubble size of $3.8 \leq \lambda \leq 4.5$, were sufficient to induce the response, while Pentolite charges of $W = 43\ g$, with a relative bubble size of $\lambda = 2.5$ were not. It was also found that the severity of 150 g events was similar to the 250 g events at their scaled stand-off distances, except for stand-off locations at amidships where the 250 g events always induced a larger whipping response. The cause of this is likely due to the closer proximity of the 250 g bubble pulsation frequency to the natural response frequency of the first bending mode of the submerged platform.

Results from the shock-only loading study, largely under-predicted the whipping responses for UNDEX stand-off locations at amidships and -2.8 m aft due to the absence of any bubble loading. For UNDEX stand-offs located at -4.3 m aft, corresponding with the node of the first bending mode shape for the submerged platform, the absence of bubble loading did not have a significant effect on the peak whipping response and the numerical results compared well with the experimental measurements. This firmly suggests that at this location, the pulsating bubble had minimal influence on the whipping response severity, and that the whipping response was purely due to the shock loading at this stand-off location. This study also demonstrated that using analysis methods based only on shock response can severely under-predict the whipping response and it is strongly recommended that these methods should not be used for an UNDEX induced whipping analysis.

Through comparison of the peak whipping responses and their respective bubble impulses, three unique whipping responses were identified: critical, resilient, and general whipping. Each response demonstrated unique trends in the severity of whipping compared to the bubble impulse and the resulting response was dependent on the UNDEX stand-off location in relation to the platform's first bending mode. With limited extrapolation of these response trends, four whipping response regimes: far-field elastic; near-field, non-contact elastic; non-contact plastic; and contact damage. The conducted investigations suggest that this theory is valid for bubble proximities of $1.40 \leq \gamma \leq 2.00$ and relative sizes of $2.5 \leq \lambda \leq 4.5$; however, the absolute limits of these regimes were not explored and are a promising area of further work.

Chapter 6. Conclusions

6.1. Research summary

This research has explored the UNDEX induced whipping response of a submerged platform, with the intention to enhance assessment capability and better inform the platform designers and operators of the UNDEX threat and requirements. Three research questions were considered in this work:

1. What variables of the UNDEX event and platform design contribute to the whipping response?

2. Are existing assessment methods appropriate for analysing the UNDEX induced whipping response of a platform?

3. How can the UNDEX induced whipping response and bubble-structure coupling be better defined?

These were investigated and addressed through experimental and numerical analysis methods. These investigations are summarised as follows:

1. A review of the UNDEX loading effects from the shock wave and pulsating bubble was conducted, primarily focused on the bubble-structure interaction in a near-field, non-contact regime and the variables that may affect the whipping response of a submerged platform. It was established that the relative size of a bubble to a structure was not explicitly considered in past investigations and the effects of the relative size on the bubble-structure interaction were not previously quantified.

2. Analysis methods were reviewed for their applicability to assess the UNDEX induced whipping response of a submerged platform. From this review it was determined that the DAA BEM was best suited for analysis, but additional experimental validation was required to ensure the method's accuracy.

3. An experimental test platform was constructed from a 12 m long, 0.4 m diameter hollow pipe. The design used large weighted ends to tune the platform's vibratory responses to the bubble pulsation frequency and control its net buoyancy. The platform was submerged at a centreline depth of 5 m and the structural response was measured by strain gauges at five locations along the platform's length. Incident pressure measurements from each UNDEX event were also recorded.

4. During the experimental investigation, the platform was subjected to eight UNDEX events to explore how the variables of charge size, stand-off distance and location would affect the UNDEX induced whipping response. This experiment expanded on past submerged platform whipping experiments by conducting them at a larger "intermediate" scale and considering a larger number of variables on the whipping response, including the stand-off location along the platform length. A new relative bubble size parameter λ was defined to characterise the bubble-structure interaction effects, along with the bubble proximity parameter.

5. A numerical model of the platform was developed in the explicit LS-Dyna code, coupled with the Underwater Shock Analysis (USA) code BEM to calculate the fluid-structure interaction using the DAA solutions. The Price-Hicks Shock Bubble (PHS-BUB) model

was used to calculate the UNDEX loads. The numerical model was validated through comparisons of the incident pressure loads, modal responses, and transient strain responses to the experimental results, and compared the performance of three damping methods.

6. The validated numerical model was used to conduct additional numerical studies that further explored how additional charge sizes and stand-off distances affected the UNDEX induced whipping response of the submerged platform.

7. A final numerical study was conducted using a shock wave only loading model, to quantify the contribution that bubble loading had on the overall UNDEX induced whipping response, and to demonstrate the implications that can arise from using analysis methods that are primarily focused on shock response.

6.2.   Overall conclusions

The findings from the experimental and numerical investigations have given new insight into the UNDEX induced whipping response of a submerged platform. The following conclusions were drawn based on the outcomes of the presented investigations and are summarised here in relation to their respective research questions.

6.2.1. Effects of UNDEX variables on whipping

Both the experimental and numerical investigations considered what effects the variables of the UNDEX charge size, stand-off distance and location have on a platform's whipping response. The conclusions of these are summarised below:

1. It was found that the UNDEX charge size, and the resulting pulsating bubble size, period, and frequency, affected the bending modes excited during the whipping response. The most severe whipping occurred when the bubble pulsation frequency was similar to the first bending mode response of the platform. In addition, it was found that the larger charge sizes tended to excite lower bending modes, while the smaller charge excited higher modes and the response from the smaller charge was generally localised near the charge stand-off location. This suggested that to induce a global whipping response, sufficient explosive energy and/or a large enough bubble was required. The investigations identified that relative bubble sizes of $3.8 \leq \lambda \leq 4.5$ were sufficient to induce a global response, while a relative bubble size of $\lambda = 2.5$ was not.

2. The UNDEX stand-off distance from the hull had no effect on the bending modes that were excited during whipping for bubble proximities of $1.40 \leq \gamma \leq 2.00$ and relative sizes of $2.5 \leq \lambda \leq 4.5$. The stand-off distance only affected the severity, where a closer stand-off distance increased the whipping response. It was found that the percent increase in the whipping response was consistent for all similar charge size and stand-off location scenarios, where the response from events of the same charge size and stand-off location at $\gamma = 1.40$ was approximately 55 % higher than their counterparts at $\gamma = 2.00$. These values are likely to be specific to the test platform, but it is suggested that characterisation of these responses at different bubble proximities for a specific platform could be utilised as a rapid assessment tool to predict a platform's survivability against UNDEX threats. This has the potential to enhance operational decision making.

3. The stand-off location had the most significant effect on the UNDEX induced whipping response and results from both investigations demonstrated that whipping is not a general response, but can take different forms depending on where the UNDEX stand-off is located in relation to the platform's first bending mode shape. These are detailed further in Section 6.2.3.

6.2.2. Assessment methods for UNDEX induced whipping

The DAA BEM was explored as an analysis tool for the UNDEX induced whipping response of a submerged platform. The following conclusions were drawn from a review of existing methods and numerical validation of the DAA method to experimental results:

1. The numerical DAA BEM was demonstrated as a capable assessment method for an UNDEX induced whipping analysis for bubble proximities $1.40 \leq \gamma \leq 2.00$ and relative sizes of $2.5 \leq \lambda \leq 4.5$. This method worked on the assumption of minimal bubble-structure interaction and for cases where the bubble is significantly affected by the platform response (or *vice-versa*) alternative analysis methods should be sought. Full fluid-structure interaction modelling has great potential to overcome this constraint, but current computation costs (in terms of both budget and time) make this difficult to access for most industries.

2. It was shown that the results from both experimental and numerical investigations can be used to characterise a platform's whipping response. This information may be used to develop rapid assessment tools for a platforms survivability that can be used directly by the operators, potentially enhancing the decision making process in regards to UNDEX threats.

3. Comparisons of the numerical shock-only loading study to experimental results demonstrated that using analysis methodologies based only on the shock response severely under-predicted the critical and general whipping responses by 39 – 54 %, but compared well for resilient whipping response scenarios. Based on these comparisons, it is strongly recommended that shock response analysis methodologies should not be used for a whipping response analysis.

6.2.3. Characterisation of whipping responses and regimes

In the past, whipping has been considered as a general platform response due to transient loading. Through these investigations it has been shown for the first time that the UNDEX induced whipping response can vary significantly, even when the UNDEX charge size and stand-off distance is the same. Based on observations from comparisons of the bubble impulse and the peak whipping response, three unique UNDEX induced whipping responses were defined:

1. The most severe whipping responses occurred when the UNDEX stand-off location was located near the anti-node of the first bending mode shape of the platform. This was especially severe when the bubble pulsation frequency was close to the first bending mode frequency, which caused the response to be dominated by the first bending mode. A whipping response of this form may be defined to as the critical whipping response due to the risk it poses to the overall survivability of a platform.

2. The whipping response was found to be far less severe when the UNDEX stand-off location was near the node of the first bending mode shape, with peak whipping response strains that were 58 % to 71 % lower than similar events at the anti-node stand-off location. The responses at this stand-off location had an absence of the first bending mode in the overall response and the platform had an apparent resistance to the loading from the pulsating bubble. Based on these observations, whipping responses similar to this may be defined to as the resilient whipping response. This form of whipping could potentially be used to the advantage of a platform's survivability, if the stand-off location of an UNDEX threat can be influenced to induce this response.

3. In between the nodes and anti-nodes of the first bending mode shape, varying degrees of the first three bending modes contributed to the overall UNDEX induced whipping response of the platform. This may be defined to as the general whipping response. Under this condition, the interaction of multiple modal responses may cause the largest whipping response to occur away from the stand-off location, making it difficult to detect without a global response assessment method.

The knowledge of these different elastic whipping response behaviours due to near-field, non-contact UNDEX will allow for better design and analysis to be performed on current and future maritime platforms, to ensure they can meet the challenges of their high-risk environment.

Through limited extrapolation of these different whipping responses, four whipping analysis regimes were identified:

1. Far-field elastic

2. Near-field, non-contact elastic

3. Non-contact plastic

4. Contact damage

The conducted investigations suggest that these regimes are valid for bubble proximities of $1.40 \leq \gamma \leq 2.00$ and relative sizes of $2.5 \leq \lambda \leq 4.5$; however, the absolute limits of these regimes were not identified and are a promising area of further work.

6.3. Recommendations

Based on lessons learned throughout this investigation, the following recommendations are suggested:

1. Transducer connections should be reduced wherever possible, particularly if these are located underwater. Compromised watertight integrity from connectors was attributed as the primary cause of pressure gauge failure during the experimental part of this investigation.

2. Pressure gauges that minimise electrical components on the transducer were found to have a better chance of surviving multiple events, though this often comes at a cost of greater difficulty in calibration.

3. Wherever possible, the cables themselves should be shielded from direct contact with the shock wave, and/or incorporate some form of damping material to help shield them. Significant distortion of the signals occurred on unprotected cables during the shock loading from this investigation.

4. If the experiment in Chapter 3 were to be repeated, the outriggers would be strengthened to limit the flexibility of the structures and the amount of cavitation that occurred. This is also recommended as general advice for similar experimental setups.

6.4. Further work

The following subjects are potential avenues for continuation of the research into UNDEX loading and structural response of submerged platforms:

1. Although the effects of the relative size of bubble and structure on the whipping response were explored in this investigation, the absolute limits of the relative size and its effects on bubble-structure interaction remain largely unexplored. Further research should be directed at determining limits of the relative bubble size, so bubble-structure interaction can be characterised.

2. It was noted in this research that without visual evidence it was difficult to determine how the bubble interacted with the platform during the second pulsation cycle. In absence of this evidence the present investigations were unable to conclude the contributions of later bubble cycles on the whipping response and demonstrate how the bubble interacted with the platform. Confirmation of the bubble structure interaction through visual evidence would be a valuable contribution to the field. It is acknowledged though that the hostility of the UNDEX environment makes this difficult to achieve with anything larger than a detonator sized explosive. Therefore, small-scale experiments offer the best initial approach.

3. In addition to unknowns of the later bubble cycle interactions, the coefficients to analyse the bubble period and radius using similitude equations have limited accuracy for explosives other than TNT, particularly when considering bubble cycles beyond the first. This work noted that those available may be based on small sample sizes, and therefore have limited accuracy ranges. Further experimental analysis to identify these coefficients for other explosive materials would be beneficial in forming a more robust database for these similitude equations, as it was found that the use of a "universal" TNT equivalent was not always reliable in this research.

4. The present research found that the charge size could affect the whipping response, where large charges induced a global response, while smaller charges were localised to part of the platform. This was attributed to an explosive energy threshold. This threshold was not identified or characterised by the present investigations. Identification of the energy threshold to induce a global whipping response, and the platform variables that affect this would be a valuable contribution to the field.

5. Only elastic whipping responses were considered in the present investigations. Extending both the experimental and numerical aspects of the present work to include inelastic effects would broaden the applicability of the proposed numerical analysis methodology. Better understanding of the inelastic whipping response may have a significant impact when considering whipping responses on the borderline of the near-field, non-contact and non-contact plastic regimes.

6. The whipping response of a submerged pressure hull was only explored under minor hydrostatic pressure in the present investigations. Under operational conditions, the hydrostatic pressure load can be substantial for submerged platforms. The effect of this additional loading on the whipping response and the potential failure modes that may be

induced warrant further investigation, as the hydrostatic pressure would likely have a significant effect on the whipping response regimes defined in the present work.

7. Past work and the present investigations have demonstrated the applicability of numerical analysis codes to conduct and UNDEX induced whipping analysis for generalised and small-scale platforms. Validation against a full-size platform remains elusive in the public domain but such work would aid in confirming that the numerical analysis methods and the bubble structure interaction effects presented in past work and this thesis are applicable to full-size platforms.

References

[1]   Burcher, R. & Rydill, L. J. *Concepts in submarine design*. 2nd Ed. (Cambridge University Press, 1998).

[2]   Hutchinson, R. *Jane's submarines: war beneath the waves from 1776 to the present day*. (Harper Collins, 2001).

[3]   Cook, M. A. *The Science of High Explosives*. 1st Ed. (Reinhold Publishing Corporation, 1958).

[4]   Reid, W., de Yong, L., Elischer, P. & Skeen, M. *Underwater shock testing with seismic air guns*. in *8th International Conference on Shock & Impact Loads on Structures* Adelaide, Australia. (2009).

[5]   Shurcliff, W. A. *Bombs at Bikini: The Official Report of Operation Crossroads*. (United States Joint Task Force One, 1947).

[6]   Swisdak, M. M. *Explosion Effects and Properties. Part II. Explosion Effects in Water*. (Naval Surface Weapons Center, Silver Spring, MD, USA, 1978).

[7]   Free, G. & Gruchy, D. *Underwater Explosions at 120,000fps - The Slow Mo Guys*, (Rooster Teeth, YouTube, 2016).

[8]   Cole, R. H. *Underwater Explosions*. 1st Ed. (Princeton University Press, 1948).

[9]   Kirkwood, J. & Bethe, H. *Basic propagation theory*. Office of scientific research and development, p. 588-595, (1942).

[10]   Swift, E. & Decius, J. C. *Measurement of Bubble Pulse Phenomena, III: Radius and Period Studies*. in *Underwater Explosion Research*. 1st Ed., Vol. II, Ch. 5, p. 553-600, (Office of Navy Research, 1947).

[11]   Reid, W. D. *The Response of Surface Ships to Underwater Explosions*. Report No.: DSTO-GD-0109, (Defence Science and Technology Organisation, Melbourne, Victoria, 1996).

[12]   Xiang, D., Rong, J., He, X. & Feng, Z. *Underwater Explosion Performance of RDX/AP-based Aluminized Explosives*. Central European Journal of Energetic Materials **14**(1), p. 60-76, (2017).

[13]   Grishkin, A., Dubnov, L., Davidov, V. Y., Levshina, Y. A. & Mikhailova, T. *Effect of powdered aluminum additives on the detonation parameters of high explosives*. Combustion, Explosion and Shock Waves **29**(2), p. 239-241, (1993).

[14]   Barker, D. *The Case for Impulse - Analysis of Conventional Structures Subjected to Blast Loads*. in *34th Department of Defence Explosives Safety Board Seminar*. Portland, Oregon. (ABSG Consulting Inc. San Antonio TX, 2010).

[15]   Cooker, M. J. & Peregrine, D. *Pressure-impulse theory for liquid impact problems*. Journal of Fluid Mechanics **297**, p. 193-214, (1995).

[16]   US Office of Naval Research & British Department of Navy. *Underwater Explosion Research: A Compendium of British and American Reports*. Vol. I, II & III (United States Office of Naval Research, 1950).

[17]   Bishop, R. E. D. & Price, W. G. *Hydroelasticity of ships*. 1st Ed. (Cambridge University Press, 1979).

[18]   Blevins, R. D. *Formulas for Natural Frequency and Mode Shape*. 1st Ed. (Van Nostrand Reinhold Company, 1979).

[19]   Hamidzadeh, H. R. & Jazar, R. N. *Vibrations of thick cylindrical structures*. 1st Ed. (Springer, 2010).

[20]   Lewis, F. M. *The inertia of the water surrounding a vibrating ship*. Trans. SNAME **37**, p. 1-20, (1929).

[21]   Deruntz, J. A. & Geers, T. L. *Added mass computation by the boundary integral method*. International Journal for Numerical Methods in Engineering **12**(3), p. 531-550, (1978).

[22]   Zukas, J. A. *Shock waves in solids*. in *Studies in Applied Mechanics*. Vol. 49, Ch. 3, p. 75-102, (Elsevier, 2004).

[23]   Keil, A. H. *The response of ships to underwater explosions*. (David Taylor Model Basin, Washington D.C., 1961).

[24]   Hicks, A. N. *The theory of explosion induced ship whipping motions*. (Naval Construction Research Establishment, St Leonard's Hill, Dunfermline, U.K., 1972).

[25]   Ultimate Military Channel. *Torpedo sinks ship*, (YouTube, 2006).

[26]   Royal Australian Navy. *HMAS Torrens (DE 53) after hit from Mark 48 torpedo*, (Commonwealth of Australia, Defence Image Gallery, 1999).

[27]   Mason, W. *Naval Mine Technologies*. (Farragut Technical Analysis Center, 2009).

[28]   Cornish, G. J. *US Naval Mine Warfare Strategy: Analysis of the Way Ahead*. (U.S. Army War College Carlisle Barracks, PA, 2003).

[29]   US Navy. *USS Princeton (CG-59) hull crack*, (U.S. Navy, Wikimedia Commons, 1991).

[30]   Chisum, J. E. & Shin, Y. S. *Explosion Gas Bubbles Near Simple Boundaries*. Shock and Vibration **4**(1), (1997).

[31]   Tomita, Y., Robinson, P. B., Tong, R. P. & Blake, J. R. *Growth and collapse of cavitation bubbles near a curved rigid boundary*. Journal of Fluid Mechanics **466**, p. 259-283, (2002).

[32]   Brett, J. M. & Yiannakopoulos, G. *A study of explosive effects in close proximity to a submerged cylinder*. International Journal of Impact Engineering **35**(4), p. 206-225, (2008).

[33]   Hung, C. F. & Hwangfu, J. J. *Experimental study of the behaviour of mini-charge underwater explosion bubbles near different boundaries*. Journal of Fluid Mechanics **651**, p. 55-80, (2010).

[34]   Zhang, A. M., Wang, S. P., Huang, C. & Wang, B. *Influences of initial and boundary conditions on underwater explosion bubble dynamics*. European Journal of Mechanics - B/Fluids **42**, p. 69-91, (2013).

[35]   Wang, Q. X., Yeo, K. S., Khoo, B. C. & Lam, K. Y. *Nonlinear interaction between gas bubble and free surface*. Computers & Fluids **25**(7), p. 607-628, (1996).

[36]   Pearson, A., Cox, E., Blake, J. R. & Otto, S. R. *Bubble interactions near a free surface*. Engineering Analysis with Boundary Elements **28**(4), p. 295-313, (2004).

[37]   Brujan, E. A., Nahen, K., Schmidt, P. & Vogel, A. *Dynamics of laser-induced cavitation bubbles near elastic boundaries: influence of the elastic modulus*. Journal of Fluid Mechanics **433**, p. 283-314, (2001).

[38]   Brujan, E. A., Nahen, K., Schmidt, P. & Vogel, A. *Dynamics of laser-induced cavitation bubbles near an elastic boundary*. Journal of Fluid Mechanics **433**, p. 251-281, (2001).

[39]   Brujan, E. A., Keen, G. S., Vogel, A. & Blake, J. R. *The final stage of the collapse of a cavitation bubble close to a rigid boundary*. Physics of Fluids **14**(1), p. 85-92, (2001).

[40]   Cui, P., Zhang, A. M. & Wang, S. P. *Small-charge underwater explosion bubble experiments under various boundary conditions*. Physics of Fluids **28**(11), (2016).

[41]   Hunter, K. S. & Geers, T. L. *Pressure and velocity fields produced by an underwater explosion*. The Journal of the Acoustical Society of America **115**(4), p. 1483-1496, (2004).

References

[42] Geers, T. L. & Hunter, K. S. *An integrated wave-effects model for an underwater explosion bubble*. Journal of the Acoustical Society of America **111**(4), p. 1584-1601, (2002).

[43] Blake, F. G. *Bjerknes Forces in Stationary Sound Fields*. The Journal of the Acoustical Society of America **21**(5), p. 551-551, (1949).

[44] Birkhoff, G. & Zarantonello, E. H. *Jets, Wakes, and Cavities*. 1st Ed. (Elsevier, 1957).

[45] Krieger, J. R. & Chahine, G. L. *Acoustic signals of underwater explosions near surfaces*. The Journal of the Acoustical Society of America **118**(5), p. 2961-2974, (2005).

[46] Gibson, D. C. & Blake, J. R. *Growth and collapse of cavitation bubbles near flexible boundaries*. in *7th Australasian Conference on Hydraulics and Fluid Mechanics*. (Institution of Engineers Australia, 1980).

[47] Blake, J., Taib, B. & Doherty, G. *Transient cavities near boundaries. Part 1. Rigid boundary*. Journal of Fluid Mechanics **170**, p. 479-497, (1986).

[48] Zhang, A. M., Cui, P., Cui, J. & Wang, Q. X. *Experimental study on bubble dynamics subject to buoyancy*. Journal of Fluid Mechanics **776**, p. 137-160, (2015).

[49] Chahine, G. L. *Numerical and experimental study of explosion bubble crown jetting behavior*. Report No.: 96003-1-ONR, (Dynaflow Inc. , Fulton, MD, 1997).

[50] Naudé, C. F. & Ellis, A. T. *On the Mechanism of Cavitation Damage by Nonhemispherical Cavities Collapsing in Contact With a Solid Boundary*. Journal of Basic Engineering **83**(4), p. 648-656, (1961).

[51] Zhang, S., Wang, S. P. & Zhang, A. M. *Experimental study on the interaction between bubble and free surface using a high-voltage spark generator*. Physics of Fluids **28**(3), p. 032109, (2016).

[52] Benjamin, T. B. & Ellis, A. T. *The Collapse of Cavitation Bubbles and the Pressures thereby Produced against Solid Boundaries*. Philosophical Transactions of the Royal Society of London. Series A, Mathematical and Physical Sciences **260**(1110), p. 221-240, (1966).

[53] Lauterborn, W. & Bolle, H. *Experimental investigations of cavitation-bubble collapse in the neighbourhood of a solid boundary*. Journal of Fluid Mechanics **72**(02), p. 391-399, (1975).

[54] Plesset, M. S. & Chapman, R. B. *Collapse of an initially spherical vapour cavity in the neighbourhood of a solid boundary*. Journal of Fluid Mechanics **47**(02), p. 283-290, (1971).

[55] Snay, H. G. *Model tests and scaling*. (DTIC Document, 1964).

[56] De Candia, S., Ojeda, R., Reid, W. D., Ratcliffe, M. & Binns, J. *The Whipping Response of a Submerged Free-Free Cylinder Due to Underwater Explosions*. in *International Maritime Conference - Pacific 2017*. Sydney, NSW. (2017).

[57] Chertock, G. *Transient Flexural Vibrations of Ship‑Like Structures Exposed to Underwater Explosions*. The Journal of the Acoustical Society of America **48**(1B), p. 170-180, (1970).

[58] Ranlet, D. & Daddazio, R. P. *A submerged shock response problem suitable for use as a benchmark*. in *68th Shock and Vibration Symposium*. Hunt Valley, MD. (SAVIAC, 1997).

[59] Kwon, Y. & Fox, P. *Underwater shock response of a cylinder subjected to a side-on explosion*. Computers & structures **48**(4), p. 637-646, (1993).

[60] Brett, J. M., Yiannakopoulos, G. & van der Schaaf, P. J. *Time-resolved measurement of the deformation of submerged cylinders subjected to loading from a nearby explosion*. International Journal of Impact Engineering **24**(9), p. 875-890, (2000).

[61] Yiannakopoulos, G. *Small Scale Elastic Deformation Studies from an Underwater Explosion on a Submerged Thin Walled Platform Cylinder*. in *77th Shock & Vibration Symposium*. Monterey, CA. (SAVIAC, 2006).

[62] Yiannakopoulos, G. *Fluid and Structure Interaction Studies on a Submerged Platformed Cylinder near an Underwater Explosion*. in *78th Shock & Vibration Symposium*. Philadelphia, PA. (SAVIAC, 2007).

[63] van Aanhold, J., Trouwborst, W. & Vaders, J. *Underwater Shock Response Analysis of a Floating Cylinder*. in *79th Shock & Vibration Symposium*. Orlando, FL. (SAVIAC, 2008).

[64] Welch, W. P. *Mechanical shock on naval vessels*. Report No.: NAVSHIPS 250-660-26, (Bureau of Ships, Washington, D.C., 1946).

[65] Hellqvist, K. *A large-scale submarine shock test carried out as part of the Swedish Shock Design Development Program*. in *The Shock and Vibration Bulletin*. Vol. 2, p. 129-136, (SAVIAC, 1981).

[66] Liu, G., Liu, J., Wang, J., Pan, J. & Mao, H. *A numerical method for double-plated structure completely filled with liquid subjected to underwater explosion*. Marine Structures **53**, p. 164-180, (2017).

[67] Bishop, J. H. *Underwater shock standards and tests for naval vessels*. in *Conference on Dynamic Loading in Manufacturing and Service*. Melbourne, VIC. (Institution of Engineers Australia, 1993).

[68] Hellqvist, K. *Submarine shock resistance*. (Kockums AB).

[69] MIL-S-901C (NAVY): *Military Specification Shock Tests, H.I. (High-Impact) Shipboard Machinery Equipment, and Systems, Requirements For* (United States Department of Defense, 1963).

[70] Clements, E. *Shipboard shock and Navy devices for its simulation*. Report No.: 7396, (U.S Naval Research Laboratory, Washington, D.C., 1972).

[71] MIL-S-901D (NAVY): *Military Specification Shock Tests, H.I. (High-Impact) Shipboard Machinery Equipment, and Systems, Requirements For* (United States Department of Defense, 1989).

[72] Belsheim, R. & O'Hara, G. *Shock design of shipboard equipment-dynamic design analysis method*. Report No.: NAVSHIPS 250-423-30, (Bureau of Ships, Washington D.C., 1961).

[73] Scavuzzo, R. J. & Pusey, H. C. *Principles and techniques of shock data analysis*. 4th Ed. (Shock and Vibration Information Analysis Center, 2011).

[74] Gaberson, H. A. *Pseudo velocity shock spectrum rules for analysis of mechanical shock*. in *IMAC XXV: A Conference & Exposition on Structural Dynamics*. Orlando, FL. (Society for Experimental Mechanics, 2007).

[75] Gaberson, H. A. & Chalmers, R. H. *Modal velocity as a criterion of shock severity*. Shock and Vibration Bulletin **40**(2), p. 31-49, (1969).

[76] *Shock Design Criteria for Surface Ships* (1995).

[77] O'Hara, G. *Shock spectra and shock design spectra*. Report No.: 5386, (U.S. Naval Research Laboratory, Washington, D.C., 1959).

[78] Chertock, G. *The Flexural Response of a Submerged Solid to a Pulsating Gas Bubble*. Journal of Applied Physics **24**(2), p. 192-197, (1953).

[79] Bannister, K. A. *Whipping analysis techniques for ships and submarines*. The Shock and Vibration Bulletin **50**, p. 83-98, (1980).

[80] Geers, T. L. *Excitation of an Elastic Cylindrical Shell by a Transient Acoustic Wave*. Journal of Applied Mechanics **36**(3), p. 459-469, (1969).

[81] Carrier, G. F. *The interaction of an acoustic wave and an elastic cylindrical shell*. (Division of Applied Mathematics, Brown University, 1951).

[82]   Lax, J., Sette, W. & Gooding, R. *Additional calculations on the response of a uniform cylindrical shell to a pressure pulse*. in *6th Conference on Progress in Underwater Explosions Research*. (1953).

[83]   Murray, W. W. *Interaction of a spherical acoustic wave with a beam of circular cross section*. Underwater Explosion Research Division Report, p. 1-55, (1955).

[84]   Forrestal, M. J. *Response of an Elastic Cylindrical Shell to a Transverse, Acoustic Pulse*. Journal of Applied Mechanics **35**(3), p. 614-616, (1968).

[85]   Forrestal, M. J. & Alzheimer, W. E. *Transient Motion of a Rigid Cylinder Produced by Elastic and Acoustic Waves*. Journal of Applied Mechanics **35**(1), p. 134-138, (1968).

[86]   Mindlin, R. D. & Bleich, H. *Response of an elastic cylindrical shell to a transverse, step shock wave*. Journal of Applied Mechanics **20**(2), p. 189-195, (1953).

[87]   Haywood, J. H. *Response of an elastic cylindrical shell to a pressure pulse*. The Quarterly Journal of Mechanics and Applied Mathematics **11**(2), p. 129-141, (1958).

[88]   Hughes, T. J. *The finite element method: linear static and dynamic finite element analysis*. Reprint Ed. (Courier Corporation, 2012).

[89]   LSTC. *LS-DYNA Theory Manual [DRAFT]*. (Livermore Software Technology Corporation, Livermore, CA, 2018).

[90]   Hicks, A. N. *MSWHIP-An Improved Computer Program to Calculate the Elastic Whipping Response of a Ship to an Underwater Explosion Including Bubble Migration*. Naval Ship Research and Development Center, (1971).

[91]   Brennan, D. *et al. Single High Fidelity Geometric Data Sets for LCM-Model Requirements*. Report No.: MARTEC-TR-06-18, (MARTEC Limited, Halifax, Nova Scotia, 2006).

[92]   Geers, T. L. *Residual Potential and Approximate Methods for Three‑Dimensional Fluid‑Structure Interaction Problems*. The Journal of the Acoustical Society of America **49**(5B), p. 1505-1510, (1971).

[93]   Geers, T. L. *Doubly asymptotic approximations for transient motions of submerged structures*. The Journal of the Acoustical Society of America **64**(5), p. 1500-1508, (1978).

[94]   Geers, T. L. & Felippa, C. A. *Doubly asymptotic approximations for vibration analysis of submerged structures*. The Journal of the Acoustical Society of America **73**(4), p. 1152-1159, (1983).

[95]   DeRuntz, J. A. *The underwater shock analysis code and its applications*. in *60th Shock and Vibration Symposium*. Virginia Beach, Virginia. (Shock and Vibration Information Center, 1989).

[96]   LSTC. *USA LS-DYNA Users Manual - USA Release 7.5.3*. (Livermore Software Technology Corporation, Livermore, CA, 2018).

[97]   Geers, T. L. & Park, C. *Optimization of the G&H bubble model*. Shock and Vibration **12**(1), p. 3-8, (2005).

[98]   Price, R. S. *Similitude equations for explosives fired underwater*. Report No.: NSWC TR 80-299, (Naval Surface Warfare Center, Dahlgren, VA, 1979).

[99]   De Candia, S., Flockhart, C. & Cannon, S. M. *Whipping assessment of a scale warship structure*. in *8th Australasian Congress on Applied Mechanics: ACAM 8*. Melbourne VIC, Australia. (Institution of Engineers Australia, 2014).

[100]   Shin, Y. S. *Ship shock modeling and simulation for far-field underwater explosion*. Computers & Structures **82**(23–26), p. 2211-2219, (2004).

[101]   Zhang, A. M., Yao, X. L. & Li, J. *The interaction of an underwater explosion bubble and an elastic–plastic structure*. Applied Ocean Research **30**(3), p. 159-171, (2008).

[102] Zong, Z., Wang, J., Zhou, L. & Zhang, G. *Fully nonlinear 3D interaction of bubble dynamics and a submerged or floating structure*. Applied Ocean Research **53**, p. 236-249, (2015).

[103] Hirt, C. W., Amsden, A. A. & Cook, J. *An arbitrary Lagrangian-Eulerian computing method for all flow speeds*. Journal of computational physics **14**(3), p. 227-253, (1974).

[104] Barras, G., Souli, M., Aquelet, N. & Couty, N. *Numerical simulation of underwater explosions using an ALE method. The pulsating bubble phenomena*. Ocean Engineering **41**, p. 53-66, (2012).

[105] Civilian-Military Joint Investigation Group. *Joint Investigation Report: On the attack against ROK ship Cheonan*. (Ministry of National Defense, 2010).

[106] Zhang, A. M., Yang, W.-S., Huang, C. & Ming, F.-r. *Numerical simulation of column charge underwater explosion based on SPH and BEM combination*. Computers & Fluids **71**, p. 169-178, (2013).

[107] Gingold, R. A. & Monaghan, J. J. *Smoothed particle hydrodynamics: theory and application to non-spherical stars*. Monthly notices of the royal astronomical society **181**(3), p. 375-389, (1977).

[108] de Graaf, K. *The bubble dynamics and pressure field generated by a seismic airgun* PhD Thesis, University of Tasmania, (2014).

[109] De Candia, S., Ojeda, R., Ratcliffe, M. & Reid, W. D. *The whipping response of a submerged platform subjected to near-field, non-contact underwater explosions*. Report No.: DST-Group-RR-0451, (Defence Science and Technology Group, Fishermans Bend, VIC, 2018).

[110] AS/NZS 1163:2009: *Cold-formed structural steel hollow sections* (SAI Global, Australia, 2009).

[111] AS 2129-2000 (R2016): *Flanges for pipes, valves and fittings* (SAI Global, Australia, 2000).

[112] LSTC. *LS-DYNA R8.0 Keyword Manual*. (Livermore Software Technology Corporation, Livermore, CA, 2015).

[113] LSTC. *USA LS-DYNA Users Manual - USA Release 7.5*. (Livermore Software Technology Corporation, Livermore, CA, 2014).

[114] Elsys AG. *TPCX & TPCE Specification*. (Elsys AG, Mellingerstrasse 12, CH-5443 Niederrohrdorf, Switzerland, 2012).

[115] PCB Piezotronics. *Model W138A05 ICP Pressure Sensor Installation and Operating Manual*. (PCB Piezotronics, Inc., 3425 Walden Avenue, Depew, NY 14043, 2015).

[116] Neptune Sonar Limited. *Shock Gauge Transducer Datasheet - Model T11*. (Neptune Sonar Limited, Kelk Lake, Kelk, East Yorkshire, 2017).

[117] Micro Measurements. *Special Use Sensors - Weldable Strain Gages*. (Vishay Precision Group, Inc., Malvern, Pennsylvania, United States, 2014).

[118] TML. *High temperature Weldable Strain Gauges Series AW*. (Tokyo Sokki Kenkyujo Co., Ltd., 8-2, Minami-Ohi 6-chome, Shinagawa-ku, Tokyo 140-8560, Japan, 2017).

[119] OriginLab. *Origin Help*. (OriginLab Corp, Northampton, MA, 2018).

[120] Walter, P. L.   (Meggitt, Endevco, San Juan Capistrano, CA, USA, 2001).

[121] Rajendran, A. M. & Bless, S. J. *High strain rate material behavior*. Report No.: AFWAL-TR-85-4009, (Air Force Wright Aeronautical Laboratories, Dayton, OH, 1985).

[122] LSTC. *LS-DYNA R10.1 Keyword Manual*. (Livermore Software Technology Corporation, Livermore, CA, 2018).

[123] Austube Mills. *Design Capacity Tables for Structural Steel Hollow Sections*. (Austube Mills, 2013).

[124] De Candia, S., Flockhart, C. & Cannon, S. M. *Whipping analysis of a submerged free-free cylinder*. in *9th Australasian Congress on Applied Mechanics (ACAM9)*. Sydney, NSW. (Institution of Engineers Australia, 2017).

[125] Stettler, J. W. *Damping mechanisms and their effects on the whipping response of a submerged submarine subjected to an underwater explosion* Master of Science (Mechancial Engineering) Thesis, Massachusetts Institute of Technology (MIT), (1995).

[126] Sturt, R. **DAMPING_FREQUENCY_RANGE notes – Version 5*. (Arup, 2015).

[127] LSTC. *DAMPING_FREQUENCY_RANGE support note February 2018*. (Livermore Software Technology Corporation, Livermore, CA, 2018).

[128] LSTC. *LS-DYNA R9.0 Keyword Manual*. (Livermore Software Technology Corporation, Livermore, CA, 2016).

[129] LSTC. *LS-DYNA R10.0 Keyword Manual*. (Livermore Software Technology Corporation, Livermore, CA, 2017).